Thèse de Doctorat

Présentée en vue de l'obtention du titre de

Docteur de l'Université de Lorraine

Spécialité Chimie Théorique et Informatique

par

Audrey DEYAWE KONGMENECK

Investigation des mécanismes d'activation et de couplage du canal potassique voltage-dépendant $K_V7.1$ dans les cardiomyocytes à l'aide de méthodes computationnelles

Investigation of activation and coupling mechanisms of the voltage-gated potassium channel $K_V7.1$ in cardiomyocytes using computational methods

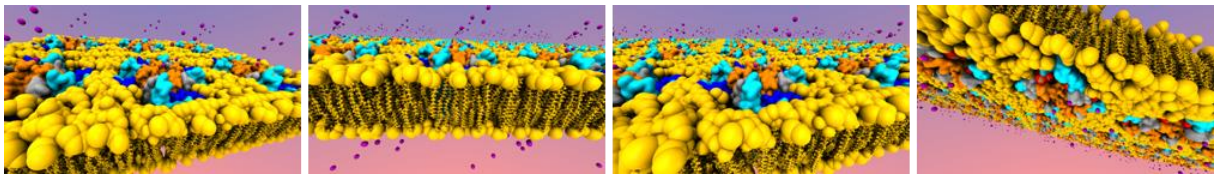

Soutenue publiquement le 07 décembre 2020

à l'Université de Lorraine, Nancy, France

Rapporteurs :

Pr. Catherine ETCHEBEST – Université Paris VII Diderot, Paris, France

Dr. Jérôme HENIN – Laboratoire de Biochimie Théorique (UPR 9080 CNRS), Institut de Biologie Physico-Chimique, Paris, France

Examinateurs :

Dr. Sara LIIN - Department of Clinical and Experimental Medicine, Linköping University, Linköping, Suède

Dr. Gildas LOUSSOUARN – Institut du thorax (UMR 1087 CNRS), Université de Nantes, Nantes, France

Dr. François DEHEZ – LPCT (UMR 7019 CNRS), Université de Lorraine, Nancy, France

Directeur de thèse :

Dr. Mounir TAREK – LPCT (UMR 7019 CNRS), Université de Lorraine, Nancy, France

Investigation des mécanismes d'activation et de couplage du canal potassique voltage-dépendant $K_V7.1$ dans les cardiomyocytes à l'aide de méthodes computationnelles

Résumé

Le canal $K_V7.1$ est une protéine transmembranaire diffusant des ions K^+ de manière sélective à travers la membrane plasmique lorsque cette dernière se dépolarise. Au sein du myocarde, $K_V7.1$ est co-exprimé avec la sous-unité auxiliaire KCNE1. Plusieurs expériences ont mis en évidence les effets de KCNE1 sur l'activité de $K_V7.1$, lui conférant des propriétés permettant au complexe $K_V7.1$-KCNE1 de générer le courant IK_S lors du potentiel d'action cardiaque. Les nombreuses mutations au niveau des séquences de $K_V7.1$ et KCNE1 associées à des arythmies cardiaques sévères font du canal $K_V7.1$ une cible thérapeutique majeure.

$K_V7.1$ est un tétramère dont chaque sous-unité α compte six hélices transmembranaires (S1 à S6). Les quatre premières hélices forment le domaine sensible au voltage (VSD), tandis que les deux dernières forment celui du pore (PD). Le mécanisme d'activation de $K_V7.1$ s'effectue par le biais d'une translation de l'hélice S4 vers le feuillet externe de la membrane en deux étapes, stabilisant le VSD en trois états stables : repos, intermédiaire, et activé. Ces conformations sont capables d'ouvrir ou de fermer le pore via un processus appelé couplage. Ainsi, les états du canal $K_V7.1$ sont Repos/Fermé (RC), Intermédiaire/Ouvert (IO) et Activé/Ouvert (AO). En présence des sous-unités β KCNE1, le couplage n'a pas lieu à l'état intermédiaire, donc les états du canal IK_S sont RC, Intermédiaire/Fermé (IC) et AO. En outre, le phospholipide PIP_2 (phosphatidylinositol-4,5-bisphosphate) joue un rôle crucial dans le couplage VSD-PD et l'ouverture du pore des canaux K_V7.

Malgré les informations apportées par les études fonctionnelles et structurales du canal $K_V7.1$, en absence et en présence de ses modulateurs KCNE1 et PIP_2, le mécanisme de son couplage à l'échelle atomistique reste à découvrir.

Nous avons abordé ce problème en exploitant des techniques computationnelles telles la dynamique moléculaire (DM). Etant donnée la complexité de la fonction de $K_V7.1$, cette étude avait trois objectifs, le premier étant d'identifier les interactions protéine-protéine stabilisant chacun de ses états, le deuxième étant de décrire les effets de KCNE1 sur son mécanisme de couplage VSD-PD, le troisième étant de caractériser les effets de KCNE1 sur les interactions des sous-unités α $K_V7.1$ avec PIP_2. Nous avons bâti des modèles par homologie de $K_V7.1$ dans ses trois états, en utilisant la structure cristallographique et des résultats de modélisations du canal homologue $K_V1.2$ comme patron.

Nous avons effectué des simulations de DM de 500 ns pour chaque modèle, encastré dans une membrane virtuelle entourée de deux couches d'une solution de [KCl] à 150 mM, afin de reproduire une dynamique réaliste du canal dans nos systèmes, et ce en absence et en présence de KCNE1 et de PIP_2.

L'analyse des trajectoires DM obtenues visait en premier lieu à valider nos modèles par rapport aux données expérimentales. Par la suite, nous avons identifié les interactions « état-dépendantes » dans les modèles les plus robustes, permettant de prédire les changements de conformation inhérents à l'ouverture de $K_V7.1$, en absence de KCNE1 d'une part, et en sa présence d'autre part. De cette manière, il a été possible d'identifier les interactions protéine-protéine permettant à KCNE1 d'inhiber le mécanisme de couplage VSD-PD de $K_V7.1$ lorsque son VSD est à l'état intermédiaire, ainsi que celles permettant à KCNE1 d'amplifier les effets de couplage de $K_V7.1$ lorsque son VSD est à l'état activé. Enfin, pour chaque état stable de $K_V7.1$, nous avons identifié et comparé les interactions protéine-lipide au sein des modèles $K_V7.1$ et des modèles IK_S.

Nos modèles ont été validés par des études fonctionnelles menées par nos collaborateurs (Pr. Jianmin Cui) de l'université Washington de Saint-Louis, Etats-Unis. Cette étude intégrative a révélé un couplage inédit, conceptualisé par un modèle « main-et-coude » ayant probablement lieu dans l'ensemble des familles de canaux K_V1 à K_V9.

L'hélice S6 de $K_V7.1$ présente un motif SFF (338-340) fortement conservé au sein des canaux de la famille K_V7. L'espace conformationnel des résidus SFF au sein des trajectoires DM de $K_V7.1$ et d'IK_S a révélé l'existence d'une porte hydrophobe inédite, définie par des orientations « état-dépendantes » de F339 et F340, et validée par des études fonctionnelles.

Les analyses effectuées sur les trajectoires DM des modèles IK_S indiquent qu'un garrot, formé par les interactions entre KCNE1 et PIP_2 autour de la région intracellulaire des hélices S6, induisent la fermeture du pore dans les états RC et IC. Enfin, la recherche des déterminants moléculaires de la modulation du couplage de $K_V7.1$ par KCNE1 indique que ce dernier perturbe le modèle « main-et-coude » conçu à la base pour le canal $K_V7.1$.

Investigation of activation and coupling mechanisms of the voltage-gated potassium channel $K_V7.1$ in cardiomyocytes using computational methods

Abstract

$K_V7.1$ channel is a transmembrane protein that opens to selectively diffuse K^+ ions across the plasma membrane upon membrane depolarization. In the myocardium tissue, $K_V7.1$ is co-expressed with the ancillary subunit KCNE1. Several experiments conducted on $K_V7.1$ along with KCNE1 revealed its effects on $K_V7.1$ function, which modify its properties allowing for the $K_V7.1$-KCNE1 complex to generate the I_{Ks} current during the cardiac action potential. As numerous mutations of $K_V7.1$ and KCNE1 sequences are linked to severe cardiac arrhythmias, $K_V7.1$ channel constitutes a major therapeutic target.

Each α-subunit of the $K_V7.1$ tetramer counts six transmembrane helices (S1 to S6), the first four ones forming the voltage-sensor domain (VSD), and the last two forming the pore domain (PD). This channel has a 2-step activation mechanism involving an upward translation of S4 across the membrane towards its outer leaflet and stabilizing the VSD in three stable states: resting, intermediate and activated. These conformations can induce pore opening or closure by a process called VSD-PD coupling. Accordingly, the states for $K_V7.1$ channel are Resting/Closed (RC), Intermediate/Open (IO) and Activated/Open (AO). In the presence of KCNE1 β subunits, the coupling is suppressed for the intermediate state, thus the states for I_{Ks} channel are RC, Intermediate/Closed (IC) and AO. Furthermore, the PIP_2 (phosphatidylinositol-4,5-bisphosphate) phospholipid plays a crucial role in the VSD-PD coupling and pore opening mechanisms of K_V7 channels.

Despite the information drawn from both functional and structural studies of $K_V7.1$ channel in absence and presence of its modulators KCNE1 and PIP_2, its VSD-PD coupling mechanism remains unclear at an atomistic level.

To address this issue, we harnessed computational techniques, including molecular dynamics (MD) simulations. Given the complexity of the $K_V7.1$ function, the study had three main objectives. The first one was the characterization of the VSD-PD coupling mechanism underlying the transitions between RC, IO and AO states of $K_V7.1$ channel. The second one was the characterization of the modulation effects of KCNE1 on the VSD activation and VSD-PD coupling mechanisms of $K_V7.1$ α-subunits. The third one was to characterize the effects of KCNE1 on the affinity between $K_V7.1$ α-subunits and PIP_2 lipids.

We built homology models of $K_V7.1$ in its three states, using the crystallographic structure and previous models of the homologous $K_V1.2$ channel as a template. We conducted 500 ns MD simulations on each model embedded in a model membrane surrounded by two slabs of a 150 mM [KCl] solution to reproduce a realistic dynamics of the channel, in absence and presence of KCNE1 subunits and PIP_2 molecules. At first, we performed analyses of MD trajectories in order to validate the models with respect to experimental data. Then, we proceeded to identify the state-dependent protein-protein interactions in the most robust models, allowing for the prediction of the conformational changes leading to the open states of $K_V7.1$ in absence of KCNE1 on one hand, and in presence of KCNE1 in the other hand. The comparison of the obtained results allowed one to determine the molecular determinants of KCNE1 inhibition of $K_V7.1$ VSD-PD coupling when the VSD reaches its intermediate state, as well as those of KCNE1 amplification of $K_V7.1$ VSD-PD coupling effects when the VSD is in its activated state. Finally, we identified and compared the state-dependent protein-lipid interactions in $K_V7.1$ models and IK_S models.

Our $K_V7.1$ models were validated via functional studies conducted by our collaborators (Pr. Jianmin Cui) from Washington University of Saint-Louis in the USA. Altogether, the joint study revealed a novel VSD-PD coupling mechanism that we conceptualized by a "hand-and-elbow model" likely to occur in all domain swapped (K_V1- K_V9) channels.

The S6 helix of $K_V7.1$ has a motif SFF (338-340), highly conserved in K_V7 family. The conformational space of SFF residues in $K_V7.1$ and IK_S MD trajectories revealed the existence of an unidentified yet hydrophobic gate defined by state-dependent orientations of F339 and F340, which was also validated by functional studies.

The analyses of IK_S MD trajectories suggest that the interactions between KCNE1 and PIP_2 form a tourniquet around the cytoplasmic region of S6, leading to pore closure in both RC and IC models. Finally, the investigation of the molecular determinants of the modulation of $K_V7.1$ VSD-PD coupling mechanism by KCNE1 in our IK_S models suggests that KCNE1 disrupts the "hand-and-elbow" model of the VSD-PD coupling we previously revealed for the $K_V7.1$ channel.

Related publications

Deyawe A, Kasimova MA, Delemotte L, Loussouarn G, Tarek M (2018) Studying Kv Channels Function using Computational Methods. Methods Mol Biol 1684:321–341 . https://doi.org/10.1007/978-1-4939-7362-0_24

Hou P, Kang PW, Deyawe Kongmeneck A, Yang N-D, Liu Y, Shi J, Xu X, White KM, Zaydman MA, Kasimova MA, Seebohm G, Zhong L, Zou X, Tarek M, Cui J (2020) Two-stage electro–mechanical coupling of a K_V channel in voltage-dependent activation. Nature Communications 11:1–14 . https://doi.org/10.1038/s41467-020-14406-w

Acknowledgements

It would be very difficult to thank everyone in only one page since the help of numerous people allowed me to finish the writing of this PhD thesis.

First and foremost, I would like to thank my supervisor Dr Mounir Tarek, for your help, your patience, and the tremendous amount of things I have learn from you, especially your work ethic and the importance to give our best, and to seek for the best. My PhD course has not been an easy road but working under your supervision made me grow up as a scientist, and also as a person, which is priceless. I want to thank my predecessor's Dr Lucie Delemotte and Dr Marina Kasimova, for the fabulous work they made before, and also after I started my PhD course, which constitute an excellent starting point and a great source of inspiration for my scientific work. I also want to thank Pr Jianmin Cui, for the opportunity he gave me to work with him and his research team, including Dr Panpan Hou and Po-Wei Kang, with which I have also learned a huge number of things. Our collaboration allowed to sublime our respective work, which is amazing.

I also want to thank Pr Catherine Etchebest, Dr François Dehez, Dr Jérôme Hénin, Dr Gildas Loussouarn and Dr Sara Liin, for the honor to save time to take part in my PhD defense as jury members. Specifically, I want to thank Pr Catherine Etchebest and Dr Jérôme Hénin, for accepting to dedicate time to review my PhD thesis.

I also want to warmly thank Dr Antonio Monari and Séverine Bonenberger, for all the insightful discussions and conversations, and of course for all the pep talks you gave me during my entire PhD course. I also want to thank everyone in the LPCT lab for their hospitality, and for the numerous good times I spent with everyone in and out of the lab. I also want to thank all my fellow PhD students, and the interns, for their support and the heartfelt laughs we shared.

My acknowledgments would not be complete without a special thank for my family. To my mother Esther, my father Roger, my step-father Philippe, my sisters Michèle, Joëlle and Gladis, my brothers Bertrand and Gérard, my nieces Téha and Tess, my nephews Ethan and Yaël, as well as my godfather Martin, the rest of my family, and of course my dear friends Anthony and Axelle, for their unconditional love and support, up to this moment when I write these words, with my eyes fogged of tears.

Outline

Table of figures

Introduction

In living organisms, membranes are made of two layers of amphiphilic lipids which are joined by hydrophobic interactions, named a lipid bilayer [1]. The specific architecture of the latter enables plasma membranes to isolate the cytoplasm from the extracellular media. Similarly, within a cell, other membranes are able to isolate the content of the various organelles from the cytoplasm.

Membranes are permeable to gas and liposoluble compounds, but not to aqueous ones. In this way, plasma membranes allow for the conservation of distinct ion charge imbalance between the cytoplasm and the extra-cellular media, maintained by the function of Na-K pumps, conferring a transmembrane electrical voltage called the resting potential. During the 18th century, it was discovered that plasma membranes are able to generate and propagate electric currents in muscle cells. Since the last decade of the 19th century, various experimental methods that belong to electrophysiology have been developed in order to characterize these currents in various cell membranes, leading to the discovery of excitable cells, such as muscular cells, myocardium cells, neuronal cells, or pancreatic β-cells. The plasma membranes of this particular type of cells are characterized by periodic sharp increase/decrease of their transmembrane potential. Named action potential, this phenomenon is generated upon a specific transmembrane voltage called "threshold voltage" and can occur across one cell, or a series of cells that are linked by gap junctions, allowing for the cytoplasms of two distinct cells to communicate.

Typically localized in plasma membranes, the main role of Voltage-Gated Ion Channels (VGICs) consists in passively transporting ions across the lipid bilayer. Triggered by specific transmembrane potentials, each VGIC is able to open in order to *selectively* diffuse ions (e.g. Na^+ K^+ Ca^{2+} Cl^-) at a given voltage value, allowing for the fast transport of these chemical entities that bear an electrical charge along their electrochemical gradient. In the remaining we will discard the Chloride channels (CLCs) as they constitute an evolutionarily family of voltage-gated channels that are structurally unrelated to the other known voltage-gated channels.

Thus, the propagation of an action potential relies on the coordination of a set of voltage-gated cation channels (VGCC) which successively open and close with various selective and specific properties. Accordingly, these action potentials are known to orchestrate numerous biological events such as muscle contraction or synaptic signaling. Therefore, VGCCs are crucial for the function of vital organs such as the brain, the heart, muscle, and pancreas. Each of these tissues possess an action potential with specific features.

Despite the major contribution of electrophysiology experiments in the unraveling of VGCC function, this discipline cannot provide information about their structure.

The emergence of DNA sequencing managed to provide a molecular insight into the structure of VGCC. Indeed, their primary sequence determination shed light on VGCC as a super family of 143 transmembrane proteins that are present in most eukaryotic cells and characterized by multiple consensus sequences. This superfamily gathers several families of ion channels which are classified by their ion selectivity. Thus, Na_V, Ca_V, and K_V families are composed of ion channels that are selective to Na^+, Ca^{2+}, and K^+, respectively. The potassium channel family is the largest subfamily among VGCC. It comprises 40 channels, clustered into 12 families, among which 9 (K_V1-K_V9) are domain-swapped. These proteins are involved in an important number of biological functions, including homeostasis, secretion, muscle contraction and transmission of the nerve impulse.

DNA sequencing has also allowed for the determination of the mutations that are associated with malfunctions of the VGCC, usually associated with the disruption of action potentials. These functional defects are related to diverse congenital diseases called channelopathies, which include epilepsy, cardiac arrhythmias, and deafness among others.

Hence, VGCC constitute numerous therapeutic targets for the treatment of a large number of diseases. To that extent, we focus our entire work on a particular potassium (K^+) ions VGCC called $K_V7.1$. Across the membranes of heart striated muscle cells, the diffusion of potassium ions through $K_V7.1$ channel generates the slow delayed rectifier current, also known as the IK_S current. It occurs specifically at the end of the action potential, allowing the membrane to return to its resting potential. This specific action potential controls the heartbeat pace, as it occurs periodically in order to elicit the heart contraction. As a consequence, $K_V7.1$ channel mutations induce channel dysfunction, which are characterized by changes of cardiac repolarization time, and therefore prolongation or shortening of the cardiac action potential.

The understanding of the modulation mechanisms of $K_V7.1$ leading to the generation of the IK_S current in the heart encompasses various scientific disciplines, including cell biology, electrophysiology, molecular biology, and computational biochemistry. A large body of experiments allowed to identify the existence of different conformations adopted by the voltage sensor domain (VSD) of $K_V7.1$, which are resting, intermediate and activated, and the effects of these conformations on the pore domain (PD) conformation, open or closed, through a particular mechanism called VSD-PD coupling. Experiments also highlighted two main effectors of $K_V7.1$ VSD-PD coupling mechanism. The first one is the ancillary subunit KCNE1, which is co-expressed along with $K_V7.1$ channel, endowing the latter distinct physical and chemical properties in relation to $K_V7.1$ alone. The second one is the phosphatidylinositol-4,5-bisphosphate (PIP_2) lipid, which has been identified as a key element of $K_V7.1$ channel function.

Thanks to the emergence of advanced structural biology techniques, a large number of protein structures have been unraveled at a nanoscopic scale [2]. However, owing to their partially hydrophobic surfaces, flexibility, and lack of stability, only a small number of VGCC have managed to be resolved through X-ray crystallography for the last two decades. In the frame of this work, the 3D structure of $K_V1.2$, the first mammalian K_V channel to be resolved by X-ray crystallography, turned out to be essential. Starting from the structure-activity relationship of evolutionarily related proteins, computational methods of molecular modeling such as comparative modeling turned out to be useful and accurate for the prediction of the tridimensional structure of $K_V7.1$ channel, whose none of the state's 3D structure was unresolved at the beginning of this project.

These obtained structures are typically used to provide a molecular insight into experimental findings, with the help of simulations. Thereby, we harnessed these computational techniques to build 3D models of the three stable conformations known for $K_V7.1$ channel. The use of experimental data as structural constraints would maximize their reliability.

To predict the molecular aspects of the function of $K_V7.1$ channel, computer simulation methods such as molecular dynamics (MD) allow one to study an isolated chemical system containing a protein alone or along with its specific environment including modulatory subunits, lipids and molecules such as water or ions. The simulation of these chemical systems allows to follow the time evolution of a protein model in its biological environment in order to obtain an atomistic insight into the dynamics of the protein, either at its equilibrium (brute-force or unbiased MD), or in certain conditions in order to induce a specific motion related to its function (under voltage for instance), or in interaction with a small compound. The collection of the time-dependent conformations generated by a simulation is defined as an MD trajectory. Here, we designed several chemical systems for the three 3D models of $K_V7.1$ along with PIP_2 lipids, in the absence and the presence of KCNE1, all mimicking the biological environment of the channel. They were submitted each to ~500 ns unbiased MD simulations. The analyses of the resulting MD trajectories consisted in the investigation of protein-protein interactions, and protein-lipid ones to determine those which stabilize each state of $K_V7.1$. These results allowed for the prediction of the mechanisms related to $K_V7.1$ function at an atomistic level of precision, as well as the effects induced by the presence of each of its known modulators, namely KCNE1 and PIP_2.

In the first chapter of this manuscript, we will present ion channels in the context of the cardiac action potential (AP) to gain a better understanding of the way in which $K_V7.1$ is implicated in its repolarization phase. The reader would hence be more familiar with the biological mechanisms that link our ion channel of interest, $K_V7.1$ and the various cardiac arrhythmias caused by its significant number of mutations. The computational methods and strategies we used to design the structure in order to study the function of $K_V7.1$ channel through the knowledge-based metastable states models we have designed will be presented in Chapter II. Results that demonstrate the key modulatory roles of both KCNE1 ancillary subunit and PIP_2 lipids on $K_V7.1$ activation and coupling mechanisms will be detailed in Chapter III, and their coherence in relation with both experimental and computational results obtained for $K_V7.1$ channel alone will be discussed in Chapter IV. The conclusions and perspectives drawn from this research project will be outlined in Chapter V.

Chapter I. State of the art

Le canal $K_V7.1$ est une protéine transmembranaire qui joue un rôle prépondérant au sein des membranes des cardiomyocytes, qui assurent la contraction du myocarde qui a lieu à chaque battement cardiaque. $K_V7.1$ assure le transport passif d'ion potassium à travers ces membranes, c'est -à-dire qu'il diffuse des ions potassium depuis le cytoplasme vers le milieu extracellulaire. La découverte des canaux ioniques à ouverture voltage dépendante tels que $K_V7.1$ est le résultat de plusieurs siècles de recherche scientifique, riches en avancées cruciales de la part de plusieurs disciplines scientifiques diverses et variées. Parmi ces disciplines, on trouve l'électrophysiologie, la biologie cellulaire, moléculaire et structurale, ainsi que la biophysique, la bioinformatique et la chimie. L'électrophysiologie s'est révélée être celle qui a joué le rôle le plus important dans l'identification des courants électriques au sein des cellules et des tissus à la fin du 18ème siècle.

Dans ce chapitre, nous avons passé en revue les avancées scientifiques clés qui ont permis de découvrir, d'identifier et de caractériser le canal $K_V7.1$ ainsi que son environnement (**Chapter I.1**). Ayant été découvert dans le cadre de plusieurs maladies génétiques à l'origine d'arythmies cardiaques, nous avons pris le parti de fournir une explication détaillée du rôle que ce canal joue dans le déclenchement des battements cardiaques (**Chapter I.2**). A partir de la description de la fonction cardiaque à l'échelle macroscopique, nous avons progressivement diminué l'échelle d'observation jusqu'à l'échelle microscopique, là où le courant ionique généré par $K_V7.1$ participe au potentiel d'action, un processus biologique défini par une série d'événements sous-tendant la contraction musculaire, qui s'effectue de façon automatique et spontanée dans le cœur (**Chapter I.3**). Par la suite, nous sommes placés à l'échelle moléculaire afin de présenter les recherches ayant permis de déterminer les structures primaire, secondaire, tertiaire et quaternaire du canal $K_V7.1$ (**Chapter I.4**). Nous nous sommes ensuite intéressés aux façons dont un peptide transmembranaire d'une part, et un lipide membranaire d'autre part, peuvent moduler l'activité du canal $K_V7.1$ au sein des cardiomyocytes, par rapport aux autres tissus au sein desquels ce canal est exprimé.

Enfin, nous avons montré comment la combinaison des résultats de biologie moléculaire et de certaines méthodes computationnelles ont permis de mieux expliquer la fonction du canal $K_V7.1$ au sein des cellules musculaires lisses du myocarde. Nous avons mis en évidence les zones d'ombre qui nécessitent de mener des recherches plus poussées. Dans le cadre de cette thèse, nos hypothèses se sont articulées autour de l'étude des différentes conformations adoptées par le canal $K_V7.1$, ainsi que les potentiels changements conformationnels inhérents à la présence du peptide transmembranaire et du lipide membranaire connus pour être capables de moduler son activité. A partir de ces hypothèses, nous avons expliqué l'intérêt que peuvent présenter l'utilisation des méthodes computationnelles dans la compréhension des mécanismes d'action et de modulation du canal $K_V7.1$ à l'échelle moléculaire.

K_V7.1 channel is an integral protein which plays a crucial role in the membranes of the cardiomyocytes, which are responsible for the contraction of the myocardium necessary for the heartbeat. Specifically, K_V7.1 diffuses potassium ions through the membranes, from the cytoplasm towards the extracellular medium. The discovery of voltage-gated ion channels has been made possible thanks to several centuries of scientific research, full of advances from various scientific fields such as electrophysiology, cellular biology, molecular biology, structural biology, biophysics and computational biology and chemistry. Among these numerous scientific areas, electrophysiology has played the most important role in the identification of these proteins since it allowed for the identification of electrical currents in cells and tissues.

In this chapter, we reviewed the key scientific milestones that allowed for the discovery of the K_V7.1 channel and its direct environment (**Chapter I.1**), followed by a thorough explanation of its role in the heart rhythm (**Chapter I.2**). Starting from a macroscopic description of the heart and its main function, we progressively decreased the scale of observation toward the microscopic level at which the K_V7.1 channel participates in the action potential, defined by a series of biological processes that are required for the automatic triggering of the heartbeat (**Chapter I.3**). Then, we focused on the molecular level by presenting the primary, secondary, tertiary, and quaternary structures of the K_V7.1 channel, and then by explaining how a transmembrane peptide and a membrane lipid were both found to be able to modulate the function of the K_V7.1 channel in the heart striated muscle cells (**Chapter I.4**).

We showed how the combination of molecular biology and computational methods allowed for a better understanding of the function of K_V7.1 in the heart muscle cells. Finally, we presented the shaded areas that still remain further research. The hypotheses we made about the modulation roles of both the transmembrane peptide and the membrane lipid on the function of the K_V7.1 channel lie on the study of its different conformations and the potential conformational modifications of the K_V7.1 channel structure in the presence of these effectors. From these hypotheses, we presented the ways in which the use computational methods can increase the level of understanding of the various mechanisms of action and modulation of the K_V7.1channel at the molecular level.

Chapter I.1. From electrophysiology to molecular modeling: A history of ion channels

Electric currents were discovered to occur through muscle and brain tissues of various species. The first known breakthrough about these currents was led by the physiologist Luigi Galvani in 1791, when he and his wife Lucia noticed that an isolated frog muscle was able to move when connected with conductive matter. Based on this discovery, they hypothesize that the frog muscle contained an electric fluid able to generate an electric current, which Galvani called "animal current" [3]. One year later, the physicist Alessandro Volta started to be interested in Galvani's work, but did not believe in his "animal current" hypothesis, convinced that the frog muscle motion was due to the connection of this electric fluid with the metals used in Galvani's experiments. Nevertheless, Volta was convinced of the existence of organic electric fluids and conducted several experiments in order to reproduce an artificial fluid able to conduct electric currents, which lead him to the invention of his famous voltaic pile in 1800 [4] in which electric currents were generated by aqueous solutions. Thirty years later, the chemist Michael Faraday showed that the currents in voltaic piles were actually the products of redox reactions. Since the 19th century, the knowledge of the electric signals occurring within the living world had led to the development of experimental techniques allowing for the tracking of the electricity across cell membranes.

This quest, which had initiated since Galvani's discovery, was marked by major scientific successes that were awarded by several Nobel prizes during the 20th century. In 1889, based on Volta's invention and Faraday's conclusions, the chemist Walther Nernst published an equation that relates the electric potential produced by a redox reaction occurring in electrochemical batteries such as the voltaic one with the energetic contribution of each chemical species involved in the redox reaction. Then he applied this equation on biological membranes to relate the equilibrium potential E_{ion} of a given ion across a membrane (also called reversal potential, it refers to the membrane potential value in which there is no flux of the ion across the membrane) with its concentration gradient [5]:

$$E_{ion} = \frac{RT}{zF} \times \ln\left(\frac{[ion]_{out}}{[ion]_{in}}\right)$$

Where E_{ion} is expressed in millivolts (mV), R is the ideal gas constant in Joules.Kelvin^{-1}.mol^{-1} (J.K^{-1}.mol^{-1}), T is the temperature in K, z is the net charge of the ion, F is the Faraday constant in Coulomb.mol^{-1} (C. mol^{-1}), while $[ion]_{out}$ and $[ion]_{in}$ are the concentrations of the ion, expressed in mol.L^{-1}, outside and inside the cell, respectively. For this breakthrough, Nernst obtained a Nobel Prize in 1920.

In early 1900s, the biophysicist Julius Bernstein, who invented the rheotome, an innovative electrophysiology tool allowing for the recording of action potential velocities in excitable cells, applied Nernst equation in order to express the electrochemical potential of a given ion across a given plasma membrane. This application lead Bernstein to establish his membrane theory which stated that the living cells are surrounded by a double-layered membrane with a selective permeability to potassium [6], inducing a charge imbalance between each side of the double-layered membrane (Figure I.1.1). During action potential, the potassium permeability of the membrane increases, and its potential is reduced to a lower value. Meanwhile, the molecular structure of plasma membranes was unknown at this time.

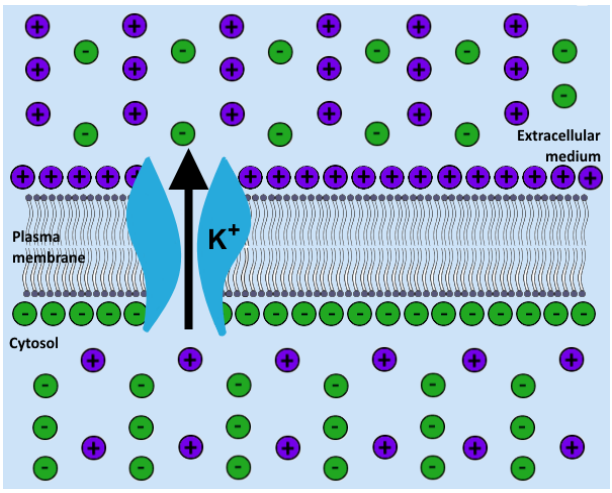

Figure I.1.1: The membrane theory of Julius Bernstein.
According to Bernstein, the ionic distribution around the double-layered cell membrane induces a charge imbalance induced by the asymmetric distribution of positive ions (in purple) and negative ions (in green) around the plasma membrane (in gray) in its resting state. The selective permeability to potassium ions (black arrow), represented by a pore (depicted in blue) allows to maintain the resting potential. Despite the membrane being depicted here as a lipid bilayer, the chemical structure of plasma membranes was unknown at the age of Bernstein theory.

The lipid bilayer was first discovered in 1925 thanks the study of Gorter and Grendel on red blood cells [7]. The experiment consisted in the centrifugation of a known number of red blood cells of several mammals, followed by the dissolution of the liposoluble sediments into benzene.

The dissolution product was then spread on a Langmuir-Blodgett trough [8] in order to measure the surface area of the red blood cells plasma membranes. This molecular architecture is mainly composed of amphiphilic phospholipids whose polar heads are facing the aqueous intra and extra cellular media, while the hydrophobic tails of the phospholipids are facing each other at the core of the membrane. This arrangement allows for the isolation of the cytoplasm from the extracellular matrix, confirming Bernstein theory. While Gorter and Grendel assumed these lipids as constituting most of the membrane surface area of red blood cells, several studies conducted afterwards proved their assumption wrong [9]. Indeed, considering the known physical properties of the membrane allowing for the cell to perform exchanges with the extracellular matrix, cell biologists tended to predict that plasma membranes were also containing proteins, without knowing how those proteins are interacting with the lipid bilayer [10, 11, 1].

With this scientific knowledge, the voltage-dependent ion selectivity of plasma membranes was partly explained a few decades later. Indeed, during the 50s, Hodgkin and Huxley managed to identify distinct ion selective current through a squid giant axon.

To do that, they conducted an experiment called voltage-clamp, which consists in the application of a given electric potential on a plasma membrane using two electrodes that are connected to an electrical circuit designed to record the intensity I of the ionic currents in picoAmpères (µA) that are flowing through the membrane (Figure I.1.2).

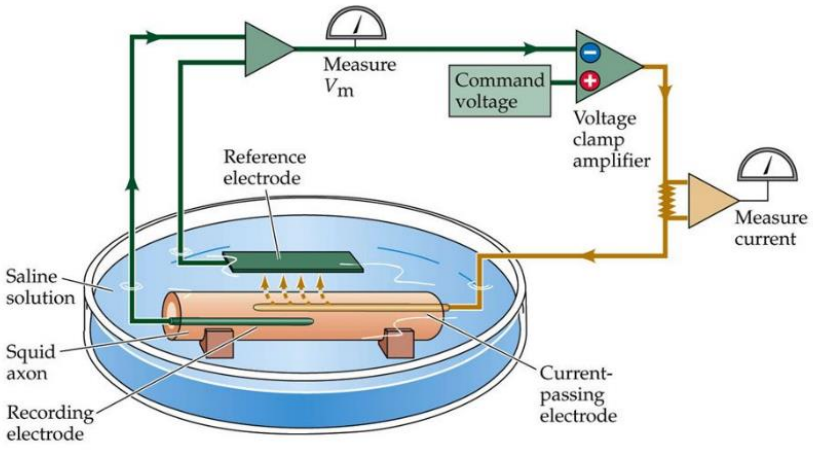

Figure I.1.2: The voltage-clamp technique applied on a squid giant axon.
This picture represents the squid axon in which both the recording electrode (in green) and the current-passing electrode (in brown) are inserted. These electrodes are plugged in an electric circuit that allows to record the current intensity I across the membrane of the squid giant axon upon an applied transmembrane voltage V_m.

Hodgkin and Huxley identified two distinct ionic currents (Figure I.1.3): an inward sodium current that occur in depolarized conditions, when the applied voltages were increasing towards positive values; and a potassium outward current in hyperpolarized conditions, when the applied voltages were decreasing towards negative values [12].

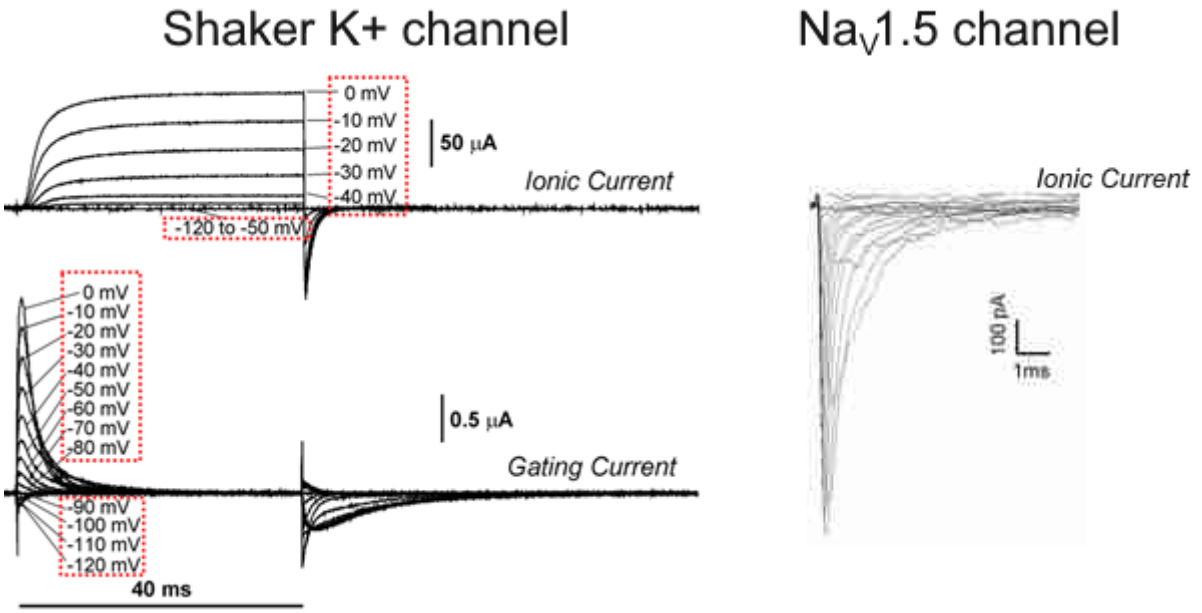

Figure I.1.3: Example of current recordings obtained by voltage-clamp experiments.
On the left panel the graphs project the time evolution of potassium current amplitudes (top panel) and gating current intensities (bottom panel) of the voltage-gated "Shaker" K^+ channel in microAmpères (µA) upon different transmembrane voltages (circled in red dots) in millivolts (mV), applied successively from -120 mV to 0 mV. The right panel depicts the time evolution of sodium current amplitudes of the voltage-gated sodium channel Na$_V$1.5 in µA. The direction of the curves indicates the direction of the ion flux, which is outward for K^+ ions and inward for Na^+ ions. Adapted from [13, 14].

Based on these results, they manage to conceptualize a mathematical model allowing for the characterization of action potentials in excitable cells [15]. The model is based upon an electric circuit (Figure I.1.4) that involves the lipid bilayer as a capacitance C_M, while ion transporters that generate the currents I_{Na}, I_K and I_l are assimilated as electrical resistances $R_{Na} = 1/g_{Na}$, $R_K = 1/g_K$ and $R_l = 1/g_l$, respectively, each of them being branched in derivation. From this model they developed a differential equation allowing to express the current intensity across a given membrane at a given time, as a function of the transmembrane voltage. The equation is expressed as follows:

$$I = C_M \frac{dV}{dt} + I_{Na} + I_K + I_l$$

where I is the total membrane current, C_M is the capacitance, V the difference of membrane potential with respect to the resting potential, t is the time.

I_{Na}, I_K and I_l are the components of the ionic current, carried by sodium ions, potassium ions, and chloride ions (along with other ions), respectively (Figure I.1.4). As these components can also be expressed as a function of their equilibrium potentials, the previous equation can also be noted as follows:

$$I = C_M \frac{dV}{dt} + g_{Na}(V - V_{Na}) + g_K(V - V_K) + g_l(V - V_l)$$

where g_{Na}, g_K and g_l are the conductances of sodium, potassium, and chloride ions, and V_{Na}, V_K and V_l their reversal potentials, respectively.

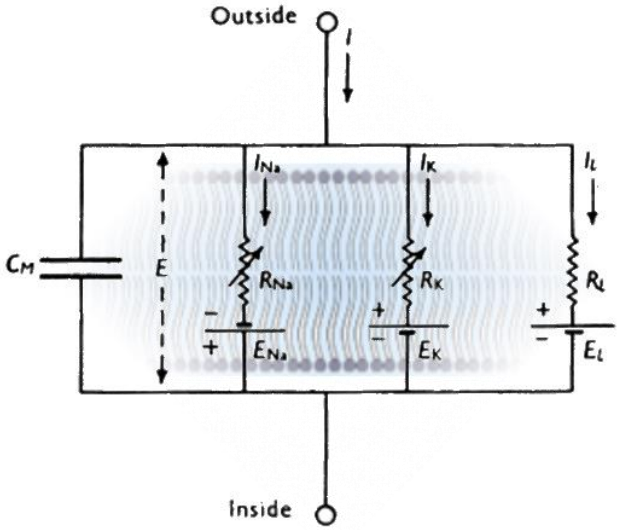

Figure I.1. 4: The electrical circuit model of the membrane by Hodgkin and Huxley.
The circuit (in the foreground) shows how the membrane current I, divided into different ion currents in the lipid bilayer (in background) are passing through the membrane upon a given voltage E. The resistances R_N, R_K and R_l are varying with both time and membrane potential.

The scientific work of Hodgkin and Huxley was awarded by a Nobel Prize in medicine in 1963, and officialized electrophysiology as a new scientific discipline. Later in that decade, they used the Nernst equation to determine the equilibrium potential of a membrane permeable to two or more distinct ions. Hence, for the membrane of squid giant axon, the Goldman-Hodgkin-Katz equation would be expressed as follows:

$$E_m = \frac{RT}{F} \ln\left(\frac{P_{Na}[Na^+]_{out} + P_K[K^+]_{out} + P_{Cl}[Cl^+]_{out}}{P_{Na}[Na^+]_{in} + P_K[K^+]_{in} + P_{Cl}[Cl^+]_{in}}\right)$$

Where the membrane potential E_m is expressed in V, the selectivity P_{ion} for a given ion is expressed in m/s, the extracellular and intracellular concentrations $[ion]_{out}$ and $[ion]_{in}$, respectively, are expressed in mol/m^3.

Moreover, Hodgkin and Huxley also identified transient currents that appeared to be triggered by a change in transmembrane potential [15]. They predicted these currents to be generated by a part of ion channels which might act as a “voltage sensor”.

Their prediction was confirmed a couple of decades later, when transient currents were recorded on isolated squid giant axons in such conditions that ionic currents were suppressed so it could not be related to the transport of ions though the membrane. In addition, the direction of these currents appeared to be voltage-dependent: outward in depolarized conditions, and inward in hyperpolarized conditions. Consequently, these currents were identified as gating currents (Figure I.1.3).

In parallel, cell biologists made significant progress in the knowledge of the chemical structure of plasma membranes during the 60’s [1], leading to Singer’s well-known membrane fluid mosaic model [16].

As lipids have been previously shown to constitute half of the membrane surface of erythrocytes [17], this model assumes that the rest of the membrane surface was occupied by integral proteins with hydrophilic intracellular and extracellular regions, and hydrophobic regions allowing for their stability in the low dielectric environment induced by the lipid tails of amphiphilic membrane lipids. Logically, the proteins that span the lipid bilayer allow for the cells to perform exchanges with the extracellular matrix such as ion transport, as shown by Hodgkin and Huxley’s experiments despite of their lack of stability in low dielectric environments [18]. Numerous experiments conducted later confirmed Singer’s fluid mosaic model, which is still assumed to be correct nowadays [19].

In the early 70s, a new advanced experimental technique called patch-clamp (Figure I.1.5), which allowed for the direct measure of transmembrane current upon an applied potential in one cell (through "whole-cell" configurations), and then in one or a few ion channels (through "cell-attached", "inside-out" and/or "outside-out" configurations), has started to be developed. This technique was basically designed for the direct observation of the open and the closed states of a single VGCC and was further made possible by Erwin Neher and Bert Sakmann [20], who obtained a Nobel Prize in medicine in 1991. By realizing a tight seal between a glass pipette filled with a saline solution and a membrane patch from a frog muscle fiber, they were able to record transitions of a single ion channel between its conducting and its non-conducting states through discrete oscillations in the recorded ionic current.

By assimilating ion channels as resistors with respect to the theory of Hodgkin and Huxley, it became possible to record the conductance of a single channel with the use of Ohm's law:

$$V_m - V_{ion} = R_{channel} \times I$$

in which V_m is the applied voltage during patch-clamp measurement, V_{ion} is the reversal potential of the diffused ion, $R_{channel}$ is the resistance of the ion channel of interest, and I the recorded current. As the resistance of a channel is the inverse of its conductance, I can be expressed as follows:

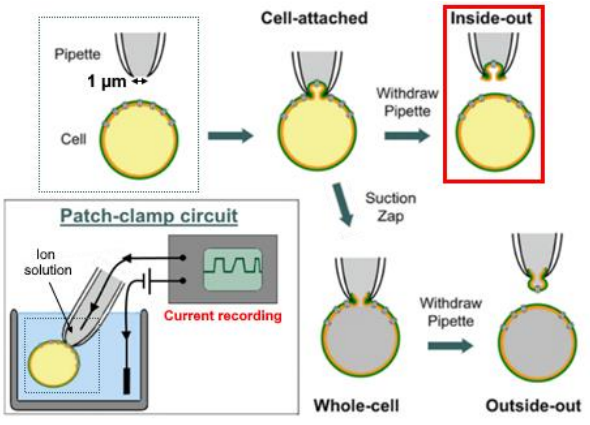

Figure I.1.5: The patch-clamp technique.
The top panel shows the distinct configurations that can be used to record ion currents of a cell membrane. The saline solution of the glass pipette is colored in gray, while the cytoplasm of the cell is colored in yellow. The lower left panel depicts the usual patch clamp circuit, in which the electrodes (in black) are put into the glass pipette and the water bath containing the cell and plugged to the device that records the current and displays the measures on an oscilloscope (in green). The "inside-out" configuration, is circled in red as it is the most common one used for the recordings of voltage-gated ion channels currents.

$$I = (V_m - V_{ion}) \times \frac{1}{R_{channel}} = (V_m - V_{ion}) \times g_{channel}$$

And the conductance of the ion channel of interest can be expressed as:

$$g_{channel} = \frac{I}{(V_m - V_{ion})}$$

Furthermore, several studies reported that ionic currents can be specifically abolished in presence of toxins [21] or small compounds [22]. With the use of the patch clamp technique in "whole-cell" configuration, it became possible to study the effects of these compounds on the ionic currents. Despite the advances in the comprehension of ion channels function, the chemistry of these macromolecules remained unknown at the end of the 70s [23].

During the 80s, the emergence of DNA sequencing allowed for the determination of primary sequences of voltage-gated ion channels, starting from the gene coding of the eel voltage-gated sodium channel [24], followed by the Shaker gene of Drosophila Melanogaster, known to code for a voltage-gated potassium channel [25]. The sequences of these two genes turned out to be relatively similar. Indeed, these genes appeared to code for protein sequences which present cytoplasmic N_{TER} and C_{TER} regions, separated by a tetrameric transmembrane region composed of four domains of six α-helices, separated from each other with intra or extra-cellular loops of various lengths. Within each domain, the first four helical segments S1 to S4 form the voltage-sensor domain (VSD), while the last two helices called segments S5 and S6 are forming the pore domain (PD).

These patterns of helices result from the oligomerization of four tetramers in K_V channels, while in Na_V channels, the four domains are joined in one single sequence (Figure I.1.6). The particular primary sequence of the voltage-gated sodium channel turned out to be found later in voltage-gated calcium channels [26]. VGCC family members are sharing a common transmembrane pore domain presenting a four-fold topology of two domains [26], composed of two transmembrane helices separated by a loop which is embedded in the hydrophobic core of the membrane, forming the tetrameric pore through which the ions are translocated. Despite of the shared transmembrane topology and consensus sequences of the primary sequences of VGCC, some members of this superfamily of ion channels are not voltage-gated only. The channels of the cyclic nucleotide-gated (CNG) family [27, 28], are ligand-gated and merely sensitive to transmembrane potential.

In addition, the ion channels of the K_{Ca}, and HCN families, despite their sensitivity to voltage, can also be activated by Ca^{2+} ions [29] and cAMP [30], respectively, as shown by their respective ligand binding sites. Despite sharing the transmembrane topology of the other VGCC [26], the nonselective cation channels of the transient receptor proteins family (TRP) are usually diffusing ion fluxes upon various stimuli [31]. Nevertheless, these channels are sharing a common function, which is the facilitated diffusion of ions across the membrane down their concentration gradient [32]. The main families of voltage-dependent channels are actively participating in action potentials, such as the Na_V, Ca_V, and K_V families which are composed of ion channels that are selective to Na^+, Ca^{2+}, and K^+, respectively.

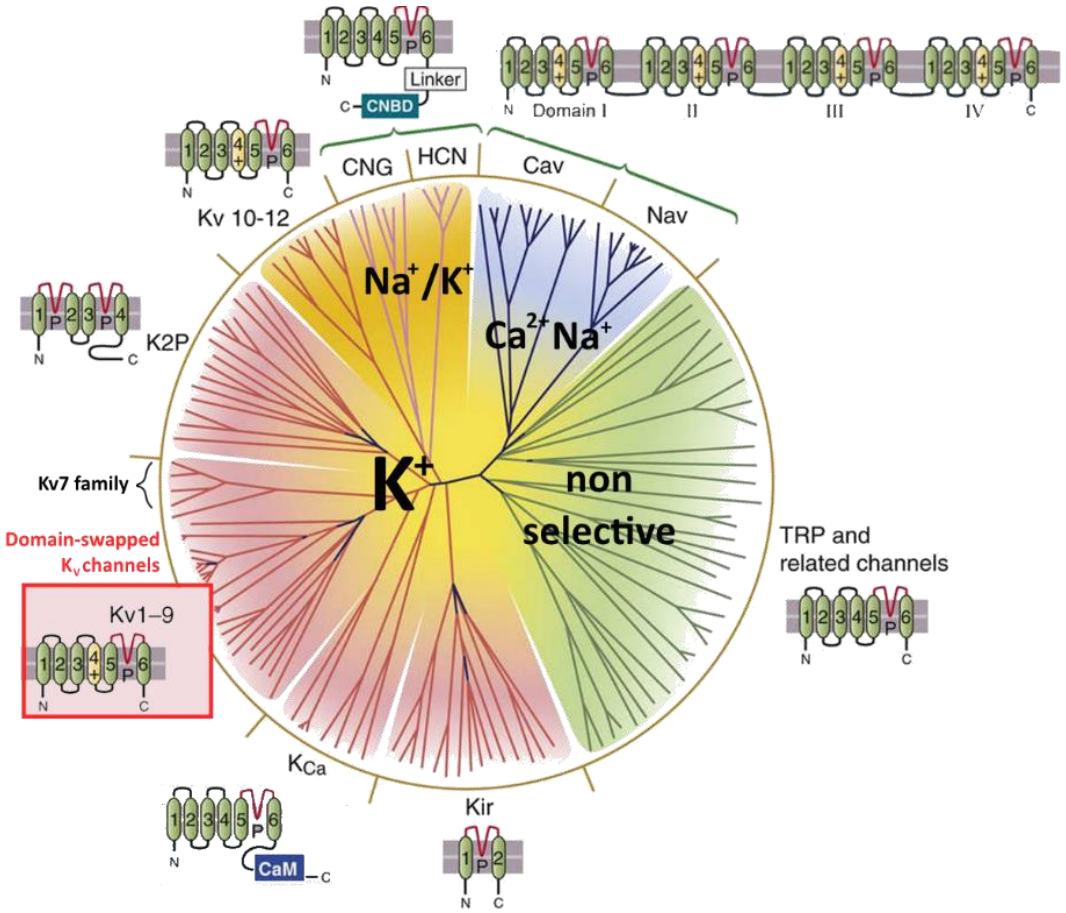

Figure I.1.6: Phylogenetic tree including the Voltage-Gated Cation Channels (VGCC) superfamily. This schematic view depicts the evolutionary related 143 members of the VGCC superfamily, which are clustered in four subfamilies. The TRP non-selective cation channels are represented in green lines, the calcium and sodium selective channels in blue lines, the CNG/HCN sodium-potassium channels in pink lines, and potassium selective channels in red lines. For each subfamily, a topology of their transmembrane segments is displayed around the circle. The binding sites of the CNG, HCN and K_{Ca} channels are represented in blue squares. The topology of the subunits of K_V channel family, which includes $K_V7.1$ channel, is framed in red. Adapted from [24].

In the fourth membrane spanning sequence of voltage-gated ion channels, numerous basic residues such as arginine or lysine were positioned every three amino acids (Figure I.1.7). Called gating charges, these residues were identified later as responsible for the gating currents [33, 34] which were discovered earlier. All together, these results constitute a second evidence that confirm the predictions of Hodgkin and Huxley.

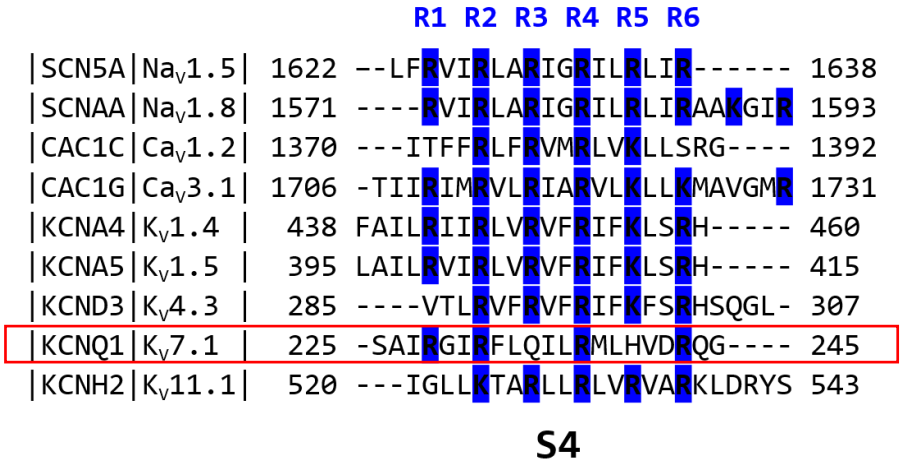

Figure I.1.7: Conserved gating charges in the fourth segment of various voltage-gated ion channels. The figure shows a sequence alignment of the S4 segment in the selective VGCC involved in the cardiac action potential. The first and second columns report the gene name and the subunit name of the channel. The strongly conserved basic residues R1 to R6, also known a gating charges, are highlighted in blue. The sequence of the channel K_V7.1, which is the object of this thesis, is framed in red.

Later, new experiments that associate electrophysiology experiments with fluorometry assays were developed in order to monitor the conformational change in relation with VSD activation as well as the conductance of a single channel, both according to the transmembrane potential. This technique, called patch-clamp fluorometry [35] is commonly used nowadays and consists in attaching a fluorescent tag to the extracellular N_{TER} region of the S4 segment of the VGCC of interest. In the same manner, voltage-clamp fluorometry [36] (VCF) allows for the independent recording of both VSD movement (optical fluorescence) and pore conductance (ionic current) in an entire cell. This method has been regularly used to study the function of K_V7.1 channel, in which a fluorophore is attached to the S3-S4 linker and tracked to record the changes of fluorescence emission during voltage-dependent activation. Before the democratization of this method, gating currents used to be monitored on wild-type VGCC in presence of channel blockers [37] or non-conductive VGCC mutants [12, 38, 39]. However, due to their small amplitudes, these currents are most often quite difficult to record.

By comparing the gating current/voltage relationship with the ionic current relationship (Figure I.1.8), using normalized gating current and ionic current values, one was able to determine the stable VSD conformations of a VGCC according to the direction of the gating current along the membrane, as well as the conductive state of each stable conformation of the channel. With this hybrid method, it is now possible to determine the voltage-dependence of VSD activation (F/V curve or Q/V curve) of a given wild-type VGCC, when the S4 segment moves across the membrane upon depolarization, along with the voltage-dependence of the conductance (I/V or G/V curve) when the channel starts to conduct ions [40]. In this way, these experiments can be performed on malfunctioning mutants or wild-type VGCC in presence of channel effectors in order to assess their effect on the channel function. The use of Xenopus oocytes to perform both gene expression and electrophysiology had a significant impact on the development of these electrophysiology techniques [41, 42]. However, these numerous methods, while being extremely enriching, cannot provide an accurate molecular insight into the tridimensional (3D) structure of VGCC, nor into their mechanism of function at a molecular scale.

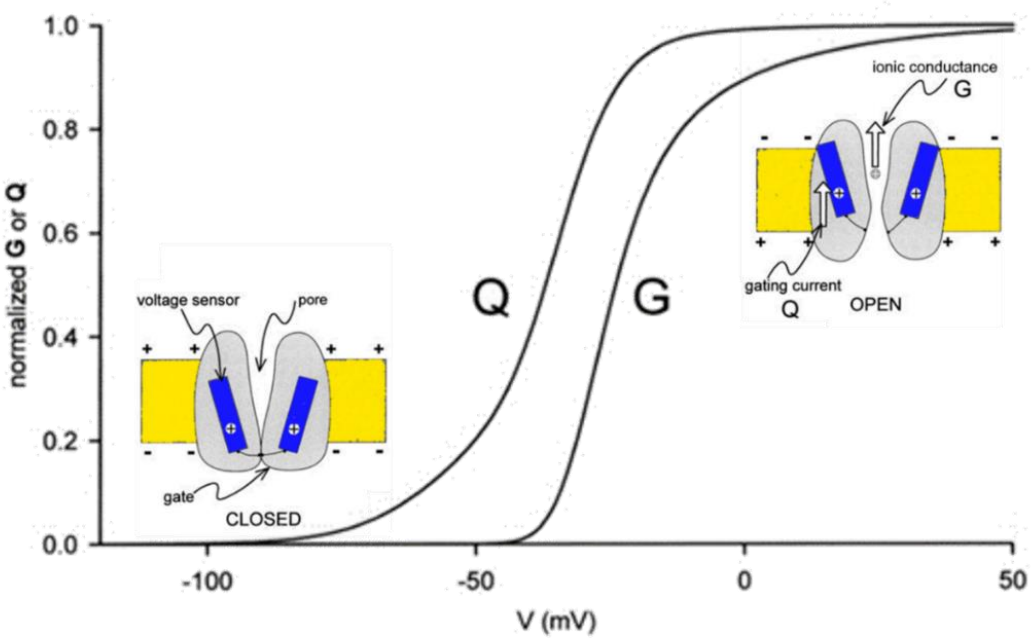

Figure I.1.8: The Q/V and G/V curves of a voltage-gated ion channel.
The graph shows the voltage-dependence (V) of the conductance (G) and the gating charge displacement (Q) for a voltage-gated ion channel. Two pictures are depicting a schematic view of voltage-gated ion channel in its closed state at hyperpolarized voltages, and in its open state at depolarized voltages. The yellow area accounts for the lipid bilayer, while the gray area represents the channel, with the S4 segment in blue, with its gating charges in a white circle, and the linker is depicted as a black line joining S4 and the gate. The direction of both gating charges and ion flux at depolarized potentials is represented by white arrows. Adapted from [40].

The hydrophobic properties of transmembrane proteins constitute a major limitation for their crystallization, which is required prior to obtain high resolution coordinates through X-ray diffraction. Indeed, it was almost impossible to obtain the transmembrane region of an integral protein through X-ray crystallography at this time. Due to their hydrophobicity and *a fortiori* their molecular weight, transmembrane proteins cannot be resolved through liquid NMR experiments either [43]. Nevertheless, the bacteriorhodopsin, a prokaryotic proton pump also known as purple membrane, was the first TM protein structure to be resolved experimentally at 7 Å by Richard Henderson through transmission electron microscopy in the middle of the 70s [44]. The protein was crystallized in a glucose solution, providing a good preservation of the protein structure. Electron diffraction was then performed on the crystal in the microscope, followed by the application of electron crystallography, a 3D reconstruction method, on the resulting 2D micrographs [45] in order to determine the protein 3D coordinates. Henderson's results contributed to the development of a new electron microscopy method allowing for the structural analysis of biomolecules at a nanoscopic scale. Called Cryo-Electron Microscopy (CryoEM), the technique was developed by Ken Taylor and Bob Gleaser in 1974 [46], and consisted in the development of a customized transmission electron microscope, in which the sample (whether a 2D crystal or a thin film) was maintained at a cool temperature (~4 K) in liquid nitrogen to minimize the deformation effects induced by the electron beam on the resulting image (Figure I.1.9,B-C). A few years later, based on their first CryoEM results, Knapek and Dubochet [47] postulated that without those damaging effects, the shape and the internal structure of the sampled biomolecules would be preserved, allowing to obtain their high-resolution images. Although the reduction of the deformation effects on "frozen" samples turned out not to be reproducible two years later [48], Jean Dubochet, firmly convinced of his theory, developed a new freezing technique called "plunged-freezing" for aqueous biological samples. By freezing the thin film sample at a fast rate, the contained water molecules have not enough time to transform into ice, allowing them to reach a vitrified state in which the structure of the macromolecule is preserved (Figure I.1.9, B).

With this new technique, Dubochet managed to resolve the structure of an entire virus through Cryo-EM in 1984 [49]. This method constituted a major breakthrough in the development of the cryo-microscopy, as it allowed for the resolution of numerous biological entities such as vesicles, organelles, chromosomes, membranes, muscle fibers and even DNA. However, the atomic resolution of membrane proteins through CryoEM still had limitations. Indeed, the micrographs obtained by microscopy could only provide 2D coordinates. Therefore, 3D reconstruction methods were still required to obtain 3D coordinates at an atomic resolution (< 4.0 Å). Despite of the high-resolution (3.5 Å) structure of bacteriorhodopsin, obtained by Richard Henderson in 1990 using electron crystallography [50], the obtention of transmembrane proteins in 2D crystals for CryoEM was not straightforward [51]. Those limitations were later overcome by the contributions of Joachim Frank in the development of single-particle analysis, a computational 3D reconstruction method which does not require to obtain a crystallized sample of the studied biomolecule (Figure I.1.9, D). With this methodology [52], he managed to obtain low-resolution 3D structure of the 70S *E.coli* ribosome obtained from CryoEM micrographs, with a 45 Å resolution of [53] in 1991. Thanks to the advances in computational speed, he managed to obtain the 3D structure of the same ribosome with a resolution of 25 Å four years later [54]. In addition, the improvements made in the CryoEM systems, including in the stability of the cryostage [55] and in the precision of the electronic detectors [56], allowed to obtain the 3D structures of several membrane proteins such as the pore domain of the nicotinic acetylcholine receptor [57] and aquaporin subunit [58], with resolutions of 4 Å and 1.9 Å, respectively in the 2000s. These high-resolution structures preceded a “resolution revolution” that occurred in early 2010s [59], as the CryoEM turned out to be a solid alternative to the NMR and the X-ray crystallography for the structural characterization of large structures such as ribosomes [60], as well as flexible structures such as membrane proteins, including ion channels [61]. One of the advantages of the Cryo-EM technique is that it allows for the direct determination of these protein in detergents, along with its long loops and/or flexible and glycosylated regions, that usually need to be removed for X-ray crystallization. Indeed, in order to determine the structure of an integral protein, the latter must be extracted from the membrane using detergent solubilization techniques.

The structural determination of transmembrane proteins through CryoEM elicited the development of specific purification methods (Figure I.1.9, A), such as detergent micelles, nanodiscs or saposin lipid nanoparticles, in order to mimic their native environment in CryoEM samples [62]. For their respective contributions in the development of CryoEM, Jean Dubochet, Joachim Frank and Richard Henderson won the chemistry Nobel Prize in 2017.

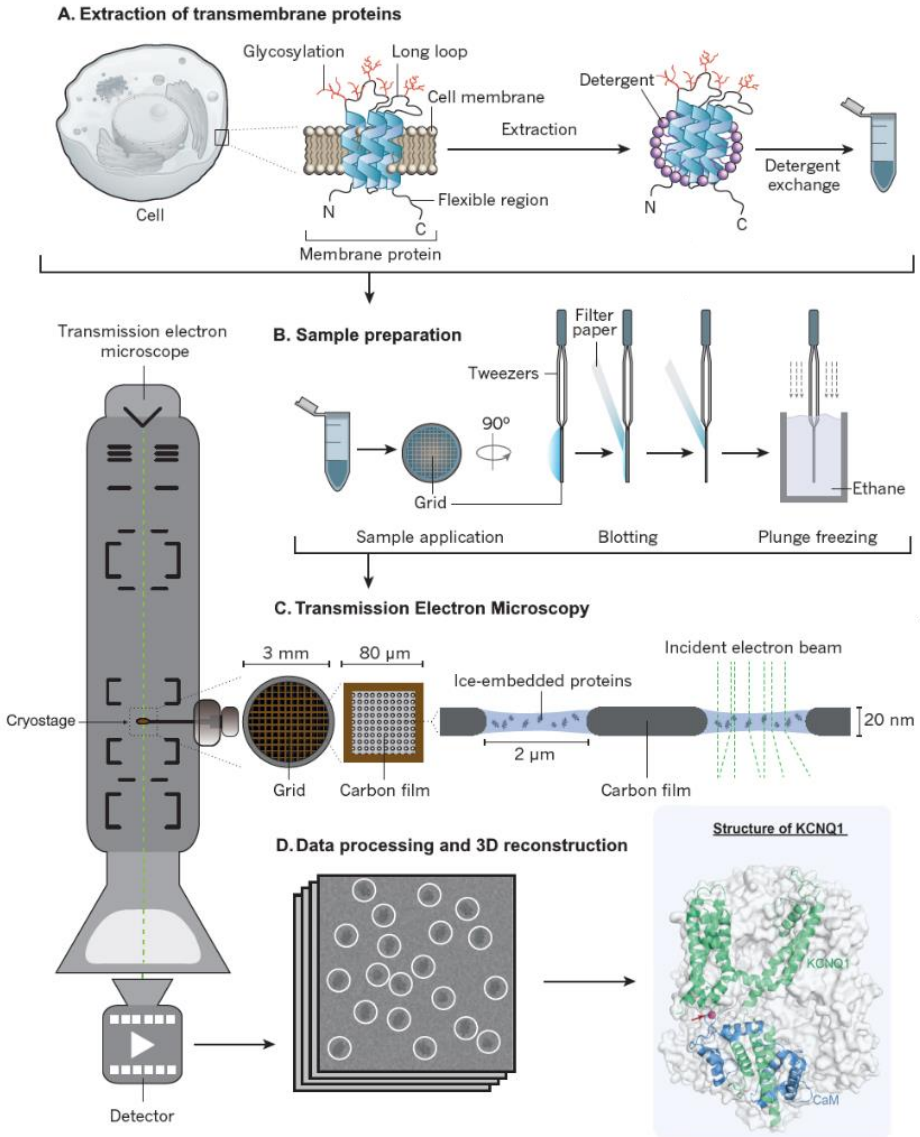

Figure I.1.9: Cryo-EM structure determination of KCNQ1 subunit.
The figure depicts the four stages involved in the protein structure determination through the Cryo-EM technique. **A.** Integral protein extraction of K_V7.1 (KCNQ1) subunit, which requires detergent solubilization; **B.** Sample grid preparation, which the purified protein is placed in a grid of a perforated carbon film, before removing the excess liquid through blotting. The sample is frozen in vitreous ice through plunge-freezing method and stored in liquid nitrogen prior to be placed into the cryostage of the transmission electron microscope, in which 2D images of protein are collected through **C.** transmission Electron Microscopy (TEM). The obtained images are combined through **D.** Data processing and 3D reconstruction, allowing to obtain the 3D structure of K_V7.1 channel. Adapted from [68] and [76].

During the 90s, the research team led by Roderick McKinnon managed to resolve the first complete 3D structure of a fungal potassium channel [63], followed by a bacterial potassium channel [64] using X-ray crystallography, despite the difficulties associated with the purification and the crystallization of transmembrane proteins [65, 66]. For this scientific breakthrough, McKinnon won a Nobel Prize in 2003. Two years later, his team published the crystallographic structure of the rat $K_V1.2$ channel, which constitutes the first mammalian K_V channel to be resolved [67]. Recently, McKinnon and his team harnessed the CryoEM technique for the structural determination of numerous ion channels. By purifying transmembrane proteins with detergents [68], they managed to obtain the 3D structure of one chloride channel [69, 70] and nine potassium channels, with a strong emphasis on the ligand-gated [71–74] and voltage-gated channels such as HCN1 [75] and additional K_V channels such as $K_V11.1$ (namely ether-à-go-go) [76, 77] and $K_V7.1$ [78, 79]. Noteworthy, all these aforementioned ion channels are known to be involved in the action potentials of human excitable cells, and most of these potassium channels are participating in the cardiac action potentials.

Thanks to the advances in the electrophysiology and structural biology techniques, the study of the biophysical properties of VGCC turned out to be accessible. Consequently, the function of a given voltage-gated ion channel can be described by a whole set of observable parameters, such as its steady-state voltage-dependence, the kinetics of its opening/closing transitions, and the time (mean open time, mean closed time) during which the channel remains conductive or not conductive. All these characteristics allowed to develop kinetic models in order to describe the activity of a given VGCC through voltage- and time-dependent transitions between a limited number of conduction states such as open and conductive, closed and nonconductive, and inactivated. Kinetic models turned out to be useful to study the regulation of the function of VGCC by its surroundings, including the membrane and its lipids, as well as transmembrane peptides [80]. In addition, molecular biology experiments such as site-directed mutagenesis allow to determine the biophysical properties of the VGCC mutants that are known to induce diseases, named channelopathies [81].

The beginning of the 21st century marks the development of computational methods applied to chemistry and biochemistry to get a deeper understanding of VGIC [82]. Indeed, the paradigm of the structure-function relationship applied in proteins leads to the assumption that two proteins derived from genes with significant sequence similarity (>30%) are likely to be homologous and thereby to share similar 3D structures [83]. This hypothesis allowed for the development of efficient knowledge-based methods of protein modeling, including Comparative modeling (More details in **Chapter II.1**). Knowledge-based approaches strongly rely on the protein structural information obtained experimentally for the prediction of tridimensional structure of a given protein primary sequence. To that extent, the publication of the rat $K_V1.2$ structure has given life to a tremendous number of computational studies involving various K_V channels including $K_V7.1$, until the second structure of the amphibian $K_V7.1$ channel was resolved by CryoEM [78].

Noteworthy, these computational methods can constitute a solid alternative to study a protein structure. Many results obtained for protein models built with knowledge-based method allowed for a better understanding of the molecular scale events that can play a crucial role in ion channel activation. In this present work, we focused on the potassium channel $K_V7.1$, which plays a significant role in the heartbeat. As a consequence, it is important to understand how the heart manages to perform its heartbeat at both macroscopic and microscopic levels, in order to obtain an insight into the implication of $K_V7.1$ channel in this complex phenomenon.

Chapter I.2. Implication of cardiac action potential in the heartbeat rate

For most animals, the heart is a vital organ whose main role is to control the circulation of the blood throughout the organism. In species such as mammals or birds, this hollow organ is divided into two parts, namely the left heart and the right heart, which are separated from each other by the septum (Figure I.2.1).

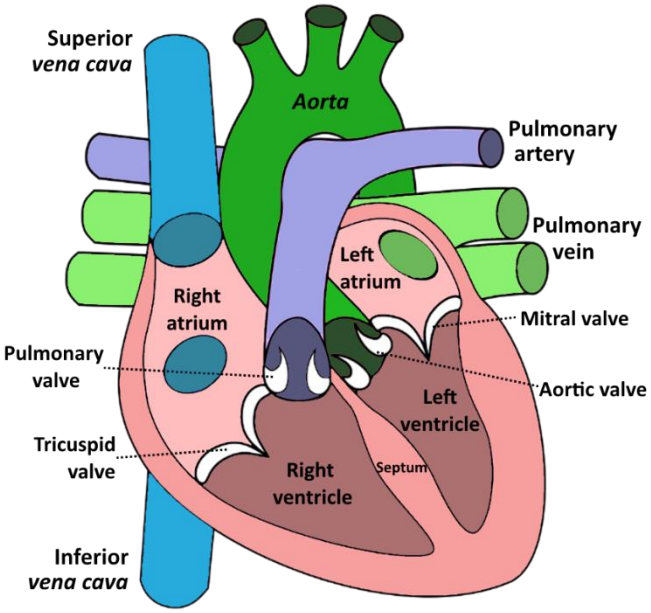

Figure I.2.1: Cartoon picture of the human myocardium and its chambers.
This picture represents the myocardium (in medium pink), which surrounds the atria and the ventricles, along with the blood vessels that are connected to the heart in order to control the blood circulation in the entire organism.

Each part is made of two chambers: an atrium on the top and a ventricle at the bottom. In both left heart and right heart, the atrium is separated from the ventricle through the mitral valve and the tricuspid valve, respectively (Figure I.2.1). Both left and right heart are connected to the general blood circulation through the *aorta* and both superior and inferior *venae cavae*, respectively, and also with the lungs through the pulmonary vein and the pulmonary artery, respectively. The heartbeat is produced by its muscular tissue, called myocardium, which contracts automatically at a periodic rate.

When the myocardium starts contracting its right and left ventricles, which are full of oxygen-depleted blood and oxygenated blood, respectively, all the valves are closed. This contraction induces an increase of the ventricular pressure exerted by the right and left ventricles on the valves until it goes beyond the arterial pressure, leading to the opening of the pulmonary valve and the aortic valves (Figure I.2.2, A, white arrows). At this moment, the left ventricle expulses the highly oxygenated blood towards the general circulation through the *aorta*, while the right ventricle expulses the oxygen-depleted blood towards the lungs through the pulmonary artery (Figure I.2.2, B, white arrows). During this phase called ventricular systole, both tricuspid and mitral valves remain closed while both the left and the right ventricular pressures are decreasing. When these pressures go below the arterial pressure, both the pulmonary valve and the aortic valve close. This marks the beginning of a new heart cycle (Figure I.2.2, C). It starts with the atrial diastole, during which both the left and the right atria are relaxing while receiving oxygenated blood from the lungs through the pulmonary vein and oxygen-depleted blood from the general circulation through both inferior and superior *venae cavae*, respectively (Figure I.2.2, C, white arrows). As a consequence, the atrial pressure increases, while the ventricular pressure remains decreasing. When the ventricular pressure falls beyond the atrial pressure, both the tricuspid valve and the mitral valve open, allowing for the blood to be sunk into the ventricles from the atria, namely the atrial systole (Figure I.2.2, D, white arrows). This phase is terminated by a small contraction of the atria that leads to the pumping of their contained blood into the ventricles prior to the closure of both the tricuspid valve and the mitral valve, leading to a new ventricular systole to complete another heartbeat (Figure I.2.2, A). As for most muscular tissues of the organism, the myocardium is irrigated by the systemic circulation. Oxygenated blood is carried to this tissue from the *aorta* through the coronary arteries, while the oxygen-depleted blood returns to the right atrium through the coronary veins.

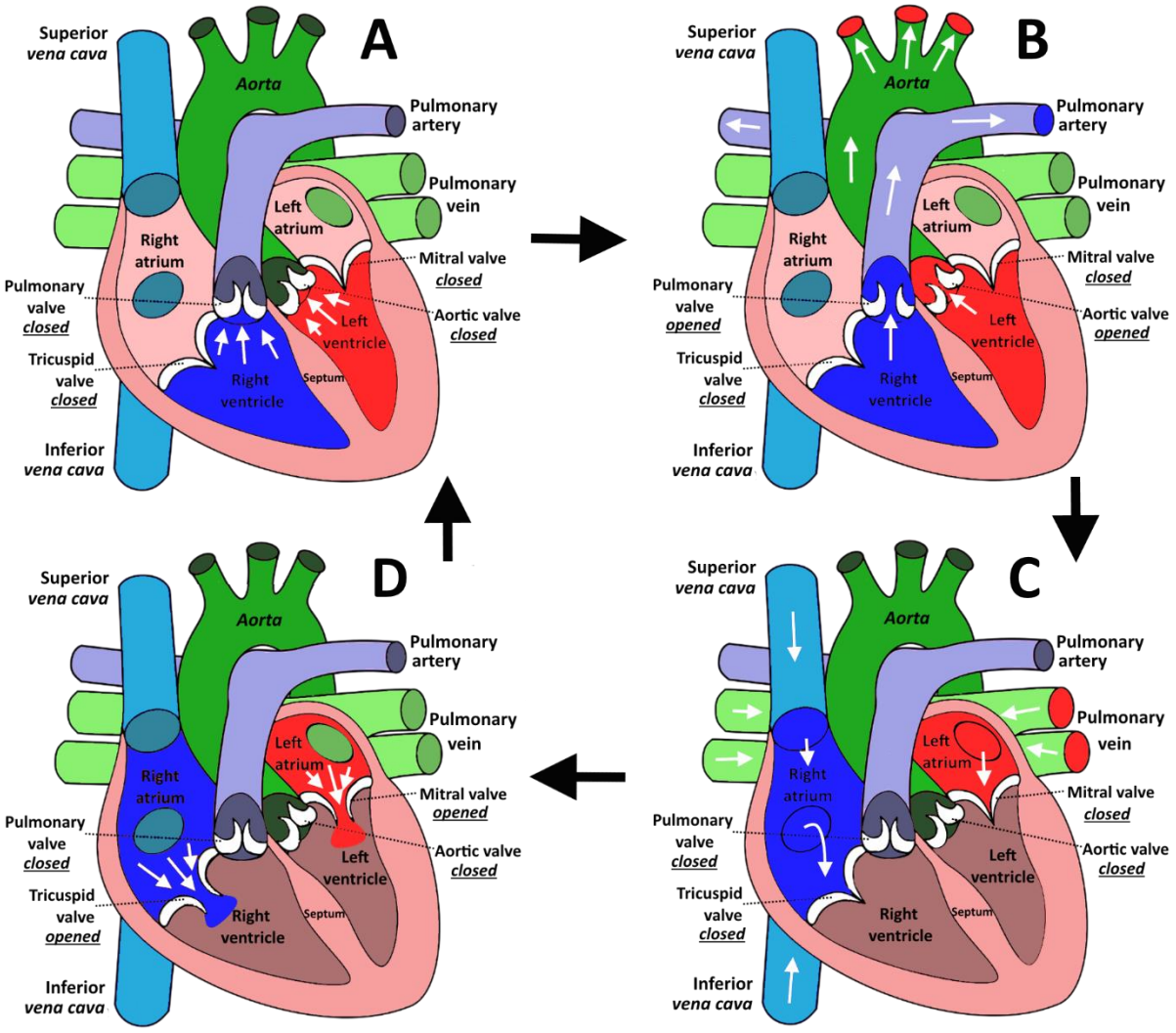

Figure I.2.2: The different phases of blood circulation in the human heart cavities.
In all panels, the oxygen-depleted blood is colored in dark red, while the oxygenated blood is colored in blue. The direction of the blood flows is depicted as white arrows the cyclic form of the blood circulation within the heart chambers is depicted as black arrows. **A.** The end of the atrial systole is described by a contraction of the atria, followed by the contraction of the ventricles that exert a pressure (in white arrows) which induces the opening of both aortic and pulmonary valves. The opening of these valves marks the start of **B.** The ventricular systole, which occurs until both aortic and pulmonary valves are closed in **C.** The atrial diastole during which the blood flows from the pulmonary vein and the *venae cavae* towards the atria until the opening of both tricuspid and mitral valves. **D.** During the atrial systole, the blood flow is coming from the atria towards the ventricles and depicted as white arrows.

At a microscopic level, one heartbeat results from a succession of biological events, starting from the electric excitation of the cardiac striated muscular cells through their membranes at a molecular level to the actual contraction of the entire myocardium at a macroscopic level [84]. In the myocardium, these muscle cells, namely the cardiomyocytes, are divided in two types: the conductive cells that represent 1% of the entire myocardium, and the contractile cells that represent the remaining 99%.

Despite being less numerous, the conductive cells called pacemaker cells are specialized cardiomyocytes organized in a network that is spread throughout the entire myocardium, in order to control the pace of the heart rhythm [85]. They are clustered into several groups of cells (Figure I.2.3) that are animated by an action potential called the pacemaker potential which is generated spontaneously and periodically [85].

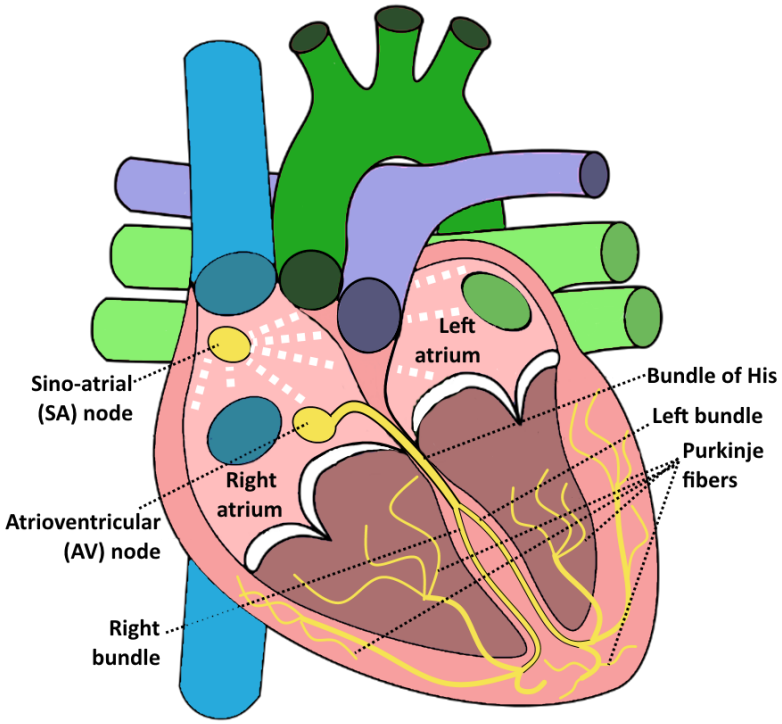

Figure I.2.3: The network of pacemaker cells in the myocardium.
In this figure, the pulmonary valve and the aortic valve are hidden for clarity. The sino-atrial (SA) node and the atrioventricular (AV) node are depicted in yellow circles. The propagation of the pacemaker potential from the SA node to the AV node through the cardiomyocytes of both the left and right atria are depicted in white dashed lines. The bundle of His and the Purkinje fibers are depicted in thick and thin yellow lines, respectively.

The cardiac action potential initiates in the sino-atrial (SA) node, localized in the right atrium (Figure I.2.3) [86]. Thanks to the gap junctions that connect each cardiomyocyte, the pacemaker potential propagates in the contractile cells of both left and right atria at a velocity of 1 m/s, until it reaches the atrioventricular (AV) node, in which the action potential propagation is temporarily slowed to an average speed of 0.04 m/s [87], allowing time for the ventricles to be completely filled with blood from the atria. Indeed, thanks to the intercalated disks which connect all the cardiomyocytes [88], the generation of the cardiac action potential in all the atrial contractile cells induce a contraction of the atria which terminates the atrial systole.

As the tricuspid valve and the mitral valve are both surrounded by fibrous tissue, the cardiac action potential from the SA node cannot propagate towards the ventricles without reaching the AV node. Thus, the pacemaker potential quickly propagates from the AV node towards the ventricles, circulating through the bundle of His at an average velocity of 2.3 m/s, which splits into the left and right branches along the septum, before reaching the Purkinje fibers [84]. The conductive cells of the Purkinje fibers generate the cardiac action potential in the contractile cells of both the left and right ventricles at a propagation speed of 0.75 m/s. This ventricular action potential induces the contraction of the ventricles during the ventricular systole.

The overall electrical cardiac activity can be clinically monitored thanks to electrocardiography. This is performed with a device called electrocardiograph, which measures the variations of the electric potential in both conductive and contractile cardiomyocytes through electrodes placed on the patient's skin on the chest and/or the limbs. The results are recorded on an electrocardiogram (ECG), which is a graphic representation of the time evolution of the cardiac signal, generally measured in millivolts, with a minimal time-precision of 0.5 milliseconds. In a nutshell, the electrocardiography is a noninvasive medical which allows to monitor the cardiac activity during each heartbeat, in order to detect possible cardiac arrhythmias and to diagnose cardiac diseases [84]. In a normal ECG, the electrical signal is featured by six main variations (Figure I.2.4). The P wave, which lasts ~ 80 ms and corresponds to the depolarization of the atrial cells prior to atrial systole. The PR segment lasts ~120-200 ms and describes the propagation of the action potential from the SA node to the AV node through the atria. The QRS complex, which corresponds to the depolarization of the ventricular cells prior to the ventricular systole, lasts ~80-100 ms. The ST segment corresponds to the plateau phase of the ventricular action potential, during which the ventricular cardiomyocytes are contracting. The T wave lasts ~160 ms and corresponds to the ventricular repolarization. It is followed by the U wave, allegedly related to the repolarization of the papillary muscles. Localized in the ventricles, these muscles are attached to both mitral and tricuspid valves in order to control their motion. ECG are often used to measure the QT interval, which corresponds to the time between the beginning of the Q wave and the end of the T wave. The QT interval lasts ~400 ms and actually stands for the duration of the ventricular cardiac repolarization.

As a consequence, both reduction and extension of this interval represent an increased risk of developing life-threatening cardiac arrhythmias.

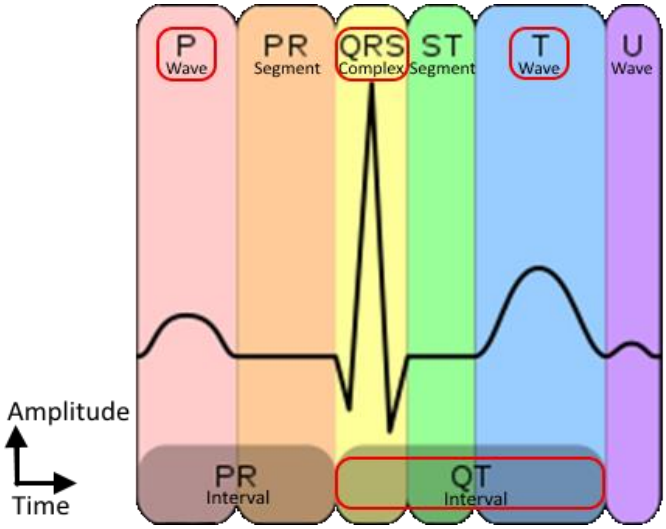

Figure I.2.4: A normal electrocardiogram (ECG)
The graph represents the normal curve of an electrocardiogram, which measures the time-dependent amplitude of the cardiac electric signal. The 6 different steps are displayed in different colors. The P and T waves, the QRS complex and the QT interval, the key events of the heartbeat, are circled in red.

Chapter I.3. How do the voltage-gated ion channels participate in the progress of the cardiac action potential?

Across the plasma membrane of all cardiomyocytes, also called sarcolemma, Na^+, K^+ and Ca^{2+} ions are submitted to an electrochemical gradient. This gradient mostly depends on the ionic concentration of each ion in the cytoplasm with respect to its concentration in the extracellular medium [48]. Hence, cardiomyocytes are containing fewer positive charges than the extracellular medium in their resting state. In both pacemaker and contractile cells, the action potential relies on the activation of several ion channels that generate inward currents of Na^+ and Ca^{2+} ions, as well as outward currents of K^+ ions in the sarcolemma [49]. At the end of each action potential, the electrochemical gradient across the membrane is restored by two proteins that are responsible for the active transport of ions through the membrane, namely the Na/K and the Na/Ca exchangers [89, 90]. Nevertheless, the progress of the cardiac action potential depends on the cardiomyocyte type, as well as on the location of the cardiomyocyte. Indeed, some ionic currents are occurring specifically in conductive tissue, while among contractile cells, an ionic current occurs only in atrial cells and not in ventricular ones [90, 91]. These differences constitute the basis of the role played by each of these tissues in the heartbeat as well as the heart rhythm.

Chapter I.3.1. Conductive tissue

In SA node, the action potential is triggered spontaneously (Figure I.3.1.1). When the fourth phase begins in these conductive cells, the contractile ones are maintained at their resting potential of ~-80 mV. During this phase, pacemaker cells are slowly depolarizing from their minimal potential of ~-50mV, thanks to the diffusion of an inward current called funny current [89, 92]. Noted I_f, this current is generated by characterized by an outward flow of Na^+ and K^+ ions [92] upon the opening of the nonselective hyperpolarization-activated cyclic nucleotide–gated (HCN) cation channels [93]. HCN channels open at hyperpolarized potentials, usually ranging from –45 mV to -40 mV [94] and their function is enhanced by cyclic adenosine-monophosphate (cAMP), a second messenger compound [75]. Then, the $Ca_V3.1$ channels open to conduct the inward transient T-type I_{CaT} current of Ca^{2+} ions to continue the depolarization of pacemaker cells [95].

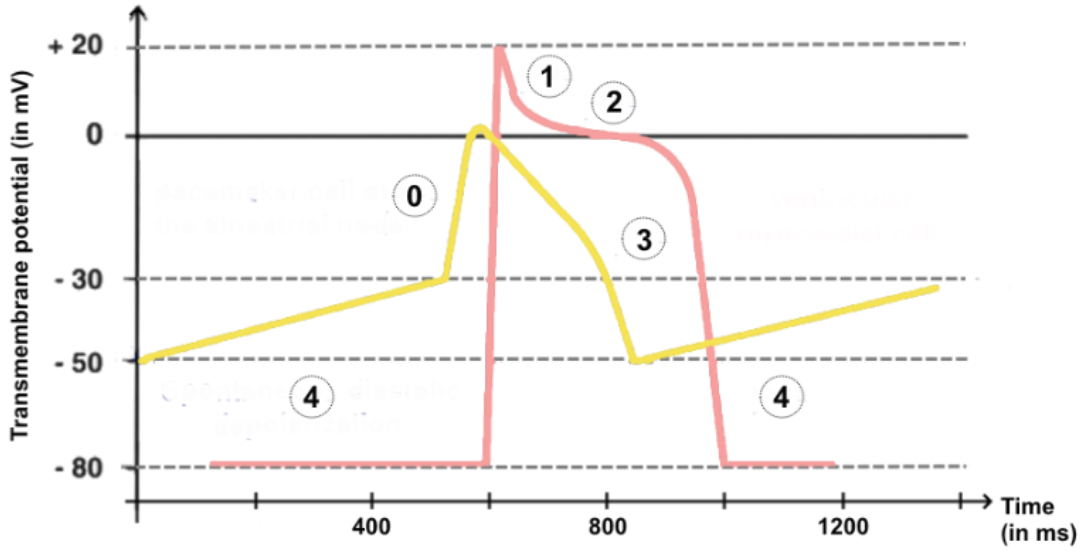

Figure I.3.1.1: Time evolution of the cardiac action potential (in mV) in cardiomyocytes.
The yellow and the pink lines depict the action potential in conductive cells (SA and AV nodes) and contractile cells, respectively. The circled numbers represent the five phases of the ventricular action potential, ranging from 0 to 4. Phases 1 and 2 are not present in the action potential of conductive cells, as they do not undergo any contraction.

Once their transmembrane potential reaches the threshold of ~-30mV, the phase 0, known as the upstroke phase (Appendix I), begins with a sharp membrane depolarization induced by the inward long L-type I_{CaL} current and conducted by $Ca_V1.2$ channel. During this phase, the I_f current is suppressed due to the deactivation of HCN4 channel, the most expressed HCN subunit in human SA node [96, 97]. Then, the upstroke phase is followed by the phase 3 of repolarization upon Ca^{2+} channels inactivation. During this phase, pacemaker cells are quickly repolarized, due to the activation of $K_V11.1$ channel, resulting from the expression of the gene KCNH2 (also known as the "human ether-à-go-go" gene (hERG)) [98], and $K_V7.1$ channel, which generate the IK_R and IK_S currents, respectively [99]. These currents are characterized by outward currents of K^+ ions. Once the pacemaker cell membrane is hyperpolarized, HCN channels are activated again.

The periodicity of the spontaneous pacemaker potential in the SA node can be modulated by the autonomic nervous system, as this tissue is innervated with autonomic nervous fibers, allowing for a regulation of the heart rhythm [85, 92]. The steepness of the depolarization curve during phase 4 can be increased by a sympathetic modulation, which elicits an increased intracellular concentration of cAMP. This increase is due to the binding of adrenaline to the β-adrenergic receptors of the SA node.

The resulting cAMP bind the HCN channels to induce a right shift in its voltage-dependence of activation. Moreover, the steep of the depolarization curve during phase 4 can also be reduced by a parasympathetic modulation. It consists in the binding of acetylcholine (Ach) to the muscarinic receptor which induce an inhibition of the adenylate cyclase, and therefore a decrease in cAMP intracellular concentration. This decrease elicits a left shift in HCN channel voltage dependence of activation.

Chapter I.3.2. Contractile tissue

The diffusion of Na^+, Ca^{2+} and K^+ ions in pacemaker cardiomyocytes is responsible for the depolarization of the neighbor contractile cardiomyocytes (Figure I.3.2.1). Indeed, these ions are quickly diffused into neighboring cells through transmembrane proteins called connexins that are forming intercellular protein complexes called gap junctions [100, 101]. These diffused ions elicit an increase of their respective intracellular concentrations in contractile cells, which triggers the activation of the voltage-gated sodium channel $Na_V1.5$. It generates the inward I_{Na} current that marks the phase 0 by inducing a sharp membrane depolarization in contractile cardiomyocytes of the atria, before inactivating rapidly due to maintained depolarization [102] (Appendix I).

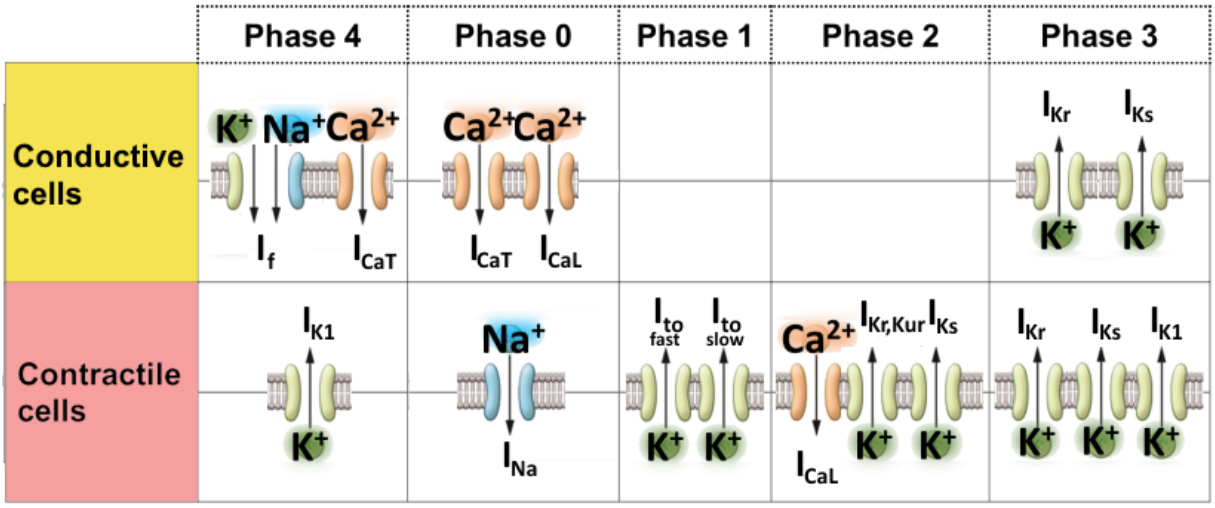

Figure I.3.2.1: The voltage-dependent ionic currents involved in the cardiac action potential.
This tab summarizes the ions conducted by the ionic currents during each phase of the action potential in conductive cells and in contractile cells. I_{CaL}: L-type Ca2+ current; I_{CaT}: T-type Ca2+ current; I_f: funny current; I_{K1}: inward rectifier current; IK_R: rapid inward rectifier current; IK_S slow delayed rectifier current; IK_{UR}: ultra-rapid rectifier current; I_{Na}: sodium current; I_{to} fast: fast transient outward current; I_{to}, slow: slow transient outward current.

Then, during phase 1, the membranes are slightly repolarized due to the transient outward potassium current I_{to}, whose fast and slow components are conducted by $K_V4.3$ and $K_V1.4$ channels, respectively [103]. The phase 2 begins when I_{to} current is suppressed as $K_V4.3$ and $K_V1.4$ channels inactivate. During this phase called plateau, the membrane potential is temporarily kept constant due to the simultaneous conduction of inward I_{CaL} current [104] and the outward ultra-rapid rectifier current, noted IK_{UR} and generated mostly in atrial contractile cells by $K_V1.5$ channel, along with IK_R and IK_S currents that are activating rapidly and slowly, respectively, during phase 2.

This phase constitutes the main difference between the action potential in atrial and ventricular tissue (Figure I.3.2.2). In atrial cells, the higher expression of $K_V1.5$ subunits and the lower expression of both $K_V7.1$ and $K_V11.1$ subunits in comparison with ventricular cells [90] are the main reason why the duration of phase 2 is shorter, as the atrial contraction is less strong during atrial systole than ventricle contraction during ventricular systole.

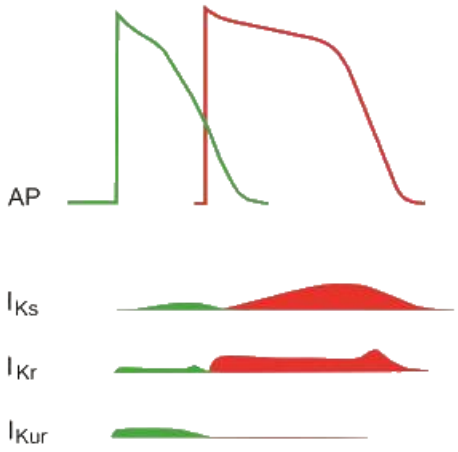

Figure I.3.2.2: Diffusion of potassium currents in contractile cardiomyocytes.
The top panel displays the cardiac action potentials occurring in atria (in green) and in ventricles (in red). The bottom panel displays the tissue distribution of IK_S, IK_R and IK_{UR} currents in the atria (green) and in the ventricles (red). Adapted from [90].

The propagation of the action potential in contractile atrial cells ends when the pacemaker potential reaches the AV node. At this moment, the atria can perform their contraction, marking the beginning of the atrial systole. Meanwhile, the action potential is slowly propagated from the AV node through the Bundle of His and the Purkinje fibers toward the ventricular contractile cardiomyocytes, which also undergo an action potential as in atrial cells [86].

In the human heart, the only action potential difference between atrial cells and ventricular cells resides in the duration of phase 2, which lasts longer at a higher voltage value in ventricular cells due to the absence of IK_{UR} current [105]. Once the ventricular cells are all depolarized, the ventricles are able to perform their contraction (Appendix II), marking the beginning of the ventricular systole. As a reminder, the ventricular systole is defined by a contraction of the ventricles which elicits the ejection of the blood from the ventricles towards the circulatory system. Noteworthy, phases 1 to 3 encompass an amount of time called the cardiac refractory period, during which no action potential can initiate in contractile cells due to an electrical stimulus [32].

Nevertheless, knowing only the progress of the cardiac action potential leaves a knowledge gap between the function of ion channels and the rhythm in which the myocardium contraction actually occurs. To that extent, one need to be aware of the biological events induced by the propagation of cardiac action potential within the cardiomyocytes in order to understand the role played by ion channels in the heartbeat process. As a matter of fact, the inward flow of Ca^{2+} ions in contractile cells during the second phase of the cardiac action potential marks the beginning of an intracellular phenomenon called cardiac excitation-contraction coupling (Figure I.3.2.3).

This biological event lasts ~200 ms (Figure I.3.1.1) and involves a regulated circulation of Ca^{2+} ions around the cytosol, allowing for the contraction of the muscular fibers of all contractile cardiomyocytes. This simultaneous contraction is due to the intercalated disks which contain the connexins allowing for the propagation of the cardiac AP, leading to the contraction of the entire myocardium as a syncytium. However, these intercalated disks are not present between atrial cells and ventricular ones, which forces the action potential to be spread uniquely through the path formed by conductive cells.

In each contractile cell, the L-type $Ca_V1.2$ channels are located in transverse tubules, which are spread around the whole cardiomyocyte membrane. These tubules are forming invaginations on the membrane surface, in order to ship the entering calcium ions towards the ryanodine receptors, located ~15 nm from L-type channels and embedded in the membrane of the sarcoplasmic reticulum [106]. The main role of this organelle is to store a significant amount of Ca^{2+} ions to be released in the cytoplasm of muscular cells (Figure I.3.2.3).

Indeed, the entering Ca^{2+} ions bind the calmodulins that are coupled to the ryanodine receptor 2 (RyR2) which form a tetrameric pore in the sarcoplasmic outer membrane [107]. Each tetramer of RyR2 is also coupled to three other proteins that are localized in the sarcoplasmic inner membrane [108]. These Ca^{2+}-calmodulin interactions activate the opening of RyR2 in order to release Ca^{2+} ions into the cytoplasm [109]. Namely this phenomenon is called calcium-induced calcium release (CICR). It elicits an increase in Ca^{2+} concentration in the cytoplasm, which itself lead Ca^{2+} ions to inactivate L-type $Ca_V1.2$ channels through a negative feedback [110].

Then, the cardiac contractile cycle begins with these released Ca^{2+} ions binding the troponin C. This protein complex, localized periodically along the fibers of tropomyosin, is shielding the myosin heads from binding the actin filaments, preventing their interaction. When Ca^{2+} ions bind troponin C, the latter become unable to ensure its shielding role. As a consequence, the hydrolysis of ATP into ADP and inorganic phosphate (Pi) occurs spontaneously in the myosin heads. Once the products of ATP hydrolysis are released from the myosin heads, they become able to bind actin filaments, which elicit muscle contraction. When new ATP molecules bind myosin heads, the contraction ends.

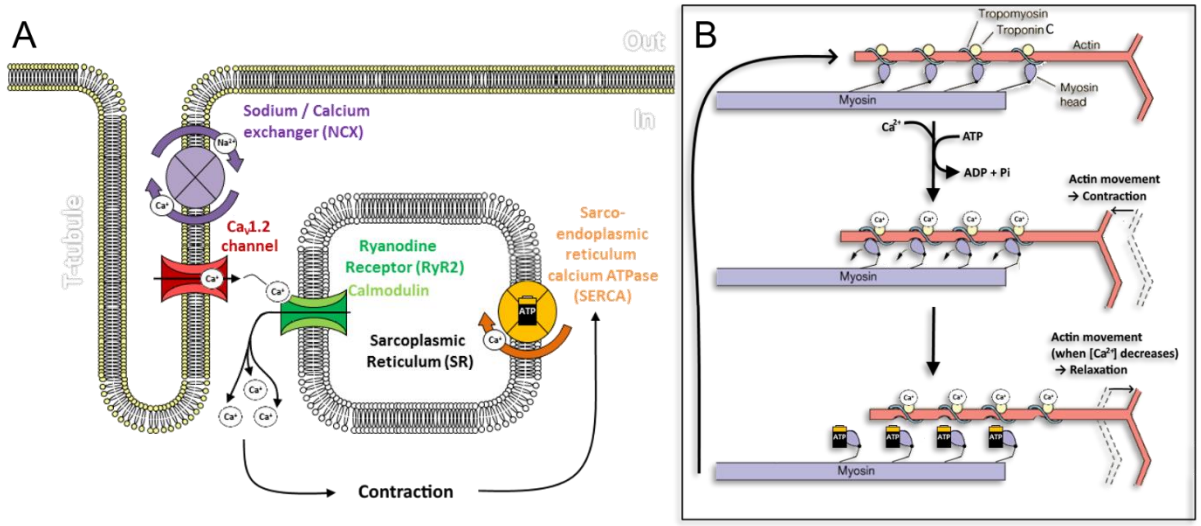

Figure I.3.2.3: The Ca^{2+} cycle in the cardiomyocytes during cardiac action potential.
A. The left panel shows a schematic view of the path taken by calcium ions cardiomyocyte cytoplasm during cardiac contraction-excitation coupling that occurs during phase 2 of cardiac action potential. **B.** The right panel shows the calcium-induced movements of muscular fibers that precede cardiac contraction.

This process is repeated in a cyclic fashion, as long as calcium ions are bound to troponin C due to CICR. When Ca^{2+} channels inactivate, the phase 2 of cardiac AP ends. In the cytoplasm, the Ca^{2+} concentration decreases due to the inactivation of RyR2, while intracellular Ca^{2+} ions are mostly returning the sarcoplasmic reticula through the sarco-endoplasmic reticulum Ca^{2+}-ATPase pumps [111, 112] , or in a lesser extent transported outside the cell through Na^{+}/Ca^{2+} exchangers, which ensures an antiport in which three Na^{+} ions enter the cell while one Ca^{2+} ion is released from the cell in order to restore their concentration gradients [113]. This cascade of intracellular events leads to the relaxation of the ventricles, which occurs at the beginning of the third phase. The repolarization phase begins when I_{CaL} is suppressed due to the inactivation of $Ca_V1.2$ channel, while the potassium currents are maintained to ensure membrane repolarization.

As in atrial contractile cells, IK_R and then IK_S currents are diffused in the membranes of ventricular contractile cells during phase 3 of cardiac AP [91]. In addition, the IK_1 outward current is also generated during phase 3, while its inward current is generated during phases 0, 1 and 2 due to Mg^{2+} and polyamines that block its outward current [100]. The repolarization phase ends with the deactivation of $K_V7.1$ and $K_V11.1$ channels, while IK_1 current, conducted by the K_{ir} 2 channels, is still diffused in order to maintain the membrane at its resting potential. In addition to I_{K1} current, the $I_{K\,ATP}$ inward current can also be diffused during phase 4 by the ATP-sensitive K^{+} channel (K_{ir} 6 channels) [114] in order to adjust the shape of the cardiac action potential to the metabolic state of the cardiomyocyte [100].

Indeed, these channels are expressed in both conductive and contractile cardiomyocytes. Their opening depends on the ratio between concentrations of both Adenosine diphosphate (ADP) and ATP in the cytoplasm. Indeed, the [ADP]/[ATP] ratio increases with the open probability of ATP-sensitive K^{+} channels. As a consequence, these channels are blocked by ATP.

Interestingly, the ventricular IK_S current can be regulated by the autonomous system, similar to I_f current in conductive cells. Indeed, acute stress/arousal, or exercise are known as sympathetic effectors, which both elicit a sharp increase in the heart rate by abbreviating the repolarization phase of the ventricular action potential. To shorten the duration of the repolarization phase, the autonomous system induces signaling pathways that enhance IK_S current [115, 116]. This highlights the importance of this current, as well as the voltage-gated K+ channel which generates it, in the cardiac function. To that extent, the next section will present the particular context in which the IK_S current has been discovered, as well as the molecular determinants that support the structure and the function of $K_V7.1$ channel.

Chapter I.4. Molecular determinants of IK_S current

In the sarcolemma of cardiomyocytes, $K_V7.1$ channel and KCNE1 subunits generate the slow delayed rectifier current IK_S, which is characterized by an outward flow of potassium ions that participates in the repolarization phase of the action potential in both pacemaker and contractile cardiomyocytes [117–119], leading to the termination of the AP. IK_S current was identified in 1990 [120], after it was discovered along with IK_R as I_{X2} and I_{X1}, respectively, by Noble and Tsien in 1969, as two components of potassium outward currents [121, 122]. During the cardiac action potential, the IK_S current slowly activates during its second phase, opens at the beginning of phase 3 and remains opened until the end of the repolarization, while IK_R activates rapidly during the second phase, to briefly open at the beginning of phase 3.

Chapter I.4.1. Discovery of $K_V7.1$ and KCNE1 through inherited cardiac arrhythmias

During the 90s, scientists started to get interested in K_VLQT1 gene, (which will later be renamed as KCNQ1 gene) and its implication in the long QT syndromes and in the termination of the cardiac action potential [119]. Indeed, KCNQ1 mutations are associated with cardiac arrhythmias that threaten infant and adult life, (among other biological processes) and for which therapeutic treatments are limited due to the difficulties associated to the study of ion channels. The primary sequence of $K_V7.1$ α-subunit results from the expression of the gene KCNQ1. Its locus was first mapped to chromosome 11p15.5, which was identified in 1991 as a DNA marker for the Romano-Ward syndrome in a large family of 400 patients [123]. This syndrome is also known as type 1 long QT syndrome (LQTS1), as it was the first LQT syndrome to be genetically mapped. Romano-Ward syndrome is a cardiac disorder with autosomal dominant inheritance [124, 125]. It is characterized by a specific cardiac arrhythmia called *torsade de pointes*, which is triggered by an acceleration of the cardiac rhythm upon sympathetic stimulation (for example during physical effort or acute stress). Defined as an abnormal acceleration of the heart rhythm in the ventricles (ventricular tachycardia), this severe arrhythmia is due to an extended duration of the cardiac action potential that corresponds to the time interval between Q and T waves in electrocardiograms, also known as QT interval [126].

Later in 1996, KCNQ1 gene was cloned and basically identified as K_VLQT1, as it is responsible for most cases of inherited Long QT syndromes and presents a significant sequence identity (30%) with Shaker potassium channel [127]. In the same year, K_VLQT1 gene was shown to be co-expressed along with KCNE1 gene in cardiomyocytes [119, 128]. Indeed, KCNE1 gene, which was first mapped to chromosome 21q22.1-q22.2 in 1993 [129, 130] was cloned for the first time in 1989 [131]. Interestingly, KCNE1 gene was localized on a putative Down's syndrome region, which is itself characterized by numerous abnormalities in cardiac formation and function [132]. KCNE1 gene codes for a membrane protein which was later identified as a minimum potassium ion channel (minK) due to the length of its primary sequence (129 amino acids) [133]. Since the discovery of KCNQ1 gene in 1996, numerous mutations of both KCNQ1 and KCNE1 genes have been identified as associated with Romano-Ward syndrome, [134–136] which is the most prevalent LQTS [137]. The next year, KCNQ1 was linked to the Jervell and Lange-Nielsen syndrome (JLNS)[138], a particular cardiac arrhythmia with autosomal recessive inheritance which is characterized by both long QT interval and deafness [139]. A few years later, additional mutations of both KCNQ1 and KCNE1 genes [140–142] were also linked to JLNS due to the expression of IK_S complexes in the inner ear [143]. JLNS is also known as LQT5, as it was linked with KCNE1, which is the fifth LQTS gene to be identified.

The cardiac arrhythmias that have been linked to both KCNQ1 and KCNE1 genes are caused by an inability of the protein complex to generate its IK_S outward current correctly in order to return the membranes of ventricular cardiomyocytes toward their resting potential. These mutations lead to a loss of function [144] which elicits a prolongation of the AP duration in ventricular cardiomyocytes. This delay in cardiac repolarization disturbs the propagation of the cardiac action potential within the myocardium tissue. Indeed, the extended duration of the repolarization phase induces a default of coordination with sinusal AP, due to a delay between the electrical signals of conductive cells and contractile ones, as well as between atrial cells and ventricular ones.

Other loss-of-function mutations are related to impaired sympathetic stimulation pathways. In response to exercise, the sympathetic stimulation of I_{Ks} current consist in the formation of a macromolecular signaling complex, in which $K_V7.1$ channel is bound to the targeting protein Yotiao through a leucine zipper motif [115] and microtubules [145]. This protein assembly then recruits the protein phosphatase 1 and the protein kinase A (PKA), and the latter, upon cAMP activation, phosphorylate the cytoplasmic region of $K_V7.1$ subunits to double its conductance. When mutated, this $K_V7.1$ phosphorylation binding site lead to LQTS [115]. Another study reports the importance of KCNE1 accessory subunits, as well as $K_V7.1$:KCNE1 stoichiometry in I_{Ks} complex for this specific autonomous control [146]. In addition, a recent electrophysiology study shed light on a second pathway for I_{Ks} sympathetic regulation. In response to acute stress/arousal, the protein kinase C (PKC) activates upon Ca^{2+} binding to phosphorylate the cytoplasmic region of KCNE1, inducing a modification of I_{Ks} complex voltage-dependence [116]. Other studies reported the inhibitory effect of the calcium/calmodulin dependent protein kinase II on I_{Ks} current upon sustained sympathetic stimulation, which usually occurs during heart failure [147].

Moreover, KCNQ1 also presents a few number of gain-of-function mutations which were associated with short QT syndrome [148, 149] and atrial fibrillation [148, 150, 151]. Hence, the numerous mutations of KCNQ1 and KCNE1 elicit various phenotypes of $K_V7.1$ channel malfunction. These phenotypes have major consequences on the heart rhythm, as the resulting cardiac arrhythmias involves severe symptoms such as syncope, seizure, and sudden death. Due to the numerous KCNQ1 mutations, which represent ~50% of LQTS cases [134, 135], the $K_V7.1$ channel constitute a major therapeutic target for the treatment of these severe LQTS.

Chapter I.4.2. IK_S complex (K_V7.1+ KCNE1): Structure and function

Over the last thirty years, KCNQ1 and KCNE1 genes have been extensively studied using various methods including biophysical [78], physiological [152, 153] and computational [154–156] techniques in order to gain an insight into the structure and the function of this protein complex in the plasma membrane. The function of KCNQ1 and KCNE1 mutants that are known to elicit several channelopathies has also been investigated in order to provide molecular determinants of IK_S current diffusion [157–162]. The primary sequence of a K_V7.1 α-subunit counts 676 residues that are separated in three distinct regions. Residues 1 to 121 are forming the N_{TERM} region, located in the cytoplasm, while residues 122 to 358 constitute the transmembrane region and counts six membrane spanning segments which are spread in two domains. The voltage-sensor domain (VSD) counts four S1-S4 segments and PD counts two S5-S6 segments [78]. Residues 359 to 676 are forming the C_{TERM} region. Specifically, this cytoplasmic region is composed of four helices, the first two ones being connected to the sixth transmembrane segment S6 [78], the last two being located deeper in the cytosol, forming the tetramerization domain [163]. Several mutagenesis studies reported the importance of calmodulin binding to the cytoplasmic regions of K_V7.1 subunits in their assembly and their gating within the IK_S complex [164, 165, 78]. As for most K_V channels, K_V7.1 α-subunits are organized to form a homotetramer with a four-fold symmetry, in which both VSD and PD are swapped (Figure I.4.2.1).

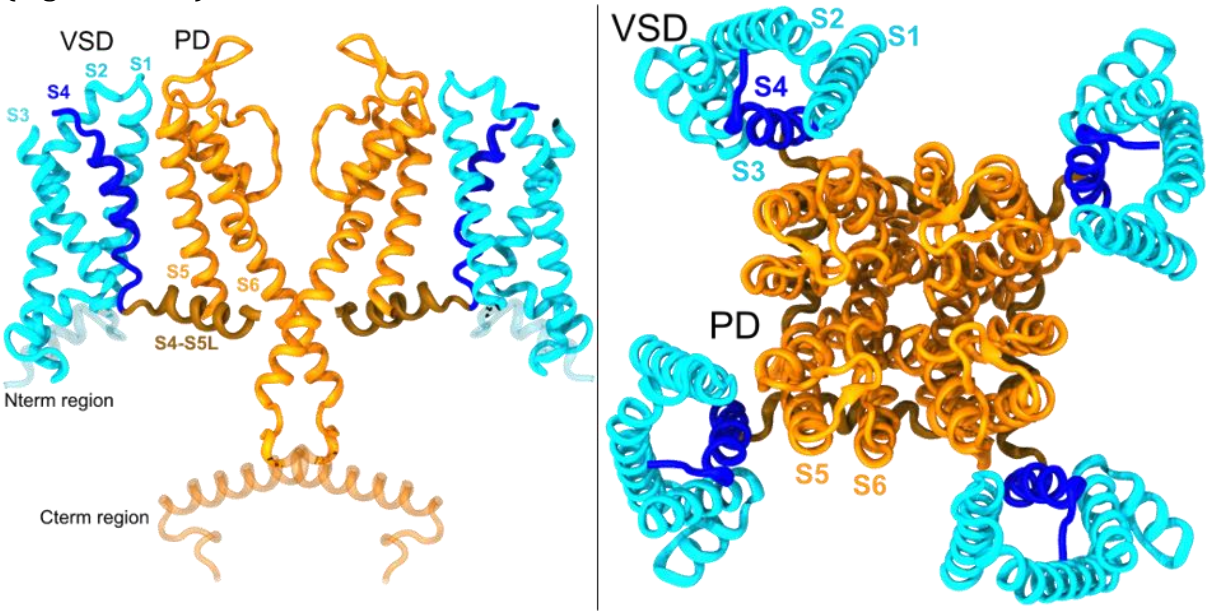

Figure I.4.2.1: CryoEM structure of the *Xenopus Laevis* K_V7.1 subunit.
Cartoon representation of the 3D structure of K_V7.1 tetramer in lateral view (left panel) and top view (right panel). On the left panel, only two subunits are shown for clarity. Truncated N_{TERM} and C_{TERM} regions are depicted in transparent cyan and orange, respectively. Transmembrane regions are depicted in solid colors.

K_V7.1 fourth segment, S4 carries four gating charges: R228 (R1), R231 (R2), R237 (R4) and R243 (R6). The position of this segment along the lipid bilayer is known to depend directly on the membrane potential. Indeed, potential changes in the membrane due to depolarization or hyperpolarization induce the presence of an electric field of a certain direction and magnitude [40, 166].

Accordingly, S4 gating charges are moving sequentially across the membrane towards the outer and the inner membrane upon depolarization and hyperpolarization, respectively. In the pore domain, the segments S5 and S6 are separated by a helical re-entering loop (P-helix), followed by the motif TXGYG, also known as the selectivity filter (SF), which is well conserved among the K_V channel family. In most of the 3D structures obtained for K_V channels at an atomic scale, the peptide bonds of the SF motif are organized in such a way that in the tetramer, the carbonyl groups of the SF peptide bonds are oriented towards the center of the pore (Figure I.4.2.2). This specific orientation aims to translocate the potassium ions into the extracellular matrix when the K_V channel is conductive.

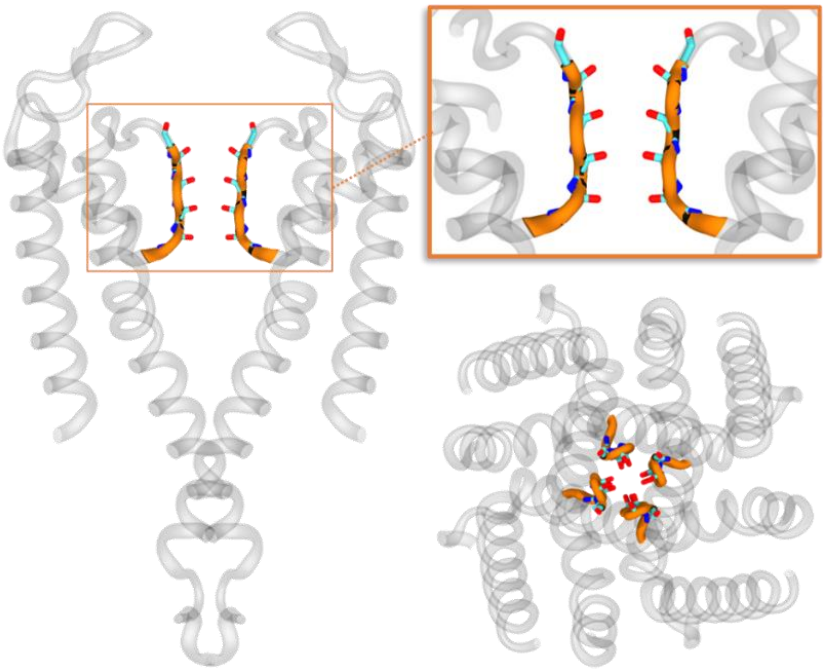

Figure I.4.2.2: Mapping K_V7.1 selectivity filter in *Xenopus Laevis* K_V7.1 structure.
This figure shows a cartoon representation of K_V7.1 PD segments (transparent colors). The selectivity filter is colored in orange, and its backbone is depicted in sticks, and carbon, nitrogen and oxygen atoms are colored in cyan, blue and red, respectively. The left panel shows a lateral view, in which two subunits are displayed for clarity. On the right panel, the upper picture shows an enlarged view of the left panel, while the lower picture displays a top view of tetrameric K_V7.1 PD.

The voltage-dependent opening of K_V7.1 channel encompass three main mechanisms: VSD activation, VSD-PD coupling, and PD opening [167]. The VSD activation mechanism is triggered by membrane depolarization and involves three stable states [168]. These conformations are known to transition from one to another through the motion of S4 gating charges. As in many VSD of most VGCC, the VSD of K_V7.1 contains two negatively charged side chains from S2 and S3 [168] that are strongly conserved among voltage-gated ion channels.

These residues constitute binding sites for S4 gating charges (Figure I.4.2.3): the first one, located in the solvent accessible surface of the VSD, is an acidic residue from S2, E160 (E1). The second one, located deeper in the membrane, is sheltered from the solvent by an aromatic residue from S2, F167, also known as the charge transfer center (CTC). It is composed of two acidic residues, E170 (E2) and D202 (D3) from S2 and S3 segments, respectively [169]. The conformational change of S4 also involves a translation of its gating charges through the CTC which was suggested to constitute the interface between the solvent accessible surface of the VSD, and its occluded site [169, 170]. Indeed, this residue is conserved in homologous potassium channels such as K_V1.2 or K_V2.1 [171], which share similar secondary, tertiary, and quaternary structures as K_V7.1.

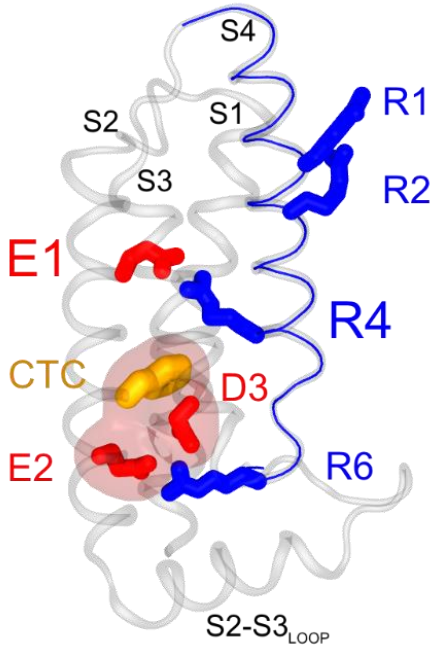

Figure I.4.2.3: S4 gating charges in K_V7.1 VSD.
This figure shows a cartoon representation of a 3D structure of K_V7.1 VSD in its activated conformation. Segments S1-S3 are in transparent colors, while S4 is colored in blue. The sidechains of the gating charges R228 (R1), R231 (R2), R237 (R4) and R243 (R6) and their countercharges E160 (E1) E170 (E2) and D202 (D3) are depicted in blue and red sticks, respectively. The charge transfer center (CTC), F167, is depicted in orange sticks. The occluded site, formed by F167, E2 and D3, is depicted in a transparent red surface.

The opening of the pore depends on another mechanism called VSD-PD coupling. The latter, which exists in most of K_V channels, is defined as protein-protein interactions between VSD and PD of distinct α-subunits that aim to couple the activation state of the VSD (resting, intermediate or activated) with the conformation (open or closed) of the PD [172, 173]. Previous voltage-clamp experiments performed on charge-reversal mutants aimed at stabilizing every stable state of $K_V7.1$ VSD suggested that both intermediate and activated state of the VSD yield to conductive channels, whereas the resting state yields to a less conductive channel [173]. Accordingly, the three stable states known for $K_V7.1$ are resting/closed (RC), intermediate/open (IO) and activated/open (AO) [168, 173] (Figure I.4.2.4, upper right panel). The exact mechanism for this electromechanical process is not completely determined. Several studies were conducted in distinct K_V channels and shed light on the importance of specific interactions between the S4-$S5_{LINKER}$ and the C-terminal region of S6, both located in the cytoplasmic side of the membrane [174, 175]. The G/V curve of $K_V7.1$ (Figure I.4.2.4, upper left panel), which represents its ionic conductance as a function of the transmembrane voltage, has a sigmoid shape, as seen on most of the studied voltage-dependent ion channels [167]. This shape, along with the "domain-swapped" quaternary structure of $K_V7.1$ subunits (Figure I.4.2.1), suggest an allosteric mechanism for the activation of the voltage sensors of these channels, as well as for their VSD/PD coupling mechanism which leads to pore opening and ion conduction. Following this assumption, previous experimental studies showed that this allosteric coupling may be realized through a ligand/receptor mechanism in which S4-$S5_{linker}$ acts an inhibitor, stabilizing the gate in a closed state [176]. Upon membrane depolarization, S4 drags S4-$S5_{linker}$ out of its S6 binding pocket, and the open probability of the channel increases. In K_V channels, the pore opening mechanism is assumed to be controlled by the residues of S6 that line the conduction pathway [167]. Particularly, the PVP motif, located on the cytoplasmic part of Shaker's S6 segment was shown to be mainly involved in S6 motion during pore opening [177, 178]. In $K_V7.1$ primary sequence, the PVP motif is substituted by the PAG motif, whose mutations P343A and G345A are hindering pore opening without altering membrane surface expression [179, 180]. In addition, electrophysiology measurements conducted on $K_V7.1$ mutations of the K_V7 specific SFF motif revealed that F339S, an LQT-related mutation, shows no current without altering VSD activation [159].

The F340W mutant turned out to induce inactivation on IK_S complex, which basically does not inactivate [181]. Finally, Ala/Trp scanning mutagenesis of $K_V7.1$ S6 C_{TERM} region (348 GSGFALKVQQKQRQK 362) highlighted several mutations of $K_V7.1$ S6 residues F351A A352W and V355W that turned out to destabilize the open conformation [182].

When $K_V7.1$ is co-expressed with the β-subunit KCNE1, its biophysical properties are modified (Figure I.4.2.4, lower left panel). Numerous voltage-clamp experiments highlighted that in comparison with $K_V7.1$ channel alone, IK_S complex ionic conductance is four to six-fold increased [119, 128]; voltage-dependence of conduction (G/V curve) is right-shifted towards more depolarized potentials , and activation/deactivation kinetics are slowed [119, 128]. In addition, several studies of voltage-clamp fluorometry were conducted on $K_V7.1$ that were expressed in *Xenopus* oocytes in both the absence and the presence of KCNE1. By placing a fluorophore on the extracellular S3-S4 loop of $K_V7.1$ subunits to track the response of S4 upon depolarization [183–186] the studies revealed the motion of S4, which occur simultaneously with pore opening in absence of KCNE1, is divided in two distinct motions in its presence.

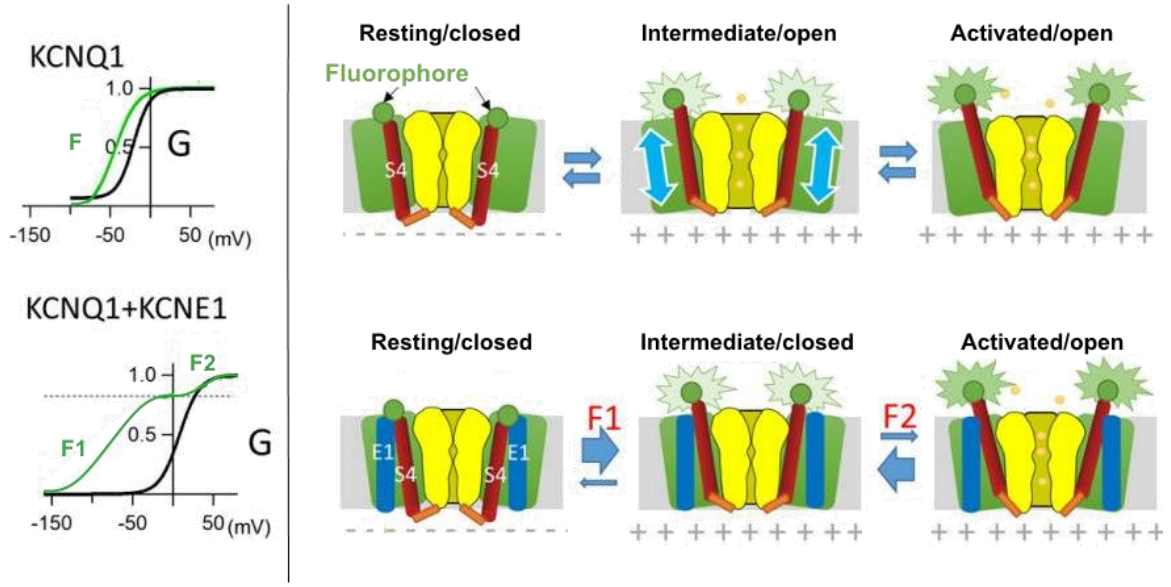

Figure I.4.2.4: Macroscopic properties of $K_V7.1$ channel in the absence and the presence of KCNE1. The left panel shows the normalized F/V (green) and G/V (black) curves that are associated with S4 motion and pore opening, respectively for $K_V7.1$ alone (top) or in the presence of KCNE1 (bottom). The right panel shows schematic models of $K_V7.1$ VSD activation and pore opening highlighted by voltage-clamp fluorometry in the absence (upper row) and in the presence of KCNE1 (lower row). Adapted from [181].

The first motion noted F1 (Figure I.4.2.4, lower left) occurs at hyperpolarized voltages, while the second one, F2, occurs at a depolarized voltage, when the channel opens, suggesting that S4 motion involves three stable states in presence of KCNE1, which confirms the previous charge-reversal mutagenesis conducted on IK_S channel [161]. In the same year, our collaborators reported that these two motions of S4 turned out to be detected $K_V7.1$ alone as well, indicating the presence of a stable intermediate state in absence of KCNE1 as well [156, 173].

Other studies have shown that the inactivation revealed by patch-clamp experiments conducted on $K_V7.1$ channel alone [187] turned out to be suppressed in presence of KCNE1. Hence, KCNE1 is known to modulate $K_V7.1$ function by disrupting both its VSD activation and VSD-PD coupling mechanisms in order to generate IK_S current [188]. At this point, the molecular determinants of KCNE1 modulation were needed to explain the experimental results. To that extent, the structure of KCNE1 was resolved by NMR [189]. KCNE1 is a transmembrane polypeptide of 129 amino acids, and divided into one extracellular N_{TER} domain, a helical transmembrane (TMD) domain, and a cytosolic C_{Term} domain (Figure I.4.2.5).

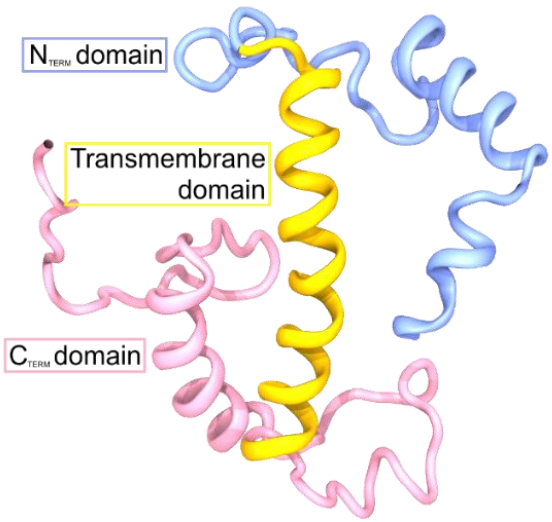

Figure I.4.2.5: Average NMR structure of the ancillary subunit KCNE1.
Cartoon representation of KCNE1 subunit with its three main regions. N_{TERM} and C_{TERM} domains and transmembrane domain are colored in blue, pink and yellow, respectively.

The location of KCNE1, between each $K_V7.1$ subunit and facing both of their transmembrane domains in IK_S complex, was determined by a series of various mutagenesis experiments [155, 190–194]. These experimental studies provided several hints on $K_V7.1$ activation mechanism in presence of KCNE1.

Tridimensional (3D) models of IK_S channel in its open [195, 155] and closed [154] states have also been proposed to provide an atomistic level of knowledge about its structure and function. Besides the major role of $K_V7.1$ and KCNE1 subunits in the cardiac action potential, it is important to note that $K_V7.1$ channel also forms complexes with each β-subunit of the KCNE family in cardiac striated muscle cells [196]. In addition, KCNQ1 is widely expressed in mammal organisms, including numerous organs such as kidney, adrenal glands, pancreas, thyroid gland [197] , in extracellular matrices such as endolymph [198, 139], as well as in several tissues such as vascular muscle cells and epithelial tissues of the gastro-intestinal tract (salivary gland, stomach, intestine, colon) [199–201].

In those different tissues, $K_V7.1$ channel is playing a diversity of roles. As seen in cardiomyocytes, $K_V7.1$ is co-expressed with KCNE1 β-subunits in kidney, the endolymph [202, 203], (the extracellular fluid around sensory cells of the inner ear) as well as in lungs, small intestine, leukocytes, ovaries and testicles [200, 201]. In the kidney, the role of $K_V7.1$/KCNE1 complex is not clearly defined besides its repolarizing role in the action potential related to the transport of Na^+ ions through the proximal tubules of the kidney. In the endolymph, the current generated by the IK_S complex is crucial for the maintain of the high potassium concentration (~150 $mmol.L^{-1}$) which is necessary for the sensory mechanisms of hearing and balance [143]. Despite being usually co-expressed with hERG gene, responsible for the IK_R current [204], several studies highlighted the co-expression of KCNE2 and KCNQ1 genes in mammalian cells on one hand [205, 206], and the synergic effect of both KCNE1 and KCNE2 subunits on the function of $K_V7.1$ channel in cardiomyocytes [207, 208].

The resulting currents are characterized by their low amplitude, along with the usual IK_S properties for $K_V7.1$/KCNE1/KCNE2 complex, and voltage-independence for $K_V7.1$/KCNE2 complex [208]. These results might explain how the identified KCNE2 mutations are associated with several cardiac arrhythmias including LQT2 syndrome [134] and atrial fibrillation [209].

Additional studies reports the role played by KCNE2 in thyroid gland [210], and brain [205] in which KCNQ1 is also expressed. Interestingly, other studies highlight the importance of both K_V7.1 [211] and KCNE2 [212] subunits in gastric acid secretion. In epithelial tissues of the gastro-intestinal tract, KCNQ1 is also co-expressed with KCNE3, in order to participate in Cl^- secretion [213]. The molecular determinants of both KCNE1 and KCNE3 constitute the object of numerous joint studies [214–216, 79, 186]. The functional studies of K_V7.1/KCNE3 channel complex have shown that it is characterized by a voltage-independent current and a linear I/V curve, which is similar as the modulation of K_V7.1 by KCNE2 subunits [204, 214]. The subunits KCNE4 and KCNE5 both induce an inhibitory effect on K_V7.1 in cardiac striated muscle cells [217]. The K_V7.1 inhibition of these subunits is lifted upon strong depolarization [218]. Specifically, KCNE4 inhibits K_V7.1 current [219, 220], while K_V7.1/KCNE5 complex generates a current only upon strong and sustained depolarization [221]. KCNE5 inhibitory effect was also observed on K_V7.1/KCNE1 complex.

Interestingly, the β-subunits of the KCNE family are able to interact with other cardiac ion channels [218]. Besides K_V7.1 α-subunits, KCNE1 β-subunits are also able to form complexes with hERG channel [222] and K_V4.3 channel [223] to increase the current amplitude of both IK_R and $I_{to,\,fast}$ currents during phase 2 and phase 1 of the cardiac AP, respectively. Both KCNE1 and KCNE2 were reported to favor hERG channel cAMP activation [224], but contrary to KCNE1, KCNE2 was shown to slow activation kinetics and to accelerate deactivation kinetics of hERG channel [225], K_V4.3 channel [226, 227] and HCN channels [228, 229] that generate the I_f current which turns out to be increased in presence of KCNE2. KCNE3 is also expressed in cardiomyocytes, in which it decreases the IK_S current through the binding of K_V7.1/KCNE1 complex.

Besides β-subunits, numerous patch-clamp studies shed light into the role played by the endogenous phosphatidyl-inositol-4,5-bisphosphate (PIP_2) in the function of numerous membrane proteins [230]. PIP_2 is a membrane phospholipid which participate in the function of many integral proteins, including voltage gated ion channels [231]. Indeed, PIP_2 is localized in the inner leaflet of the lipid bilayer at a 1% rate [232], and numerous experimental studies have shown that PIP_2, whose polar head carries four negative charges, activates the opening of several cardiac ion channels [233] including HCN [234], hERG [235], Kir6.2 [236] and Kir2.1 [237], responsible for I_f, IK_R, IK_{ATP} and IK_1 currents, respectively, as well as the Na/Ca exchanger which is the first integral protein to be proved to be activated by PIP_2.

The mutagenesis studies that allowed the identification of PIP_2 binding sites in the Kir6.2 [238] and the Kir2.1 [239] channels were used as starting points for the identification of the PIP_2 binding sites of $K_V7.1$ [240], since the lipid was shown to be crucial for the activity of K_V7 channels, as well as increasing their pore opening probability [241, 242]. The first functional studies conducted on IK_S channel in order to assess PIP_2 effects reported crucial interactions between PIP_2 and basic residues of the cytoplasmic C_{TERM} region of $K_V7.1$ [80, 157]. These interactions were predicted to stabilize the open conformation of $K_V7.1$, as suggested for the Kir6.2 and the Kir2.1 channels.

Later, thanks to the discovery [243] and the use of the *Ciona intestinalis* voltage-sensitive phosphatase (CiVSP), which specifically hydrolyzes PIP_2 during membrane depolarization [244], advanced functional studies were conducted on $K_V7.1$ channel in both the absence and presence of KCNE1 in order to identify whether PIP_2 regulates VSD activation, VSD-PD coupling between the voltage sensor and the gate [245], or both mechanisms. Among these studies, several ones [246, 247] shed light on the S6 residues of $K_V7.1$ that may possibly interact with PIP_2 in order to ensure the closed-open transition of the channel. Moreover, our collaborators from the Washington University of Saint-Louis have strongly contributed to address these questions. Indeed, they first highlighted the additional PIP_2 binding site on KCNE1 in IK_S channels [162], then dismissed the effects of PIP_2 on VSD activation and confirmed the essential role of PIP_2 in VSD-PD coupling, both through the use of CiVSP, which does not change F/V curve, while left-shifting the G/V curve, both with respect to the wild-type $K_V7.1$ channel.

Finally, they confirmed the PIP_2 binding site located on S6 cytoplasmic region of $K_V7.1$, and identified a second one in S2-$S3_{LOOP}$ which faces the inner membrane surface [245, 248]. Our previous MD study [249] of $K_V7.1$ homology model in open and closed states, allowed to localize the binding site of PIP_2 interaction in $K_V7.1$ subunit, and also to characterize the key elements of $K_V7.1$ modulation by PIP_2. (Figure I.4.2.6, A-B). The lipid was shown to participate in VSD/PD coupling of $K_V7.1$ channel through state-dependent interactions, preventing repulsive forces between basic residues from S2-$S3_{LOOP}$ and S4 in RC model, between basic residues from S2-$S3_{LOOP}$ and S6 in AO model and with S4-$S5_{LINKER}$ residues in both models. In this study, PIP_2 was shown to induce pore closure when the VSD is in its resting state. These MD simulations also suggested that PIP_2 may also constitute a third binding site for S4 gating charges. Indeed, the lipid was found to form salt-bridges with R4 and R6 in the RC model of $K_V7.1$, and not in the AO model (Figure I.4.2.6, B-C). Along with our collaborators, our previous integrative study of the IK_S complex revealed through the use of CiVSP that PIP_2 induces pore opening in both intermediate and activate states of the VSD [156].

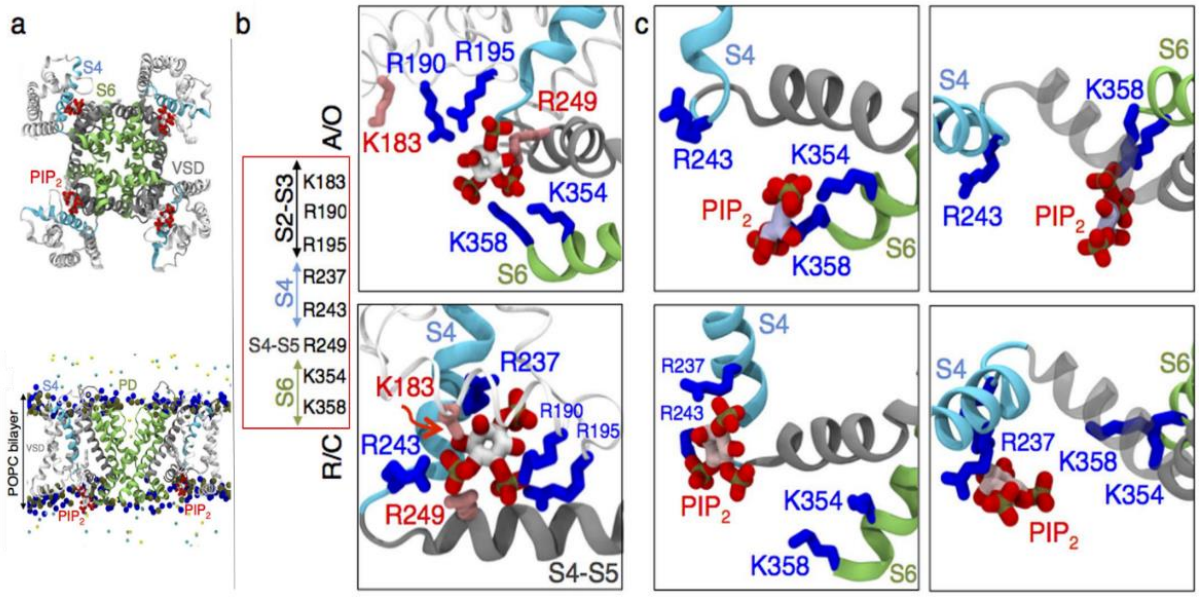

Figure I.4.2.6: MD simulations of $K_V7.1$ channel reveal its state-dependent PIP_2 binding sites.
The figure shows the $K_V7.1$ channel in its activated/open state (in ribbons) and its PIP_2 intrasubunit binding site after 50 ns of the equilibration. Color code: the VSD and the PD are shown in white and green respectively; S4 is highlighted in cyan. PIP_2 molecules are present as sticks with white hydrocarbon tails. Oxygen and phosphorus atoms of PIP_2 head groups are colored in red and tan. **A.** The upper and the lower panel display the bottom and side views of $K_V7.1$ model, respectively. On the lower panel, only the phosphorus (tan) and nitrogen (blue) atoms of the POPC bilayer head groups are shown for clarity. **B.** The pictures show extended views of the two modes of protein-lipid interactions, each favored either in the activated/open (A/O, top panels) or resting/closed (R/C, bottom panels) states of $K_V7.1$. The sidechains that form PIP_2 binding site are framed in red. **C.** Side (left panel) and top (right panel) views of the representative equilibrium position of PIP_2 at the intrasubunit binding site. Adapted from [248].

In the same year, an integrative study [250] which included a cysteine scanning of the basic residues from S2-S3$_{LOOP}$, S4-S5$_{LINKER}$ and S6 residues of K_V7.1 and a MD study conducted on the same K_V7.1 models in the presence of KCNE1 subunit, allowed for the identification of similar binding sites which were located in the region of S2-S3$_{LOOP}$ in the RC model, and in the region of S6 in the AO model.

In order to get a further insight into the mechanisms of K_V7.1 channel VSD-PD coupling/PD opening, as well as into the modulatory effects of both PIP_2 lipid and KCNE1 β-subunits, a molecular level of observation of these channels is of primordial interest. To date, among the IK_S 3D models that have been published for the last decade [154, 155, 195, 250, 251], the main goal of these models was not really focused on studying the dynamics of the IK_S channel complex. Besides, few of those were modeled along with PIP_2. Moreover, those which were modeled with the lipid aimed at validating experimental results for PIP_2 binding site identification in IK_S complex [250], without providing any molecular insight about the way PIP_2 interact with K_V7.1 nor KCNE1 subunits.

Recently, a 3D homology model [252] of IK_S complex was submitted to Molecular Dynamics (MD) simulations in a POPC:PIP_2 membrane with a 10:1 ratio, but IK_S-PIP_2 interactions were not extensively investigated in this study. Hence, these models do not provide molecular comprehension of PIP_2 nor KCNE1 effects on the VSD-PD coupling mechanism of K_V7.1. Besides, despite the studies which prove that IK_S complexes can be expressed with a 4:4 K_V7.1:KCNE1 stoichiometry [146, 253–255] most of the aforementioned models have not been built with this ratio, mostly due to several studies that reported contradicting results, suggesting that IK_S current is rather induced by IK_S complexes with a 4:2 K_V7.1:KCNE1 stoichiometry [155, 201, 256].

Therefore, the dynamics of the identified molecular determinants of both VSD-PD coupling and PD opening of the K_V7.1 channel, along with those allowing for the modulation of K_V7.1 function by KCNE1, as well as the ones describing a second PIP_2 binding site in IK_S complex at an atomistic scale are yet to be investigated. To address these questions, computational chemistry methods are the most insightful ones to unravel the elements of protein function at a molecular level of precision.

In the frame of this PhD work, we harnessed several computational techniques, from computational biology to computational chemistry, in order to provide a molecular insight into the mechanisms inherent in the main function of $K_V7.1$ channel, which is pore opening. The obtained results would allow to confirm the allosteric aspects of $K_V7.1$ channel that have been previously highlighted by several studies [152, 156, 257], as well as the roles played by PIP_2 and KCNE1 in the frame of the allosteric gating mechanism suggested by the previous experimental studies.

Appendix I. A cartoon insight into the cardiac upstroke

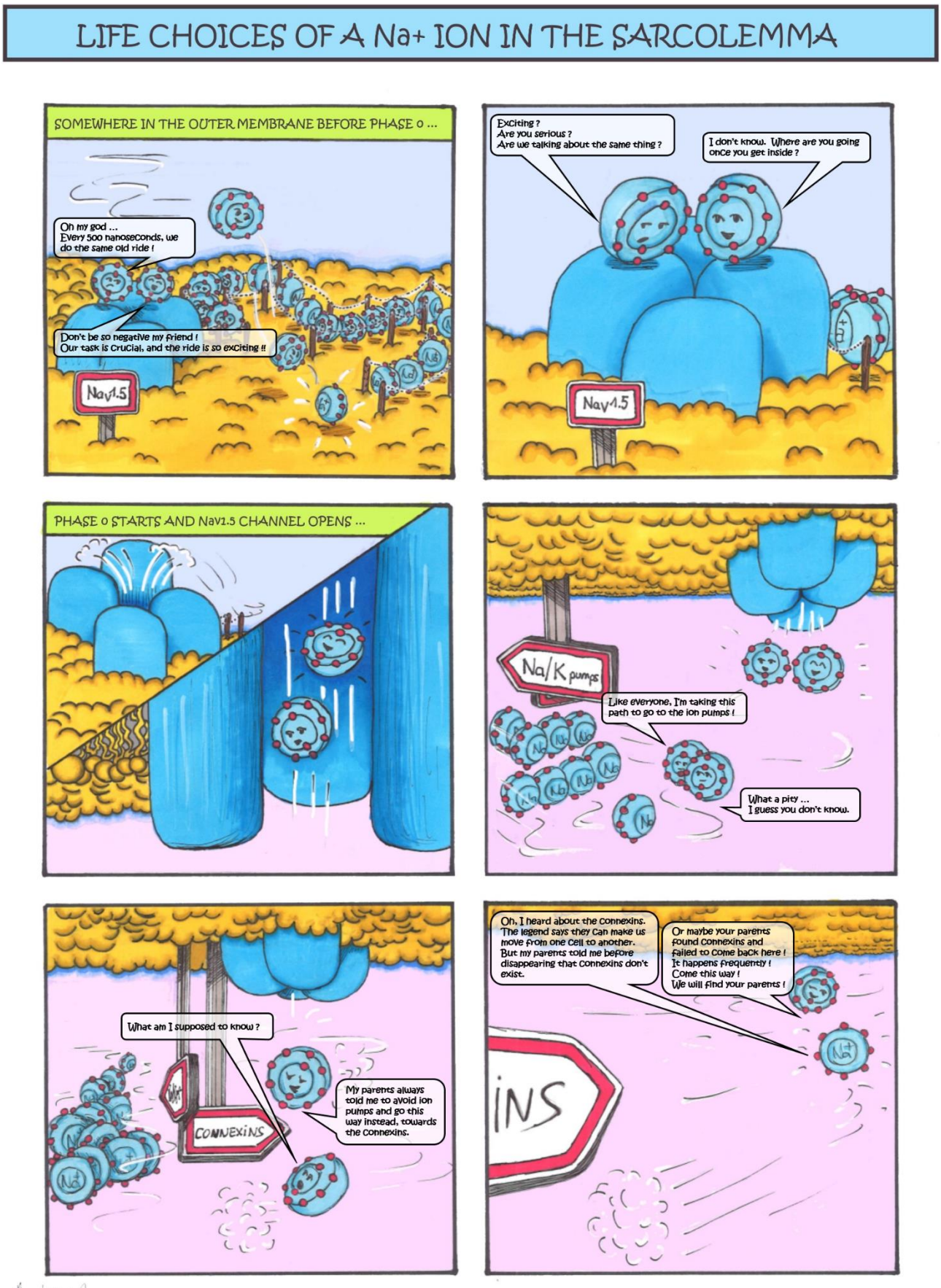

Appendix II. A cartoon insight into the cardiac repolarization

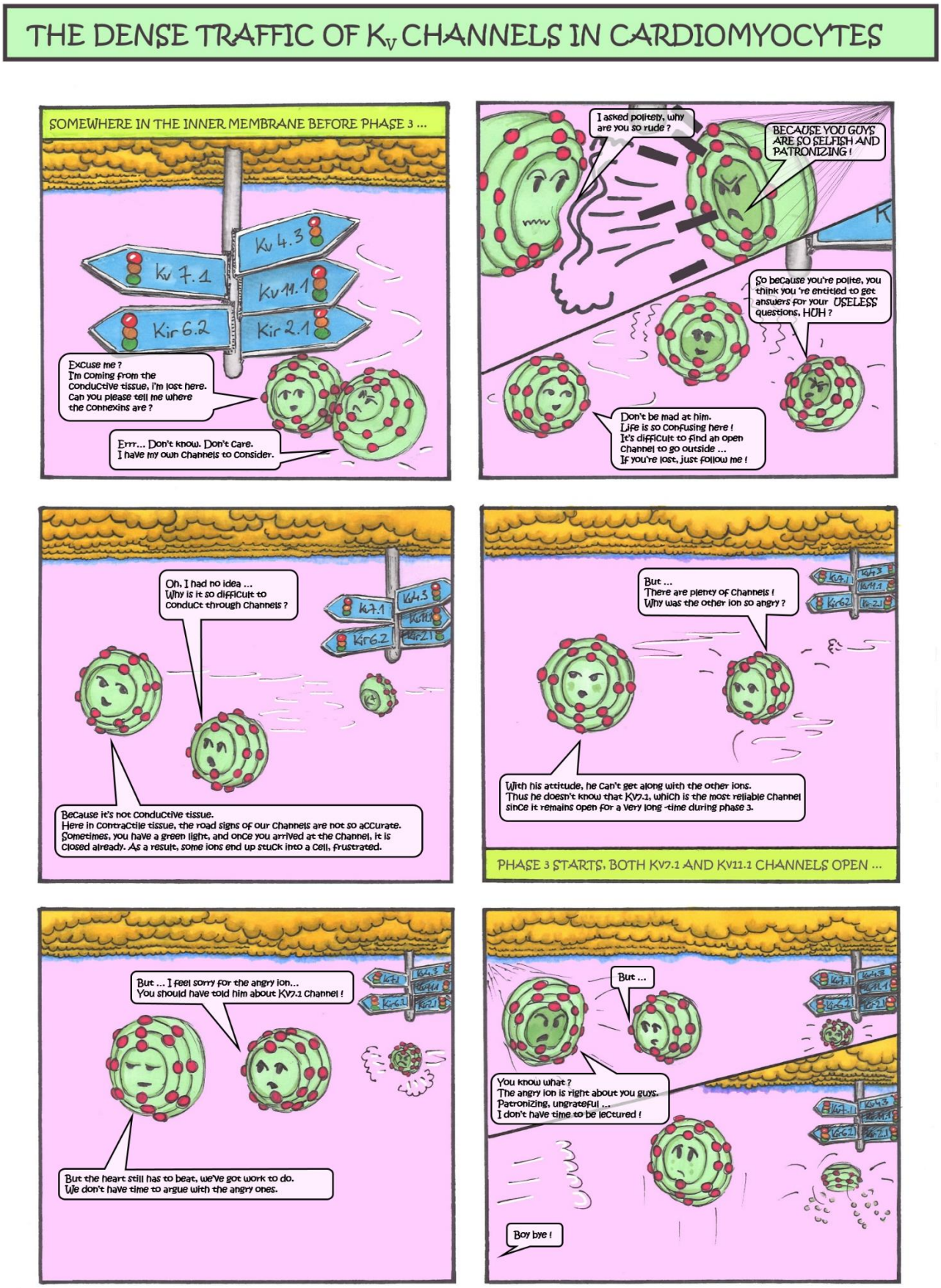

Chapter II. Methods

Lorsque nous avons débuté ce projet de recherche, la structure du canal K_V7.1 n'avait pas encore été résolue par le biais de méthodes expérimentales. Aussi, les approches relevant de la modélisation moléculaire computationnelle constituaient la seule alternative pour obtenir un support de visualisation de ce canal ionique particulier à l'échelle moléculaire. Grâce au principe de relation structure-activité, ainsi qu'aux nombreux résultats de biologie moléculaire obtenus pour K_V7.1, nous avons détaillé comment nous avons réussi à construire des modèles 3D de ce canal à partir de structures que nous avons précédemment généré pour un canal K_V homologue, le canal K_V1.2, à l'aide d'une technique appelée modélisation par homologie (**Chapter II.1**).

Une fois nos conformères 3D du canal K_V7.1 obtenus, notre but était d'étudier leur dynamique dans des conditions biologiques. Pour se faire, nous avons immergé chaque conformère dans une bicouche lipidique virtuelle contenant des phosphocholines et des molécules de PIP_2 ayant été précisément placées sur la couche interne, au niveau des sites d'interaction avec K_V7.1. L'ensemble « protéine + membrane » a ensuite été entouré de deux dalles d'une solution de KCl, afin de représenter l'intérieur et l'extérieur de la cellule. Ensuite, nous avons présenté en détails les principes qui sous-tendent la technique de Dynamique Moléculaire (DM), que nous avons utilisée afin de simuler la dynamique de nos conformères K_V7.1 à l'intérieur d'une membrane à l'équilibre dans des conditions expérimentales pour une durée de 500 ns (**Chapter II.2**).

Etant donnée la complexité de la fonction du canal K_V7.1, l'analyse des résultats obtenus sous la forme de trajectoires DM (**Chapter II.3**), avait deux objectifs distincts. Le premier était d'identifier les interactions protéine-protéine qui permettaient de stabiliser chaque conformère de K_V7.1 (Chapter II.3.1-2). Le deuxième était de caractériser les effets de KCNE1 et de PIP_2 sur ces interactions protéine-protéine.

Afin de caractériser les interactions clés présentes au sein de nos modèles, nous avons passé en revue la littérature pour identifier les types d'interactions majeurs ayant lieu entre les résidus d'une protéine transmembranaire, qui contribuent le plus à leur stabilité conformationnelle (Chapter II.3.3) : liaisons ioniques, liaisons hydrogène, interactions de Van Der Waals, les interactions de π-stacking et cation-π, ainsi que les interactions spécifiques de la méthionine que sont les interactions « Méthionine-Aromatique » et « Méthionine-Leucine ».

Nous avons également passé en revue les aspects géométriques de ces interactions, et nous avons utilisé certaines distances interatomiques en tant que descripteurs afin de d'identifier les interactions les plus importantes au sein de nos conformères de K_V7.1. Pour se faire, nous avons focalisé nos recherches sur les résidus qui avaient préalablement été associés à des mutations liées au syndrome du QT long (LQTS) de type « perte-de-fonction » qui avaient déjà fait l'objet d'études fonctionnelles alliant mutagénèse dirigée et électrophysiologie. Ces investigations ont permis d'effectuer la validation structurale de nos modèles par rapport aux données expérimentales préexistantes, ainsi que de prédire les changements conformationnels requis pour les transitions du canal K_V7.1 lorsque la membrane se dépolarise, depuis son état de repos vers son état activé, via son état intermédiaire.

At the beginning of this project, the structure of the K_V7.1 channel has not been resolved experimentally. Hence, computational molecular modeling approaches constituted the only way to obtain a molecular insight into this particular ion channel. Thanks to the famous structure-activity relationship, and the numerous molecular biology results obtained for the K_V7.1 channel, we detailed how we managed to build a 3D model of the K_V7.1 channel in its three known stable conformations from the structures we previously obtained for a homologous K_V channel with the use of the Comparative Modeling technique (**Chapter II.1**).

Once we obtained our K_V7.1 channel 3D conformers, our goal was to study their dynamics in their biological conditions. To do that, we embedded each model into a virtual atomistic lipid bilayer composed of phosphocholines and PIP_2 lipids located at their K_V7.1 binding sites and surrounded the ensemble "protein + lipid" by two slabs of a KCl solution. Then, we presented in detail the principles that underlie Molecular Dynamics (MD) simulations (**Chapter II.2**), as we used this technique to simulate the behavior of each K_V7.1 conformer at the equilibrium in experimental conditions for 500 ns.

Given the complexity of the K_V7.1 channel function, the analyses of MD simulations results (**Chapter III.3**), the MD trajectories, had two objectives. The first one is to validate each K_V7.1 state model against experimental data (Chapter II.3.1-2). The second one is to characterize the effects of both KCNE1 and PIP_2 on the protein-protein interactions that stabilize each K_V7.1 state model.

In order to characterize the key interactions that may occur in our MD systems, we reviewed the literature in order to identify the main interactions that occur between the residues of transmembrane proteins which contribute the most for their stability (Chapter II.3.3). Then, we also collected the geometrical aspects of these residue-residue interactions, including electrostatic interactions such as ionic bonds, hydrogen bonds, Van Der Waals interactions, π-stacking and cation-π interactions and specific interactions involving methionine residues, "Methionine-Aromatic" and "Methionine-Leucine" interactions. We use those interactions as descriptors in order to characterize the most important interactions within our K_V7.1 channel conformers.

To do that, we focused our research on the residues that were already associated with Long QT syndrome loss-of-function mutations. Thus, we listed all the residues whose mutants are both LQTS-related and studied through functional studies which combine site-directed mutagenesis and electrophysiology experiments. These investigations allow for the structural validation of our MD systems against experimental data, as well as the prediction of the conformational changes required for $K_V7.1$ transitions during membrane depolarization, from its resting state towards its activated state, through its intermediate state.

Chapter II.1. Comparative Modeling

The availability of the experimental and computationally derived 3D structures of K_V1.2 channel allows for designing tridimensional models of related K_V channels previously characterized as therapeutic targets and for which high-resolution crystal structures are not available. When we started to work on this research project, this was the case of K_V7.1 channel. Hence, it required building atomistic structural models of K_V7.1 channels as reliable as possible with respect to experimental results. The two main approaches that belong to the field of molecular modeling we used to obtain relevant K_V7.1 models will be presented in the next section.

Chapter II.1.1. Principle

Homology modeling, also known as comparative modeling, aims at building a protein structure (proper fold) from its primary sequence. This method starts from the structure-activity relationship, which implies that two proteins sharing similar primary sequences will display similar folds (3D structures). Since functional regions, including the S4 transmembrane segment in the VSD, and the selectivity filter in the PD, are relatively well conserved among K_V channels, this method was particularly interesting to build a 3D model of K_V7.1 channel since its structure had not been resolved yet. Hence, several 3D models of K_V7.1 channel were built using homology modeling [258, 155]. Noteworthy, several on-line servers [259–261] allow one to perform all of the homology modeling steps automatically, using protein sequence of interest as a query.

Chapter II.1.2. Template selection

In order to select a template structure for a known protein sequence, search algorithms on protein sequences can be launch from the Protein Data Bank (PDB), such as BLAST, or its protein-specific version, PSI-BLAST [262] to find the best template for a sequence of interest. Yet, if available, several templates can be used, in order to maximize the robustness of the model. In the case of K_V7.1, the refined X-ray structure of K_V1.2 [263] was directly selected as a template from the PDB (ID: 3LUT), without using any of these algorithms, to build the AO state of K_V7.1 α-subunits (Figure II.1.2.1).

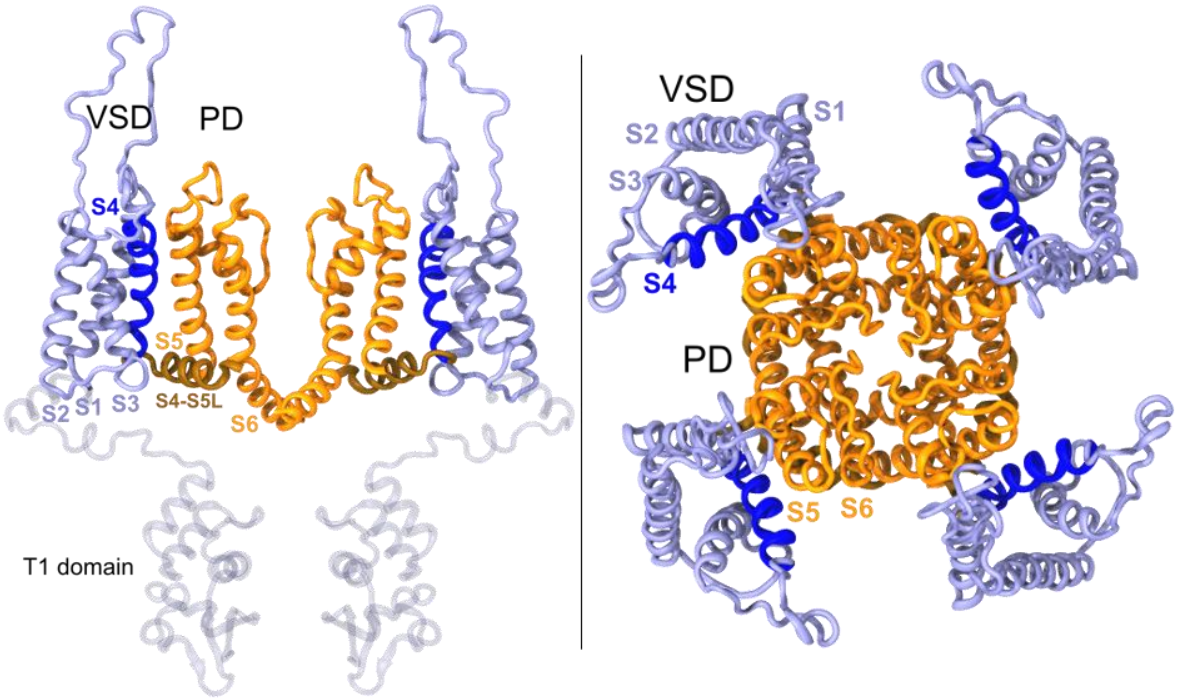

Figure II.1.2.3: Crystallographic structure of *rattus norvegicus* Kv1.2 channel.
The figure shows a cartoon representation of both transmembrane and cytoplasmic N_{TERM} region of Kv1.2 tetramer in a side view (left panel) and an extracellular view (right panel). On the left panel, only two subunits are displayed for clarity.

The γ and ε intermediate structures of the Kv1.2 channel (Figure II.1.2.2), obtained by a previous 1.5 μs MD simulation in hyperpolarized conditions in order to generate the voltage-dependent stable states known for the VSD of Kv1.2 channel [264], were used as templates to build Kv7.1 intermediate and resting states, respectively.

Recently, a tridimensional (3D) structure of *Xenopus Laevis* Kv7.1 channel, obtained by cryo-electron microscopy (CryoEM), was deposited in the PDB (ID: 5VMS). In this structure, the channel is in its uncoupled activated/closed (AC) state [78]. As stated by the authors, the conformation of the PD might be explained by the absence of PIP_2, which is known to be essential for the coupling of the activated state of the VSD with the open state of the PD in Kv7 channel family [242]. Accordingly, we used the CryoEM structure of *Xenopus Laevis* Kv7.1 to build a human model of Kv7.1 in its non-native activated state.

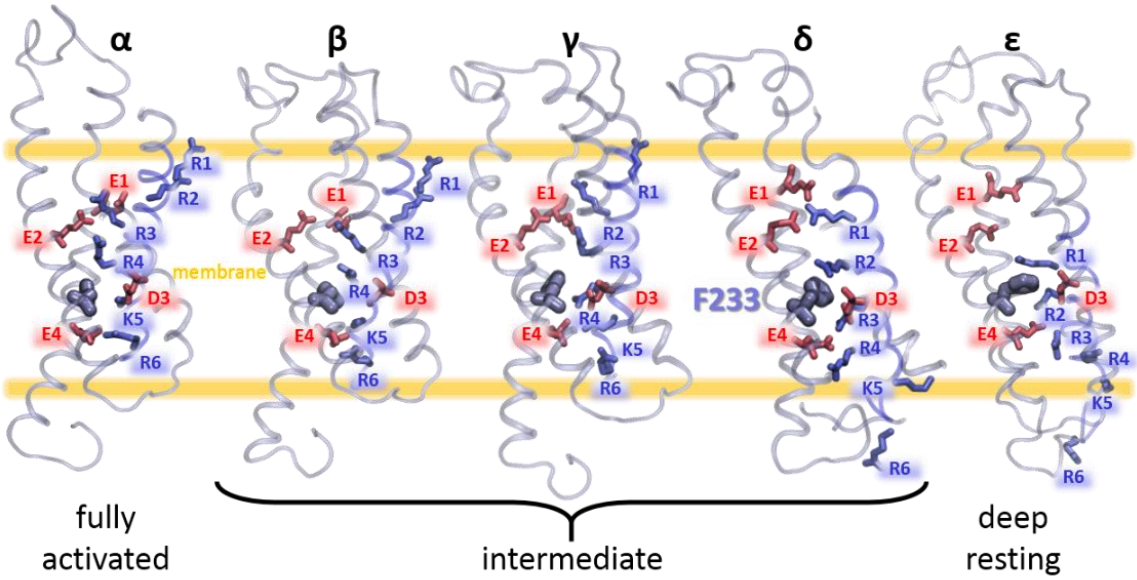

Figure II.1.2.4: Multiple VSD conformations obtained by MD simulations of Kv1.2.
This picture shows cartoon representations of the VSD of $K_V1.2$ subunit in the different conformations obtained from our previous MD simulations in hyperpolarizing conditions. Basic S4 gating charges R1-R6 are depicted in blue sticks, while acidic countercharges E1 from S1, E2 and E4 from S2, and D3 from S3, are depicted in pink sticks. The charge transfer center F233, located between E2 and E4 on S2, is depicted in thicker blue sticks. Adapted from [245, 246]

Chapter II.1.3. Sequence alignment

As the quality of the resulting model depends on that of the sequence alignment, this step is by far the most important of the homology modeling method. Thus, it is needed to evaluate the similarity between the template sequence and the query sequence. This similarity is called sequence identity and is expressed in percentage values. Generally, the minimum sequence identity required to obtain a model of sufficient quality is ≈30%.

To that extent, the alignment of K_V7.1 and K_V1.2 primary sequences was first conducted automatically, using the program ClustalW2 [265]. To obtain a multiple sequence alignment, which strengthens the confidence of the procedure, the K_V7.1 sequence was aligned to K_V1.2 along with protein sequences of the four other α-subunits from the K_V7 family. For the PD, the percentage of identity between K_V7.1 and K_V1.2 sequences is 36%. For the VSD, the percentage is 19.5%. This lower sequence identity is mainly due to the S2-S3 loop, whose primary sequence is longer in K_V7.1 than in K_V1.2. In order to overcome this discrepancy, this alignment was refined both manually and locally (Figure II.1.3.1). Indeed, in order to optimize the sequence identity of the VSD, the conserved residues of Kv7.1 which were identified as crucial for canonical K_V channels function (Figure II.1.3.1, blue) were specifically aligned with similar K_V1.2 ones, and insertions and deletions were concentrated in the loop regions. Eventually, without S2-S3 loop, the percentage of identity was increased to 25% for the VSD.

For the AC model of K_V7.1, we aligned KCNQ1 human sequence with the primary sequence of *Xenopus Laevis* K_V7.1, whose 3D structure has recently been obtained by CryoEM. This sequence presented 70% of identity with the human K_V7.1 sequence. For the transmembrane region of K_V7.1, the sequence identity between these orthologue genes increased up to 92%. Hence, the 3D structure of human K_V7.1 subunit could be easily predicted from this CryoEM structure.

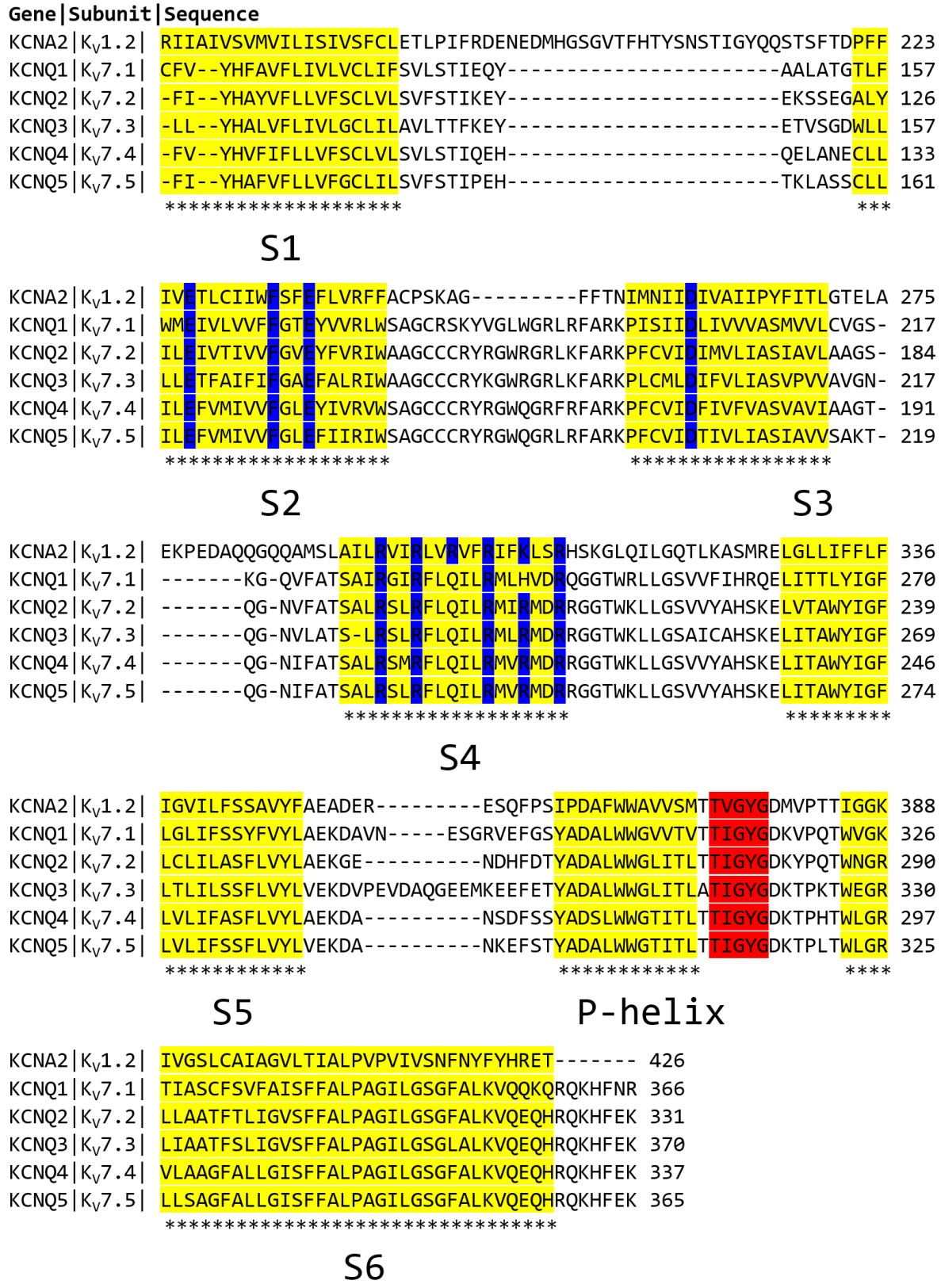

Figure II.1.3.1 : Edited sequence alignment of the K_V1.2 channel and the K_V7 subunit family.
This figure shows the edited alignment of the primary sequences of K_V1.2 channel and the K_V7 channel family. The transmembrane segments S1-S6 are highlighted in yellow. The conserved gating charges in S4, as well as its conserved countercharges in S2 and S3 segments, are highlighted in blue. The selectivity filter, strongly conserved among K_V channels, are highlighted in red.

Chapter II.1.4. Model building and optimization

As our study is focused on the function of K_V7.1, we created models containing only the transmembrane region of K_V7.1 (residues 122 to 358) in each known state to obtain a larger spectrum of possible K_V7.1 α-subunits conformations. As a consequence, N_{TER} and C_{TER} cytoplasmic regions of K_V7.1 were ignored. For the AC model of Kv7.1, the primary sequence used for the transmembrane region of Kv7.1 subunit was slightly extended, as we used residues 122 to 366. To build IK_S complex models, we built each metastable state of the extended transmembrane region of K_V7.1 (residues 122 to 366) along with the TMD (residues 39 to 76) of human KCNE1 NMR structure [189] using a K_V7.1:KCNE1 subunit ratio of 1:1 that is the maximal possible ratio for this complex [253].

For each state of K_V7.1 α-subunit, we used MODELLER [266] to build fifty K_V7.1 models. This software allows one to perform constrained modeling, a technique which uses template coordinates and sequence alignment information as constraints for the 3D model building. Thus, bond and non-bonded lengths, as well as angle and dihedral values are drawn from template structures are used as stereochemical constraints to build the K_V7.1 model in is required state. We used a specific template 3D structure extracted from NMR data [267] to model S2-S3 loop. Indeed, the NMR coordinates suggest a helical structure for S2-S3 connecting loop. In addition, MODELLER allows for the setting of specific geometric restraints. Thereby, several constraints were applied according to site-mutagenesis results to increase reliability of K_V7.1 models with respect to experimental data. In order to adjust K_V7.1 salt-bridges patterns of the VSD , we imposed in agreement with respect to experimental results [161, 168], that E1 charged groups to be constrained towards R1 and E2 towards R2 in the resting/closed state, that E1 be constrained towards R2 in intermediate/open state, and that E1 be constrained towards R4 in the activated/open state.

In order to accommodate the conformation of KCNE1 subunits in IK_S models, we used the coordinates of KCNE1 in the 3D models of K_V7.1-KCNE1 complex [154] in the AO and RC states as templates for the IK_S AO and RC models, respectively. For the IK_S IC model, we used the same KCNE1 coordinates as for the IK_S RC model, as experimental studies showed that the IKs complex is not conductive when the VSD is in its intermediate state [156, 161].

Among these 50 obtained models, we harnessed the DOPE (Discrete Optimizing Protein Energy) [268] knowledge-based scoring function, implemented in MODELLER to select the best ten ones according to their potential energy values.

Chapter II.1.5. Evaluation of the obtained molecular model

The most common way to evaluate the stereo chemical quality of a 3D model is to verify, for each residue, if the torsion angle values of its backbone, usually defined as φ and ψ, are well included in the favored areas of the Ramachandran plot. To do this on the 10 best models that were previously selected for each stable state of Kv7.1 subunit, the software PROCHECK [269] was used. The models that present the highest number of torsion angles in Ramachandran's plot well favored areas (>95%), as well as the lowest number of torsion angles in the disfavored areas (<5%), were selected to design the chemical systems which would be submitted to molecular dynamics simulations.

Chapter II.2. Classical Molecular Dynamics

Chapter II.2.1. Principle

Molecular dynamics (MD) simulations refer to a computational method aimed at simulating a macroscopic behavior of a microscopic many-body system through the numerical integration of the classical equations of motion. Microscopic properties are expressed as functions of N particle coordinates $(r_1, r_2, \dots, r_N,)$ and/or momenta, which are computed along a phase space trajectory generated by classical dynamics [270–272]. MD simulations require the choice of a potential energy function $U_{ri}(r_1, r_2, \dots, r_N,)$, usually defined as a Force Field (FF), by which the N particles interact. In chemistry and biophysics, the most commonly used FFs such as GROMOS [273], CHARMM [274], and AMBER [275] or OPLS [276] are based on molecular mechanics and a classical treatment of particle-particle interactions that precludes bond dissociation and therefore the simulation of chemical reactions. The FF is usually expressed as a summation of bonded forces associated with chemical bonds stretching, bond angles and bond dihedrals deformation, and non-bonded forces associated with Van der Waals (VdW) and electrostatic interactions. The parameters associated with each term are optimized to reproduce structural and conformational changes of the macromolecular system. To simulate $K_V7.1$ models, we used the CHARMM22 all atom FF, whose potential energy is expressed as follows:

$$U = \sum_{bonds} k_b(b - b_0)^2 + \sum_{angles} k_\theta(\theta - \theta_0)^2 + \sum_{dihedrals} k_\phi\,[1 + \cos(n\phi + \delta)] + \sum_{impropers} k_\omega(\omega - \omega_0)^2 + \sum_{Urey-Bradley} k_u(u - u_0)^2 + \sum_{nonbonded} \epsilon\left[\left(\frac{R_{min_{ij}}}{r_{ij}}\right)^{12} - \left(\frac{R_{min_{ij}}}{r_{ij}}\right)^{6}\right] + \frac{q_i q_j}{\epsilon r_{ij}}$$

where k_b is the bond force constant, $b - b_0$ is the interatomic distance between the position of the atom i and its equilibrium position ; k_θ is the angle force constant and $\theta - \theta_0$ is the angle difference from equilibrium between three bonded atoms. In the torsion angle term, k_ϕ is the dihedral force constant, n is the multiplicity of the periodic function, ϕ is the dihedral angle and δ is the phase shift.

The impropers are defined as out of plane bending angles, where k_ω is the force constant and $\omega - \omega_0$ is the out of plane angle difference from the equilibrium. The Urey-Bradley component accounts for angle bending of 1, 3 non-bonded interactions, where k_u is the respective force constant and $u - u_0$ is the distance between the 1, 3 atoms in the harmonic potential. The last two terms account for the non-bonded interactions between pairs of atoms (i, j). By definition, the non-bonded forces are only applied to atom pairs separated by at least three bonds. The Van der Waals (VdW) energy is calculated with a standard 12-6 Lennard-Jones potential and the electrostatic energy with a Coulombic potential. In the Lennard-Jones potential above, the $R_{min_{ij}}$ term is not the minimum of the potential, but rather where the Lennard-Jones (L-J) potential crosses the x-axis (*i.e.* where the Lennard-Jones potential equals to zero).

The speed of execution of the programs, and the availability of computer power limits the system size. As a consequence, computer simulations are usually performed on a small number of molecules (from few tens to few hundred thousand atoms). In order to mimic a macroscopic system and to eliminate edge effects, simulations of condensed phase systems consider a central simulation cell in which a small patch of molecules are confined. This cell is replicated by the use of periodic boundary conditions (PBCs) in the three directions of the Cartesian space (Figure II.2.1.1). For instance, a simulated system containing a phospholipid bilayer hosting ion channels would correspond to the channel incorporated into a small fragment of a plasma membrane. Each particle leaving the central box during MD simulation by one side is reintroduced in the box by its opposite side.

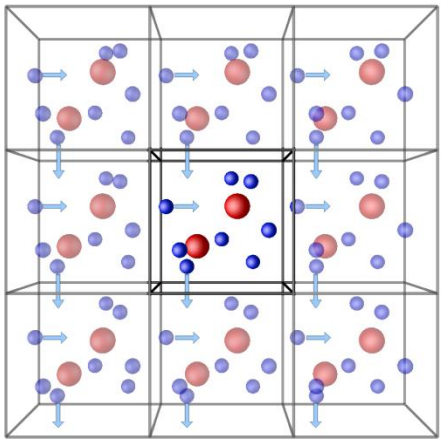

Figure II.2.1.1: Periodic boundary conditions in MD simulations.
The particles of the central simulation box are depicted in solid colors, while those of its 3D periodic images are represented in transparent colors. Only two dimensions of periodic images are shown for clarity.

In order to run the MD simulations, we need to be sure that our parameter file has all the terms specified in the FF we are using (*i.e.* the equation specified above). At $t = 0$, random velocities are set to each particle of the system. At a given instant in time t, the MD simulations use information (positions, velocities or momenta, and forces) to predict the positions and momenta at a later time $t + \delta t$. The time step δt is of the order of a femtosecond and considered as constant throughout the simulation. Numerical solutions to the following equation of motion:

$$F_i(t) = m_i\, d^2r_i/dt^2 = m_i a_i(t) = -\nabla U_{ri}(r_1, r_2, \dots, r_N,)$$

are thus obtained for each particle i by iteration of this elementary step, using for instance the Velocity Verlet algorithm [277] in PBC. As such, at time $t + \delta t$, the position r is expressed as:

$$r(t + \delta t) = r(t) + v(t)\delta t + \frac{1}{2}a(t)\delta t^2$$

The velocity is first computed as a function of the half time step $t + \frac{1}{2}\delta t$ to obtain the full-time step velocity:

$$v\left(t + \frac{1}{2}\delta t\right) = v(t) + \frac{1}{2}a(t)\delta t$$

$$v(t + \delta t) = v\left(t + \frac{1}{2}\delta t\right) + \frac{1}{2}a(t + \delta t)\delta t$$

Finally, the time step acceleration is directly calculated from Newton's classical equation of motion:

$$F(t) = ma(t) = -\nabla U\big(r(t)\big)$$

$$a(t + \delta t) = -\frac{1}{m}\nabla U(r(t + \delta t))$$

When PBCs are applied on a MD system, its particles have the same movement in each periodic box. As no physical boundaries are set between these boxes (otherwise it would not replicate a macroscopic system), the computing of potential energies associated with long-range interactions such as non-bonded ones can constitute a problem. To overcome this problem, an approximation function is usually applied in order to optimize the computation of the VdW energy term during MD simulations.

Among the several existing functions of approximation (shift, truncated), the most commonly used in molecular dynamics simulations is the switch potential (Figure II.2.1.2), which is defined between two cut-off distance values r_{c1} and r_{c2} in a way that the potential follows to L-J potential curve until the interatomic distance reaches r_{c1}, after which the potential is smoothly brought to 0 when the distance reaches r_{c2}.

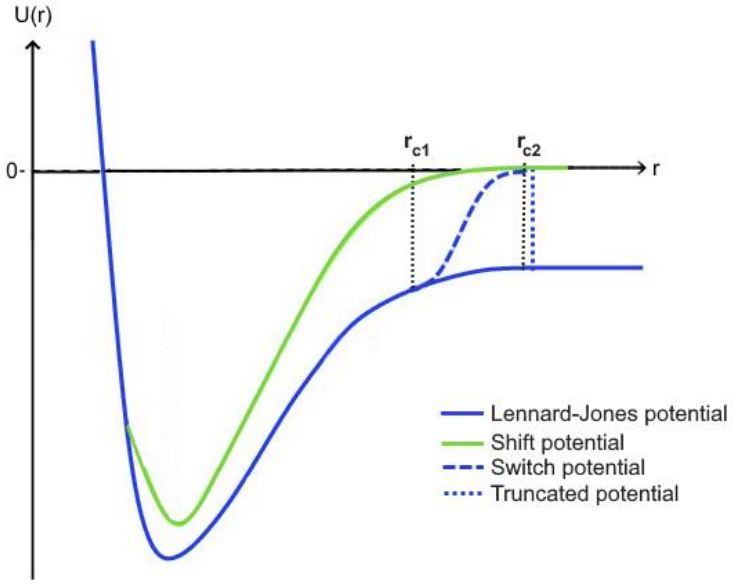

Figure II.2.1.3: Approximate functions of the Van der Waals (VdW) non-bonded energies.
The graph represents the evolution of the potential energies U(r) against the distance r in the Lennard-Jones potential (plain blue lines), and the truncated (dotted blue line), shift (plain green line), and switch (dashed blue line) cut-off functions.

To compute long-range electrostatic interactions, whose range is greater than the half of the of the simulation cell, the Particle Mesh Ewald (PME) algorithm [278] is commonly used to minimize the computational cost of the MD simulation. Directly derived from the Ewald summation [270], which was basically developed for crystallographic purposes, it consists in calculating the electrostatic energy $\phi(r)$ as a sum of a short-range interaction energy term $\phi_{sr}(r)$ calculated in real space and a long-range interaction energy term $\phi_{lr}(r)$, calculated in Fourier space. As such, the electrostatic interaction energy between particles i and j, noted E_{TOT} is expressed as follows:

$$E_{TOT} = \sum_{i,j} \phi(r_j - r_i) = E_{sr} + E_{lr}$$

The short-range energy E_{sr} which converges rapidly in real space (defined by r coordinates) is expressed as:

$$E_{sr} = \sum_{i,j} \phi_{sr}(r_j - r_i)$$

The long-range energy E_{lr} , which converges rapidly in Fourier space (defined by k coordinates) is expressed as:

$$E_{lr} = \sum_{k} \widetilde{\phi_{lr}}(k)|\tilde{\rho}(k)|^2$$

where $\widetilde{\phi_{lr}}$ and $\tilde{\rho}(k)$ are the Fourier transforms of the electrostatic potential and the charge density, respectively.

Chapter II.2.2. Modeling Kv7.1 channels in their membrane environment

In order to reproduce the dynamics of the transmembrane region of Kv7.1 channel in molecular dynamics simulations, it is crucial to build a system in which the channel remains embedded in lipid bilayers to mimic its membrane environment. To do this, two strategies are commonly used. The first one consists in modeling a very large patch of lipids, then placing the channel structure in the middle of the patch prior to remove all the lipids that are in direct contact with the protein. The second method, available in the input generator of a CHARMM-GUI interface [279], is the one we chose to design our MD systems of Kv7.1 channel and consists in aggregating lipid molecules around the protein structure [280]. As phosphatidylcholine (PC) lipids such as Palmitoyl-oleylPC (POPC) are the most abundant phospholipids found in cell membranes, they are used in most simulation studies involving lipid bilayers (Figure II.2.2.1, upper panel). The phospholipid PIP_2 (Figure II.2.2.1, lower panel), which is present only in the inner leaflet of the membrane at a 1% rate, and required for the activation mechanism of Kv7 channels [241] has been considered as an important molecule in modeling the models of this study. Since the specificities of PIP_2 binding to Kv7.1 channels were not clearly understood, two strategies have been used to determine its binding sites in the models of Kv7.1 channel absence and presence of KCNE1.

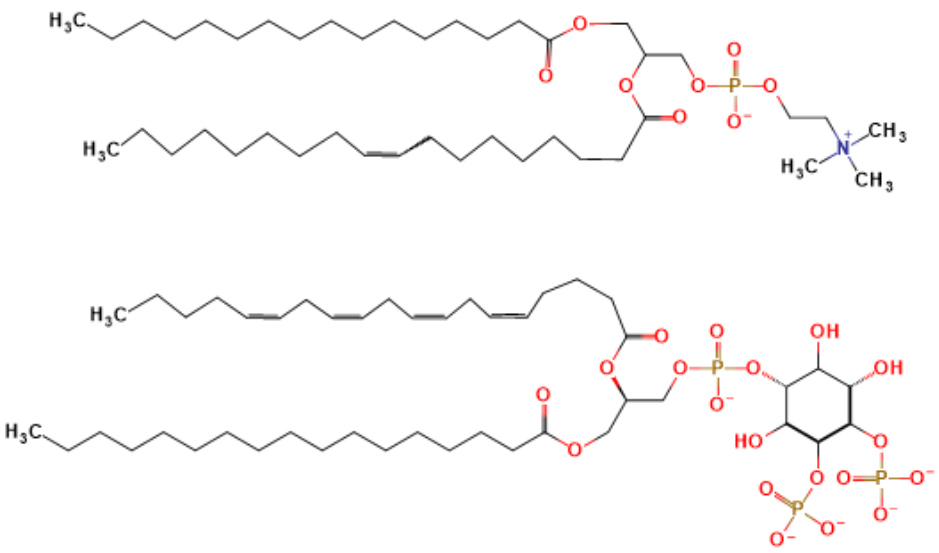

Figure II.2.2.1: Membrane lipids used in MD systems.
Topological formulas of Palmitoyl-Oleyl-Phosphatidylcholine (POPC, upper panel) and Phosphatidyl-inositol-4,5-bisphosphate (PIP_2, lower panel). Each molecule is represented with the charge set in the MD parameters of CHARMM FF.

CHARMM-GUI offers the possibility to model multi-components and more adequate lipid membranes in symmetrical or asymmetrical bilayers composed of several types of lipids, we used this program for the first strategy, applied in order to determine its binding sites in $K_V7.1$ α-subunits [249]. It consists in flooding the inner leaflet of the bilayer with an excess of PIP_2 lipids prior to equilibrate the system through MD simulations. The second strategy relies on experimental data to place PIP_2 lipids in proximity with particular side chains identified as potential binding sites [250] and was used to determine PIP_2 binding sites in KCNE1 ancillary subunits.

Hence, we designed a total of ten MD systems. The first three include $K_V7.1$ α-subunits in its RC, IO and AO states (Figure II.2.2.2, left panel). To address the modulation effects of PIP_2 on $K_V7.1$ channel, we added one such lipid per $K_V7.1$ monomer. PIP_2 molecules were placed in their predicted interaction sites with $K_V7.1$ subunits, located at the bottom of each VSD (PIP_2 intra) [246, 248–250]. In order to get a better understanding of the VSD-PD coupling mechanism of $K_V7.1$ channel, we also built a fourth human model of $K_V7.1$ in an uncoupled state by homology (Figure II.2.2.2, right panel).

To do this, we used the CryoEM structure of Xenopus Laevis $K_V7.1$ subunit as a template [78]. Indeed, this subunit was resolved in a non-native conformation, as its VSD is in its activated state, while the PD is in its closed state. According to the authors, this structure represents an uncoupled state of $K_V7.1$ due to the absence of PIP_2 lipid. Hence, the MD system for $K_V7.1$ AC model was built without PIP_2 lipids.

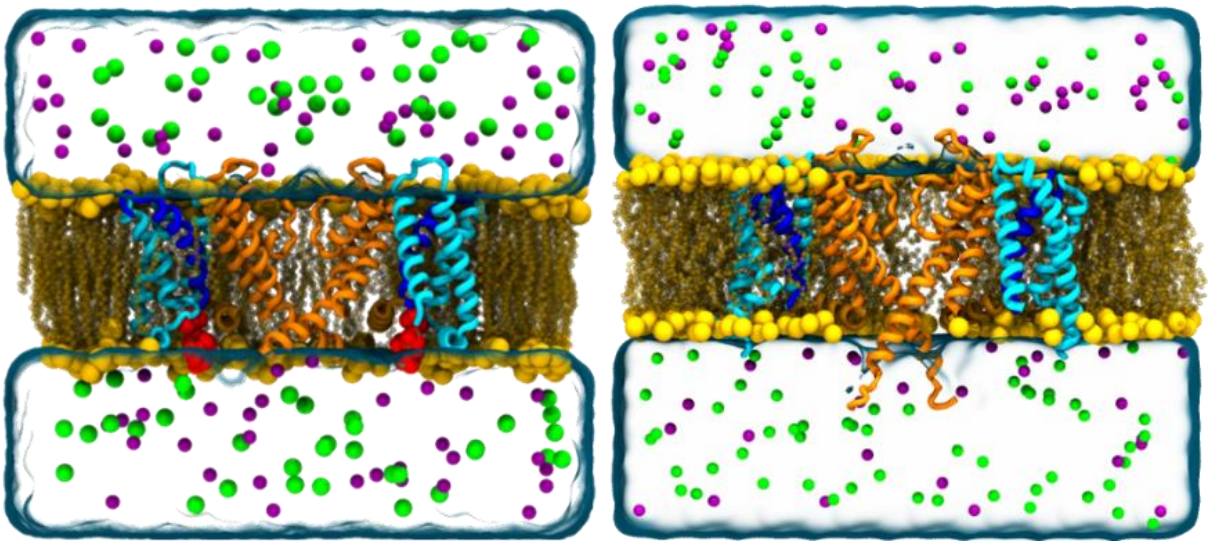

Figure II.2.2.2: Onset MD systems of Kv7.1 models.
Representation of $K_V7.1$ in its AO state with one PIP_2 lipid (red spheres) per $K_V7.1$ monomer (left) and AC state (right). Two $K_V7.1$ subunits are shown for clarity. Transmembrane segments are represented in cartoon and colored as follows: S1-S3 segments in cyan, S4 in blue, S4-$S5_{LINKER}$ in brown and PD segments in orange. Models are embedded in a POPC membrane whose polar heads are represented in solid yellow spheres, while lipid tails are depicted in transparent yellow spheres. Membrane-embedded models are surrounded by two slabs of water (in transparent blue surface), each containing K^+ (purple spheres) and Cl^- (green spheres) ions.

For IK_S models, we embedded the three RC, IC and AO models of $K_V7.1$ along with one KCNE1 subunit for $K_V7.1$ monomer in two distinct environments. In the first system, labeled as $4PIP_2$ (Figure II.2.2.3, left panel), we added only PIP_2 intra, corresponding to the binding site of $K_V7.1$ subunits. In the second system, labeled as $8PIP_2$ (Figure II.2.2.3, right panel), we added a second PIP_2 molecule at the bottom of each KCNE1 subunit (PIP_2 inter) in addition to PIP_2 intra, according to experiments that highlighted a second PIP_2 binding site in IK_S channels [162].

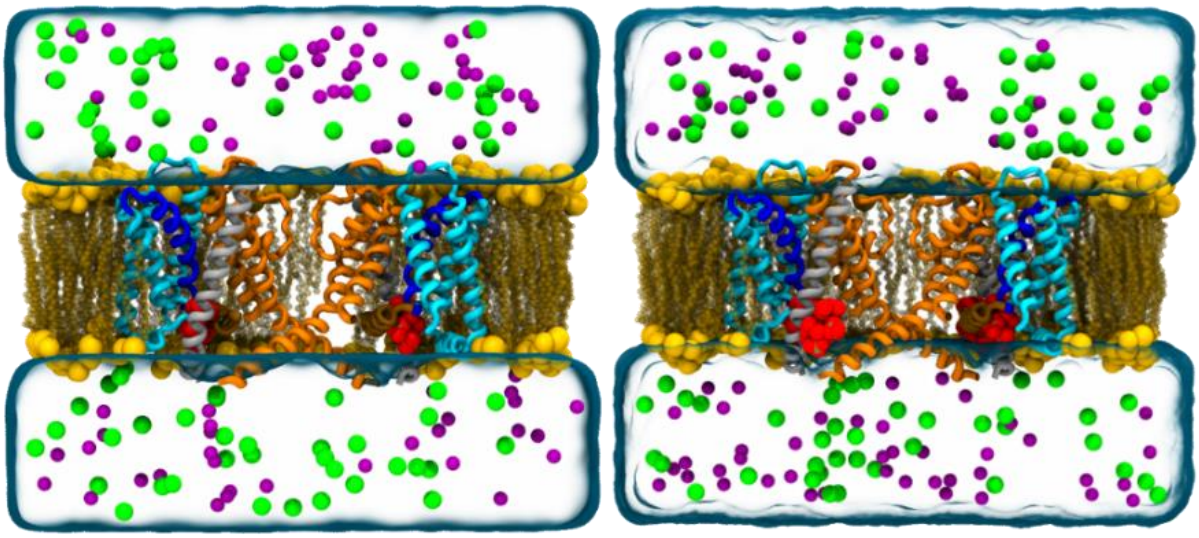

Figure II.2.2.3: Onset MD systems of IK_S models.
Representation of IK_S AO models in $4PIP_2$ (middle) and $8PIP_2$ systems (right), each containing one or two PIP_2 lipid (red spheres) per $K_V7.1$ monomer, respectively. Two $K_V7.1$ subunits are shown in cartoon for clarity. Transmembrane segments and POPC lipids are colored as in Figure II.2.2.1. KCNE1 subunits are colored in gray.

To reproduce the true dynamics of the transmembrane region of $K_V7.1$ channel, we reconstituted its biological environment in all our MD systems. Hence, we embedded each model along with its respective number of PIP_2 lipids in a virtual POPC membrane. Each system (lipids+ channel) was surrounded by two slabs of a 150 mM KCl electrolyte bath. As in the majority of MD systems containing a lipid bilayer that is supposed to represent a plasma membrane, we assumed by convention the upper bath and the lower bath as the extracellular medium and the cytosol, respectively. Each simulated system contains a total of ~200 000 atoms.

Chapter II.2.3. MD simulations

Generally, MD simulations aims at studying the time evolution of a classical system containing a constant number of particles N, evolving in a constant volume V. To satisfy the principle of energy conservation, MD simulations solve differential equations by numerically integrating the equation of motions in an iterative manner with a time step δt in the order of the femtosecond, (1 fs = 10^{-15} second). Ideally, as K_V channels activate is the millisecond time scale, MD simulations should reach this time range in order to provide a molecular insight of this mechanism. Nowadays, the time range that can be reached by this technique is rather of the order of the microsecond, at the exception of few extremely rare cases [281] using for instance special purpose machines.

During MD simulations, the calculations are providing microscopic level of information. In order to extract relevant macroscopic properties of a system, usually defined as a thermodynamic state, it is common to ensure that our MD systems are thermodynamically consistent. To achieve this goal, MD systems are usually assimilated as thermodynamic ensembles, which can be defined by macroscopic terms [270]. Newton's equations of motion are used to keep the total energy constant, which enables the system to sample a micro-canonical ensemble (NVE) along the MD trajectory. Two other ensembles can be used in order to mimic the experimental conditions, namely the isothermal-isobaric (NPT) ensemble where both the temperature and the pressure are controlled, or canonical ensemble (NVT) where the volume and the temperature are kept constant [282]. For the MD systems of this present work, simulations were carried out using the NPT ensemble for the equilibration of the systems to reproduce experimental conditions, at a fixed temperature $T_0 = 300$ K, and a fixed pressure of 1 atm.

In order to keep both the temperature and the pressure of the systems constant, two distinct algorithms implemented in NAMD were applied, namely the Langevin dynamics thermostat [283] and the Langevin piston barostat [284], respectively. The thermostat is applied on each particle i of the MD system by the resolution of the Langevin equation, which is defined as follows:

$$m_i a_i(t) = F_i(t) - \gamma_i m_i v_i(t) + R_i(t)$$

where m_i, a_i, F_i and v_i are the mass, the acceleration, the force exerted by the other MD particles, and the velocity of the particle i, respectively. The collision frequency γ_i is defined by:

$$\gamma_i = \frac{\xi_i}{m_i}$$

where ξ_i is the friction constant of the particle i. R_i is the temperature-dependent random force, which follows a Gaussian distribution of zero mean value, whose variance is expressed as:

$$\langle R_i^2 \rangle = \frac{2 m_i \gamma_i k_B T_0}{\delta t}$$

where k_B is the Boltzmann constant, δt is the integration timestep and T_0 is the fixed temperature (300 K). Noteworthy, POPC bilayers have a transition temperature of ~270 K at full hydration, *i.e.* at 300K the bilayers are in the liquid crystal phase. The Langevin piston barostat is derived from the weak coupling algorithm [285]. The latter starts from the premise that the volume of a cubic system with a constant pressure will necessarily vary. As such, the algorithm treats the volume of the MD system as a dynamic variable noted V, whose second derivative is expressed as:

$$\ddot{V} = \frac{1}{W}[P(t) - P_0] - \gamma \dot{V} + R(t)$$

Where W is the "mass" of a piston, expressed in ML^{-4} dimensions, $P(t)$ is the instantaneous pressure, P_0 the fixed pressure, γ is the collision frequency, and $R(t)$ is a random force that follows a Gaussian distribution of zero mean value, whose variance is expressed as:

$$\langle R(0)\, R(t) \rangle = \frac{2 \gamma k_B T_0 \delta t}{W}$$

Among the available efficient codes dedicated to perform MD simulations, including CHARMM [286], AMBER [287], GROMACS [288], NAMD [289] and Desmond [290], we used NAMD [289] to perform all MD calculations. In our specific runs we used a combination of the CHARMM22 [274] and CHARMM36 [291] force-fields, which are parameterized for proteins and POPC lipids, respectively. For PIP_2 lipids, we considered the specific force field parameters previously developed through quantum mechanics calculations [292].

We also used the CMAP correction [293] to calculate the potential energy of the system using accurate parameters for the different molecules included in our heterogeneous MD systems. Chemical bond lengths between hydrogens and heavy atoms were all constrained at their equilibrium values with the SHAKE algorithm [294] so that a δt of 2.0 fs could be used. MD simulations were conducted on stable state models of $K_V7.1$ channel in order to stabilize the conformation of each model in the absence and the presence of its modulators KCNE1 and PIP_2 within a virtual membrane. To reproduce as best as possible the topologies of this channel protein, simulations were carried out in four steps, during which motion constraints were applied on the whole system, and then gradually released. These steps are usually clustered into two main phases.

The first one, the equilibration phase, is necessary to proceed carefully, as the lipid bilayer and the electrolyte solution need to equilibrate around the channel prior to fully solvate the protein within its MD system. Regardless of the nature of the starting coordinates, (either a channel crystal structure or a homology model) the equilibration phase of a MD simulation should always be performed with all protein atoms fixed, until a constant density of the system is reached. This normally takes few tens of nanoseconds. In the present case, the equilibration phase was divided into four steps. The first one of 200 ps aimed at fully solvating $K_V7.1$ α-subunits in the membrane, by letting lipid molecules rearrange themselves around the protein. Accordingly, constraints were set up on all protein atoms.

The constraints applied on the protein were then gradually released, by imposing a second run (of few tens of ns) with constraints on the motion of the protein backbone atoms, allowing for the side chains to relax. Accordingly, the second step of 6ns was run to relax the side chains of the protein, so the constrains were kept only on IK_S backbone. During the first and the second steps, the positions of PIP_2 phosphorus atoms in the system were kept constant, to maintain this lipid in its correct binding sites. The third step was conducted to allow PIP_2 lipids to rearrange around the protein complex and within the lipid bilayer. Hence the constraints on PIP_2 phosphorus atoms were removed but maintained on the protein backbone. This step of 70 ns was also conducted to let the density of the system reach a constant value.

The second phase, the production phase, which constitutes strictly speaking the MD simulation is usually performed without constraints unless for a specific aim. The main goal of the present MD simulations is to study each stable state of $K_V7.1$ channel in various conditions in order to assess the modulation effects of both KCNE1 and PIP_2. Therefore, we need to simulate stable conformations of our models, which is merely possible if the channel is conducting K+ ions through the selectivity filter. As a consequence, the backbone of the selectivity filter, corresponding to the K_V channel conserved TTIGYG (311-316) motif was spatially constrained, to prevent ion conduction during simulations. To make sure the behavior of the channel is fine, the entire second phase corresponded to MD runs of ~500 ns.

Chapter II.3. Knowledge-based analysis of MD trajectories

Our strategy was to analyze only the production phase of MD simulations, which were performed with the least number of constraints. First, we conducted root mean square deviation (RMSD) calculations in order to compare the conformations obtained for $K_V7.1$ subunits in our MD trajectories with the experimental 3D structures known for $K_V7.1$ subunit. Considering the activated VSD and the closed PD of $KCNQ1_{EM}$ structure, we conducted separated structural alignments for VSD and PD during which the connecting loops were excluded. For AO state models, we monitored the RMSD between the backbones of each VSD segment of AO models and the VSD of $KCNQ1_{EM}$ structure, and between each PD segment of RC models with the PD of $KCNQ1_{EM}$ structure, every 2ns throughout the MD trajectory. For $K_V7.1$ intermediate models, we performed the RMSD calculations between their respective VSD and the unpublished NMR structure of $K_V7.1$ VSD (PDB: 6MIE). To obtain an insight into the flexibility of the protein backbone of our models during MD simulations, we calculated the root-mean-square fluctuation of the Cα atoms with respect to their initial position.

Chapter II.3.1. Structural mapping of known $K_V7.1$ neighbor residues for structural validation

To assess the reliability of our simulations with respect to experimental data, we confronted the MD trajectories of each $K_V7.1$ model against a set of molecular biology results reported for $K_V7.1$ channel. To do this, we first gathered all the site-directed mutagenesis studies conducted on $K_V7.1$ and IK_S channels in order to identify: the VSD salt-bridge patterns, $K_V7.1$ intersubunit and intrasubunit neighbor residues, KCNE1/ $K_V7.1$ neighbor residues, and the residues of $K_V7.1$ and KCNE1 which bind PIP_2. Among the reported site-directed mutagenesis, cysteine cross-linking experiments start from the principle that, in a transmembrane protein, a pair of interacting residues can form disulfide bonds when mutated into cysteine with a significant formation rate constant if the distance between their C_β atoms is below 13.2 Å [295].

Accordingly, we evaluated the C_β-C_β distances (Figure II.3.1.1) of each pair of residues in the MD trajectories we obtained for our models of $K_V7.1$ and IK_S channels and reported their average values in tables S2-S3. A pair was considered as present in the model if the average distance between C_β atoms was below 13 Å over MD production phase for at least 3 subunits out of four.

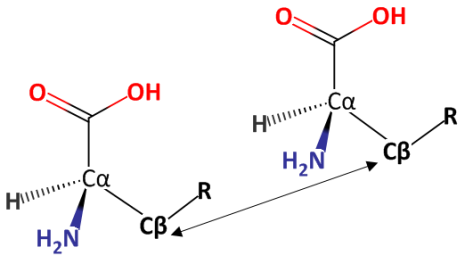

Figure II.3.1.1: Distance calculations of neighbor residues in MD trajectories according to Cysteine cross-linking experiments.
Topologic formula of two amino acids in which α and β carbons are mapped. The C_β-C_β distance calculated for each residue pair is represented by a double arrowed black line. R stands for the sidechain of the residues involved.

To assess the interactions of high energy such as electrostatic interactions and hydrogen bonds that are expected between S4 gating charges and S2 negative ones, as well as the ones between basic side chains from the cytoplasmic region of KCNE1 and PIP_2 were also monitored every 2ns and were considered as valid if their average distance between their respective charge moieties are below 3.5Å, which is the average distance encountered for ion pairs in protein NMR structures [296].

For these calculations (Figure II.3.1.2), we had to consider the fact that the arginine guanidinium group is conjugated. As a consequence, this functional group is a combination of three canonical structures, as its π electrons are delocalized between its three coplanar nitrogen atoms. Thus, the positive charge of arginine guanidinium group can be carried by each of these nitrogen atoms. In the same way, the carboxylate group in both glutamate and aspartate side chains is also conjugated, so this functional group is a combination of two canonical structures, each carrying the negative charges on one of its two coplanar oxygen atoms.

In PIP_2 lipids, one negative charge is delocalized on oxygen atoms O1 and O2 of its phosphodiester group (Figure II.3.1.2), while each phosphate group carries two negative charges which are delocalized in O3 O4 O5 O6 O7 O8 oxygens, each bound to a phosphorus atom. At neutral pH, one negatively charged oxygen (among O3 O4 O5 O6 O7 O8) of one phosphate group is protonated, so PIP_2 lipids have a net charge of -4. However, this proton may be displaced when a PIP_2 lipid is bound to a protein, leading to a net charge of -5 [297].

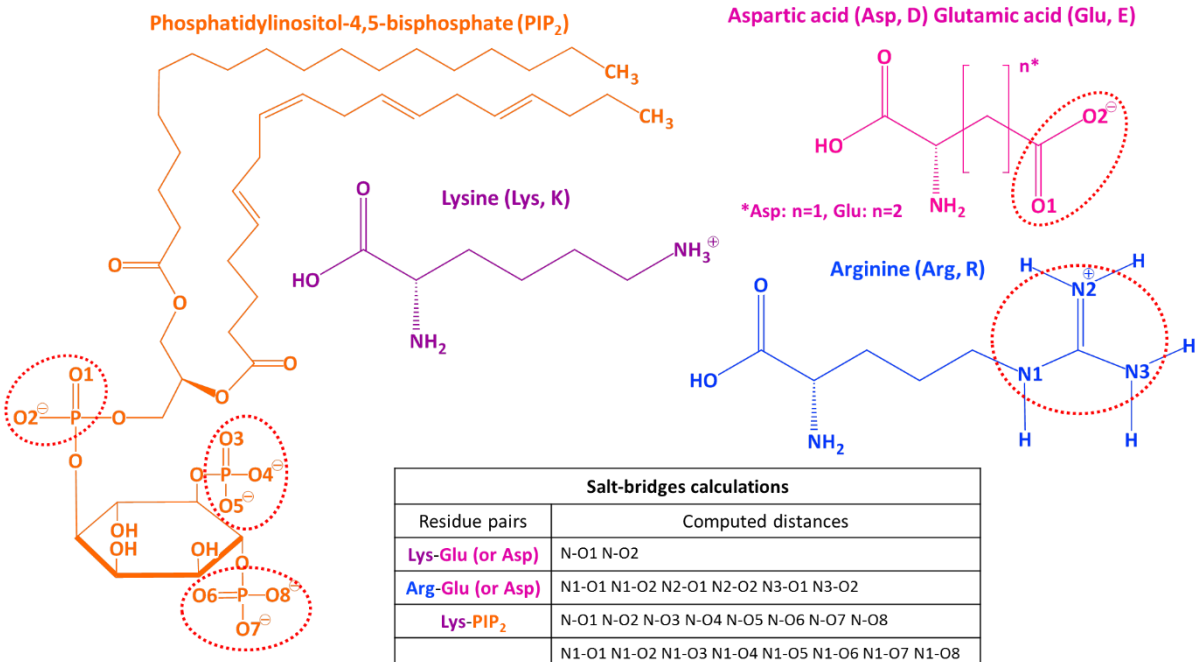

Salt-bridges calculations	
Residue pairs	Computed distances
Lys-Glu (or Asp)	N-O1 N-O2
Arg-Glu (or Asp)	N1-O1 N1-O2 N2-O1 N2-O2 N3-O1 N3-O2
Lys-PIP_2	N-O1 N-O2 N-O3 N-O4 N-O5 N-O6 N-O7 N-O8
Arg-PIP_2	N1-O1 N1-O2 N1-O3 N1-O4 N1-O5 N1-O6 N1-O7 N1-O8 N2-O1 N2-O2 N2-O3 N2-O4 N2-O5 N2-O6 N2-O7 N2-O8 N3-O1 N3-O2 N3-O3 N3-O4 N3-O5 N3-O6 N3-O7 N3-O8

Figure II.3.1.2: Distance calculations of electrostatic interactions in MD systems.
This figure shows topologic formulas of the residues that might engage in salt-bridges throughout MD trajectories. The negatively charged lipid PIP_2 is colored in orange. Acidic amino acids (aspartic and glutamic acid) are both depicted in pink, while basic amino acids Lysine and Arginine are colored in purple and blue, respectively. In all molecules, the charged moieties are circled in red dashed lines. The table summarizes the pairs of atoms for which the distance was computed to assess the presence or absence of a salt bridge in each frame of the MD trajectory. Among these distances, the shorter one was recorded.

Thus, as the MD simulations have been conducted on Kv7.1 and KCNE1 subunits in the presence of PIP_2 in order to investigate the protein-lipid interactions, the net charge of PIP_2 molecules was set to -5 in the FF parameters. Accordingly, the resonance effects on both phosphodiester and phosphate groups engage the five negative charges of PIP_2 to be delocalized in a total of eight oxygen atoms. Accordingly, salt bridges were monitored by computing each of the atom pair combinations of terminal nitrogen atoms from Arg guanidinium group and terminal oxygens from Glu or Asp carboxyl groups, or oxygens from PIP_2 phosphate groups.

The distances between each residue pair were all monitored every 2 ns over MD trajectory, using a set of several designed programs, each written in TCL language and executed within the scripting interface of Visual Molecular Dynamics (VMD) software [298]. The distance graphics were designed using R scripting language [299]. For each pair of residues, an interaction was considered present if it was found in at least three out of four subunits.

To visualize the evolution of these computed distances, we wrote an R script in order to generate four graphs per residue pair which represent interatomic distances throughout MD trajectories in each subunit. In this way, it became possible to distinguish the interacting residue pairs (Figure II.3.1.3, upper row) from those which do not interact (Figure II.3.1.3, middle row). In addition, these graphs indicate clearly if a distance remains steady, or fluctuates, or falls beyond its threshold value at the end of the MD trajectory (Figure II.3.1.3, lower row), when the system has reached its equilibrium.

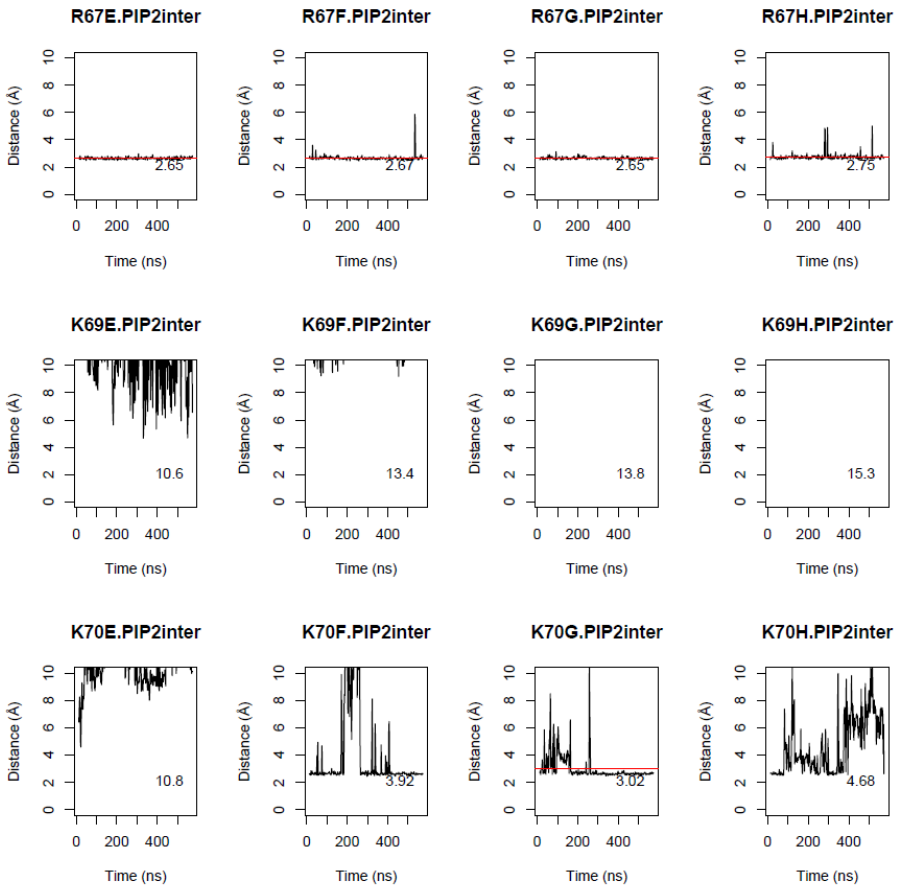

Figure II.3.1.3: Example of distances graphs for MD analysis.
The graphs represent the distance computed for protein-lipid salt-bridge interactions between KCNE1 residues R67 (upper row) K69 (middle row) K70 (lower row) and PIP_2 inter in each KCNE1 subunit (noted E F G H) throughout the MD trajectory of IK_S RC model ($8PIP_2$ system). In each graph the average distance is indicated in the lower right corner. The average distances below the 3.5 Å threshold are also represented as red lines.

Chapter II.3.2. Pore size

Starting from the premise that the pore radius of hydrophobic gates such as K_V7 channels energetically favors ionic conduction, as it increases ion hydration [300–302], one can assume that channel models with larger pore radii at the level of the conduction gate are more likely to facilitate ion conduction and therefore to generate ionic currents as those recorded using experimental techniques. Therefore, in our hypothesis we assumed if the ionic current is increased in presence of KCNE1 when the VSD of $K_V7.1$ reaches its activated state, then the IK_S AO model should present a wider pore radius than the $K_V7.1$ AO model. However, for the intermediate and RC states, the ionic current is merely present in presence of KCNE1, so the IK_S models should present a shorter pore radius than the $K_V7.1$ ones. To verify our hypothesis, pore radii and pore solvent accessible surfaces of all models were calculated and generated every 20ns of their respective MD trajectory, both using HOLE program [303] (Figure II.3.2.1).

For each model, we estimated the average pore radii values along the pore axis, which corresponds to the normal to the membrane plane whose origin is located at the center of the conduction pathway. The solvent-accessible surfaces of the pores were rendered with VMD software. For each IK_S stable state, the model which presents the most relevant average pore radius in comparison to the $K_V7.1$ model of the same state (wider pore radii than $K_V7.1$ in activated models, and narrower pore radii in both resting and intermediate models). These pore radii measurements also allow for the identification of the pore-lining residues facing the center of the pore. Indeed, these residues are likely to play a role in the pore opening, while the pore lining residues whose sidechains are oriented towards the outside of the pore might play a role in VSD-PD coupling.

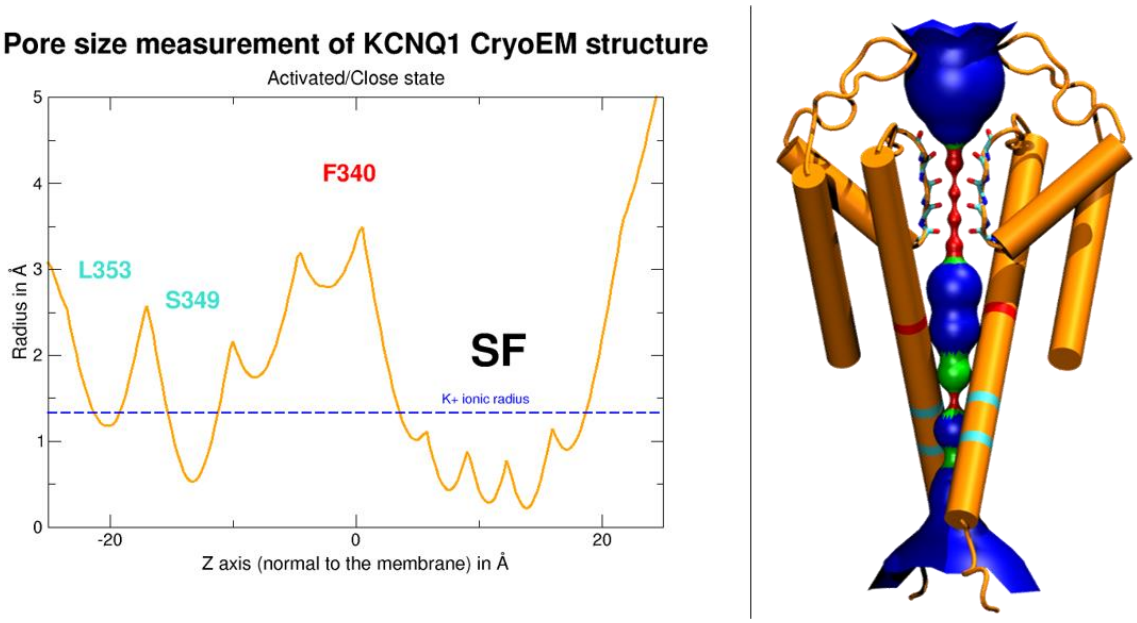

Figure II.3.2.1: Example of pore domain analysis using HOLE program.
This figure shows pore radius measurement of Kv7.1 CryoEM structure (left panel) and a cartoon representation of its pore domain along with the solvent accessible surface of its conduction pathway (right panel). The default colors for this surface are set by HOLE as a function of the pore radii values. Those ranging from 0 to 0.6 Å are colored in red, while those ranging between 0.6 Å and 1.15 Å are colored in green, and those superior to 1.15 Å are colored in blue. Residues F340, S349 and L353 are mapped in both panels with corresponding colors. The backbone atoms of the selectivity filter are depicted in sticks, in which oxygen, carbon and nitrogen atoms are colored in blue, cyan and red, respectively.

Chapter II.3.3. Knowledge-based determination of weak interactions in MD trajectories

Integral proteins that are mostly made of transmembrane helices such as ion channels are characterized by their specific primary sequences. Indeed, transmembrane proteins present in average three times less charged side chains and 50% more hydrophobic side chains than water soluble proteins [304]. The stability of transmembrane proteins within the lipid bilayer is logically maintained by Van der Waals nonspecific interactions that occurring between alpha helices. These transmembrane helices often act as dynamic domains that are able to move relative to each other, arising several conformational states [305]. In the case of K_V7.1, for which we created models of its transmembrane region, we simulated the three stable states at the equilibrium in order to predict the possible transitions between those states. Hence, the weak interactions between hydrophobic residues and electrostatic interactions between polar residues need to be thoroughly characterized and monitored throughout the MD simulation in order to assess their stability. The stability of the identified interactions will constitute a more solid proof of the protein stability in its different stable states than root-mean-square deviations or fluctuations.

Depending on the nature of the concerned residue, we computed a significant number of distance calculations in our MD trajectories in order to characterize several types of interactions that commonly found in transmembrane protein structures [305]. To do this, we calculated these distances every 2 ns throughout the entire production phase of the MD trajectory of each model. Salt-bridges and hydrogen bonds were characterized in the same manner as for IK_S model validation, by computing the atom pair combination of polar nitrogen atoms of basic side chains such as Arg, Lys or His, polar oxygen atoms of acidic sidechains such as Glu or Asp, or polar side chains such as Ser, Thr or Tyr to record the shortest distance, using a cut-off distance $D_{CUT} = 3.5$ Å (Figure II.3.3.1).

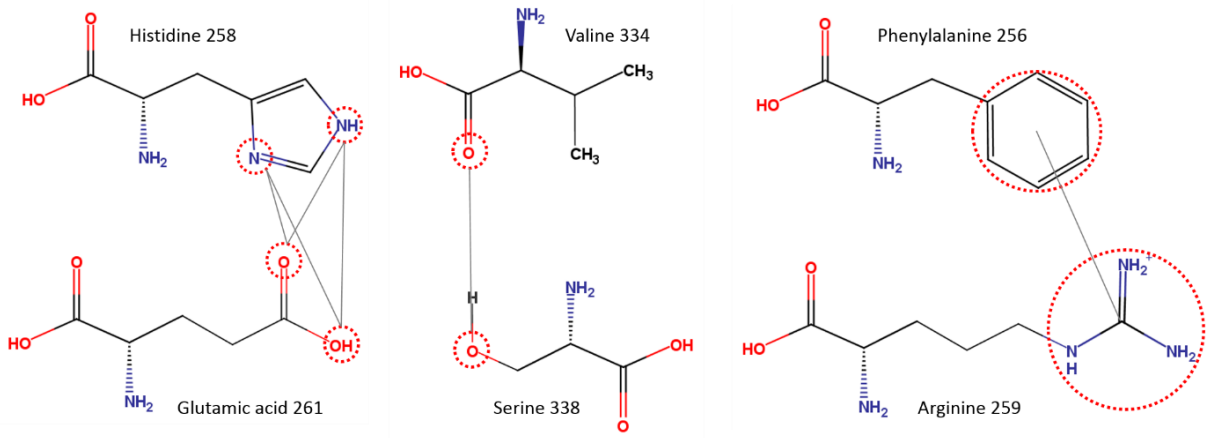

Figure II.3.3.1: Computed distances for assessing electrostatic interactions.
This figure displays topologic formulas of the residues that might engage in electrostatic interactions throughout MD trajectories. The calculated interatomic distances are depicted in blue lines. Kv7.1 residue pairs H258/E261 (left) and V334/S338 (middle) are taken as examples of hydrogen bonds. The residue pair F256/R259 (right) is taken as an example of cation-π interaction. The atoms considered for the distance calculations are circled in dashed red lines. When aromatic rings or functional groups are circled, their geometric center is considered for the distance calculation. When several interatomic distances are computed for a residue pair, only the one with the shorter value is recorded at each frame of the MD trajectory.

This cut-off distance was also used for a specific type of hydrogen bonds that occur between the carbonyl oxygen of a peptide bond in one helix and the alpha carbon from a second helix, which was showed to stabilize membrane protein conformations [306]. For cationic residues, we characterized cation-π interactions [307] by calculating the shortest distance between polar nitrogen atoms from Arg or Lys sidechains and the aromatic ring center of the closest aromatic residues , using a cut-off distance $D_{CUT} = 5.1$ Å (Figure II.3.3.1).

We also characterized Met-Arom interactions [308] that usually occur between methionine sulfur atom and aromatic side chains (Tyr, Trp, Phe) of TM helices [309], using a cut-off distance of 7.1 Å between sulfur atom and aromatic ring centers (Figure II.3.3.2). Similarly, we characterized Met-Leu interactions [310], by calculating the distance between methionine sulfur atom and leucine ramified carbon, using a cut-off of 6.1 Å.

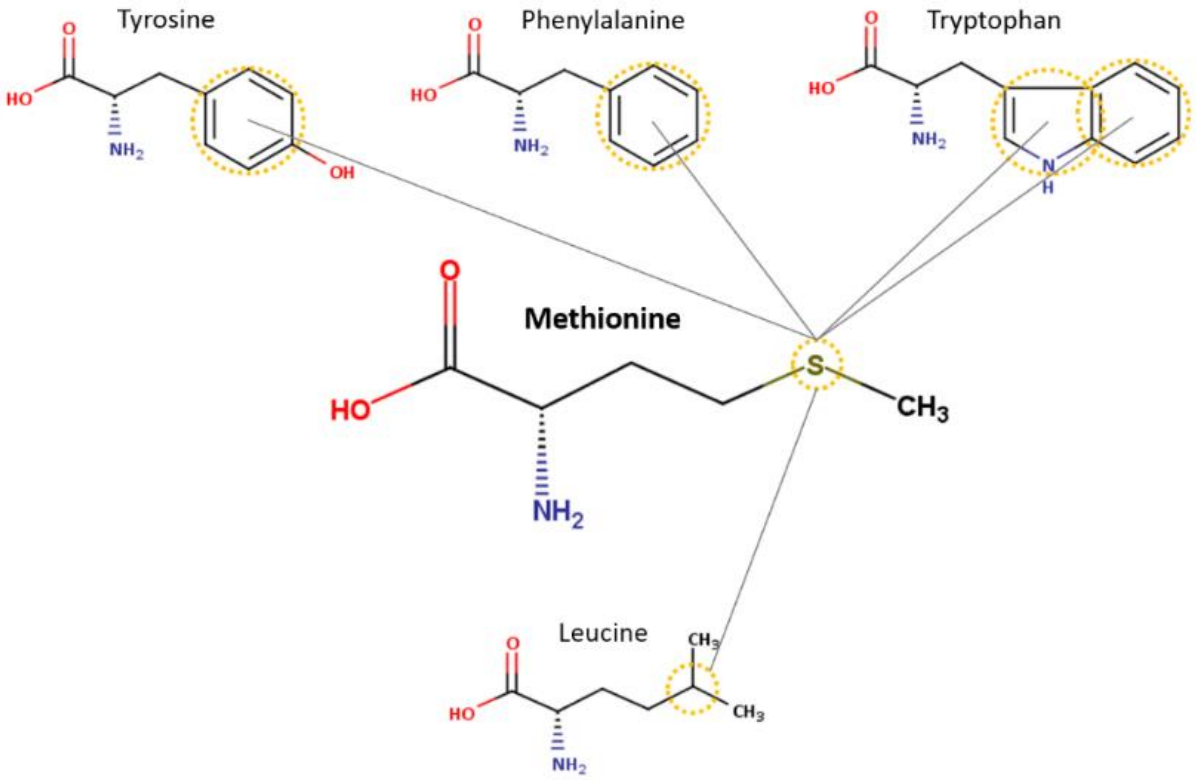

Figure II.3.3.2: Computed distances for assessing methionine interactions.
This figure displays topologic formulas of the residues that might interact with Methionine sidechains throughout MD trajectories. The calculated interatomic distances are depicted in blue lines. The atoms considered for the distance calculations are circled in dashed yellow lines. When aromatic rings are circled, their geometric center is considered for the distance calculation. When several interatomic distances are computed for a residue pair, only the one with the shorter value is recorded at each frame of the MD trajectory.

For aromatic residues, we characterized π-stacking interactions by a computed distance between the geometric centers of their aromatic rings, using a cut-off distance of 5.1 Å (Figure II.3.3.3). This cut-off value represents the distance between aromatic rings engaged in a π-stacking interaction usually found in protein crystallographic structures [311]. The same cut-off distance was also used to characterize VdW interactions between hydrophobic residues (Figure II.3.3.3), by computing the shortest distance between their respective terminal methyl groups over MD trajectory.

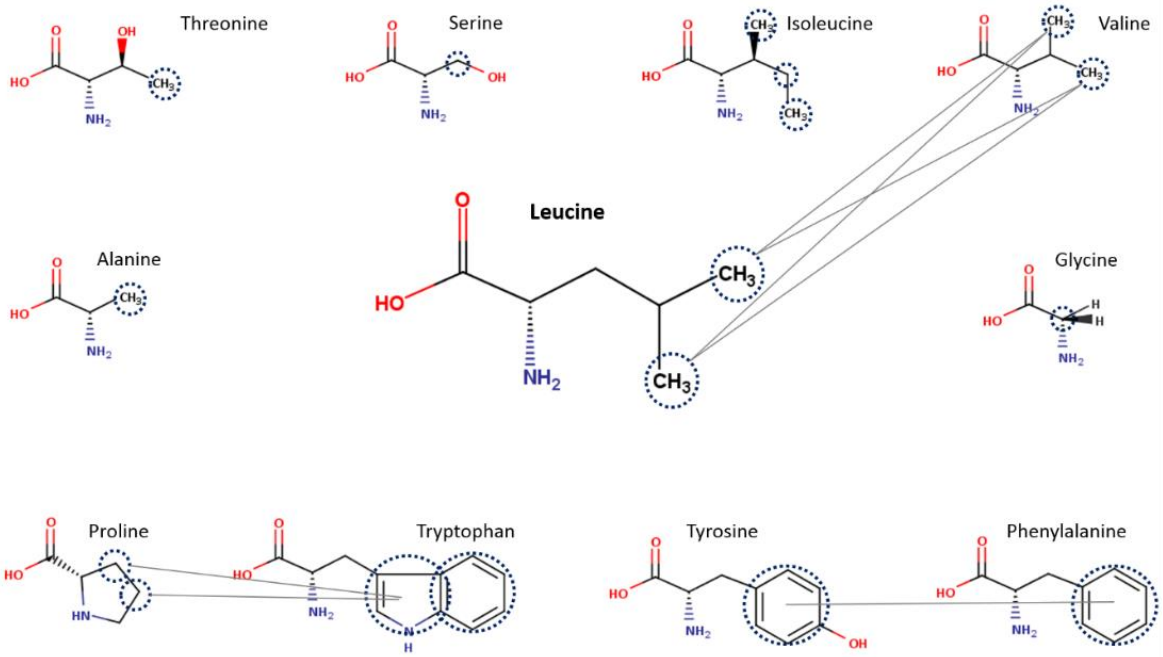

Figure II.3.3.3: Computed distances for assessing hydrophobic interactions.
This figure displays topologic formulas of the residues that might be involved in hydrophobic interactions throughout MD trajectories. The sidechains of Leucine and Valine are taken as an example to show the atoms considered (dashed blue circles) for the calculation of their interatomic distances (blue lines) to characterize VdW interactions between aliphatic residues. The sidechains of Proline and Tryptophan are taken as an example for the VdW interactions between aliphatic and aromatic sidechains. For π-stacking interactions between aromatic residues, Tyrosine and Phenylalanine sidechains are displayed as an example. On the remaining sidechains, the carbon atoms considered for the distance calculations also are circled in dashed blue lines. When aromatic rings are circled, their geometric center is considered for the distance calculation. When a residue pair requires to compute several interatomic distances, only the one with the shorter value is recorded at each frame of the MD trajectory.

According to the physicochemical properties of the considered side chain, the neighbor search was limited to the residues with similar properties. For example, to search the neighbor residues of an aromatic one, we restrained the search on aromatic, aliphatic and basic residues only. Altogether, we computed the distances of 113 and 156 residue pairs on the four subunits of $K_V7.1$ and IK_S models, respectively, throughout their MD trajectories.

As in Figure II.3.1.3, we generated graphs for each computed distance, which make totals of 452 and 624 graphs per $K_V7.1$ and IK_S MD trajectory, respectively, which make a total of 3680 graphs to interpret in order to complete our entire MD analysis. At this point, it became crucial to find a way to summarize this huge amount of data, while preserving the variability of the fluctuating distances throughout the MD simulations. In this way, we could obtain a concise presentation of our numerous results.

To that extent, we came up with the idea of computing interaction frequencies of each residue pair in the entire model tetramer in our MD trajectories. For each pair of residues P, we calculated at each frame n the frequency f_n at which its interatomic distance values A_n, B_n, C_n and D_n were below its assigned cut-off D_{CUT} in subunit A, B, C, D, respectively throughout the MD trajectory. To do that, we computed F_P as follows:

$$F_P = \frac{\sum_{n=1}^{N} f_n}{N}$$

where N is the total number of MD trajectory frames, and f_n is the interaction frequency of the residue pair at the frame n which is computed as follows:

$$f_n = \frac{d(A_n) + d(B_n) + d(C_n) + d(D_n)}{4}$$

With the function $d(x)$ operating as follows:

$$d(x) = \begin{cases} 1, & x \leqslant D_{CUT} \\ 0, & x > D_{CUT} \end{cases}$$

An interaction between a pair of residues P was considered present in a model if the frequency F_P was higher than 0.6. For residue pairs that present frequencies lower than 0.6 in all MD trajectories, we considered their interactions as present in a model if F_P was higher than 0.4.

These analyses were performed with the use of several home-made script programs written in TCL language and executed within the shell of VMD software [312]. The data we generated with VMD was used as input to run a script program written in R language that aimed at computing the interaction frequencies as well as the related bar plots.

Chapter III. Results

Les méthodes de modélisation moléculaire sont par nature basées sur l'étude des représentations virtuelles d'entités chimiques et biologiques. Le but principal de l'utilisation de ces méthodes, dans le cadre de cette étude, est d'acquérir un aperçu des événements qui se produisent à l'échelle macroscopique, et qui sont observables par le biais d'études expérimentales. Les analyses des trajectoires DM obtenues ont été menées en deux parties. La première partie visait à valider rigoureusement l'ensemble de nos modèles de conformères $K_V7.1$ par rapport aux données expérimentales afin de s'assurer de la précision des prédictions que l'in prévoyait d'effectuer par la suite (**Chapter III.1**). Dans un premier temps, nous avons évalué la présence et la stabilité des interactions protéine-protéine de $K_V7.1$, qui incluent les ponts salins états-dépendants ayant été préalablement identifiés par des mutagénèses « à inversion de charge », ainsi que des paires de résidus voisins identifiés par des doubles mutagénèses dirigées, à travers chacune de nos trajectoires DM (Chapter III.1.1). Pour les systèmes DM qui contiennent des sous-unités $K_V7.1$ et KCNE1, nous avons également testé la présence et la stabilité de 20 paires supplémentaires de résidus voisins, extraits de diverses études de mutagénèse dirigée. Nos modèles de canal $K_V7.1$, en absence et en présence de KCNE1, sont tous en accord avec les données expérimentales. Nous avons aussi analysé la présence et la stabilité des interactions protéine-lipide en se focalisant sur les sites d'interaction à PIP_2 qui sont localisés sur les sous-unités $K_V7.1$ et KCNE1, respectivement (Chapter III.1.2). Les résultats obtenus pour le système DM qui contient huit molécules de PIP_2 satisfait mieux les résultats expérimentaux que les systèmes qui n'en contiennent que quatre, localisés sur les sites d'interaction aux sous-unités $K_V7.1$. D'autres résultats de validation (Chapter III.1.3-4) témoignent également, dans une moindre mesure, de la robustesse de nos modèles du canal $K_V7.1$.

Les résultats que nous avons obtenus à partir de la seconde partie des analyses de trajectoires DM des modèles $K_V7.1$ (**Chapter III.2**) ont été validés par des études expérimentales menées par nos collaborateurs (Pr. Jianmin Cui et son équipe de recherche) de l'université Washington de Saint-Louis aux Etats-Unis (Chapter III.2.1).

Les résultats issus des études expérimentales et computationnelles menées sur le canal $K_V7.1$ en l'absence de KCNE1 indiquent que les mécanismes de couplage des états IO et AO du canal sont régis par une interface d'interactions intra sous-unité et état-indépendantes entre S4-$S5_{LINKER}$ et S6, ainsi qu'une seconde interface état-dépendante entre les segments S4, S4-S5L d'une sous unité $K_V7.1$ et les segments S5 et S6 d'une sous unité adjacente. Ces interfaces nous ont permis de prédire un modèle de mécanisme de couplage VSD-PD pour le canal $K_V7.1$ lorsque le VSD atteint ses états intermédiaire et activé. Nous avons conceptualisé nos résultats en un modèle appelé "main-et-coude". D'autres analyses, focalisées sur les trajectoires DM obtenues pour les modèles du canal $K_V7.1$ en présence de quatre sous-unités auxiliaires KCNE1 et de 8 molécules de PIP_2 (Chapter III.2.2), ont mis en évidence la manière dont KCNE1 perturbe le mécanisme "main-et-coude", apportant des élément permettant d'expliquer les nombreux résultats expérimentaux qui montrent que KCNE1 réduit drastiquement la conductance de $K_V7.1$ au états RC et IO tout en augmentant celle de l'état AO de manière significative.

L'analyse conformationnelle du motif SFF, situé au milieu du segment S6 (Chapter III.2.3) a mis en évidence les différences d'orientation des chaines latérales du résidu F340 entre les modèles fermés et les modèles ouverts. En effet, deux conformations qui semblent dépendre de la conformation ouverte ou fermée du pore ont été observées. Les chaines latérales de F340 sont orientées vers le centre du pore (modèles RC, IC AC), fermant ce dernier lorsque le canal est découplé ou partiellement couplé. Lorsque le canal est couplé (modèles IO, AO), les chaînes latérales de F340 s'orientent en direction tangente à la surface du pore, ou en direction du milieu du segment S5, laissant de l'espace aux ions de diffuser à travers le pore du canal $K_V7.1$.

Les analyses destinées à valider nos modèles ont montré que les interactions protéine-protéine et protéine-lipide des modèles de complexes $K_V7.1$+KCNE1 sont plus stables en présence de 8 molécules de PIP_2 qu'avec 4 seulement. Les résultats obtenus permettent de comprendre à quel point la présence du site d'interaction à PIP_2 localisé sur KCNE1 est nécessaire à la stabilité du complexe. En effet, sur les modèles RC et IC, on constate que KCNE1 est également capable de se lier à PIP_2 via son site d'interaction, mais également via le site d'interaction à $K_V7.1$, ce qui peut lui permettre de modifier la conformation des segments S6 au niveau de la face interne de la bicouche lipidique (Chapter III.2.4.).

Dans l'ensemble, ces résultats satisfaisants nous ont permis de prédire les changements conformationnels inhérents aux mécanismes de couplage VSD-PD du canal $K_V7.1$, et ceux du mécanisme d'ouverture du pore, et ce à l'échelle moléculaire. A partir de ces prédictions, nous avons également pu apprécier les effets de KCNE1 et de PIP_2 sur ces changements conformationnels.

Molecular modeling methods are, by nature, based upon the study of virtual representations of chemical and biochemical entities. The main goal of using these computational methods, in the frame of this study, is to gain an atomistic insight of the macroscopic phenomena that were unraveled by experimental studies. The analyses of resulting MD trajectories were conducted in two parts. The first part aimed at thoroughly validating all our models of $K_V7.1$ against experimental data to ensure accuracy (**Chapter III.1**). First, we determined the presence and the stability of $K_V7.1$ state-dependent protein-protein salt bridges previously identified by charge reversal mutagenesis, as well as the presence of pairs of protein-protein neighbor residues, extracted from both Cys scanning experiments and double mutant cycle analyses were monitored throughout our MD trajectories (Chapter III.1.1). For the MD systems that contain both $K_V7.1$ and KCNE1 subunits, we investigated twenty additional neighbor residue pairs between $K_V7.1$ and KCNE1 residues that we obtained from various mutagenesis studies. Regarding the state-dependent protein-protein interactions within $K_V7.1$ on one hand, and between $K_V7.1$ and KCNE1 on another hand, our models are fully satisfying experimental data. We also addressed the presence and the stability of protein-lipid interactions by analyzing PIP_2 binding sites on both $K_V7.1$ and KCNE1 subunits (Chapter III.1.2). We have monitored the distance between charge moieties of the $K_V7.1$ and KCNE1 basic residues and those of PIP_2 lipids. The results obtained with the MD systems that contain 8 PIP_2 molecules are also in good agreement with experimental data. Additional validation results (Chapter III.1.3-4) were also confirming, in a lesser extent, the robustness of our $K_V7.1$ models.

The results we obtained from the second part of analysis of $K_V7.1$ MD trajectories (**Chapter III.2**) were validated by functional studies of $K_V7.1$ channel conducted by our collaborators (Pr. Jianmin Cui and colleagues) from Washington University of Saint-Louis in the US (Chapter III.2.1). Computational and experimental results both indicate that the $K_V7.1$ VSD-PD coupling in both IO and AO states is mediated by an interface of state-independent intrasubunit interactions between S4-S5L and S6, as well as a second interface of state dependent intersubunit interactions between S4, S4-S5L and PD segments, in the absence of KCNE1.

These interfaces allowed us to predict a model of VSD-PD coupling mechanism for $K_V7.1$ channel when the VSD reaches its intermediate and activated states. We conceptualize all of our findings in this study into a "hand-and-elbow" gating mechanism for voltage-dependent activation of $K_V7.1$ channel. Further analyses, focused on the MD trajectories of systems containing the $K_V7.1$ tetramer (Chapter III.2.2), four KCNE1 subunits, and two PIP_2 molecules per $K_V7.1$ monomer, highlighted how KCNE1 disrupts the "hand-and-elbow model" of the VSD-PD coupling we previously designed for $K_V7.1$ channel, providing hints allowing to explain the numerous experimental results that pointed out that KCNE1 reduces drastically the ionic conductance of $K_V7.1$ channel in RC and IO states, while increasing it when $K_V7.1$ VSD is in its activated state.

The conformational analysis of SFF motif, located in the middle of S6 segment (Chapter III.2.3) shed light on the differences of F340 sidechain conformation between the MD trajectories of closed state models and open state models. Indeed, we found 2 distinct conformations that seem to depend on the coupling state of the channel. F340 sidechains adopts the inside conformation, which closes the pore when the channel is uncoupled or partially coupled (RC, AC, IC models). When the channel is coupled (IO, AO models) F340 sidechains adopt the outside conformation, as they are oriented tangent to the pore or towards S5 segment, leaving space for potassium ions to enter the gate.

The analysis of protein-protein and protein-lipid electrostatic interactions in the MD systems containing both $K_V7.1$ and KCNE1 showed that S2-S4 salt-bridges, as well as the protein-lipid interactions, both turned out to be more stable with $8PIP_2$ molecules due to the presence of an additional PIP_2 lipid placed in the KCNE1 binding site previously identified by our collaborators. In addition, the protein-lipid interactions we found in presence of $8PIP_2$ molecules shed light on the fact that KCNE1 is able to bind the PIP_2 lipid located in its own binding site, as well as the lipid located in $K_V7.1$ binding site in both RC and IC models (Chapter III.2.4). These specific interactions between KCNE1 and PIP_2 might influence the conformation of the pore in both states.

Altogether, these results allowed us to predict a molecular scale mechanisms of VSD-PD coupling and pore opening, along with the effects of PIP_2 and KCNE1 on these mechanisms.

Chapter III.1. Structural validation of MD trajectories

To predict the molecular mechanisms associated to the function of $K_V7.1$ channel in absence and in presence of KCNE1, we need to maximize as much as possible the compliance of our models with respect to available structural biology data. To achieve this goal, we built our 3D models using structural constraints that were directly drawn from experimental data, and then we monitored the stability of these constraints over the collection of conformations generated by MD simulations (i.e. MD trajectories). To gain a finer insight in the molecular determinants allowing for the stabilization of each metastable state of $K_V7.1$ and IK_S channels, MD simulations were performed to equilibrate each metastable model within a POPC membrane and considering PIP_2 lipids.

Chapter III.1.1. Protein-protein sidechain proximities

The extensive molecular dynamics (MD) simulations of $K_V7.1$ models in four different states, namely the RC, the IO, the AO and the AC state have been conducted in a membrane environment, in line with our previous studies of the $K_V7.1$ channel in order to obtain relaxed channel models. The analyses of the MD trajectories were validated rigorously against experimental data to ensure the robustness of these models (Figure III.1.1.1). In various K_V channels, the activation mechanism of the VSD is mostly characterized by state-dependent salt-bridges between basic residues of S4 and acidic residues of the S2 and S3 segments. This succession of salt-bridges is describing an upward translation of S4, as well as a clockwise rotation during VSD activation.

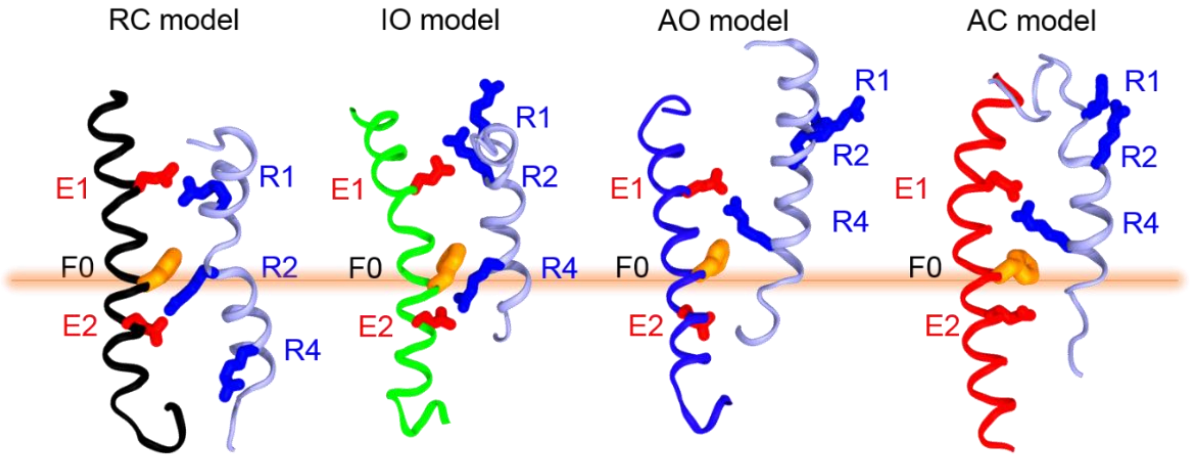

Figure III.1.1.1: State-dependent salt-bridges in the VSD of $K_V7.1$ models.
Representation of S2 (in black, green, blue and red cartoon) and S4 (in light blue cartoon) segments in $K_V7.1$ RC, IO, AO and AC models, respectively. S4 gating charges are represented in blue sticks, while its S2 countercharges are represented in red sticks. The hydrophobic plug F167 (F0) is represented in orange sticks.

To validate the state dependent structures of the VSDs of our models, we monitored the distance between each pair of charge groups that are supposed to interact according to the literature, in order to characterize the state-dependent salt bridges involving the VSD gating charges in the $K_V7.1$ models. The interactions between R1 and E1 (Figure III.1.1.2, upper row) and between R2 and E2, which are specific of the resting state, were both present at a rate of 3 subunits out of four only in the MD trajectory of $K_V7.1$ RC model. In addition, the interactions between R2 and E1 (Figure III.1.1.2, middle row), and between R4 and E2 which are specific of the intermediate state, were both present only in the MD trajectory of $K_V7.1$ IO model, at a rate of 4 and 3 subunits out of four, respectively.

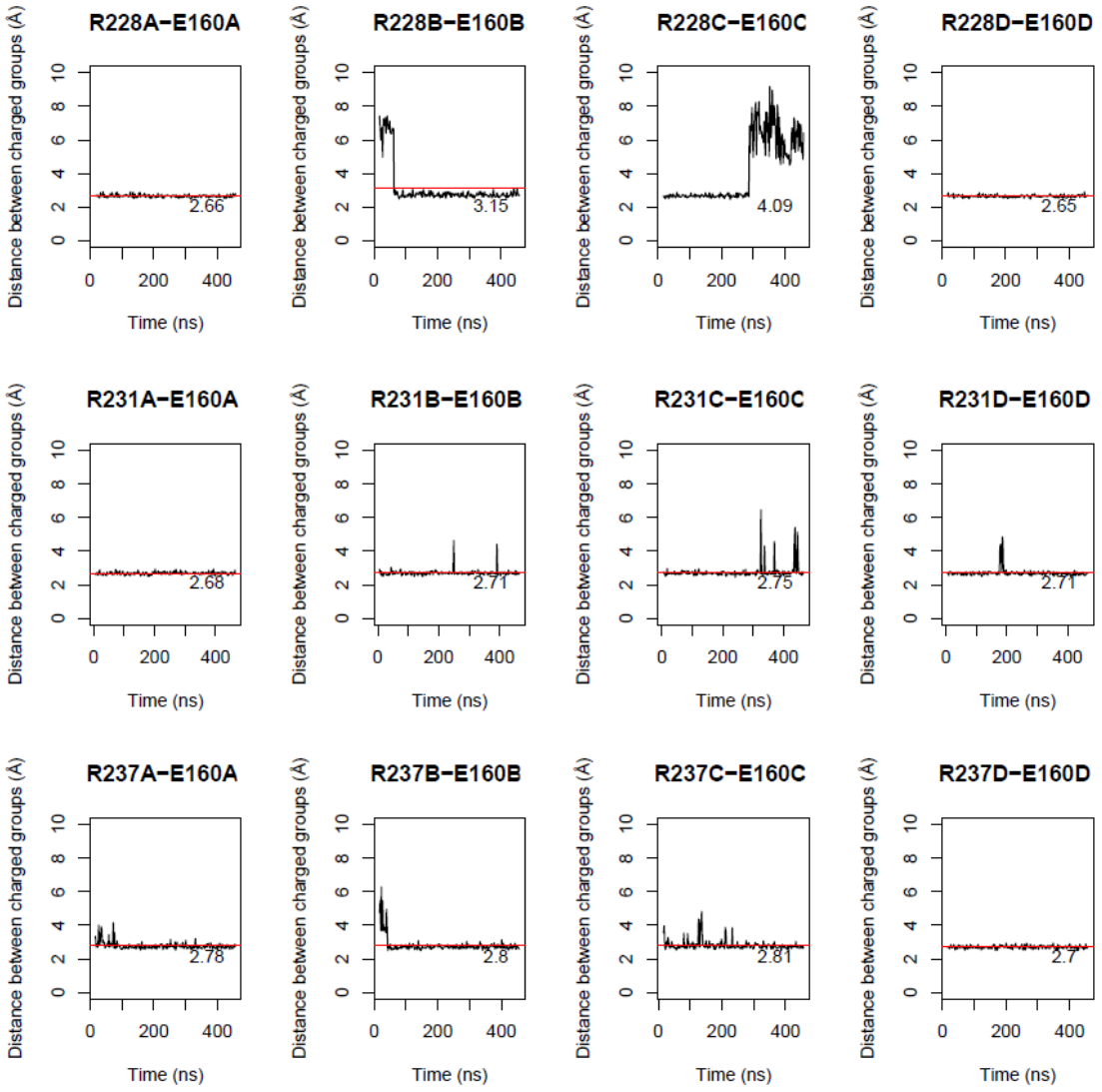

Figure III.1.1.2: State-dependent VSD salt-bridges involving E160 (E1) in $K_V7.1$ MD simulations. This figure displays the graphs of interatomic distances involving E1 and S4 gating charges R228 (upper panel) in RC model, R231 in IO model, and R237 in AO model, all throughout their respective MD trajectories. On each graph, the distance average value is shown in the lower right corner, and depicted as a red line when the value is below the threshold of 3.5 Å.

Finally, the salt-bridge interaction between R4 and E1 (Figure III.1.1.2, lower row), which is specific of the activated state, is also present in the MD trajectories of both K_V7.1 AO and AC models, in all subunits.

In the MD trajectories obtained for IK_S models, the interactions between E1 and R1 and between E2 and R2, which are specific of the RC state, are both present specifically in our RC model of 8 PIP_2 system in all subunits. In RC model of 4PIP_2 system, the interaction between R1 and E1 is present, but there is no specific interaction between R2 and E2, as R2 interacts with E1 in only two subunits out of four. This first result indicates that the presence of two PIP_2 binding sites in IK_S models may be crucial for the stabilization of the VSDs. In the IC state, S4 translates upwards and rotates clockwise, which leads to E1 interacting with R2, while E2 interacts with R4. These interactions have been specifically found in the IC model of 8PIP_2 system, in all subunits for E1-R2 interaction, and in 3 subunits out of 4 for E2-R4 interaction. In the 4PIP_2 system, E1-R2 interaction is present as expected, but the E2-R4 interaction is not absent.

Interestingly, R4 also interacts with D3 in all subunits of both systems. The latter forms the charge transfer center (CTC) along with F167 from S2 and E2. Therefore, R4-D3 interaction may indicate that R4 is fully anchored in the CTC in 8PIP_2 system and remains only partially anchored in the CTC in 4PIP_2 system. In the AO state, a second upward translation and clockwise rotation of S4 lead to E1-R4 interaction. This interaction is present only in our AO models of both 8PIP_2 and 4PIP_2 systems. In these models, R6 appears to be anchored in the CTC in all subunits, interacting with both E2 and D3 (data not shown). Noteworthy, the pairs of salt-bridges determined in our IK_S models are also present in their respective states of K_V7.1 models. These MD results show that the different conformations of the VSD correspond to interaction patterns which remain very stable over time. However, in our 4PIP_2 systems, state dependent salt-bridge pairs are satisfying experimental data for the AO model, but not for the IC and RC models.

Overall, regarding the state dependent salt-bridges previously identified experimentally in the K_V7.1 subunits, our models are fully satisfying experimental data (Tab III.1.1.1). For the IK_S models, these results suggest that models of 8PIP_2 are in better agreement with experimental results, as their state dependent VSD interactions are more numerous, and more stable throughout MD trajectory than 4PIP_2.

Charge reversal mutants	References	State	Number of subunits (over 4)									
			$K_V7.1$				IK_S ($4PIP_2$)			IK_S ($8PIP_2$)		
			RC	IO	AO	AC	AO	IC	RC	AO	IC	RC
E1R/R4E	[156, 168, 161]	AO	0	0	**4**	4	**4**	0	0	**3**	0	0
E2R/R4Q		IC	0	**3**	0	0	0	**2**	1	0	**3**	0
E1R/R2E		IC	1	**4**	0	0	0	**4**	2	0	**4**	0
E1R/R1E		RC	**3**	0	0	0	0	0	**4**	0	0	**4**
E2R/R2E		RC	**3**	0	0	0	0	0	**1**	0	0	**4**

Tab III.1.1. 1 : State dependent VSD salt bridges in $K_V7.1$ subunits.
Summary tab of state-dependent $K_V7.1$ VSD salt-bridges identified by charge reversal mutagenesis in the subunits of $K_V7.1$ models.

Noteworthy, the distinct patterns of gating charge salt-bridges determined in our models support the sliding helix model of VSD activation [313] in $K_V7.1$ channels, as well as in voltage-gated sodium channels [314]. Besides stable electrostatic interactions, site-directed mutagenesis can provide some information about the relative position of $K_V7.1$ α-subunits within $K_V7.1$ tetramer (Tab III.1.1.2).

Residue pairs	Reference	State	Number of subunits (over 4)									
			$K_V7.1$				IK_S ($4PIP_2$)			IK_S ($8PIP_2$)		
			RC	IO	AO	AC	AO	IC	RC	AO	IC	RC
T144/S298	[155]	AO	4	3	4	4	**4**	4	4	**4**	4	4
T144/Y299			4	4	4	4	**4**	1	4	**4**	0	4
T144/A300			4	3	4	4	**4**	0	4	**4**	0	3
F232/F279	[315]	IC	3	4	4	4	4	**4**	3	4	**4**	3
L250/L353	[174]	RC	4	4	4	0	4	4	**4**	4	4	**4**
V254/L353			4	4	4	4	4	4	**4**	4	4	**4**
H258/L353			4	4	4	4	4	4	**4**	4	4	**3**

Tab III.1.1.2: State-dependent protein-protein interactions involving $K_V7.1$ residues.
Summary tab of state dependent $K_V7.1$ neighbor residues identified by cysteine scanning studies in the subunits of $K_V7.1$ and IK_S models.

The interatomic distances between residue pairs previously identified by Cys scanning experiments [155] and double mutant cycle analyses [174, 315], and calculated in $K_V7.1$ MD trajectories, suggest that these residue pairs (Figure III.1.1.3) are prone to interact in all models.

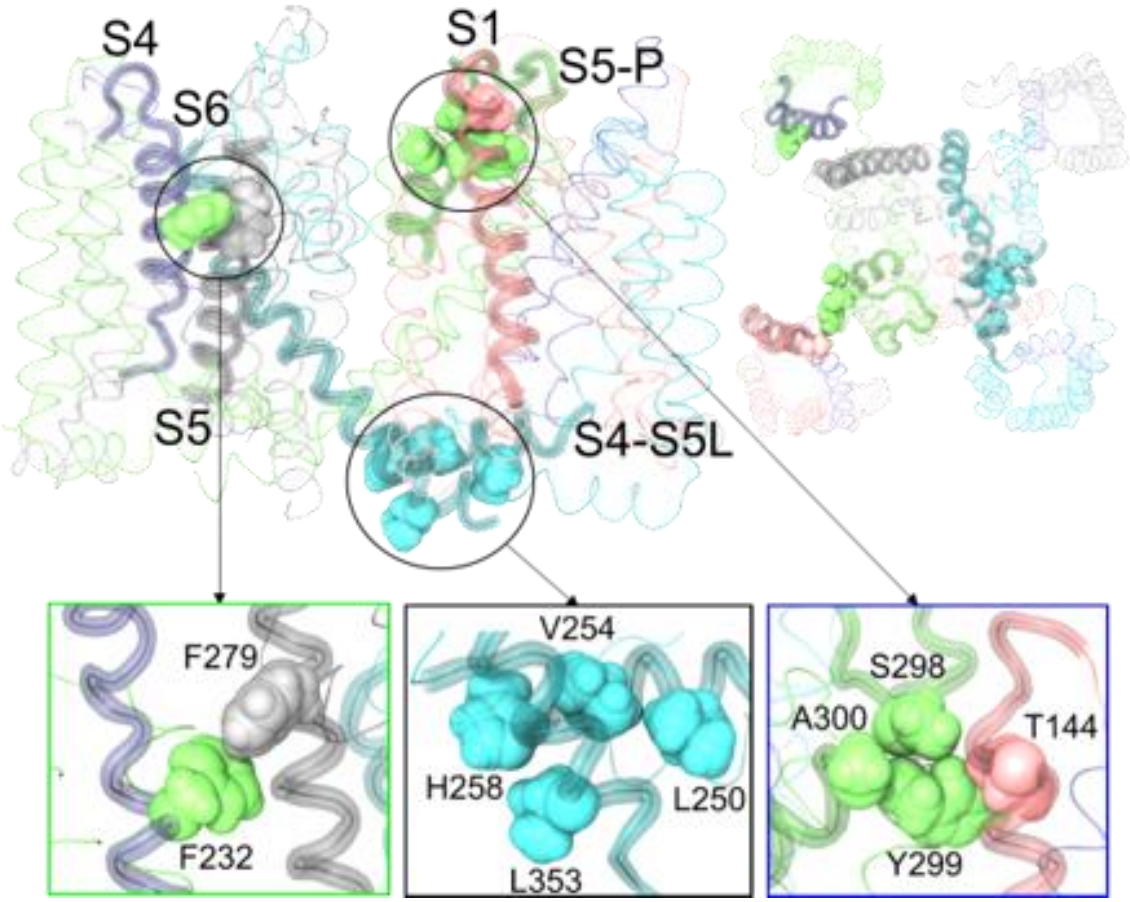

Figure III.1.1.3: State-dependent pairs of $K_V7.1$ neighbor residues.
The upper panel shows the side view (left) and the extracellular view (right) of the seven pairs of neighbor residues in $K_V7.1$ IO model. The transmembrane segments (in cartoon) carrying the residues of interest are highlighted in transparent colors. The lower panel displays the zoomed views of IO state specific interaction in IO model (left), RC state specific interactions in RC model (middle), and of AO state specific residue pairs in AO model (right).

In the MD trajectories obtained for IK_S models, the intersubunit pair assigned to intermediate state (Figure III.1.1.3, left), as well as the intrasubunit ones assigned to the resting state (Figure III.1.1.3, middle) are present in all models, regardless of their respective activation state and the amount of PIP_2 lipids. For the three pairs assigned to the AO state (Figure III.1.1.3, right), one of those is present in all models, whereas the other two are predominant in most subunits of the AO and RC models, but absent in the IC models.

One can be intrigued about the coherence of our models, yet it is important to note that the mentioned states are the result of assumptions and/or predictions of the authors drawn from electrophysiological properties of disulfide bonded Cys double mutants, which may not present the same phenotype as a channel with its two original residues engaged in a specific interaction.

The other site-directed mutagenesis experiments that were performed in order to determine the relative position of KCNE1 β-subunits with respect to K_V7.1 α-subunits in the IK_S models allowed to gather twenty intersubunit pairs involving K_V7.1 and KCNE1 residues. Most of those which have been assigned to the AO state of IK_S channel by the authors are present in both AO models (Figure III.1.1.4). Surprisingly, the only pair of residues assigned to the AO state and not present in our AO model is mostly present in RC models only. Among the six residue pairs assigned to the RC state, five are present in the RC model of $8PIP_2$ system, against four of them in the one of $4PIP_2$ system. The pairs of residues which are not interacting in the RC models are not present in any other model.

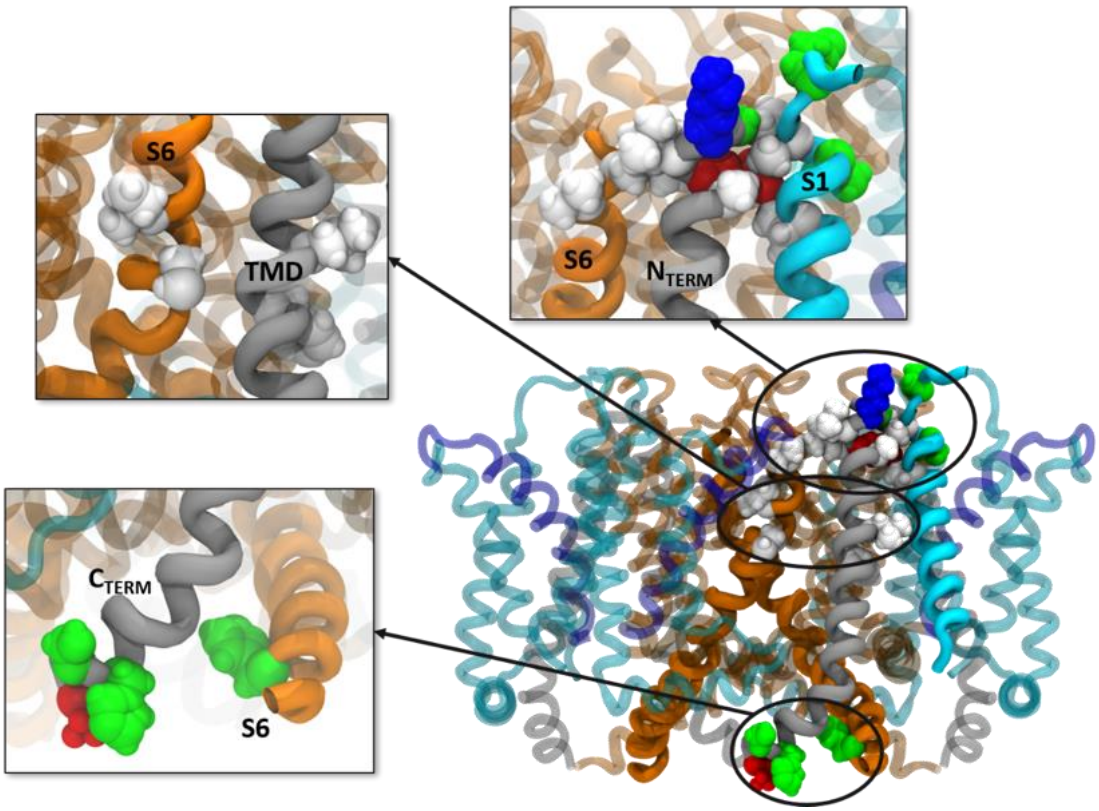

Figure III.1.1.4: Structural mapping of state-dependent protein-protein interactions in IK_S models. For K_V7.1 subunits, transmembrane segments are depicted in cartoon representation and colored as follows: S1-S3 in cyan, S4 in blue, S4-S5L in brown, and S5-S6 in orange. KCNE1 subunits are colored in gray. The segments containing the residue pairs of interest are depicted in solid colors while the others are in transparent colors. Neighbor residue pairs are circled in black and connected to a zoomed with a black arrow. Residues of interest are colored according to the chemical nature of their sidechains: apolar residues are colored in white, acidic residues in red, basic residues in blue, and polar residues in green.

Finally, for the nine remaining pairs, which were not assigned to any state of the channel, all of them are present in at least one model of each system. Among the three residue pairs that include K_V7.1 S6 residues and KCNE1 C_{TERM} residues, only one pair is present in both systems. The second pair is present in 4PIP_2 system only, and the last pair is absent in both systems.

Overall, the K_V7.1-K_V7.1 and the K_V7.1-KCNE1 residue pairs (Tab III.1.1.3) are mostly present in all IK_S models, regardless of the number of PIP_2 lipids in the system. Although the presence and the stability of the interactions between each residue pair in our models is testifying for their robustness, these results alone cannot allow to select the most reliable IK_S system with respect to experimental data. However, the structural analyses we report in the next two sections have provided additional information that will allow for the selection of the best MD system for IK_S models, on which further analyses have been conducted.

Residue pair				State	Reference	Number of subunits (over 4)					
						IK_S 4PIP_2			IK_S 8PIP_2		
KCNE1 region		K_V7.1 segment				AO	IC	RC	AO	IC	RC
Gly40	N_{TERM}	**Thr144**	S1	AO	[194]	**4**	0	1	**4**	0	3
Gly40	N_{TERM}	**Ile145**	S1		[316]	**4**	2	3	**4**	0	2
Gly40	N_{TERM}	**Gln147**	S1		[194]	**4**	0	1	**4**	0	2
Lys41	N_{TERM}	**Gln147**	S1		[194]	1	1	**3**	1	0	3
Leu42	N_{TERM}	**Val324**	S6		[192]	**4**	2	1	**4**	3	1
Lys41	N_{TERM}	**Thr144**	S1	RC	[192]	2	2	**4**	3	1	**3**
Lys41	N_{TERM}	**Ile145**	S1		[316]	4	3	**4**	4	2	**3**
Lys41	N_{TERM}	**Val324**	S6		[192]	0	2	2	0	2	**3**
Leu42	N_{TERM}	**Ile145**	S1		[192]	4	3	**4**	4	2	**3**
Leu42	N_{TERM}	**Gln147**	S1		[194]	0	0	**3**	0	0	**3**
Glu43	N_{TERM}	**Gln147**	S1		[194]	2	0	0	1	0	1
Glu43	N_{TERM}	**Trp323**	S6	Not specified	[317]	4	4	4	4	4	4
Leu51	TMD	**Cys331**	S6		[190]	3	4	4	4	4	4
Glu43	N_{TERM}	**Val141**	S1		[317]	4	3	3	4	2	4
Ala44	N_{TERM}	**Val141**	S1		[317]	4	3	3	4	3	2
Phe54	TMD	**Cys331**	S6		[190]	4	3	4	4	4	2
Leu51	TMD	**Ile328**	S6		[190]	0	3	4	0	4	4
Ser74	C_{TERM}	**His363**	S6		[193]	0	3	2	0	3	2
His73	C_{TERM}	**His363**	S6		[193]	0	1	2	0	1	0
Asp76	C_{TERM}	**His363**	S6		[193]	0	1	4	0	1	2

Tab III.1.1.3: State-dependent protein-protein interactions involving K_V7.1 and KCNE1 residues. Identification of the K_V7.1-KCNE1 neighbor residue pairs previously identified through Cysteine cross-linking studies on our IK_S models. Each residue is colored according to the chemical nature of its sidechain. Apolar residues (aliphatic, aromatic) are written in black, basic residues in blue, acidic residues in red, and polar residues in green.

Chapter III.1.2. Protein-lipid electrostatic interactions

Besides protein-protein interactions, several mutagenesis studies conducted on $K_V7.1$ in absence and presence of KCNE1 also have highlighted ten basic residues from $K_V7.1$ and three others from KCNE1 which can possibly interact with PIP_2. As the protein-lipid interactions in $K_V7.1$ MD trajectories remain similar as those identified in our previous computational study [249], this analysis is focused on IK_S models (Table III.1.2.1). To characterize these interactions in our IK_S models, we calculated average distances between charged groups of each basic residue and PIP_2. Among the thirteen $K_V7.1$ and KCNE1 basic residues which have been shown to be involved in electrostatic interactions with the lipid, a total of ten residues interact with PIP_2 in at least one MD trajectory of IK_S model in $8PIP_2$ system. The results obtained for these models show that PIP_2 inter and PIP_2 intra are specifically anchored to the VSD and the PD, respectively, in a state independent manner (Figure III.1.2.1).

Mutation	Segment	Reference	Number of subunits in IK_S models (over 4)								
			PIP_2 intra ($4PIP_2$)			PIP_2 intra ($8PIP_2$)			PIP_2 inter ($8PIP_2$)		
			AO	IC	RC	AO	IC	RC	AO	IC	RC
Arg190Cys	S2-$S3_L$	[248, 250]	**4**	**4**	**3**	**4**	**4**	**4**	0	0	0
Arg195Gln			**4**	**3**	**3**	**4**	**4**	2	0	0	0
Arg192Cys			2	**3**	0	**3**	0	0	0	0	0
Lys183Cys			**3**	0	2	2	0	2	0	0	0
Arg243His	S4	[157]	0	**3**	**4**	0	2	**4**	0	0	0
Arg249Cys	S4-$S5_L$	[248, 250]	**3**	**4**	**4**	2	**4**	**4**	1	0	0
Lys354Cys	S6		**3**	**3**	1	2	2	0	0	0	0
Lys358Cys		[246, 248]	1	2	1	1	0	0	**3**	2	1
Lys362Cys			0	0	0	0	0	0	**4**	**4**	**3**
Arg366Ala			1	0	1	0	0	0	**4**	**4**	**3**
Arg67Gln	KCNE1 C_{TERM}	[162]	1	0	0	1	0	0	0	**4**	**4**
Lys69Cys			0	**4**	2	0	**4**	2	**4**	0	0
Lys70Cys			0	0	0	0	1	0	0	1	**3**

Tab III.1.2.1: Protein-lipid interactions between $K_V7.1$/KCNE1 basic residues and PIP_2.
Identification of the basic residues from $K_V7.1$ and KCNE1 subunits which have been previously shown to interact with PIP_2 through neutralizing point mutations and site-directed mutagenesis studies. In the first column, residue names are colored according to its sidechain chemical nature. Apolar residues are colored in black, basic residues in blue, and polar residues in green.

In each model, residues R190 from the S2-S3$_{LOOP}$ and R249 from the S4-S5$_{LINKER}$ interact with PIP_2 intra, while residues K362 and R366 from S6 interact with PIP_2 inter. In addition, some basic residues are also interacting with PIP_2 in a state dependent manner, such as R192 and R195 from S2-S3$_{LOOP}$, as well as K358 from S6, whose interactions with PIP_2 are favored in AO model, as well as in IC model for R195. State independent interactions involving VSD residues are related to a motion of PIP_2, which appears to progressively anchor S2-S3$_{LOOP}$, while remaining bound to S4-S5$_{LINKER}$ residue R249 during VSD activation. State dependent interactions involving PD residues are related to the movement of S6 upon pore opening. PIP_2 inter progressively binds basic residues of S6 cytoplasmic helices as they spread away from the pore axis towards inner membrane surface where PIP_2 is localized.

On the contrary, the interaction between residue R243 from S4 and the lipid is favored in the RC model, which suggests that R243 loses its interaction with PIP_2 as S4 translates upward during the VSD activation. In IK_S models of $4PIP_2$ system, state-independent interactions between VSD residues and PIP_2 intra are present, but those between S6 residues and PIP_2 are merely present. Contrary to the $K_V7.1$ models in which PIP_2 intra can bind S6 in the AO model, K354 is the only S6 residue that is able to bind PIP_2 in both the IC and AO models of IK_S complex. Residues K358, K362 and R366 are located too far away to reach PIP_2 intra in any of these models.

Four residues are not interacting with PIP_2 in any IK_S system. R181 and K196 from the S2-S3$_{LOOP}$, remain too far from PIP_2 intra throughout the MD simulations. R360 from S6, whose sidechains remain tangent to the conduction pathway, was unable to interact with PIP_2 inter. R259 guanidinium group, despite being close to PIP_2 lipids, cannot get close to the phosphoryl groups of PIP_2 because of the steric hindrance induced by presence of KCNE1 subunits.

Surprisingly, KCNE1 residues R67, K69 and K70 have their sidechains oriented in two opposite directions, allowing for the ancillary subunit to interact with both PIP_2 binding sites in a state-dependent fashion in IK_S models of $8PIP_2$ system. In the RC model, residue K69 binds PIP_2 intra in two opposite subunits, while R67 and K70 are both binding PIP_2 inter in all subunits. In IC model, the interaction with K70 is absent, while those with both R67 and K69 are still present. In AO model, K69 is the only KCNE1 residue interacting with PIP_2.

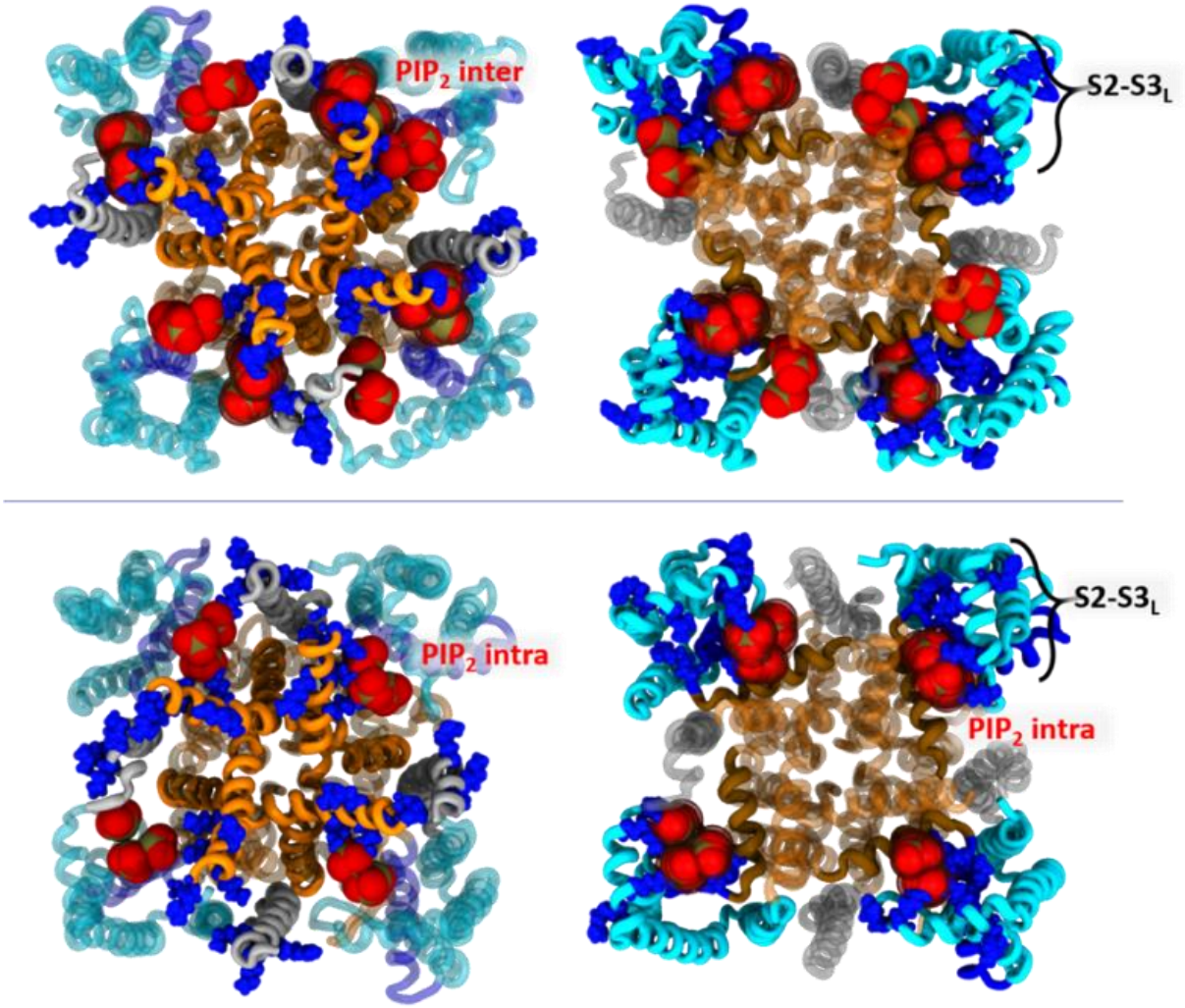

Figure III.1.2.1: Structural mapping of the salt-bridges between IK_S complex residues and PIP_2. Cytoplasmic view of Kv7.1 subunits in cartoon representation in the presence of KCNE1 subunits (in gray) and PIP_2 phosphate groups (in red spheres) in $8PIP_2$ system (top) and 4 PIP_2 system (bottom). In all panels, K_V7.1 segments are colored as follows: S1-S3 in cyan, S4-S5L in brown, and S5-S6 segments in orange. The IK_S basic residues which interact with PIP_2 inter (left) or PIP_2 intra (right) in $8PIP_2$ system are represented in blue spheres and carried by the K_V7.1 and KCNE1 segments represented by solid-colored ribbons, while the other segments are in transparent ribbons.

These subsequent interactions over all our stable state models of IK_S of $8PIP_2$ system suggest that KCNE1 undergoes two clockwise rotations during VSD activation, each occurring during the RC-IC and the IC-AO transitions, respectively. In the IC and RC models, KCNE1 residues are binding both inter and intra PIP_2, forming a circle around the cytoplasmic region of S6 helices. This PIP_2-KCNE1 circle was not observed in the AO model, as KCNE1 does not bind PIP_2 intra. Thus, the cytoplasmic region of S6 can spread away from the pore axis towards PIP_2 inter. Quite interestingly, in the MD trajectories of IK_S models in the $4PIP_2$ system, a likewise PIP_2-KCNE1 circle cannot be formed due to the absence of PIP_2 inter. Indeed, interactions involving R67 and K70 are impaired, while those involving K69 are conserved. However, in the AO model, the interaction between K69 and PIP_2 is impaired, and basic residues of KCNE1 are facing those of S6 that strongly interact with PIP_2 inter in $8PIP_2$ systems, which might generate electrostatic repulsions, leading to the collapse of S6 segments and pore closure.

In summary, our results provide a molecular insight into an additional PIP_2 binding site in IK_S channel, with which KCNE1 interacts in a state dependent manner. These state-dependent interactions suggest a clockwise rotational motion of KCNE1 C_{TER} region when the VSD activates from its Resting state to its Activated state upon membrane depolarization. This additional PIP_2 binding site, which is present only in $8PIP_2$ system, will be further discussed in chapter III.2.4, as it might play a role in the pore shape of IK_S RC and IC models.

Chapter III.1.3. Average pore radii calculations

Based on the correlation identified between the pore size of a K_V channel and the free energy associated to the conduction of a potassium ion [302], the analysis of the pore size of our models can allow to assess the reliability of our IK_S models with respect to those of $K_V7.1$ model, and also with respect to experimental data. Integrative studies conducted on the Shaker channel [318] highlight the fact that the cytoplasmic region of K_V channel conduction pathway need to be able to accommodate a solvated potassium ion, whose minimal radius is ~3.6 Å, to be open. Hence, we compared first the pore radii profiles of IK_S MD trajectories in its distinct systems, and then we compared the most robust model of IK_S in its three states with those of $K_V7.1$ models.

Pore radius measurement of the conduction pathway of $KCNQ1_{EM}$ structure in its Activated/Closed state reveals three regions of constriction in the cytoplasmic side of the conduction pathway: the upper constriction is formed by the backbones of G345; the middle constriction is formed by hydrogen bonds between S349 hydroxyl groups, and the lower constriction is formed by the L353 side chains that are oriented towards the center of the pore and binding each other to form a hydrophobic seal. These three regions of constriction present pore radii of ~2 Å for G345, ~0.8 Å for S349, and ~1.15 Å for L353, which may prevent a K^+ ion to go through this pathway, as its ionic radius is ~1.33 Å [78]. This pore radius profile provides a hint on the constriction zones of Kv7.1 pore when the channel is decoupled due to the absence of PIP_2 lipids.

The MD trajectories of our models suggest that the backbone of G345 is oriented toward the center of the pore, while the side chains of both S349 and L353 remain tangent to the pore surface in all models. Nevertheless, the average pore radii estimated on these regions sheds light on state dependent opening/closure of the conduction pathways. In the AO models (Figure III.1.3.1, right), values are between 2.7 Å and 5 Å. In the Intermediate models (Figure III.1.3.2, right), these values are between 2 Å and 4.5 Å. In the resting models (Figure III.1.3.3, right), the average pore radii at the level of constricted regions assume values between 1 Å and 3 Å for the three models.

In the AO state, the $K_V7.1$ ionic currents are increased in presence of KCNE1, thus IK_S AO models should present wider pore radii than the $K_V7.1$ AO model at the level of constriction regions. Among our AO models (Figure III.1.3.1, left), $K_V7.1$ and IK_S of $8PIP_2$ system present similar values at the regions of constriction. Pore radii values are centered around 3 Å, 3.9 Å and 4.5Å at the levels of G345, S349 and L353, respectively. Thus, increasing radii of subsequent constriction zones observed in AO models of $K_V7.1$ and IK_S of $8PIP_2$ system may favor pore opening. However, the IK_S model of $4PIP_2$ system appears to be more constricted at the level of S349.

Although its average pore radii are only 0.9 Å lower than those of other AO models, it is important to note that a decrease of 1 Å in the radius value of a nanopore in a low dielectric membrane can lead to a sharp increase of the energetic cost necessary for its opening [18, 302]. Thereby, the pore radius difference between IK_S AO models of $4PIP_2$ and $8PIP_2$ system allow us to assume the widening of S6 cytoplasmic region in IK_S AO model might require more energy with one PIP_2 binding site than with two PIP_2 binding sites.

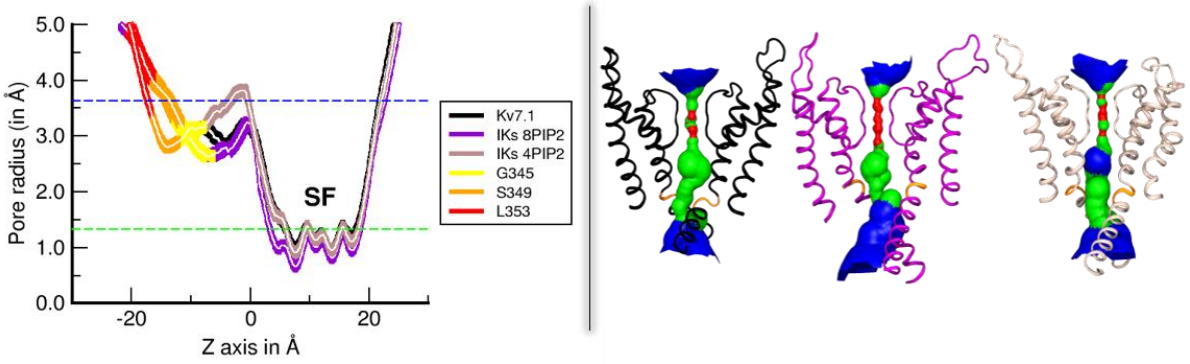

Figure III.1.3.1: Pore size comparison of IK_S models in their activated state.
On the left panel, the graph reports the average pore radii (in white lines) of the activated of $K_V7.1$ models along the z axis, which is perpendicular to the membrane plan and centered on the conduction pathway, along with their standard deviations (in colored horizontal bars) throughout their respective MD trajectories. SF stands for the average radii of the selectivity filter. K+ ionic radius (1.33 Å) and hydrodynamic radius (3.6 Å) are represented by green and blue dashed lines, respectively.
On the right panel, the pictures show cartoon representations of the pore domains of $K_V7.1$ (black) IK_S $8PIP_2$ (purple) and IK_S $4PIP_2$ (beige) models, along with the solvent accessible surfaces of their respective conduction pathways. For each model, two subunits are shown for clarity. PAG motif residues are colored in orange. Pore solvent accessible surfaces are colored as follows. The pore radii values inferior to K+ ionic radius, are colored in red. The pore radii values ranging from K+ ionic radius and K+ hydrodynamic radius, are colored in green. The pore radii values superior to K+ hydrodynamic radius, are colored in blue.

In the Intermediate state, the ionic current is abolished in presence of KCNE1, so IK_S models should present a smaller pore radius than in $K_V7.1$. In the intermediate models (Figure III.1.3.2, left), the pore radii of the constriction zone of L353 are ~3.6 Å in all models. Therefore, we only considered G345 and S349 constriction zones. The $K_V7.1$ model present the highest average pore radii values, (~ 2.7 Å and 2.9 Å at the levels of G345 and S349, respectively) compared to the IK_S models (both ~ 2 Å). Hence, in a nutshell, the results for the intermediate state models suggest that $K_V7.1$ conduction pathway is ~0.8 Å narrower in presence of KCNE1, regardless of the number of PIP_2 lipids in the system, which agrees with experiments.

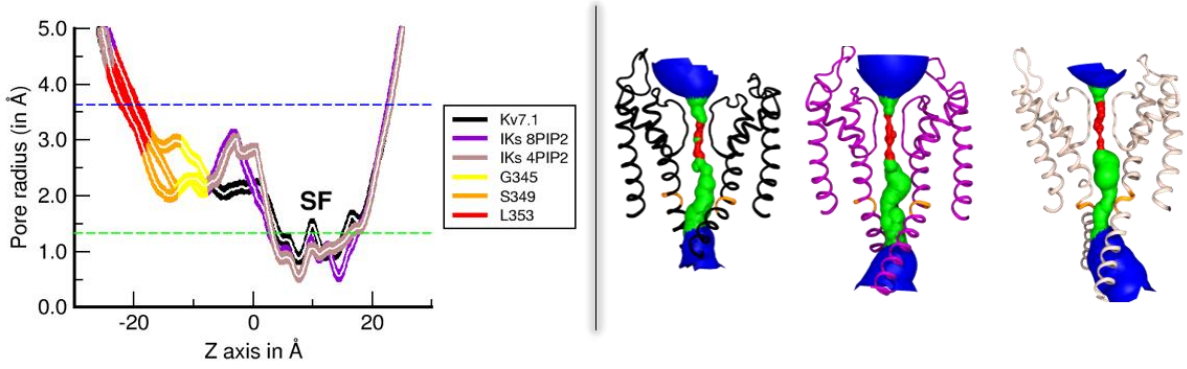

Figure III.1.3.2: Pore size comparison of IK_S models in their Intermediate state.
On both panels, the color code used for $K_V7.1$ and IK_S models is similar as Figure III.1.3.1.
On the left panel, the graph reports the average pore radii of the Intermediate state of Kv7.1 models along the z axis, along with their standard deviations throughout their respective MD trajectories.
On the right panel, the pictures show cartoon representations of the pore domains of $K_V7.1$ (left) IK_S $8PIP_2$ (middle) and IK_S $4PIP_2$ (right) models, along with the solvent accessible surfaces of their respective conduction pathways. For each model, two subunits are shown for clarity.

The constriction zones of the RC models (Figure III.1.3.3, left) present pore sizes below the minimal hydrodynamic radius of K^+ ions of 3.6 Å, which suggests that in the RC models, the pore is more likely to be closed regardless of the presence of KCNE1 or the number of PIP_2 lipids. Among these models, $K_V7.1$ presents the largest pore radii at the level of G345 and S349, as its pore radii values are centered on 2.7 Å and 1.7 Å, respectively. Then, in the IK_S model of $4PIP_2$ system, the pore radii of both G345 and S349 constriction zones are centered around 2.1 Å and 1.5 Å. Finally, the IK_S model of the $8PIP_2$ system presents the lowest pore radii values at the levels of G345 and S349 (~ 1.7 Å and 1.3 Å, respectively). However, the trend is reversed at the level of L353. Indeed, in this region, $K_V7.1$ is the most constricted with pore radii ~ 1.5 Å, while the IK_S model of $4PIP_2$ and $8PIP_2$ systems' pore radii are ~ 2.0 Å and 2.2 Å, respectively.

Nevertheless, the maximum pore radii in the L353 region in IK_S model of $8PIP_2$ system remains too small to accommodate a solvated K^+ ion. For all RC models, the region of S349 is the most constricted, and the IK_S models present shorter pore radii values than $K_V7.1$, which agrees with experiments.

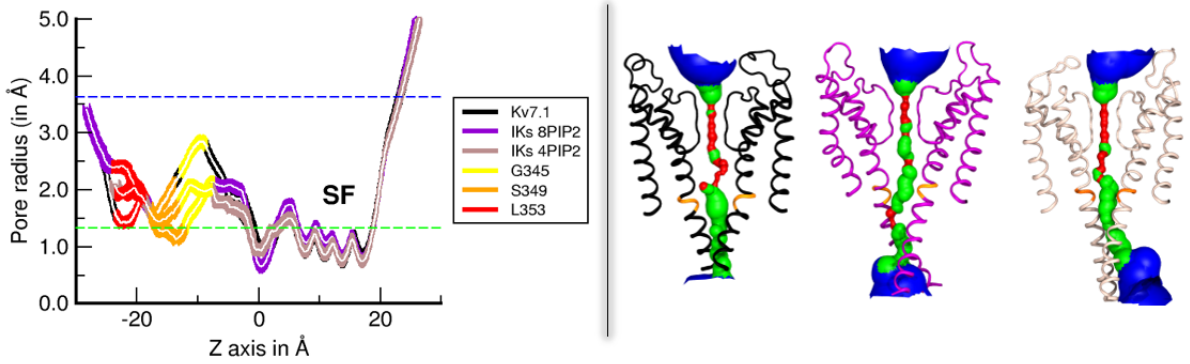

Figure III.1.3.3: Pore size comparison of IK_S models in their resting state.
On both panels, the color code used for $K_V7.1$ and IK_S models is similar as Figure III.1.3.1.
On the left panel, the graph reports the average pore radii (white lines) of the resting state of $K_V7.1$ models along the z axis, along with their standard deviations (colored lines) throughout their respective MD trajectories. On the right panel, the pictures show cartoon representations of the pore domains of $K_V7.1$ (left) IK_S $8PIP_2$ (middle) and IK_S $4PIP_2$ (right) models, along with the solvent accessible surfaces of their respective conduction pathways. For each model, two subunits are shown for clarity.

The differences observed between the average pore radii calculated over the MD trajectories obtained for $K_V7.1$ and IK_S models indicate that KCNE1 may increase the tightening of the inner pore in the RC and IC states, while inducing a closer proximity between S6c region and the inner membrane surface in the AO state, which agrees with the experimental studies. The comparison of the average pore radii obtained for the IK_S models of both $4PIP_2$ and $8PIP_2$ systems with those obtained for the $K_V7.1$ models indicate that the MD trajectories of the IK_S models of $8PIP_2$ system fit better the ionic conductance measures of the IK_S channel [161] compared to the $K_V7.1$ channel.

Furthermore, the average pore radii of the $K_V7.1$ models at the level of the SFF motif correlate quite well with the experimental ionic currents measured on $K_V7.1$ in absence and presence of KCNE1 [156, 161]. Indeed, at the level of the F340 side chains, the pore radii are of 1 Å, 2 Å and 3 Å in average throughout the MD trajectories of the RC, The Intermediate and AO models, respectively (Figure III.1.3.4, top panel).

In the trajectory obtained for $K_V7.1$ AC state, the average pore radius at the level of F340 is 1 Å, which is similar to that found in the RC models. The above pore radii analyses already hint to the presence of a state dependent *hydrophobic seal* formed by the F340 residues (Figure III.1.3.4, bottom panel). Mostly present in the RC models, as well as in the AC model (pore radius similar to that of the selectivity filter), the seal tends to loosen up with VSD activation, as observed in the intermediate and activated models. However, the pore size is not enough to indicate, for each state, whether or not one channel would conduct higher or lower ionic currents.

Nevertheless, we investigated the Van der Waals interactions involving the SFF residues in the $K_V7.1$ and in the IK_S models in order to understand what conformational changes lead to the formation of this seal. The results obtained will be detailed in Chapter III.2.2.

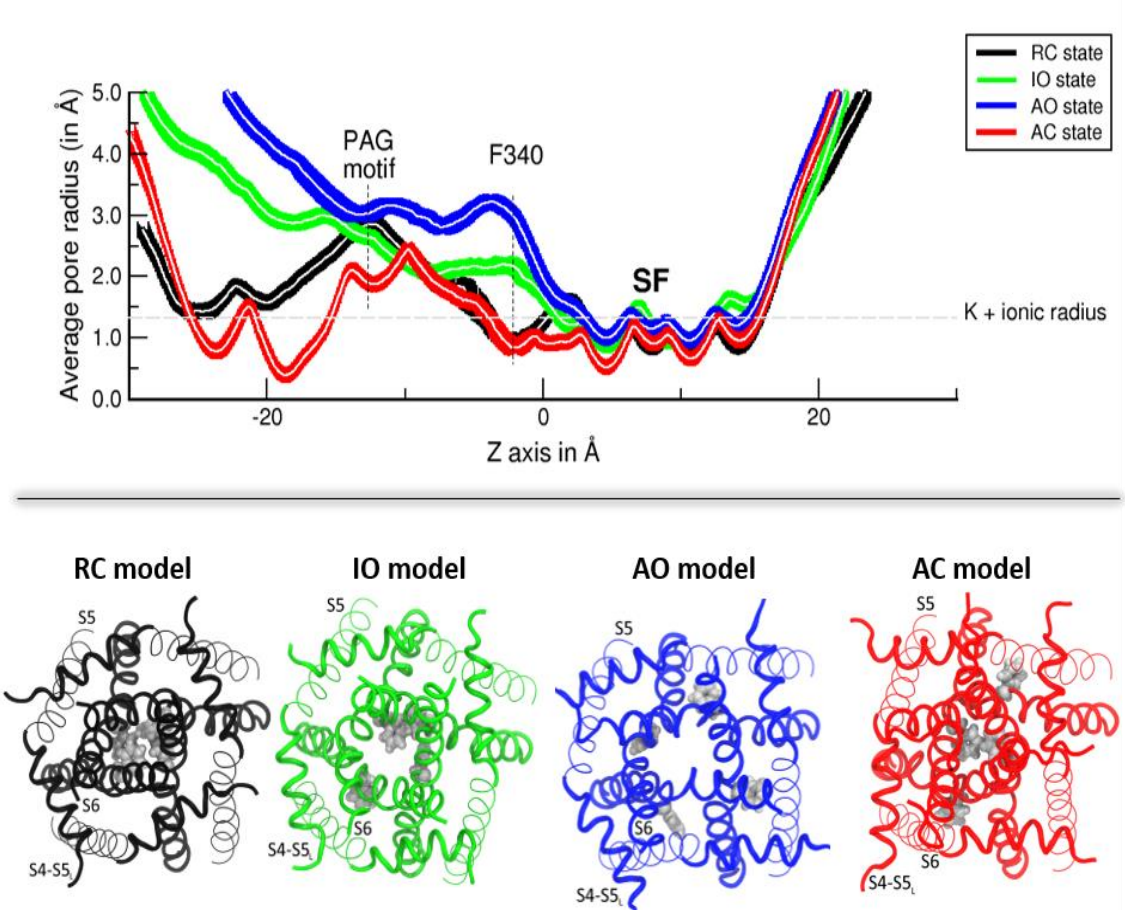

Figure III.1.3.4: Pore size calculations of $K_V7.1$ models.
The top panel shows a projection of average pore radii of the conduction pathways of $K_V7.1$ models on the normal axis to the membrane. Standard deviations are represented by black, green, blue and red horizontal bars for the MD trajectories obtained from RC, IO, AO and AC models, respectively.
The bottom panel shows a cartoon representation of the **i**ntracellular side of S4-$S5_L$ and PD segments in $K_V7.1$ RC (black), IO (green), AO (blue), and AC (red) models. In each picture, S4-$S5_L$ and S6 segments are highlighted in thick ribbons, while S5 is depicted in thin ribbons. The sidechains of F340 are represented in gray spheres.

Chapter III.1.4. Structural comparison with $K_V7.1$ (CryoEM) experimental structure

To confirm the robustness of our models with respect to available structural data, we estimated their RMSD with respect to the $KCNQ1_{EM}$ structure. Based on the previous MD analyses of the protein-lipid interactions in IK_S models, we selected the IK_S models of $8PIP_2$ system (called hereafter IK_S model) for further MD analyses. Furthermore, we have not considered the $K_V7.1$ AC model for this analysis, as we used the present $KCNQ1_{EM}$ structure as a template to design it. Hence, the structural comparison of our models with the novel $KCNQ1_{EM}$ structure included the $K_V7.1$ models and the IK_S models of $8PIP_2$ system. For the VSD, we first aligned the S1-S4 segments of each subunit of our AO models (Figure III.1.4.1) with the VSD of $KCNQ1_{EM}$, and then calculated the RMSDs over the corresponding trajectories.

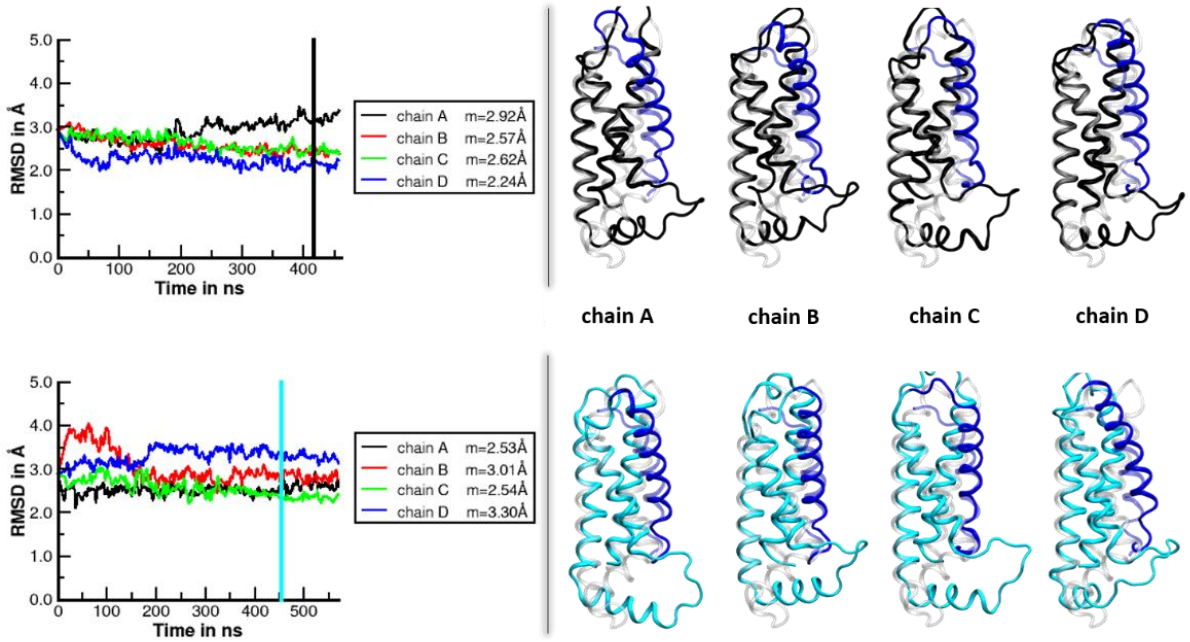

Figure III.1.4.1: Voltage sensor domain comparison of AO models with $KCNQ1_{EM}$ structure
On the left panels, the graphs project the root-mean-square deviation (RMSD) between the VSD segments of $K_V7.1$ (top) and IK_S (bottom) AO models with respect to $KCNQ1_{EM}$ structure throughout their MD simulation time (in ns). Average RMSD values are displayed for each subunit (labeled chain A, B, C, D). The right panels show a cartoon representation of the structural alignment of the VSD of $KCNQ1_{EM}$ structure (in transparent colors) with those of $K_V7.1$ (top) and IK_S (bottom) AO models, each captured at ~420 ns and ~450 ns, respectively. On each graph, the vertical line represents the simulation time at which the pictures displayed on the right panels were captured. The S1-S3 segments of $K_V7.1$ models and IK_S models are colored in black and cyan, respectively, while the S4 segment is colored in blue in all the representations.

The average RMSD values obtained for the VSDs of the $K_V7.1$ subunits (Figure III.1.4.1, top left) of the AO model remain below 3.0 Å during MD simulation. For the IK_S AO model (Figure III.1.4.1, bottom left), the average RMSD values remain below 3.5 Å. These results suggest that the structure of our activated VSDs are in very good agreement with the experimental structure. As expected, the VSDs of the $K_V7.1$ model (Figure III.1.4.1, top right) are slightly closer to the structure than those of the IK_S model (Figure III.1.4.1, bottom right).

For the PD, we aligned the S6 segment of each subunit of our RC models with the S6 segment of $KCNQ1_{EM}$ and calculated the RMSD over the corresponding MD trajectories (Figure III.1.4.2). As the S6 segments are truncated above residue 358 in the $K_V7.1$ models, we did not consider the S6 residues 359 to 366 for these alignments, despite of their presence in both IK_S models and $KCNQ1_{EM}$ structure. For $K_V7.1$ (Figure III.1.4.2, top, left), the average RMSD of the RC models remain below 1.9 Å. For IK_S (Figure III.1.4.2, bottom, left), the average RMSD of the RC models remain below 2 Å.

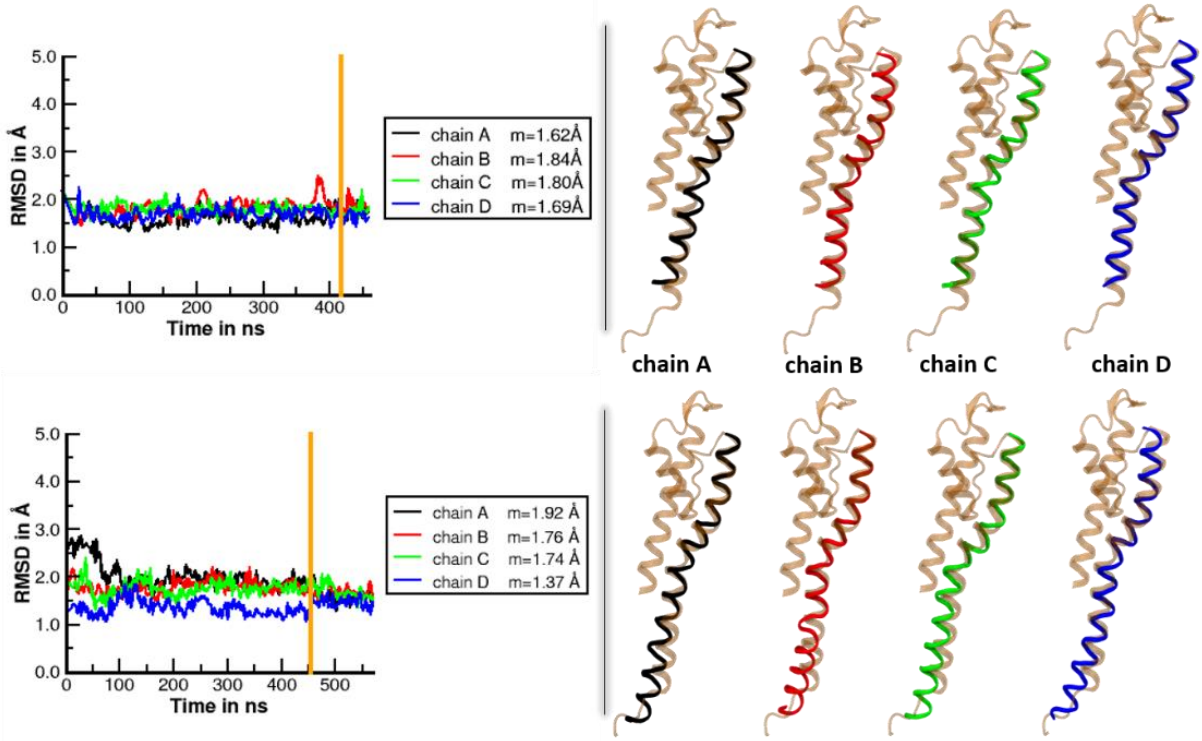

Figure III.1.4.2: Pore domain comparison of RC models with $KCNQ1_{EM}$ structure
On the left panels, the graphs project the root-mean-square deviation (RMSD) between the PD segments of $K_V7.1$ (top) and IK_S (bottom) AO models with respect to $KCNQ1_{EM}$ structure throughout their MD simulation time (in ns). Average RMSD values are displayed for each subunit (labeled chain A, B, C, D). On each graph, the orange vertical line represents the simulation time at which the pictures displayed on the right panels were captured. The right panels show a cartoon representation of the structural alignment of the S6 segment of $KCNQ1_{EM}$ structure (in transparent orange) with those of $K_V7.1$ (top) and IK_S (bottom) RC models, each captured at ~420 ns and ~450 ns, respectively. For both models, each subunit is represented in solid black, red, green and blue cartoon, respectively.

Overall, these results provide an additional evidence of the reliability of our theoretical models of both the $K_V7.1$ channel and the IK_S complex. The MD trajectories have shown that both VSD and PD segments of $K_V7.1$ subunits remain structurally closer to $KCNQ1_{EM}$ in $K_V7.1$ models than in IK_S models. This difference might be due to the presence of KCNE1, which advocates for the modulation effects of KCNE1 on $K_V7.1$ subunits. Altogether, these results increase the confidence in our AO and RC models with respect to KCNQ1 AC state structure.

To validate the IO model of the $K_V7.1$ channel, we compared the structure of its VSD segments with those of the refined NMR structure of human KCNQ1 VSD [319], which has recently been deposited in the PDB database (PDB ID: 6MIE). The average RMSD values obtained for each VSD of IO model lay between 4.22 Å and 5.24 Å (Figure III.1.4.3, left). These results can be explained by the fact that our model was submitted to MD simulations in a system that considers explicitly PIP_2. These lipids turned out to engage in strong electrostatic interactions with both S4 and $S2\text{-}S3_{LOOP}$ during MD simulation (see Chapter III.1.2). This is likely to induce a conformational change of the VSD segments in our IO model with respect to the NMR structure of KCNQ1 VSD, which has been refined using MD simulations but in absence of this phospholipid. Moreover, the S4 segments of our model are slightly tilted with respect to the NMR structure (Figure III.1.4.3).

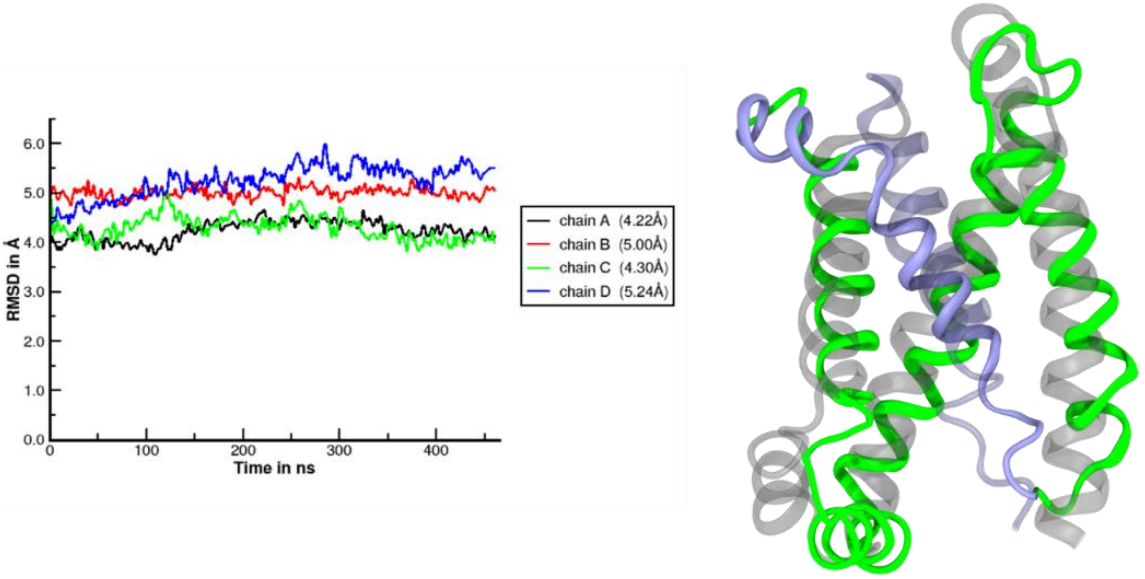

Figure III.1.4.3: Comparison of $K_V7.1$ IO model with NMR structure of human $K_V7.1$ VSD.
The left panel projects the backbone RMSD to the NMR structure (PDB ID: 6MIE) of the transmembrane helices of each VSD of $K_V7.1$ IO model. The average RMSD over the course of the MD simulation trajectory is displayed in parenthesis. The right panel shows the centroid of chain A VSD of $K_V7.1$ IO model (in solid green) and the average NMR structure of human $K_V7.1$ VSD (in transparent gray. In MD simulations the 4 subunits are identified as chain A, B, C and D.

The four molecular models of $K_V7.1$ α-subunits will be used as the basis for additional structure-function studies in Chapter III.2.1 to further validate their accuracy and to investigate the state-dependent interactions which mediate the VSD-PD coupling mechanism of the full $K_V7.1$ channel. The results obtained will constitute the basis for the MD analysis conducted on IK_S models (Chapter III.2.3) in order to determine the molecular determinants of the modulation of $K_V7.1$ VSD-PD coupling by KCNE1 subunits.

Chapter III.2. Characterization of K_V7.1 channel state dependent conformations

The second large set of analyses was conducted on the production phase of the 500 ns MD trajectories obtained with the four models of K_V7.1. This knowledge-based analyses consisted in the determination of the weak interactions that stabilize each K_V7.1 model within the POPC membrane, in presence of the PIP_2 lipids. These interactions, by their state-dependence or independence, as well as their nature and their stability, allow for the unraveling of the molecular determinants involved in the VSD-PD coupling mechanism of K_V7.1 channel, which constitutes one of the three main mechanisms of the function of domain-swapped K_V channels.

Chapter III.2.1. Functional validation of K_V7.1 VSD-PD coupling mechanism.

To facilitate our investigation, as well as to add further proof of the reliability of our models, we confronted the computational results we obtained against the functional studies of K_V7.1 channel conducted by our collaborators from Washington University of Saint-Louis. For the last decade, they have reported several studies that confirm the classic view of voltage-dependent activation K_V7.1 [167], as it conducts ionic current when its VSDs occupy the activated conformation. Contrary to the other members of the K_V superfamily, our collaborators recently showed that K_V7.1 turns out to conduct ionic current when its VSDs occupies the intermediate conformation as well [156, 173]. However, from a physiological perspective, the classic framework is limited in its ability to explain how and whether the VSD-PD coupling interactions contribute to these two open states, as well as to explain the effects of the multiple LQT-associated mutations that include both VSD and PD residues [320]. Some of these mutations yield both K_V7.1 IO and AO states to non-conductive channels [248], whereas other mutations specifically affect only one of these two K_V7.1 open states [156, 173]. Moreover, the molecular basis underlying how each mutation leads to channel dysfunction and disease remains unclear. For example, a mutation located in the VSD might affect either VSD activation, VSD-PD coupling, or both mechanisms to cause channel dysfunction [321, 322].

In order to fill these knowledge gaps in the K_V7.1 voltage-dependent activation and to unravel the molecular basis of these LQT-related mutations, we harnessed the combination of both experimental and theoretical methods. This integrative approach allowed us to provide a clear picture of K_V7.1 function, from its VSD activation to its VSD-PD coupling and pore opening. To achieve our goal, our collaborators confronted the results we obtained from K_V7.1 MD simulations with the functional results they obtained for the IO state, followed by those they obtained for the AO state using powerful bioengineering methods such as site-directed mutagenesis and double mutant cycle analysis in order to obtain a series of several K_V7.1 LQT mutants. Then these mutants were transfected and expressed in oocytes in order to perform two electrophysiology experiments: voltage-clamp recordings, to measure the current of the channel mutants at various potentials as well as the voltage dependence of pore opening, and voltage-clamp fluorometry assays to record the voltage-dependence of VSD activation. Site-directed mutagenesis were performed on the S4-S5L and C_{TER} of S6 (S6c) regions that have been classically identified as critical for the VSD-PD coupling of K_V7.1 [176, 182]. The results obtained allowed for the identification of five mutations (V254M, A341V, H258W, P343A, G345A) that suppressed ionic currents without preventing the VSD's movements (Figure III.2.1.1) or the plasma membrane channel expression [323].

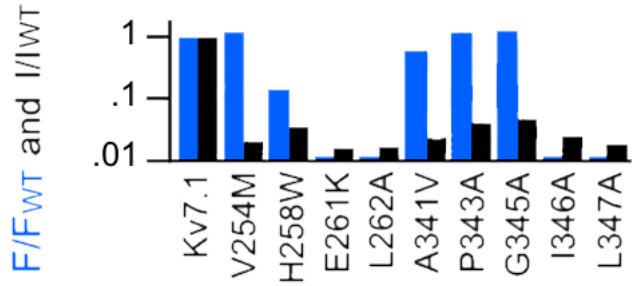

Figure III.2.1.1: Site-directed mutagenesis of K_V7.1 residues involved in IO state coupling.
The barplot displays the fluorescence (F/F_{WT}) and current intensity (I/I_{WT}) ratios between WT K_V7.1 and mutations. VSD activation (blue) and pore opening (black) were normalized to the WT. (Courtesy from Pr. J. Cui Lab)

Among those mutations, two of them (V254M and A341V) are associated with LQTS [324]. Four additional mutants (E261K, L262A, I346A, L347A) located on S5 and S6c, were also identified as they do not yield any ionic current. Furthermore, their VCF fluorescent signals and membrane expression suggest an absence of VSD activation and a strongly reduced membrane expression (Figure III.2.1.2).

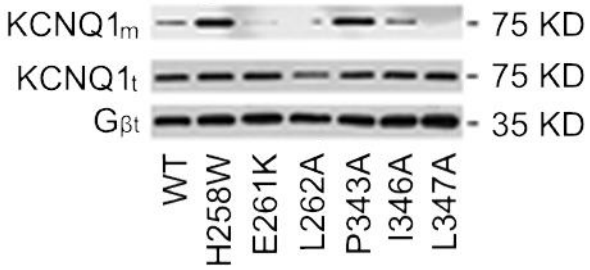

Figure III.2.1.2: Membrane surface expression of K_V7.1 S4-S5L/S6 region mutants.
Western blot data show the membrane ($KCNQ1_m$) and total expression ($KCNQ1_t$) of some mutants of K_V7.1 channel, H258W, and P343A were shown as positive control (Courtesy from Pr. J. Cui Lab).

With these functional results, these residues altogether are suspected to be crucial for VSD-PD coupling when S4 reaches its intermediate state. MD simulations suggest that the interactions in which residues V254, A341, H258, E261, L262, P343, G345, I346 and L347 (Figure III.2.1.3) are involved can be clustered into two distinct groups:

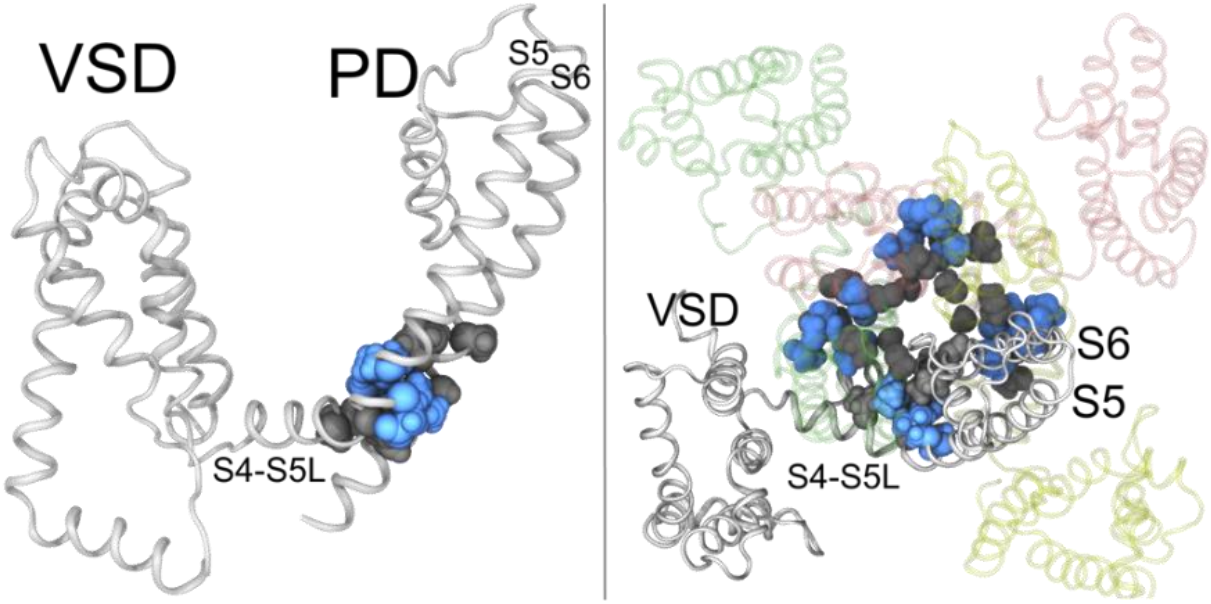

Figure III.2.1.3: Structural mapping of K_V7.1 residues involved in IO state coupling according to functional study results.
The left panel shows a lateral view of one subunit of K_V7.1 IO model (in silver cartoon) in which residues that yield to non-conductive mutants are depicted in gray balls, while residues that yield to low membrane expression mutants are depicted in blue balls. The right panel shows a top view of the entire tetramer, in which the mutated residues of the left panel are depicted in all subunits (in green, pink and yellow transparent cartoon). The subunit of the left panel is depicted in solid silver cartoon.

The first group is composed of V254 and H258 from S4-S5$_L$, L262 from S5 and P343, I346 and L347 from S6. The results we obtained indicate that these residues are engaged in VdW interactions throughout the MD trajectories of all the K_V7.1 models. Indeed, the interaction frequencies we calculated between V254 and L347, H258 and I346, L262 and V255, L262 and L347 and between P343 and T265 are all superior to 0.6 in all K_V7.1 models (Figure III.2.1.4).

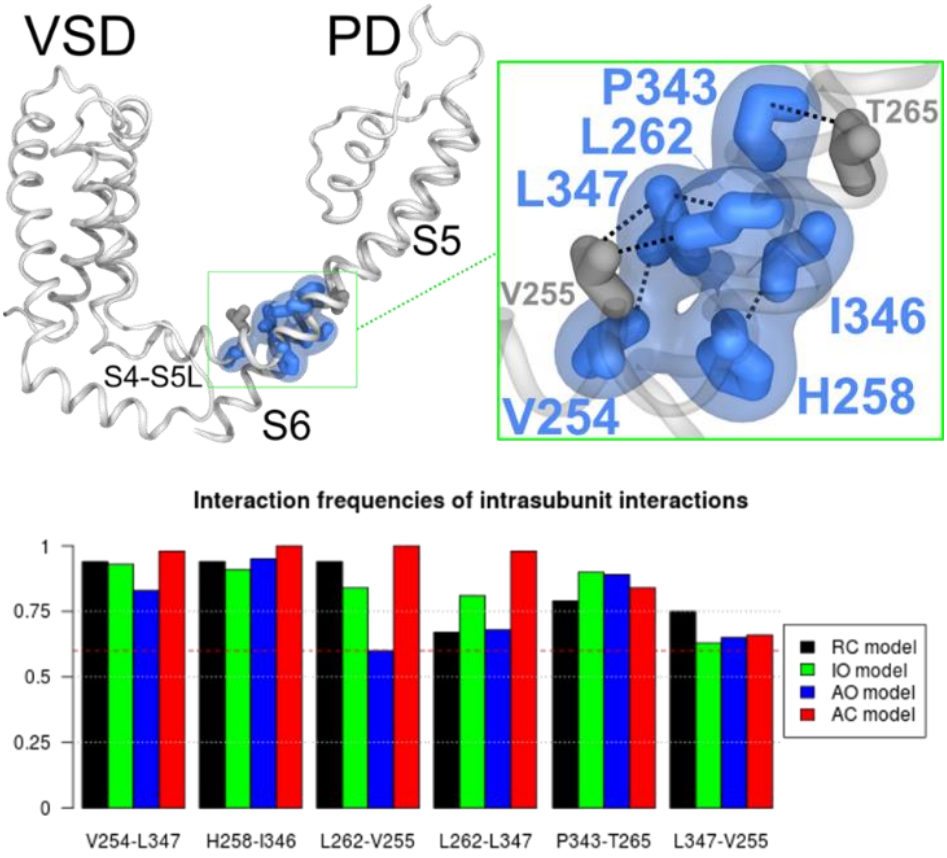

Figure III.2.1.4: MD simulation results of K_V7.1 residues involved in IO state coupling.
The top panel is a cartoon representation of the IO state of K_V7.1. An entire subunit (in gray) is shown with insets of enlarged structures of the boxed area. Residues identified as important for E-M coupling in experiments are colored in blue. Residues V255 and T265, which are identified in MD simulations as possibly involved in sidechain interactions, while mutations still show functional currents are colored in grey. The bottom panel displays the interaction frequencies of K_V7.1 residue pairs including those key residues in the top panel throughout the MD trajectories obtained for K_V7.1 RC, IO, AO, and AC models. The frequency threshold of 0.6 is marked by a red dashed line.

The state-independent aspect of these interactions suggests some of these residues may be involved in the protein folding and/or the intrinsic structure of the KCNQ1 subunits. This is in strong agreement with functional studies, which showed that these residues, when mutated, can induce either a defective K_V7.1 membrane expression (for E261K, L262A and L347A mutants) or a complete loss of function (for H258W and I346A mutants).

The second group is composed of three intrasubunit interactions which present a similar trend throughout the MD trajectories of the RC, the IO and the AO models of $K_V7.1$, and a different one in the trajectory of the AC model (Figure III.2.1.5, bottom panel). The first two pairs of residues involve V254 and P343 in a VdW interaction with F351 and L262, respectively. Their frequencies indicate that these interactions are absent in all $K_V7.1$ models, except in the AC state, suggesting that these interactions may need to be broken to elicit VSD-PD coupling in both the IO and the AO states.

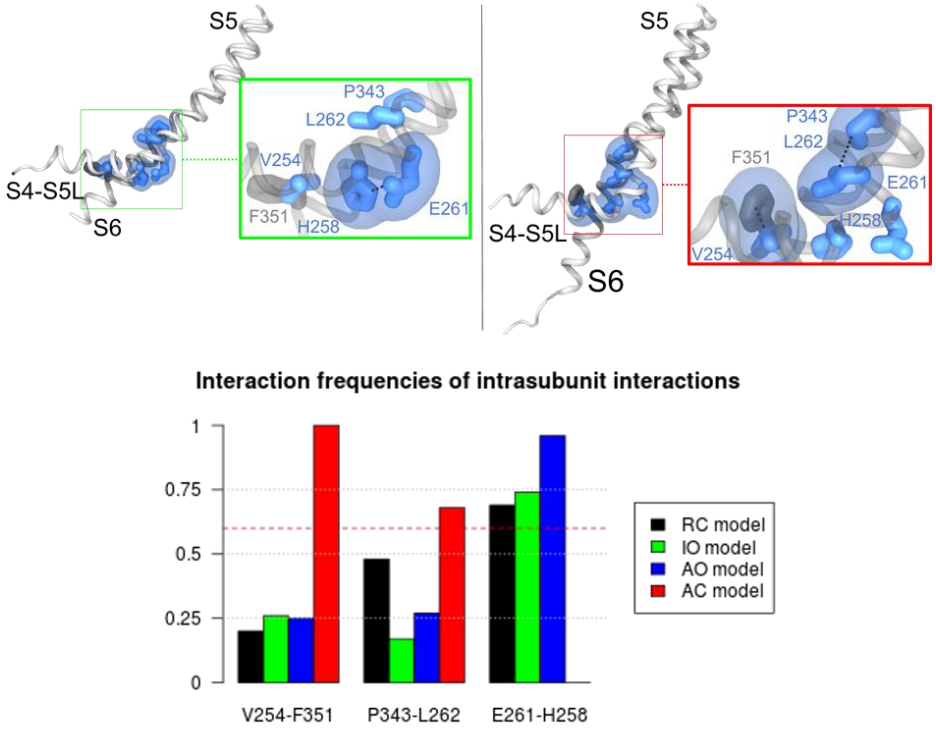

Figure III.2.1.5: Molecular basis of S4-S5L/S6 LQT mutations of $K_V7.1$ revealed by MD simulations. The upper panel displays a lateral view of $K_V7.1$ S4-S5L, S5 and S6 segments (in gray cartoon) of $K_V7.1$ IO model (left) and AO model (right) along with an extended view of the interaction that is present in all models but $K_V7.1$ AC model (left) and the interactions that are absent in all models but $K_V7.1$AC model. The lwer panel shows barplots of the state-dependent interactions involving the residues V254 (S4-S5L), L262 (S5) and P343 (S6). The frequency threshold of 0.6 is marked by a red dashed line.

The properties of V254M and P343A non-conductive mutants revealed by the functional studies can possibly lead to a strengthening of this couple of interactions in both the IO and the AO states. Indeed, a mutation of V254 into a Methionine, whose sidechain is longer and more flexible than a Valine, can prevent pore opening by making a strong Met-Arom interaction with F351 without hindering the upward movement of S4-$S5_{LINKER}$ in response to VSD activation, due to its enhanced flexibility with respect to Valine.

Similarly, a mutation of P343 into an Alanine, which can make stronger VdW interactions while providing less flexibility for a α-helix than a Proline, can prevent pore opening due to the possible strengthening of the VdW interactions with L262. Moreover, the P343A mutation can also disrupt the entire hinge region of the S6 segment, inducing an inability of the latter to tilt upwards at the level of PAG motif when the pore opens. The S4-S5$_{LINKER}$ residue H258 and the S5 residue E261 are both polar, and the interaction frequencies are above 0.6 in MD trajectories of the Kv7.1 RC, IO and AO models, but not in the AC one. This result indicates that these residues may be involved in a hydrogen bond or, depending on the ionization state of histidine side chains, in an ionic interaction.

Despite the absence of any noticeable interaction involving A341 or G345, the effects of their mutations can easily be predicted. For the A341V mutant, its tangent orientation with respect to the inner pore surface might induce the formation of a hydrophobic seal when mutated into Valine, whose side chains are bulkier than Alanine. This hydrophobic seal in the conduction pathway can lead to the phenotype of A341V mutant that has been characterized by the functional study. Considering the location of G345 (in the PAG motif) and the extended flexibility of a glycine due to its absence of side chain [325], one can easily predict that a mutation of its residue into an alanine would limit the flexibility of S6 segment during pore opening, leading to the phenotype of G345A mutant.

Taken together, the functional experiments and MD simulations results suggest that the residues located in the S4-S5L and in the S6c form intra-subunit interactions that appeared to be crucial for the pore opening of K$_V$7.1 channel in both IO and AO states.

According to the MD trajectories of the K$_V$7.1 models, most of these interactions appear to be state independent. Therefore, they might need to be maintained for the pore to open when the VSD reaches both its IO and AO states. This indicates their key roles not only in the VSD-PD coupling, but also in protein expression and/or in folding, consistent with the experimental studies showing that some mutations result in defective membrane expression (E261K, L262A, and L347A) or non-functional channels (I346A) [326]. Our results are consistent with previous studies that reported this region as important for the VSD-PD coupling in homologous K$_V$ channels [167, 172, 182, 327, 328]. As a consequence, the mutations on this particular region leads to a loss of VSD-PD coupling in both the IO and AO states of K$_V$7.1 (Figure III.2.1.1).

In order to determine the residues that play a crucial role in the VSD-PD coupling of $K_V7.1$ in its AO state, our collaborators analyzed the effects of the known $K_V7.1$ activator ML277 on a series of mutants obtained by Alanine scanning of the residues from S4-S5L, S5 and S6. Indeed, ML277 is known to specifically enhance the coupling of $K_V7.1$ in its AO state, by doubling its ionic current amplitude [329]. Therefore, our collaborators hypothesized that the residues important for the VSD-PD coupling of $K_V7.1$ in its AO state must be the ones whose current is not enhanced in presence of ML277 when mutated. This experiment allowed for the identification of thirteen mutants, including five from S4-$S5_L$ (W248R, L250W, L251A, V255W, and F256A), four from S5 (Y267A, I268W, L271E, and G272A) and four from S6 (F335A, S338F, F339S, and L342A) whose current is either suppressed or significantly reduced in presence of ML277. Meanwhile, according to the VCF results, the VSD activation of these mutants is not affected. Hence, they decided to perform a second mutagenesis experiment in order to determine if these mutants are actually disrupting the $K_V7.1$'s AO state. When these mutants are co-expressed in the $K_V7.1$ charge reversal mutants E1R/R2E and E1R/R4E that are locking the VSD in its intermediate and activated state, respectively, all of them turned out to generate normal current in the E1R/R2E mutant, and not in the E1R/R4E one. Interestingly, four S4 mutants (M238W, L239W, D242W, R243H) which were reported in a previous study as specifically disrupting the VSD-PD coupling in IK_S channel [161, 173] were also tested and yielded to similar results as the thirteen ones mentioned above. In this way, our collaborators managed to highlight a total of 17 residues that are crucial for $K_V7.1$ VSD-PD coupling when the VSD is in its AO state (Figure III.2.1.6).

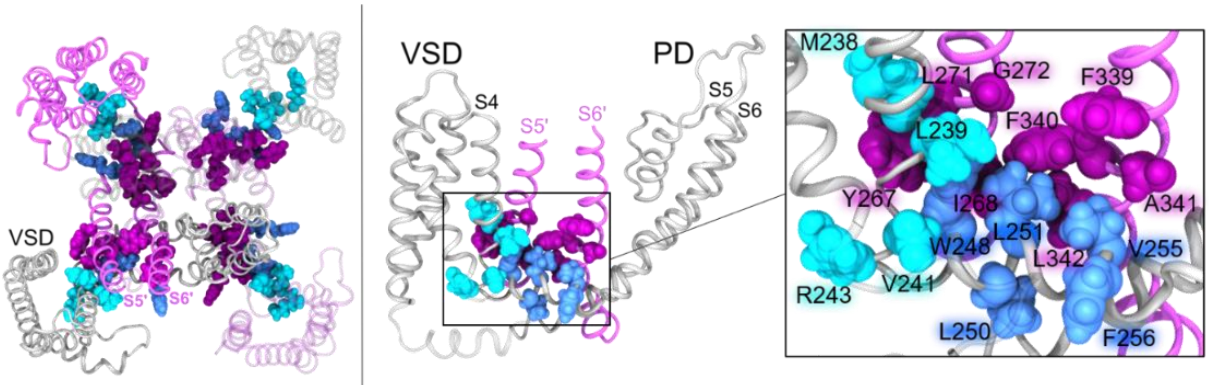

Figure III.2.1.6: Residues involved in $K_V7.1$ AO state coupling according to functional studies.
On each panel, the figure shows a cartoon representation of KV7.1 AO model at ~400ns of its MD trajectory, in a top view (left panel)and a lateral view (middle panel) which only shows two adjacent subunits (in solid gray and magenta) for clarity. These two subunits are also depicted in solid colors in the left panel. The right panel is an extended view of the middle panel, in which S4 residues are labeled and colored in cyan, S4-S5L residues in blue, and pore domain residues in purple.

To unravel the role played by these seventeen residues in the VSD-PD coupling mechanism, we analyzed their interactions throughout the trajectories obtained from K_V7.1 MD simulations. The results of this analysis shed light on several state dependent interactions, clustered in two distinct groups. The first group (Figure III.2.1.7) counts all the interactions that are specific of K_V7.1 AO model (Figure III.2.1.7, top), as none of these interactions are present in the RC, IO and AC models.

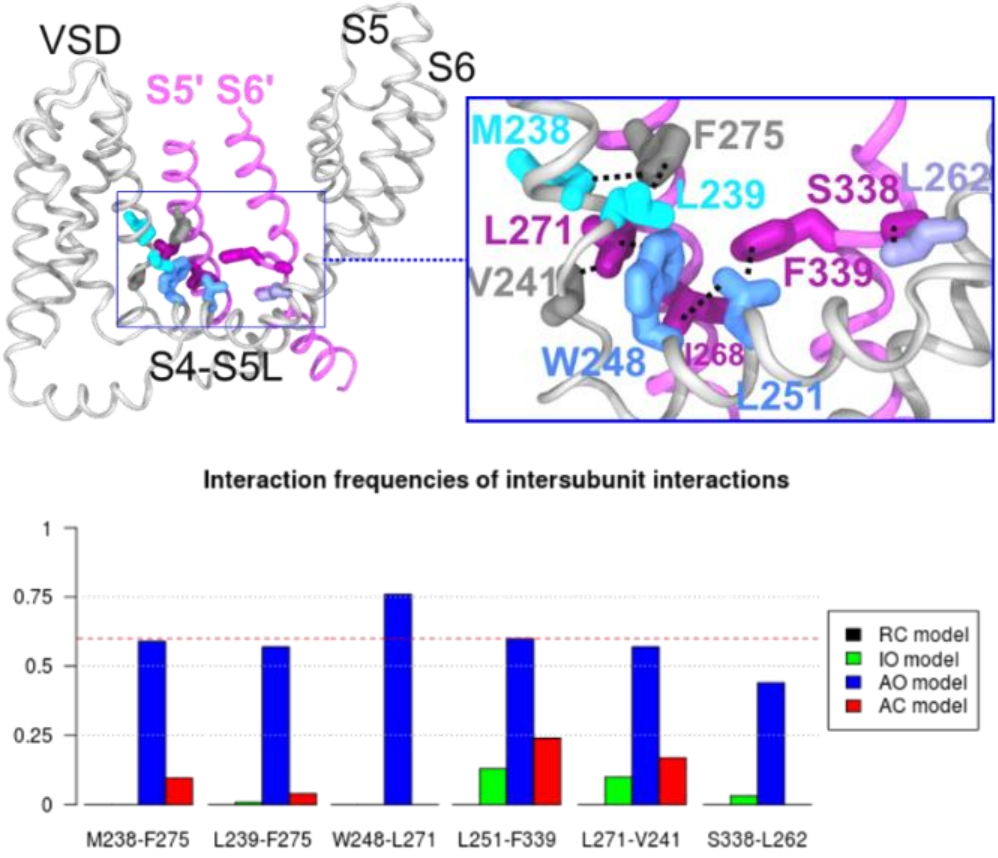

Figure III.2.1.7: MD simulation results show the crucial interactions for the K_V7.1 AO state coupling. The top panel shows cartoon representations of the AO state of K_V7.1. An entire subunit in the foreground (in gray) as well as S5 and S6 segments of an adjacent subunit (in purple) are shown with insets of enlarged structures of the boxed area. Residues in S4c are colored in cyan, S4-S5L in blue, and S5 and S6 segments from the adjacent subunit in purple. Residues V241 and F275, which are identified in MD simulations as possibly involved in sidechain interactions, but mutations do not alter AO states are colored in dark grey. Each pair of residues is represented by a black dashed line connecting their respective sidechains.
The bottom panel displays the interaction frequencies of AO model specific residue pairs including four S4c residues and thirteen S4-S5L and PD residues throughout the MD trajectories obtained for K_V7.1 RC, IO, AO, and AC models. The frequency threshold of 0.6 is marked by a red dashed line.

These interactions are present in the AO model MD trajectory with a frequency at least 40% higher than in MD trajectories of the remaining K_V7.1 models (Figure III.2.1.7, bottom). This constitutes a compelling proof that confirms these interactions are crucial for the K_V7.1 VSD-PD coupling when the VSD reaches its AO state.

Among the 10 residues involved in these interactions (Figure III.2.1.7), five (W248 L251 L271 S338 F339) are from Class2 residues, and two are located in S4c (M238 and L239). The last two residues, V241 and F275, located in the S4 and S5 segments, respectively, have been highlighted by MD simulations. In the K_V7.1's AO model, M238 is engaged in a Met-Arom interaction with F275 from S5, while the remaining S4 residues are engaged in VdW interactions with residues from the adjacent S5 segment. W248, L251 and L262 are engaged in interactions that appear to anchor the S4-$S5_L$ to its adjacent PD segments while the S4 segments are engaged in salt-bridges that stabilize its activated state. Specifically, the frequency obtained for the interaction between L251 and F339 supports the DMC results.

Overall, these results are in good agreement with experimental data. In addition, the structural models of the K_V7.1 channel we studied are providing a molecular insight of the residues whose crucial role in the AO's state VSD-PD coupling has been highlighted by the present functional study. Despite being identified as important for K_V7.1 coupling by our collaborators, it remains important to note that F275S mutant has been associated with a familial LQTS [330]. Similarly, the mutant V241G also has been reported to elicit LQTS [136].

The second group counts four residue pairs, involving W248 from S4-S5$_L$, as well as Y267 and L271 from S5 and L342 from S6 that engage in VdW interactions with I268 from S5, V133 from S1, L239 from S4, and L251 from an adjacent S4-S5$_L$, respectively (Figure III.2.1.8). These interactions are present with a frequency > to 0.6 in the IO model, but not in the AO model (Figure III.2.1.8, bottom). This indicates that these interactions might be important for the VSD-PD coupling in the K$_V$7.1's IO state (Figure III.2.1.8, top). However, their absence in the AO model suggest that the have to be broken (loosen) in order for the VSD-PD coupling to occur when the VSD reaches its activated state.

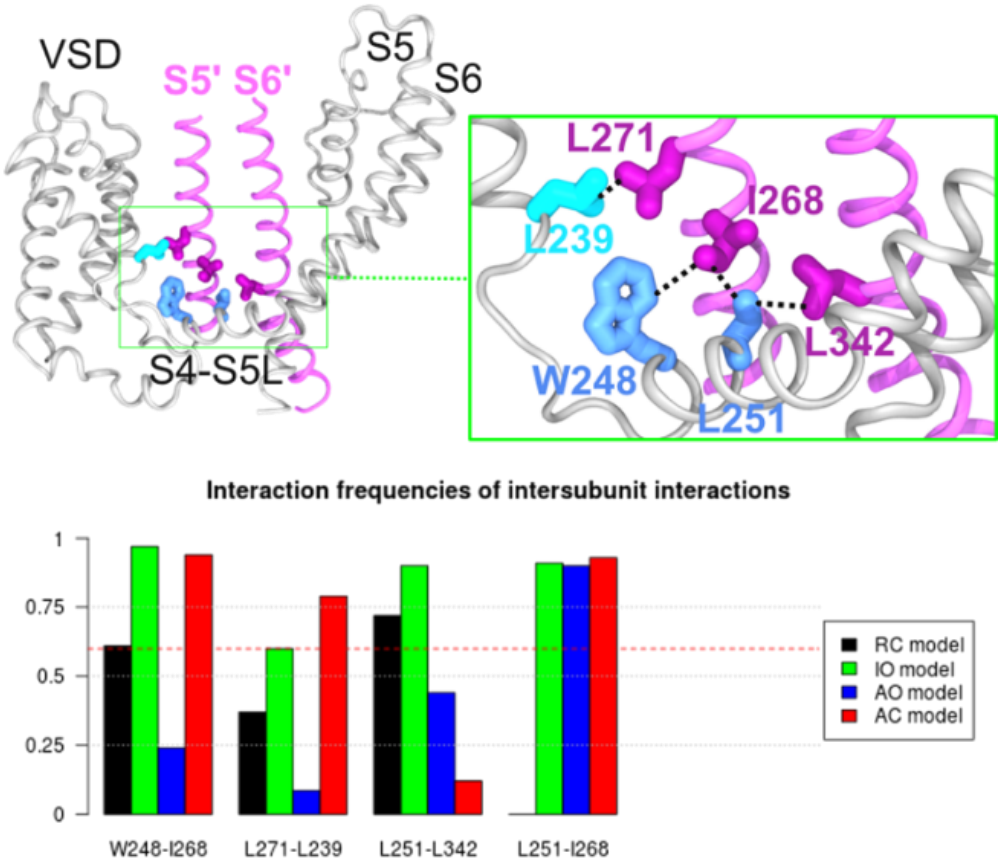

Figure III.2.1.8: MD simulation results shows the crucial interactions for K$_V$7.1 IO state coupling.
The top panel shows cartoon representations of the IO state of K$_V$7.1. An entire subunit in the foreground (in gray) as well as S5 and S6 segments of an adjacent subunit (in purple) are shown with insets of enlarged structures of the boxed area. The color code is similar as Figure III.2.1.7.
The bottom panel displays the interaction frequencies of IO model specific residue pairs including four S4c residues and thirteen S4-S5L and PD residues throughout the MD trajectories obtained for K$_V$7.1 RC, IO, AO, and AC models. L251 and I268 show high interaction frequencies in both IO and AO. The frequency threshold of 0.6 is marked by a red dashed line.

In a nutshell, our results show that these interactions are crucial for the K$_V$7.1 VSD-PD coupling when the VSD activates to the intermediate state. However, their absence in the activated models indicate that these interactions are lost when the VSD reaches its activated state.

Hence, these results confirm those obtained for the AO model, as residues L239 W248 L251 and L271 are involved in distinct interactions that stabilize K_V7.1 AO state specifically. Moreover, the interaction between L251 and L342 might rather depend on the activation state of the VSD, as L251 translates upwards to bind F339 in AO model. The W248-I268 and L271-L239 interactions are in good agreement with the results obtained from double mutant cycle analysis and indicate their participation in the IO state coupling of K_V7.1 channel.

In order to validate our MD results, we selected some of the residue pairs we identified as specific for the IO state and/or the AO state VSD-PD coupling of K_V7.1 and suggested they be submitted to double mutant cycle (DMC) experiments performed by our collaborators.

This site directed mutagenesis (DMC) method [331] aims at detecting protein-protein interactions by identifying the pairs of residues whose energetic contribution is coupled during a state transition, *e.g.* from close state to open state in the case of K_V7.1 channel. This method has been successfully used for the identification of protein-protein interfaces, the most known to date being the barnase-barstar interface [332]. This method has also allowed to identify specific interactions in K_V7.1 subunits [176, 315]. Considering a pair of residues noted 1 and 2 that are suspected to interact with each other during the activation of a given channel, the DMC approach consists in the calculation of pore opening free energy differences between three mutants. These mutants are obtained by mutating residue 1 and 2 separately, as well as creating a mutant in which both residues are mutated, prior to recording the free energies G_1, G_2 and $G_{1\to2}$ associated with the voltage-dependent activation of each mutant, respectively. Then, the free energy differences ΔG of each obtained mutant with respect to the free energy G_0 associated with the activation of the wild-type channel are calculated as follows:

$$\Delta G_1 = G_1 - G_0$$

$$\Delta G_2 = G_2 - G_0$$

$$\Delta G_{1\to2} = G_{1-2} - G_0$$

Finally, the net energy change ΔΔG between the single mutants ΔG_1 and ΔG_2, and the double mutant ΔG_{1-2} is calculated as follows:

$$\Delta\Delta G = (\Delta G_1 + \Delta G_2) - \Delta G_{1\to2}$$

Thus, a positive value of ΔΔG indicates that the residue pair forms significant interactions during the voltage-dependent activation of the channel. Ideally, the aim of DMC is to create combinations of mutants in which the resulting mutants are supposed to interact with each other in order to restore the conductance of the WT channel in relation with the conductance measured in the single mutants. Thus, one could conclude that the energy between the two considered residues is coupled with the free energy associated to the pore opening of the channel in our present case. Practically, this scenario rarely happens. Indeed, in order to completely restore the function of the WT channel, the two residues need to exclusively interact with each other during gating and with no other partners. However, the residue pairs we assessed mostly involve residues that interact with at least two partners in each of our models.

Hence, our collaborators established specific decision rules in order to identify the pairs of residues that interact during $K_V7.1$ channel gating. To do so, they proceeded as follows: for a pair of residues 1 and 2, they verify if the G/V curve of residue 1 (or residue 2) single mutant was similar as the G/V curve of the double mutant (Figure III.2.1.9, upper panel, left; lower panel). By doing so, they start from the premise that if residues 1 and 2 are actually interacting throughout the pore opening mechanism of $K_V7.1$, then the mutation of either residue 1 or 2 is sufficient to disrupt the interactions between these residues, and thereby alter gating. Therefore, if residues 1 and 2 are interacting during gating, then the values of ΔG_1 and ΔG_2 will not linearly sum up to the $\Delta G_{1\rightarrow 2}$, which will be expressed as:

$$\Delta G_{1\rightarrow 2} \neq \Delta G_1 + \Delta G_2$$

However, if residues 1 and 2 are not interacting during gating, then $\Delta G_{1\rightarrow 2}$ will linearly add as:

$$\Delta G_{1\rightarrow 2} \cong \Delta G_1 + \Delta G_2$$

This decision rule was also applied as it was suitable for the application of the DMC method using the single mutants that were already obtained from previous Alanine-scanning of PD residues [333], and Trp scanning of S4 residues [173]. To that extent, the original double mutant that was created in order to assess the interaction between F339 and L251 was F339S/L251A. Unfortunately, the obtained results were not exploitable. Hence, we took the joined decision to create the double mutant L251F/F339L instead. Indeed, this reversed-residue double mutant was engineered in agreement with the ideal DMC *scenario*, in which each single mutant would disrupt the voltage-dependence of pore opening, while the double mutant would restore the WT G/V curve, which was almost the case for that pair (Figure III.2.1.9). Among the seventeen residues which turned out to be crucial for the AO state VSD-PD coupling of Kv7.1, the DMC shed light on five pairs of residues whose ΔΔG value is positive. Three residue pairs indicate interactions between S4-S5$_L$ and PD segments (Figure III.2.1.9, upper panel, right): L251A/I268A (ΔΔG= 1.8 kcal/mol), W248A/I268A (ΔΔG= 1.4 kcal/mol) and L251F/F339L (ΔΔG= 2.7 kcal/mol). The last two pairs of residues indicate interactions between S4c and S5 segments: M238W/L271E (ΔΔG= 1.7 kcal/mol) and L239W/L271E (ΔΔG= 4.4 kcal/mol).

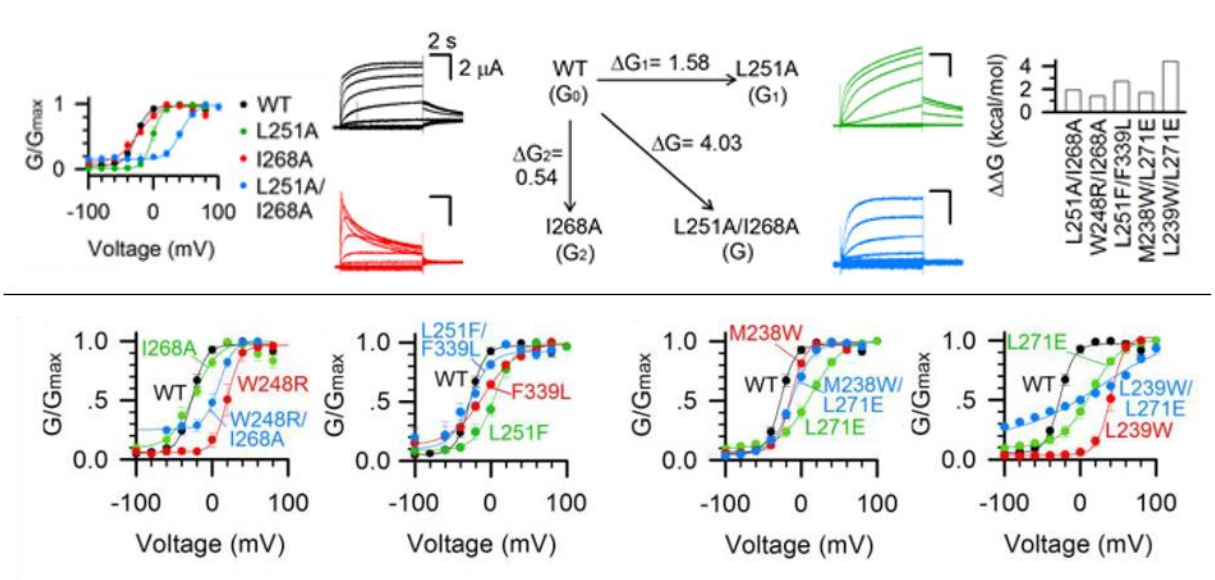

Figure III.2.1.9: Double mutant cycle analysis results obtained for K$_V$7.1 channel.
On the upper panel, the graph on the left displays the G/V curves obtained for the double mutant cycle (DMC) analysis of the inter-subunit interactions between L251 (S4-S5L) and I268 (S5). The ΔΔG= 1.91 kcal/mol. n ⩾3. The middle panel shows the voltage-clamp results obtained for each mutant engineered for the DMC analysis of L251-I268 interaction. The right panel summarizes the DMC analysis of the inter-subunit interactions between S4-S5L/pore interface: W248 and I268 (ΔΔG= 1.4 kcal/mol), L251 and I268 (ΔΔG= 1.9 kcal/mol), and L251 and F339 (ΔΔG= 2.7 kcal/mol), as well as the S4c/S5 interface: M238 and L271 (ΔΔG= 1.7 kcal/mol), and L239 and L271 (ΔΔG= 4.4 kcal/mol). n ⩾3.On the lower panel, the graphs display the G/V curves for the DMC analysis result of the following pairs (from left to right): W248/I268, L251/F339, M238/L271, L239/L271.

In summary, the VSD-PD coupling mechanism of $K_V7.1$ channel in the RC, IO and AO states is mediated by a cluster of 14 residues. It includes residues W248 R249 L250 L251 V254 V255 F256 H258 and R259 from S4-$S5_{LINKER}$, residues E261 L262 from S5 and residues I346 L347 and V355 from S6 (called hereafter PD cluster) which correspond to the predicted molecular determinants of $K_V7.1$ VSD-PD coupling in both IO and AO states, which have been functionally validated by our collaborators. More specifically, the PD cluster residues are spread in two opposite surfaces (Figure III.2.1.10). The first one is oriented toward the lipid bilayer and constitute the outer surface of the pocket. It is composed of four S4-$S5_{LINKER}$ residues: W248 R249 L251 and F256.

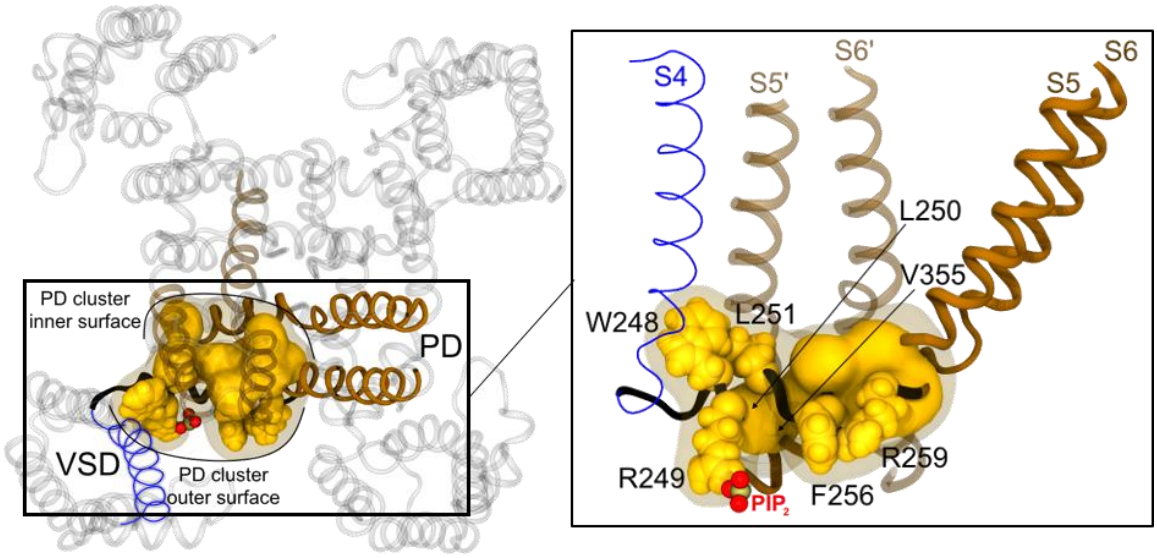

Figure III.2.1.10: Structural mapping of PD cluster residues in $K_V7.1$ 3D model
Cartoon representation of Kv7.1 channel in its AO state in extracellular view (left) and the lateral view of the framed region (right). On both panels, PIP_2 phosphate group is represented by red spheres. PD cluster outer surface residues are depicted in solid yellow spheres, while PD cluster inner surface residues are depicted in solid yellow surface. On the left panel, on one subunit, PD cluster residues are framed by a transparent yellow surface. S4 is colored in blue, S4-$S5_L$ in black, S5 and S6 in solid brown, while the segments S5' and S6' of the adjacent subunit are colored in transparent brown.

Among these residues, W248 and L251 are involved in state dependent interactions, including intersubunit ones with adjacent PD segments and intrasubunit ones with S4 segment.

The second PD cluster surface is facing the conduction pathway of the channel, and thereby constitutes the inner surface. It counts a total of eight residues that are engaged in two types of state-independent interactions: An electrostatic interaction between H258 and E261, (Figure III.2.1.5, bottom) along with VdW interactions between residues V254 V255 H258 from S4-S5$_{LINKER}$, and residues L347, L262 and I346, respectively (Figure III.2.1.4, bottom). In addition, in the PD cluster inner surface, the frequencies between aliphatic residues L250 and V355 are above 0.7 in the MD trajectories obtained for K_V7.1 RC, IO and AO models, suggesting that these residues are also involved in state independent VdW interactions (Figure III.2.1.11). These results also suggest that S4-S5$_{LINKER}$ motion drags the cytoplasmic region of S6 helices during both RC-IO and IO-AO transitions, and therefore induce the spreading of S6 helices away from the pore axis during pore opening. Interestingly, the structural validation of K_V7.1 MD trajectories suggests that PD cluster outer surface has three residues that are also involved in state independent interactions (Figure III.2.1.11): R249 interacts with PIP_2 (intra) with a frequency higher than 0.95 in every K_V7.1 native state model through a salt-bridge interaction.

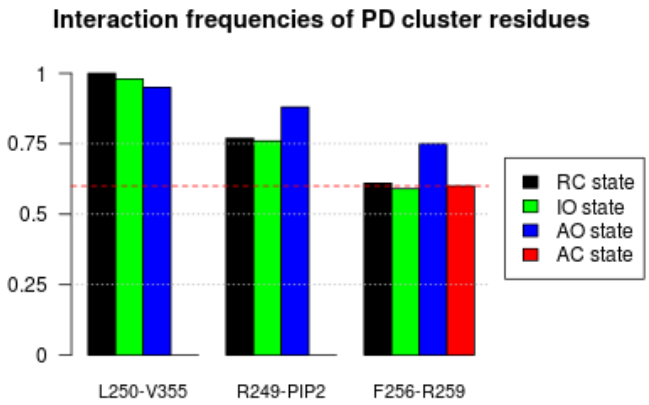

Figure III.2.1.11: State-independent interactions of PD cluster residues in K_V7.1 models.
The barplots display the frequencies of the intrasubunit interactions involving PD cluster residues throughout the MD trajectories obtained for K_V7.1 RC (black), IO (green), AO (blue), and AC (red) models. The threshold value, set at 0.6, is represented by a red dashed line.

The aromatic ring center of F256 is located close to the guanidinium carbon of R259 sidechain, allowing these residues to be engaged in a cation-π interaction, with frequencies higher than 0.6 in all models. Meanwhile, the remaining outer surface residues W248 and L251 are acting as hydrophobic hooks that allow PD cluster to be anchored in the PD of adjacent subunits as well as in the VSD of its own subunit, in a state dependent manner.

Indeed, W248, bound to the bottom of adjacent S5 in the RC model, goes upwards along S5 to reach S4 in IO and AO models; L251, bound to the bottom of adjacent S6 in the RC model, moves up along S6 to reach S5 in the IO and AO models (Figure III.2.1.12).

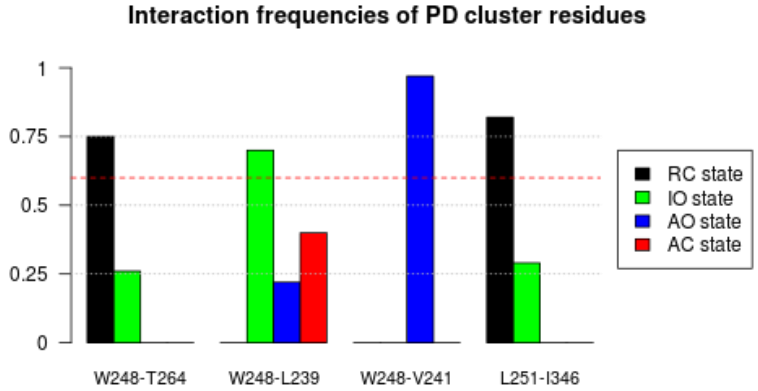

Figure III.2.1.12: State-dependent interactions of PD cluster hook residues in K_V7.1 models.
The barplots display the frequencies of the intersubunit interactions involving PD cluster residues W248 and L251 throughout the MD trajectories obtained for K_V7.1 RC, IO, AO and AC models. The color code used is similar as in Fig III.2.1.10. The frequency threshold of 0.6 is marked by a red dashed line.

In the RC model (Figure III.2.1.13, A), the benzene ring center of the W248 indole group is engaged in VdW interactions with the methyl group of T264 from S5 with a frequency of 0.75. The terminal methyl groups of L251 are maintained between the sidechains of both L342 (Figure III.2.1.8, lower panel) and I346 (Figure III.2.1.12) from S6 via VdW interactions, with frequencies of 0.7 and 0.8, respectively. In the IO model (Figure III.2.1.13, B), the benzene ring center of W248 is interacting with the terminal methyl groups of L239 from S4 (Figure III.2.1.12) and I268 from an adjacent subunit (Figure III.2.1.8), while those of L251 are trapped between S5 and S6 segments through VdW interactions with I268 from S5 and L342 from S6 (Figure III.2.1.8). These suggests that during RC-IO transition, the S4-$S5_{LINKER}$ has risen up along its adjacent S5 and S6 segments and has rotated anticlockwise towards its own VSD, allowing the linker to reach the bottom of S4. In the AO model (Figure III.2.1.13, C), the sidechain of W248 is engaged in a set of VdW interactions between V241 from S4 and L271 from S5 of an adjacent subunit.

The other hook residue L251 still has its terminal methyl groups anchored between S5 and S6, but it has slightly translated upwards to engage in VdW interactions with F339 from S6 and I268 from S5. The interactions of both W248 and L251 in the K_V7.1 AO model suggest that the PD cluster hook residues are facing S4 residues located deeper in the membrane during the IO-AO transition.

This may be due to the upward movement of S4 segment during the IO-AO transition. The PD cluster has risen for a second time along its adjacent S5 and S6 segments while still bound to S4 of its own subunit, leaving space for S6 cytoplasmic region to spread away from the pore axis toward the inner membrane surface. The state-dependent interactions of the PD cluster hook residues suggest that the S4-S5$_{LINKER}$ undergoes subsequent upward translations (Figure III.2.1.13, A-B, black arrows) and clockwise rotations (Figure III.2.1.13, A-B, yellow arrows) of the PD cluster hook residues during the K_V7.1 transitions from RC to IO model, then to the AO model. This mechanism appears to be induced by the motion of S4 upon the VSD's activation, which is also characterized by subsequent upward translations normal to the bilayer, as well as subsequent clockwise rotations.

This S4 motion pulls the S4-S5$_{LINKER}$ from the bottom of adjacent S5 and S6 segments in RC state to reach the middle of these segments and the bottom of S4 of its own subunit in the IO and AO states. Moreover, the intersubunit VdW interaction between L251 and I346 suggest that the latter might be crucial not only for the VSD-PD coupling (as shown in the previous section), but also for the stabilization of the relative position of S4-S5$_L$ with respect to S6c when the VSD is in its resting state (Figure III.2.1.3, left). This relative position might be crucial for the initiation of K_V7.1 VSD-PD coupling upon resting-intermediate VSD transition. As a consequence, the loss of the I346-L251 interaction induced by the I346A mutation might lead to a loss of function of K_V7.1, characterized by an inability of VSD activation in response to membrane depolarization (for I346A).

Noteworthy, the K_V7.1 AC model, which represents the K_V7.1 tetramer with an activated VSD and a closed PD, led us to identify possible molecular determinants of the VSD-PD coupling in the AO state. Hence, we have measured the interaction frequencies between the pairs of residues that specifically interact in the K_V7.1 AO model. The interactions of PD cluster hook residues indicate that S4-S5$_L$ is more buried in the membrane, as the pore is in its closed state (Figure III.2.1.7-8, bottom).

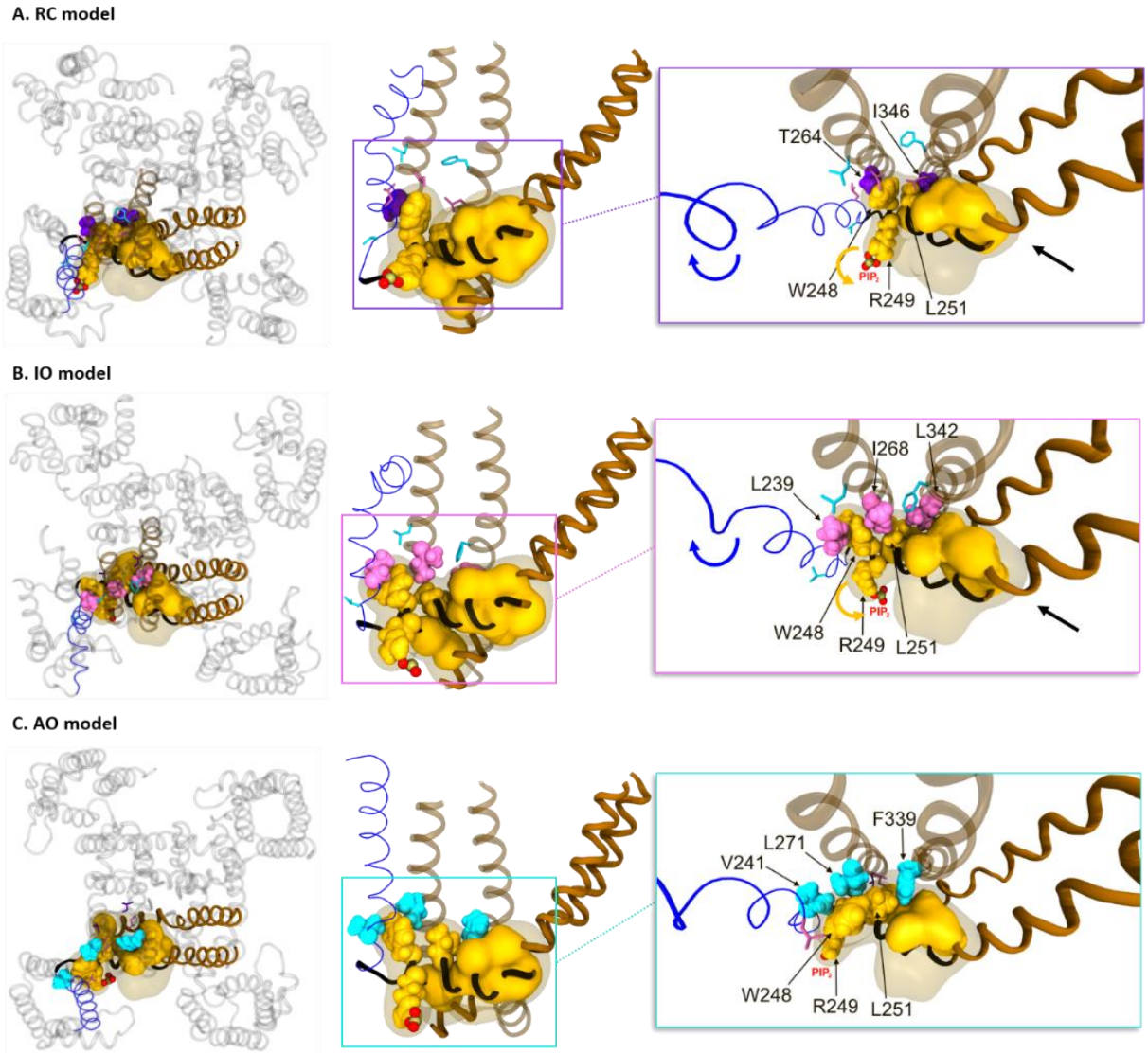

Figure III.2.1. 13: State dependent VSD-PD coupling interfaces in $K_V7.1$ models.
Each panel shows a cartoon representation of PD cluster residues in top view (left), lateral view (middle) and zoomed view (right) of **A.** RC model, **B.** IO model and **C.** AO model of $K_V7.1$. The color code used for transmembrane segments is similar as in Figure III.2.1.10. In all panels, the entire PD cluster is depicted in transparent yellow surface, and PIP_2 phosphate groups in red spheres. Hook residues W248, R249, L251 and PD cluster inner surface residues are represented in solid yellow spheres and surface, respectively. In each panel, residues which interact with PD cluster are represented in spheres, while those which do not are represented in sticks. The residues which interact with PD cluster in **A.** RC models are purple-colored, while those which interact in **B.** IO model are pink-colored, and those which interact in **C.** AO models are cyan-colored. Rotational motions of S4, and PD cluster residues W248, R249, L251 are represented by blue, and yellow arrows, respectively. Translational movement of PD cluster is represented by a black arrow.

Among the hook residues, L251 interactions are modified with respect to the K_V7.1 AO model. Its interaction with I268 is still present with a frequency of 0.9, but its interaction with F339 is lost (frequency ~ 0.2). However, those of W248 are modified: interactions with both V241 and L271 are lost, as their interaction frequencies are 0 and 0.2, respectively. Instead, W248 interacts with I268 from an adjacent S5, with a frequency of 0.8, as observed in the K_V7.1 IO model. These interactions suggest that W248-V241 and W248-L271 are crucial to induce pore opening when the VSD is in its activated state. The presence of these interactions in the AO models is probably due to the presence of PIP_2 intra, which ensures the VSD-PD coupling by forming a bridge between the S2-$S3_{LOOP}$ and the S4-$S5_{LINKER}$ in the AO state (Tab III.1.2.2). Regarding the inner surface residues of the PD cluster, the electrostatic interaction between H258 and E261 is absent in the K_V7.1 AC model. This interaction might also be crucial for the coupling since it seems to maintain the angle between S4-$S5_L$ and S5 in all K_V7.1 states except the non-native AC one. Therefore, a mutation of E261 into a Lysine might maintain its interaction with H258 through a cation-π interaction [334]. However, considering the length of a Lysine side chain, which is longer than the one of a Glutamate, the angle between S4-S5L and S5 induced by E261-H258 interaction might not be conserved. The loss of this crucial structural aspect of K_V7.1 might explain the phenotype of E261K mutation, characterized by the inability of the channel to be addressed to the membrane.

Moreover, according to the pore radii calculations, the conduction pathway of the K_V7.1's AC model also turned out to be the most constricted among the K_V7.1 models (Figure III.1.3.4). The resulting MD trajectory allowed to determine the molecular determinants of VSD-PD coupling of K_V7.1 channel in its AO state. This mechanism depends not only on the presence of PIP_2, but also on an effective communication between PD cluster residues and both S4 and adjacent S5 to stabilize the position of S4-$S5_{LINKER}$ allowing for the pore to open. Both the computational and the experimental results indicate hence an interface of state independent intrasubunit interactions between S4-S5L and S6c, along with a second interface of state dependent intersubunit interactions between S4, S4-S5L and the PD segments. The MD simulations allowed for the identification of residues from both interfaces, as well as the state-dependent and state-independent interactions among them in the four K_V7.1 models.

Thanks to these interfaces, we manage to predict a model of VSD-PD coupling mechanism for $K_V7.1$ channel when the VSD reaches its intermediate and activated states. We conceptualize the results of this integrative study into a "hand-and-elbow" gating mechanism for voltage-dependent activation of the $K_V7.1$ channel (Figure III.2.1.14). In this model, the S4 segment and the PD cluster residues are depicted as a bent arm. During membrane depolarization, S4 (upper arm) moves upwards in two resolvable steps, first to the intermediate state and then to the activated state. These sequential movements engage distinct VSD-PD coupling interactions to the pore through distinct mechanisms.

(i) During the transition from the resting to the intermediate state, the upper arm (S4) translational and rotational movement triggers the hand (S4-$S5_L$ C-terminus residues H258 and L262) which grips S6c (residues I346 and L347) of the same subunit through VdW interactions, while the elbow (PIP_2 and PD cluster hook residues W248 R249 and L251) releases the bottom regions of both S5 and S6 in the pore and nudges their middle region as well as S4c through an anticlockwise rotation to promote channel opening at the IO state.

(ii) Subsequently, the VSD transition into the activated state involves a second upward motion of the upper arm, dragging the hand further from the pore axis, while the elbow undergo a slight upward movement to be engaged in direct interactions with the S4 of its own subunit as well as the S5 and S6 of a neighboring subunit to nudge the pore open at the AO state.

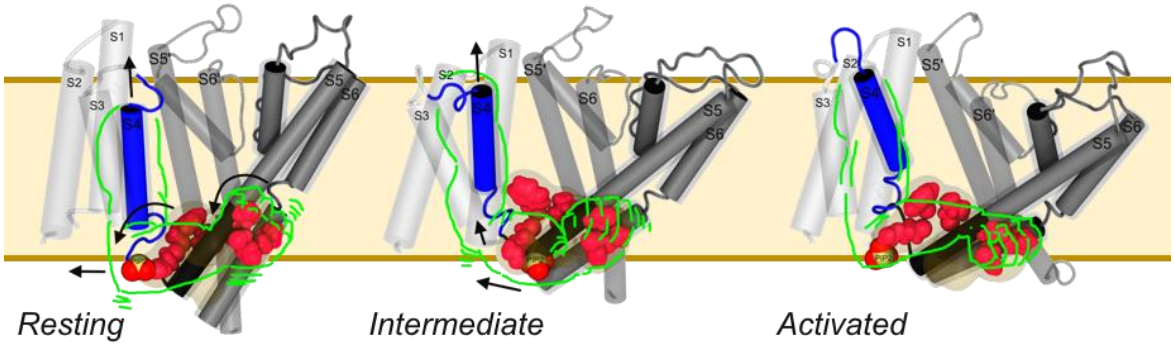

Figure III.2.1.14: Hand-and-elbow model for $K_V7.1$ state-dependent VSD-PD coupling mechanism. This figure shows a cartoon representation of $K_V7.1$ transmembrane segments, including one entire subunit on the foreground with the VSD (transparent light gray) S4 (blue), S4-S5L (black) and PD segments (solid gray) along with the PD segments of an adjacent subunit (transparent gray). The "elbow" residues W248 R249 L251 and the "hand" residues H258 L262 I346 L347 are depicted in pink spheres. PIP_2 phosphate groups, in state independent interaction with the elbow (R249) is shown in red spheres. The entire arm that models the whole conformational changes is drawn in green. The motions of both the elbow and the arm during RC-IO and IO-AO transitions are depicted by black arrows.

Chapter III.2.2. Molecular determinants of the modulation of $K_V7.1$ VSD-PD coupling mechanism by KCNE1 ancillary subunits: Protein-protein interactions involved in VSD-PD coupling

The structural validation of the protein-lipid interactions in the IK_S models shed light on the fact that the set of conserved basic residues of KCNE1 C_{TERM} domain undergo a rotational movement during VSD activation, as described by its state-dependent electrostatic interactions with PIP_2 in two distinct binding sites (Chapter III.1.2). Here we investigated the hydrophobic interactions in which KCNE1 residues are involved with the $K_V7.1$ ones. These interactions allowed us to predict how they might induce the conformational changes in $K_V7.1$ subunits that can explain the conductivity results obtained for each state of $K_V7.1$, both in presence and absence of KCNE1 [161, 168]. Considering the conclusions drawn from the structural validation of the IK_S models in Chapter III.1, we conducted this study on the MD trajectories obtained with IK_S models in $8PIP_2$ system. To investigate the modulation of $K_V7.1$ VSD-PD coupling by KCNE1, we focused on the residues from S4-$S5_{LINKER}$, S5, S6 and KCNE1 residues, and we monitored the distance to their closest residues (within a 5 Å radius) every 2 ns over MD trajectories.

In the previous chapter we mentioned numerous experimental studies that pointed out that KCNE1 modulates the structure and the function of the $K_V7.1$ subunits. More specifically, the presence of KCNE1 reduces drastically the ionic conductance of the $K_V7.1$ channel in the RC and IO states, but increases it when the $K_V7.1$ VSD is in its activated state. We used this experimental data, as well as our previous findings on the $K_V7.1$ coupling mechanism and state dependent hydrophobic gate to investigate how KCNE1 interacts with $K_V7.1$subunits in the IK_S models, allowing for the modification of $K_V7.1$ channel VSD-PD coupling mechanism. First, we monitored the state-independent intrasubunit interactions, as well as the state-dependent intersubunit interactions highlighted by the integrative study we conducted on $K_V7.1$ models and presented in the previous section.

The MD trajectories obtained for the $K_V7.1$ models shed light on a cluster of residues in the pore domain, called the PD cluster. It is composed of 13 residues from S4-$S5_{LINKER}$, S5 and S6 which overlap the predicted molecular determinants of $K_V7.1$ VSD-PD coupling in both IO and AO states, which have been functionally validated by our collaborators (see Chapter III.2.1). Here we assessed the interactions of PD cluster residues in the MD trajectories of the IK_S models.

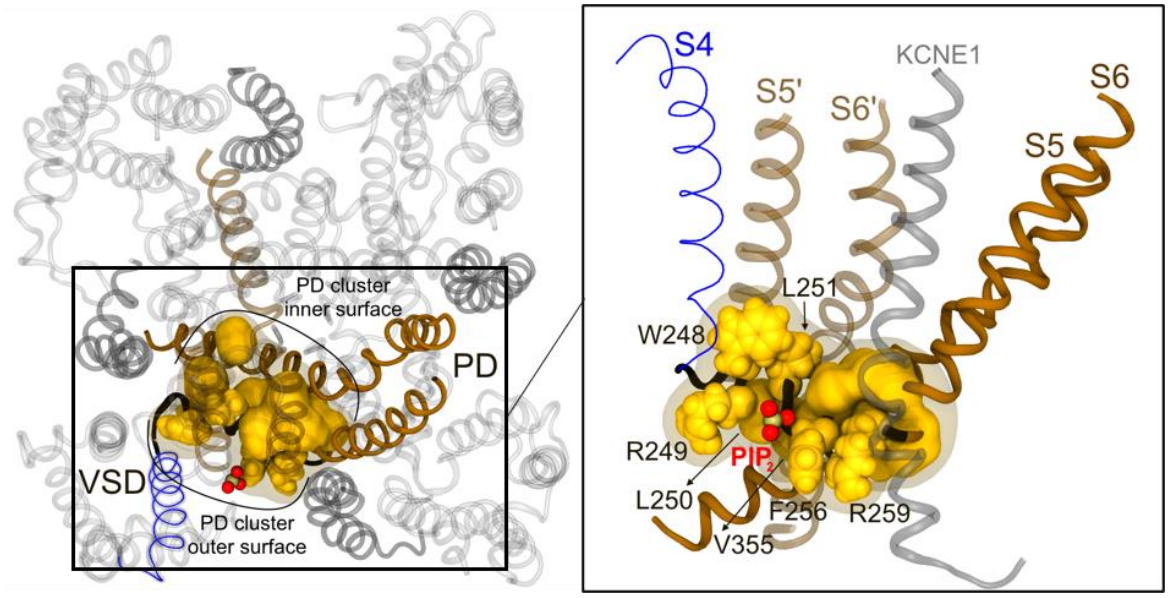

Figure III.2.2.1: Structural mapping of PD cluster residues in IK_S AO state model
Cartoon representation of Kv7.1 channel in its AO state in extracellular view (left) and the lateral view of the framed region (right). KCNE1 subunits are colored in dark grey. On both panels, PIP_2 phosphate group is represented by red spheres. PD cluster outer surface residues are depicted in solid yellow spheres, while PD cluster inner surface residues are depicted in solid yellow surface. On the left panel, on one subunit, PD cluster residues are framed by a transparent yellow surface. S4 is colored in blue, S4-$S5_L$ in black, S5 and S6 in solid brown, while the segments S5' and S6' of the adjacent subunit are colored in transparent brown.

The results we obtained suggest that the KCNE1 subunits induce a modification of state-dependent interactions between PD cluster outer surface residues and the rest of the channel. To that extent, we conducted additional analyses to identify among $K_V7.1$-KCNE1 interactions those which might explain how KCNE1 subunits can modify the PD cluster interactions. Indeed, the state independent interactions in which PD cluster outer surface residues R249, F256 and R259 (Figure III.2.2.1) are involved in the $K_V7.1$ models are impaired.

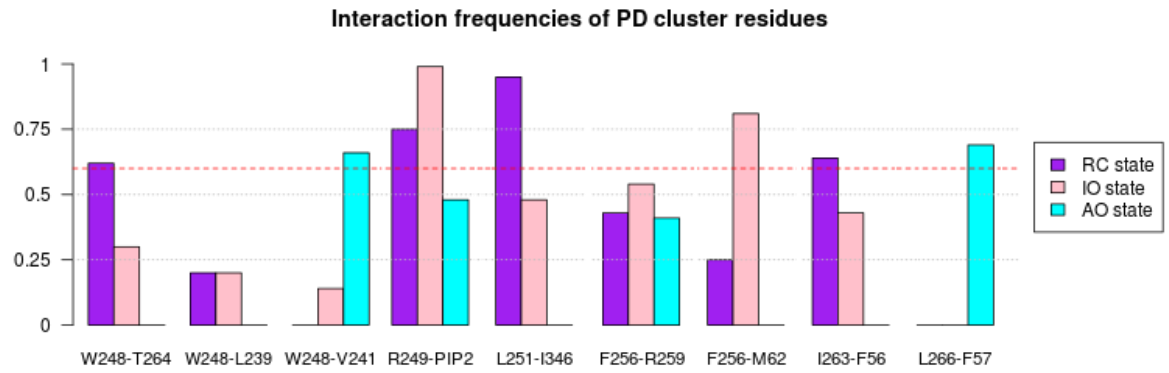

Figure III.2.2.2: Interactions of PD cluster outer surface residues in IK_S models.
The barplots display the frequencies of the interactions involving PD cluster residues and KCNE1 TMD residues throughout the MD trajectories obtained for IK_S RC (purple), IC (pink), and AO (cyan) models. The threshold value, set at 0.6, is represented by a red dashed line. All interactions are intrasubunit, except for the one between L251 and I346 and those involving KCNE1 residues, which are intersubunit. The frequency threshold of 0.6 is marked by a red dashed line.

While R249 still interacts with PIP_2 through a salt-bridge interaction with a frequency higher than 0.8 in the IK_S RC and IC models (Figure III.2.2.2), this frequency is only 0.4 in the IK_S AO model, which indicates that the R249-PIP_2 interaction is either unstable or present in less than three subunits out of four throughout the IK_S MD trajectories. F256-R259 interaction is merely present in all IK_S models compared with the $K_V7.1$ models. The aromatic ring center of F256 is not close enough to the guanidinium group of the R259 sidechain to engage in a cation-π interaction. The PD cluster hook residues W248 and L251 also present different set of interactions in the IK_S models. In the RC model (Figure III.2.2.2), W248 is trapped between T264 and I268 with frequencies of 0.6, indicating that W248 is less buried in the membrane in the IK_S RC model than in the $K_V7.1$ RC model. The L251 interactions remain unchanged in the IK_S RC model with respect to $K_V7.1$, as its methyl groups are bound to those of L342 and I346 with frequencies of 0.8 and 0.9, respectively.

Altogether, these interactions between the hook residues and the adjacent PD segments show that the PD cluster residues are slightly less buried into the membrane. In the IK_S IC model, the PD cluster hook residues are not binding S4, as the interaction frequency between W248 and L239 has dropped to 0.2. This interaction is impaired since W248 are located two far away from L239 in the IC model. Instead, the W248 aromatic ring remains bound to the I268 methyl groups, at a frequency of 0.6. L251 sidechain leaves I346 to bind I268 as well, at a frequency of 0.9. In the AO model, W248 has finally reached S4, as its aromatic ring center is engaged in VdW interactions with methyl groups of both V241 from S4 and L271 from S5, with frequencies of 0.6 and 0.7, respectively. Meanwhile, L251 side chains remain bound to both I268 from S5 and L342 from S6, with frequencies of 1 and 0.8, respectively. Besides the interactions involving the PD cluster inner surface residues, we also assessed in the MD trajectories obtained for our IK_S models, the intrasubunit interactions involving residues that were identified as important for $K_V7.1$ IO state, as well as the intersubunit interactions which turned out to be specific for $K_V7.1$ IO model and the ones specific for $K_V7.1$ AO models.

In the IK_S models, the results we obtained for the state-independent interactions involving $K_V7.1$ S4-S5L and S6 residues have lost their state-independence in IK_S models (Figure III.2.2.3, A). Indeed, in the RC model, the interactions involving S5 residues E261, L262 and T265 are impaired, which might explain how the current usually observed in $K_V7.1$ E1R/R1E (which mimics the resting state) is suppressed in presence of KCNE1.

Analyses of the PD cluster residues in our IK_S models also show that the state-independent intrasubunit interactions involving inner surface residues are slightly modified in the RC and AO models with respect to the Kv7.1 models (Figure III.2.2.3, B). Indeed, in the RC model, S5 residues E261 and L262 are not interacting with the rest of the PD cluster residues. As a result, V255 is bound to L342 from an adjacent S6 segment instead of L262, with a frequency of 0.9, and P343 does not interact with T265. This S5-S6 interaction might be impaired by the aromatic ring center of residue F56 from KCNE1 TMD, which interacts with residue I263 from S5 segment through a VdW interaction at a frequency of 0.6 (Figure III.2.2.2). Considering the position of I263, next to the PD cluster inner surface residues E261 and L262, one can assume this additional interaction with KCNE1 might modify the shape of PD cluster, leading it to engage in an intersubunit interaction with an adjacent S6. These observed modifications with respect to the $K_V7.1$ models in the IK_S RC state, in which S5 residues are split off from the PD cluster, may allow for a deeper burying of S4-S5 linker in the bilayer, and thereby for a narrower pore, as shown in the radii calculations of the RC models (Figure III.1.3.3).

In the IK_S IC model, the $K_V7.1$ IO state specific interactions are conserved in IK_S IC state, which indicates that KCNE1 is not inhibiting VSD-PD coupling through the impairment of these interactions (Figure III.2.2.3, C). Nevertheless, the PD cluster inner surface is finally reassembled in IK_S IC model, as $S4\text{-}S5_{LINKER}$ may have undergone an upward movement upon RC-IC transition of $K_V7.1$ subunits. As a consequence, S5 residues E261 and L262 are bound to the inner surface of PD cluster, but V255 still interacts with adjacent L342 with a frequency of 0.6. This interaction might prevent the PD cluster to reach S4 as in $K_V7.1$ IO model, as it remains bound to an adjacent subunit. In addition, the aromatic ring center of residue F256 from the outer surface of the PD cluster is engaged in a Met-Arom interaction with the sulfur atom of M62 from KCNE1, with a frequency of 0.8 (Figure III.2.2.2). Met-Arom interactions are known to be in the same energetic range as salt-bridges interactions [308], so one can predict that this interaction might disrupt the motion of $S4\text{-}S5_{LINKER}$ during RC-IC transition.

In the IK_S AO model, the $K_V7.1$ AO state specific interactions are mostly present, except for those that involve the S6 SFF motif residues S338 and F339 (Figure III.2.2.3, D). Indeed, S338 and F339 do not interact with L262 and L251, respectively. Instead, L251 remains bound to L342 with a frequency of 0.8 (Figure III.2.2.3, C). This discrepancy may be due to the additional interaction between the KCNE1 TMD and the middle region of S5. Indeed, the VdW interactions between F54 from KCNE1 and L266 from S5 (Figure III.2.2.2) is present at a frequency of 0.7. This interaction might pull the S4-S5L/S5 region away from the pore axis, and farther from its adjacent S6 segments. Furthermore, the PD cluster inner surface is slightly modified (Figure III.2.2.1, left panel). The terminal methyl groups of L250 sidechains interact with both the aromatic ring center of F351 and the methyl groups of V355 with frequencies of 0.9 and 0.75, respectively (Figure III.2.2.3,B). Since F351 is located above V355 along S6 and considering the relative position of $S4\text{-}S5_{LINKER}$ with respect to the membrane in $K_V7.1$ activated state, this interaction indicates that the cytoplasmic region of S6 segments is closer to the inner membrane surface in presence of KCNE1.

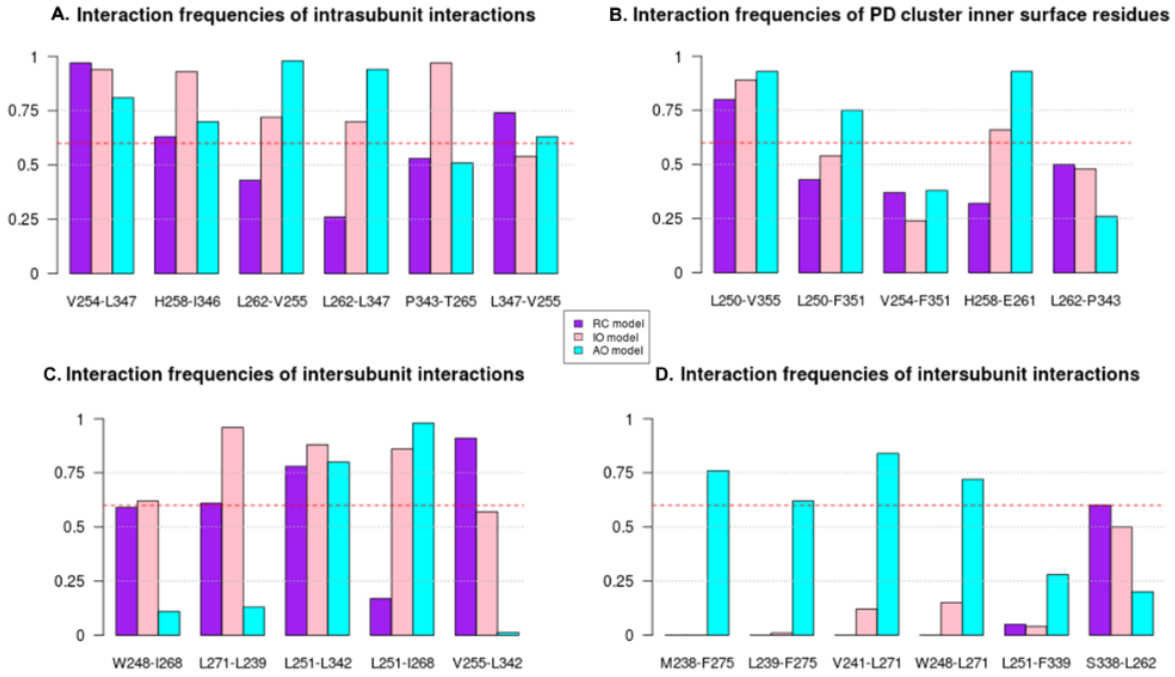

Figure III.2.2.3: Interactions of $K_V7.1$ VSD-PD coupling and PD cluster inner surface in IK_S models. Each panel depicts the barplots of the interaction frequencies throughout IK_S MD trajectories of RC (purple), IC (pink) and AO (cyan) models. **A.** State-independent S4-S5/S6 interactions. **B.** Interactions of PD cluster inner surface residues. **C.** $K_V7.1$IO state specific interactions. **D.** $K_V7.1$ AO state specific interactions. In all panels, the frequency threshold of 0.6 is marked by a red dashed line.

Overall, the K_V7.1-KCNE1 state-dependent interactions we found in our IK_S models suggest consecutive clockwise rotations of the ancillary subunit during the VSD activation of IK_S (Figure III.2.2.4). These motions appear to induce a modification of state dependent interactions involving the PD outer surface residues. In the IK_S RC model (Figure III.2.2.4, A), the presence of KCNE1 turned out to stabilize the position of the PD cluster residues along its adjacent PD segments. In the IK_S IC model (Figure III.2.2.4, B), the presence of KCNE1 appeared to prevent the translation of S4-$S5_{LINKER}$ from its adjacent PD segments towards S4 segment of its own subunit, which may prevent pore opening as well, as shown in the IC model pore radii values. In the IK_S AO model (Figure III.2.2.4, C), the S4-$S5_{LINKER}$ appears to be eventually anchored to the bottom of S4, while KCNE1 binds the middle of the S5 segment to stabilize the open state of the PD. These interactions indicate that KCNE1 pulls S5 away from the pore axis, in the same direction as the S4-$S5_{LINKER}$ translational motion upon VSD activation (Figure III.2.2.4, C, right panel).

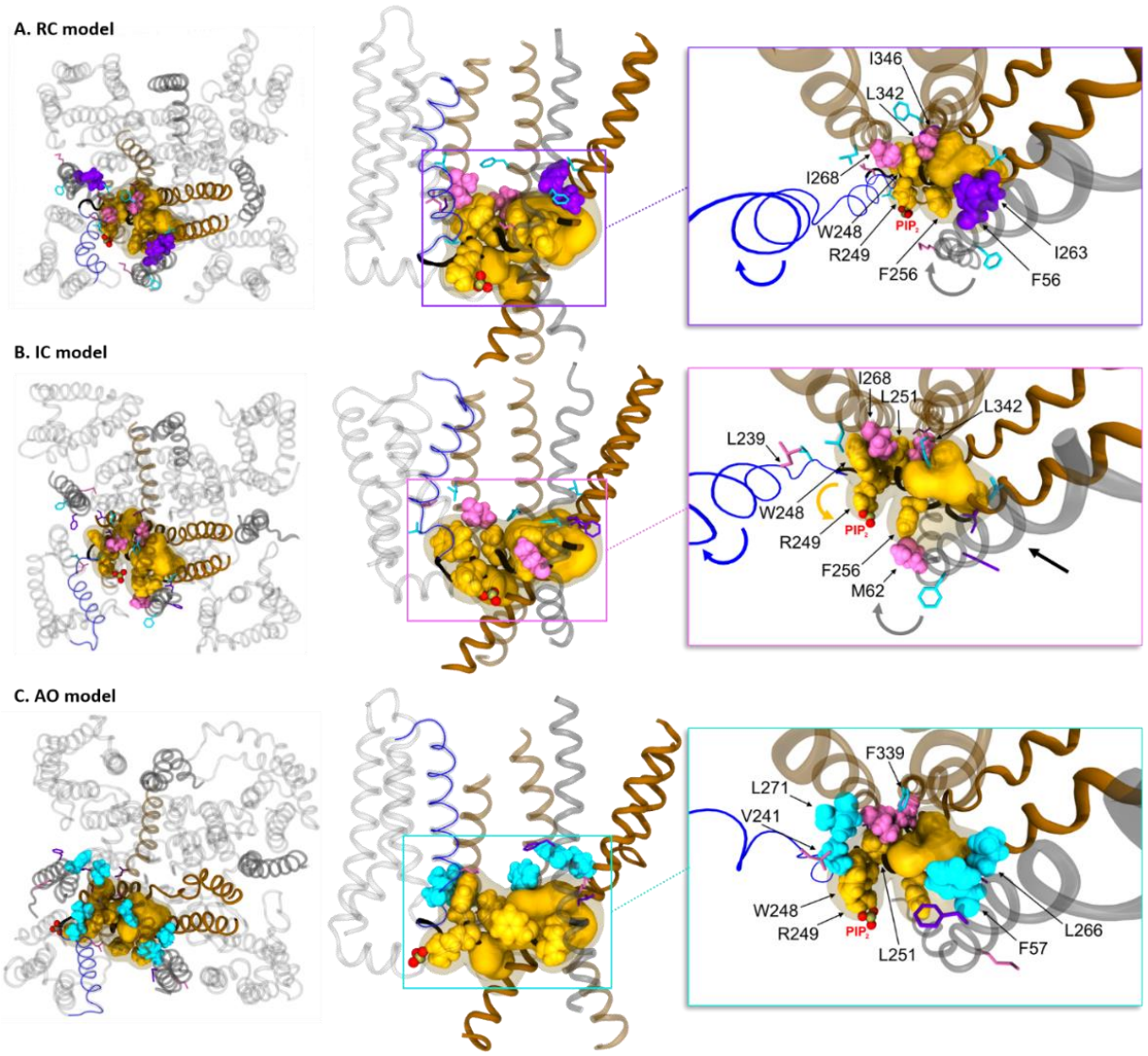

Figure III.2.2.4: State dependent VSD-PD coupling interfaces in IK_S models.
Each panel shows a cartoon representation of PD cluster residues in top view (left), lateral view (middle) and zoomed view (right) of A. RC model, B. IC model and C. AO model of IK_S. The representations and the color code used for transmembrane segments, PIP_2 phosphate groups, the entire PD cluster , hook residues W248, R249, L251 and PD cluster inner surface residues is similar as in Figure III.2.1.14. In each panel, residues which interact with PD cluster are represented in spheres, while those which do not are depicted in sticks. Rotational motions of S4, KCNE1 and PD cluster residues W248, R249, L251 are represented by blue, gray, and yellow arrows, respectively. Translational movement of PD cluster is represented by a black arrow.

Consequently, the KCNE1 subunits act as Velcro strip in the "hand-and-elbow" model we predicted for the VSD-PD coupling mechanism of the $K_V7.1$ subunits (Figure III.2.2.5).

(i) During the VSD's activation from the resting to intermediate state, the rotation of KCNE1 places its lower Velcro strip (located on the KCNE1 M62 residue) in front of F256, located on the outer surface of the $K_V7.1$ PD cluster, blocking the rotation of the elbow and the hand, as well as its translation along the inner membrane surface that promote pore opening.

(ii) During the VSD transition into the activated state, the second clockwise rotation of KCNE1 releases the lower Velcro strip, allowing for the elbow and the hand to rotate counterclockwise to reach both S4c and adjacent PD segments and promote channel opening. The rotation of KCNE1 places another Velcro strip (located on KCNE1 residue F57) in front of L266 on S5. These strips are assumed to pull PD segments farther from the pore axis than in $K_V7.1$ AO state, which can explain the pore radii differences observed between $K_V7.1$ and IK_S AO models (Figure III.1.3.1).

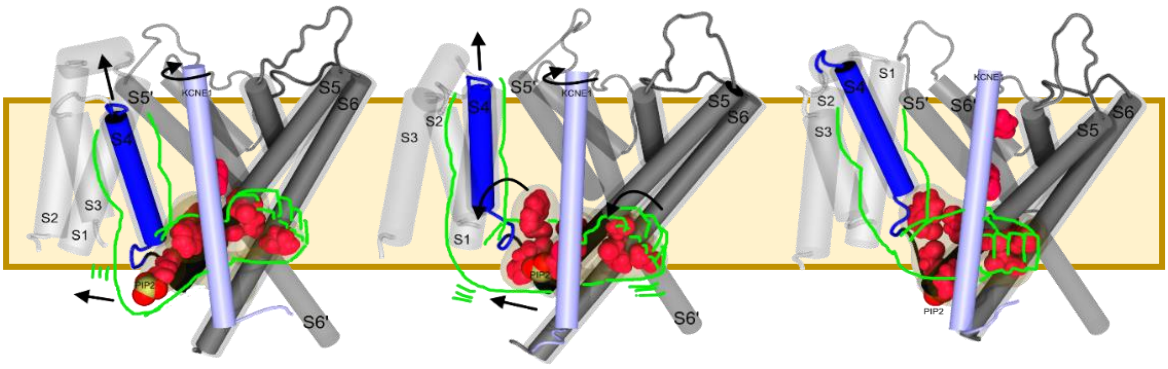

Figure III.2.2.5: Hand-and-elbow model for IK_S state-dependent VSD-PD coupling mechanism.
This figure shows a cartoon representation of $K_V7.1$ transmembrane segments, including one entire subunit on the foreground with the VSD (transparent light gray) S4 (blue), S4-S5L (black), PD segments (solid gray) and KCNE1 segments (light blue) along with the PD segments of an adjacent subunit (transparent gray). The "elbow" residues W248 R249 L251, the "hand" residues H258 L262 I346 L347 and KCNE1 residues 46 57 62 are depicted in pink spheres. PIP_2 phosphate groups, in state independent interaction with the elbow (R249) is shown in red spheres. The entire arm that models the whole conformational changes is drawn in green. The motions of both the elbow and the arm during RC-IO and IO-AO transitions are depicted by black arrows.

Interestingly, a recent computational study, which consisted in the use of machine learning methods to generate a conformational space of IK_S channels, have yielded to the design of a structure-based predictor of IK_S channel experimental properties including its subconductance and gating current [251].

The two sequential translations and rotations of S4 and the rotations of KCNE1 leading to VSD activation we predicted from our models are supported by the results obtained with this structure-based predictor. The fact that the molecular determinants of the mechanism of KCNE1 modulation has been unraveled by two distinct computational studies involving different methods is quite promising. Moreover, the rotational motion of KCNE1 subunits during the VSD's activation was also suggested by previous functional studies [191, 192]. Altogether, these results increase the trustworthiness of our predictions.

Chapter III.2.3. A K_V7 conserved motif constitutes a hydrophobic gate in the pore of the $K_V7.1$ channel

The structural validation of the $K_V7.1$ models against experimental knowledge (Chapter III.1) included the calculation of the average pore radii values of $K_V7.1$ models throughout their respective MD trajectories (see Chapter III.1.3). The results we obtained (Figure III.1.3.4, top) present a major region that discriminates open models against closed ones at the level of residue F340, which is included in the SFF motif located in the middle of S6 segment. Indeed, the particularity of this SFF primary sequences of K_V7 subunits comprise a unique conserved motif, (338-340 in $K_V7.1$ sequence) mutations of which are related with LQT syndromes (Figure III.2.3.1).

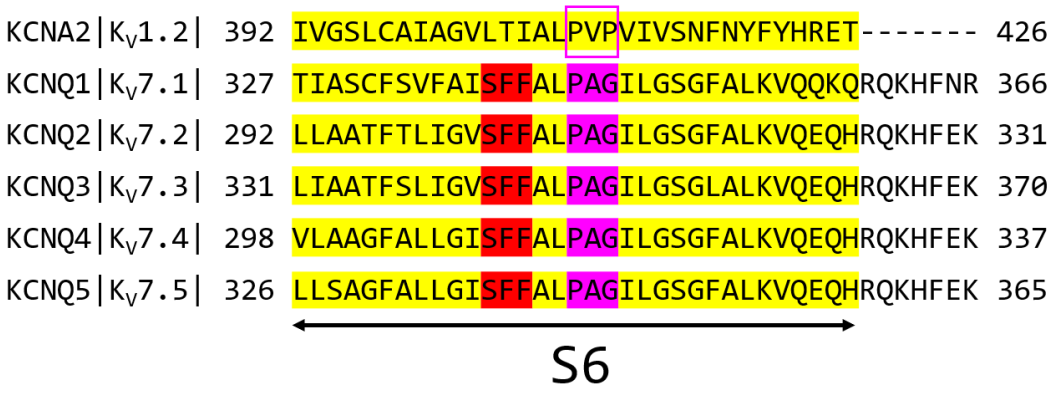

Figure III.2.3.1: Conserved motifs in the sixth segment of K_V channels.
The figure shows a sequence alignment of the transmembrane region of S6 segment (highlighted in yellow) in $K_V1.2$ and K_V7 subunits. The SFF motif (highlighted in red) is specifically conserved among K_V7 subunits. The PVP motif (framed in magenta), present in most K_V channels, is partially conserved in K_V7 family as the PAG motif (highlighted in magenta) in which the valine and the proline are changed into an alanine and a glycine, respectively, with similar properties.

In this regard, the functional properties of the SFF mutants of $K_V7.1$ have been extensively studied for the last fifteen years. First considered as a possible binding site for the KCNE subunits [215, 335], this hypothesis was invalidated a decade later [155]. The cytoplasmic part of $K_V7.1$ S6 segment was shown to be mainly involved in $K_V7.1$ pore gating both in presence and absence of KCNE1 [176, 182]. Other studies indicated that the VSD-PD coupling is lost in the $K_V7.1$ LQTS related mutants S338F [173] and F339S [159]. The biophysical properties of the IK_S F340W mutant [181] have been investigated as well. This mutant channel, while being constitutively open, is able to undergo inactivation upon sustained depolarization, contrary to the wild-type IK_S channel which does not inactivate.

As this inactivation process was shown to be voltage dependent, F340 was described as a hub for cross talk between activation and inactivation gates of $K_V7.1$, as its substitution for tryptophan was shown to uncouple the pore opening from the VSD activation. In addition, an alanine scanning study conducted on $K_V7.1$ revealed an increase of the constitutively open component and a 26.7 mV left-shift of the midpoint voltage of activation for F340A mutant [257]. These results indicate that the F340 sidechains might stabilize the pore in its open conformation in both the IK_S and the $K_V7.1$ channels. Given the hydrophobic nature of F340, one can conclude that F340 might play a crucial role in both VSD-PD coupling and pore opening mechanisms (Figure III.1.3.4, bottom). Indeed, the average pore radii estimated from the simulations are wider in IO and AO models, compared to the RC and AC models, where these radii are smaller than the ionic radius of a potassium ion (1.33 Å).

Starting from these results and the experimental knowledge of this particular SFF motif, we focused our attention on the conformations of F340 sidechains, along with those of F339 and S338, in our $K_V7.1$ models. To investigate the conformational space of the SFF motif residues, we listed, for each SFF residue, its closest neighbors by selecting the ones which were the most frequently located within a distance cutoff of 5 Å from the center of the residue side chain throughout the MD trajectories of each $K_V7.1$ and IK_S ($8PIP_2$) models. Then, we selected the ones which appeared to adopt state-dependent contacts.

The MD trajectories we obtained for the $K_V7.1$ RC and AC models suggest that the four F340 residues form a state-dependent hydrophobic seal, which entirely closes the pore through π-stacking interactions. This hydrophobic seal is barely present in $K_V7.1$ IO and AO models. One could distinguish two conformations for F340 side chains (Figure III.2.3.2). The “inside” conformation, in which F340 sidechains are facing each other at the center of the pore, leads to a complete obstruction of the conduction pathway, and is favored in the closed state models. The “outside” conformation, in which F340 side chains interact with a hydrophobic pocket located between S5, the P-loop and S6 from the same subunit, is favored in the open state models. This pocket is composed of residues L266, Y267, I268, G269, F270 and L271 from S5, residues V310 and T311 and T312 from the pore helix as well as residues V334 and I337 from S6.

These residues constitute the PD middle pocket and anchor the SFF residues in a state-dependent manner during the VSD activation of both the IK_S and the $K_V7.1$ models. In the intermediate states, both conformations are present. However, the π-stacking interactions fond in the RC model are mostly impaired.

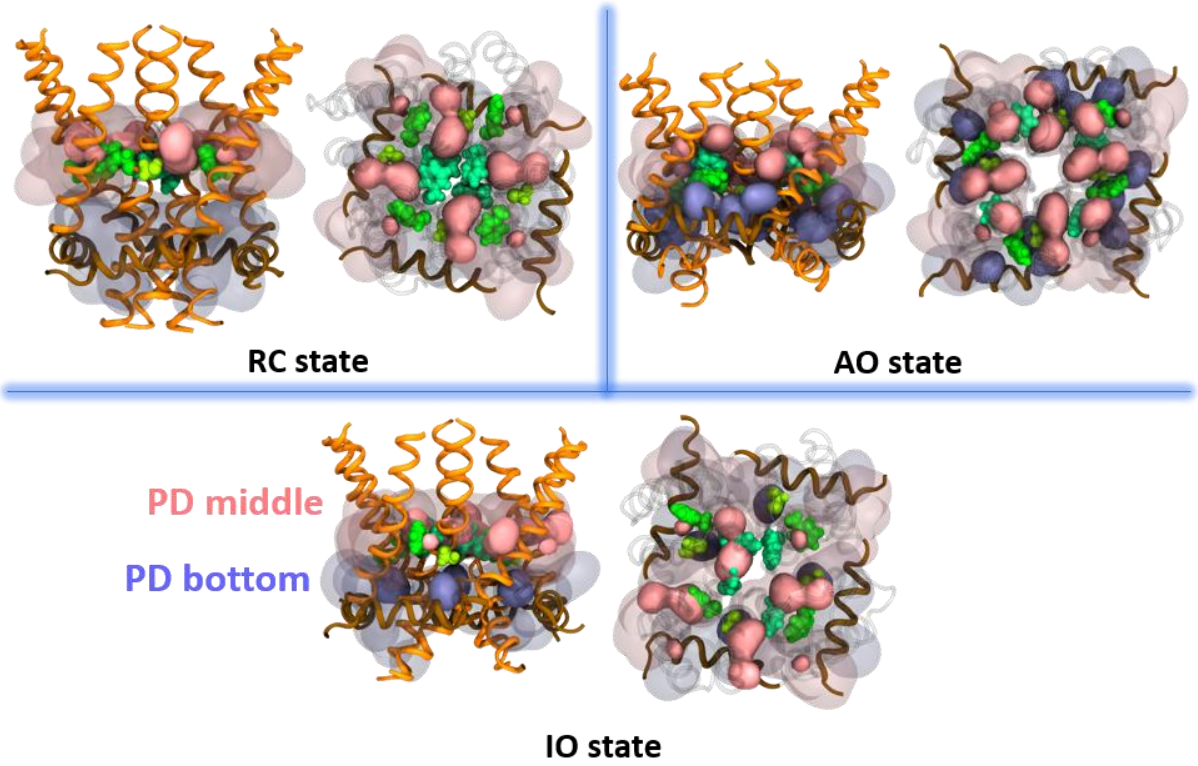

Figure III.2.3.2: State-dependent conformations of F340 sidechains in $K_V7.1$ models.
Each panel displays a side view (left) and an extracellular view (right) of $K_V7.1$ pore domain segments (in orange) and S4-S5 linker (in brown), on RC,IO and AO models. S338, F339 and F340 are represented in light green, bottle green and blue green spheres, respectively. S4-S5 bottom and S5 middle pockets are represented by transparent blue and pink surfaces, respectively. Among PD middle and PD bottom residues, those which interact with SFF residues are depicted in solid colors.

Both of the conformations adopted by F340 may directly depend on the orientation of F339, as it either points towards the PD middle pocket from its own subunit to induce the F340 "inside" conformation, or toward the residues of PD cluster from an adjacent subunit, which constitute a second hydrophobic pocket located deeper in the membrane. We recall that the PD cluster is composed of 13 residues from $S4\text{-}S5_{LINKER}$ (W248 L250 L251 V254 V255 F256 H258 R259), the bottom of S5 (E261 L262) and the C_{TER} region of S6 (I246 L347 V355). These residues form the PD bottom pocket and have been previously shown (referred as PD cluster in Chapter III.2.1. and III.2.2.) to play a crucial part in the electromechanical coupling of $K_V7.1$ in both IO and AO states, in the absence and the presence of KCNE1 ancillary subunits.

The specific intersubunit interaction between F339 and L251 appears to induce the F340 "outside" conformation, stabilized by its own interactions with G269 and V310. However, the intrasubunit interaction between F339 and G269, which is predominant in K_V7.1 RC state, appears to induce the "inside" conformation of F340 aromatic sidechains. The conformation of F340 might also depend on the orientation of S338, which appears to interact with both PD middle and PD bottom pockets in K_V7.1 IO and AO models.

In the CryoEM K_V7.1 structure ($KCNQ1_{EM}$), F340 was captured in its "outside" conformation (Figure III.2.3.3), as the aromatic ring centers of its sidechains are located too far away from each other to interact. Instead, they are anchored in the PD middle pocket to bind both G269 and V310. F339 is oriented towards PD bottom pocket, interacting with L251 and not with G269, which indicates that F339 does not interact with the PD middle pocket. Contrary to the K_V7.1 AO model, S338 only binds V334 from the PD middle pocket. Throughout the MD trajectory obtained for the K_V7.1 AC model, that has been built using $KCNQ1_{EM}$ structure as a template, the sidechains of S338 remain bound to V334 (PD middle pocket) but its intersubunit interactions with both L262 and L347 are impaired, while those of F339 have progressively left the PD cluster pocket to reach PD middle one, which has led F340 sidechains to adopt the "inside" conformation in two subunits out of four (Figure III.2.3.3, lower panel). Although these two F340 sidechains are not engaged in a pi-stacking interaction (Figure III.2.3.4), their conformational change that occurred during the MD simulation appears to be enough to seal the conduction pathway, considering the average pore radii results obtained at the level of F340 sidechains throughout the MD trajectory of K_V7.1 AC model (Figure III.2.3.3, upper panel). These results support the idea that the absence of VSD-PD coupling in K_V7.1 channel when its VSD reaches its activated state might induce pore closure [248].

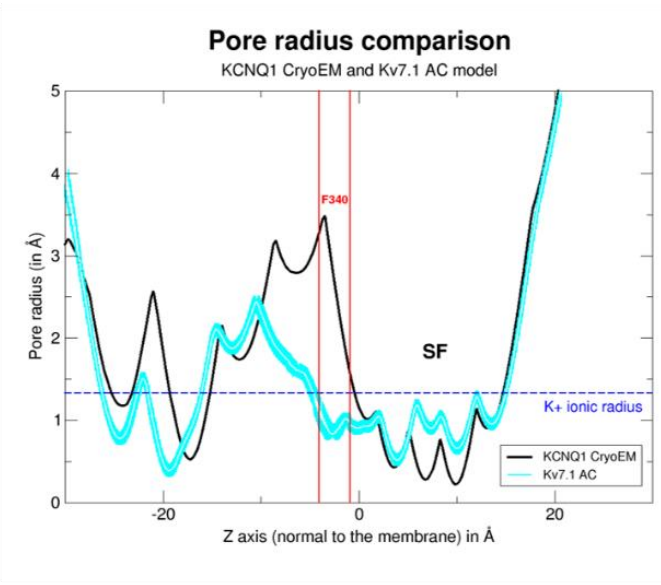

Interatomic distances in $KCNQ1_{EM}$ structure (in Å)	
S338-L262	7.0
S338-V334	3.3
S338-L347	5.6
F339-L251	4.7
F339-G269	5.3
F340-G269	4.9
F340-V310	3.7
F340-F340	16.7

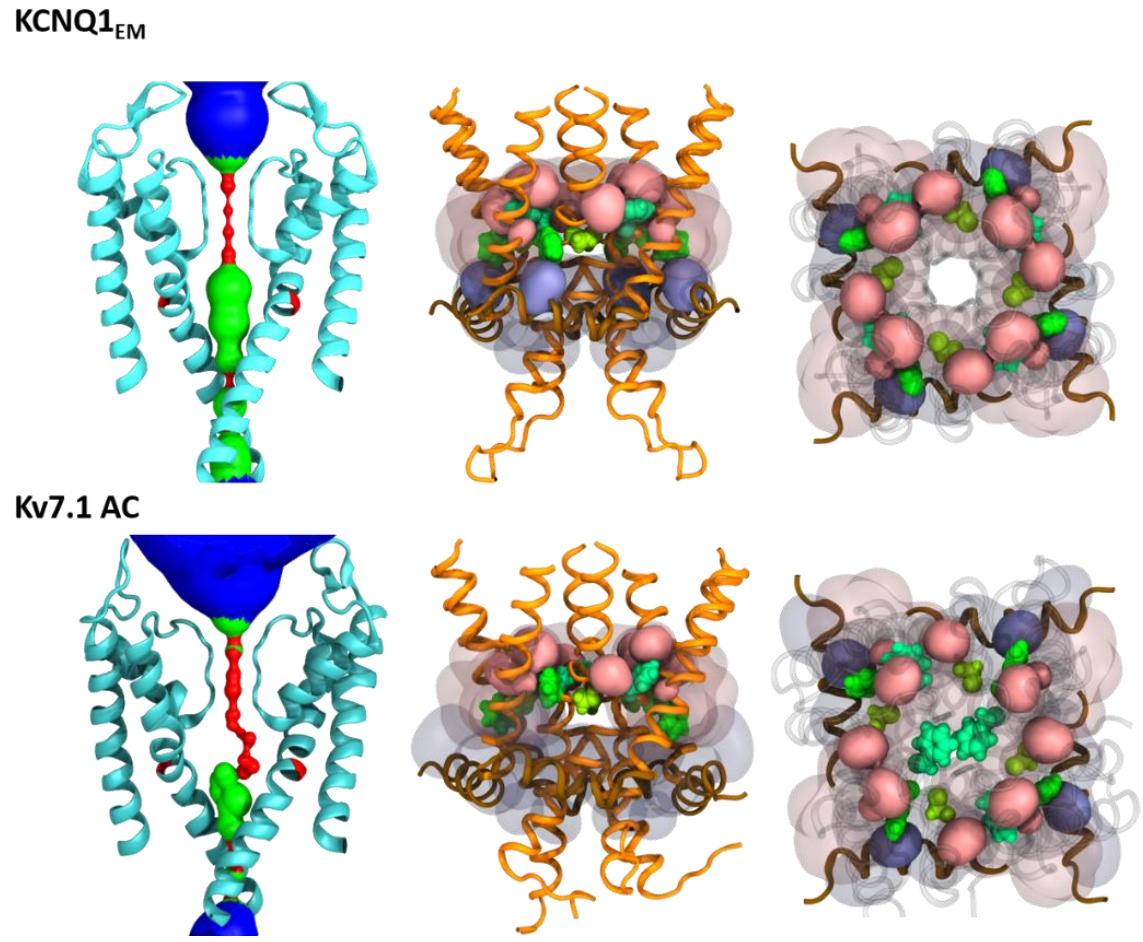

Figure III.2.3.3: Conformations of F340 side chains in $KCNQ1_{EM}$ structure and $K_V7.1$ AC model.
The upper left panel shows a graph of the pore radii of $KCNQ1_{EM}$ structure and the average pore radii of the MD trajectory of $K_V7.1$ AC model, both along the axis normal to the membrane plan. The upper right panel displays a tab which reports the key interatomic distances of SFF motif residues in the $KCNQ1_{EM}$ structure. The lower panel cartoon representations of the pore shape (left) the side view (middle) and the extracellular view of the PD segments of $KCNQ1_{EM}$ structure (top) and $K_V7.1$ AC model. On the left, the PD segments are shown in cyan. The pore surfaces are colored as follows: red for pore radii $\leqslant$ 1.33 Å, green for pore radii ranging from 1.33 Å to 3.6 Å (the hydrodynamic radius of K^+ ions), blue for pore radii $\geqslant$3.6 Å. The middle and right panels depict the conformations of SFF residues with respect to PD segments and both PD middle and PD bottom pockets. The color code used is the same as in Figure III.2.3.2.

In the K_V7.1 models, the SFF motif residues present mostly state-dependent interactions (Figure III.2.3.4). The only state independent interaction we found involves the hydroxyl group of S338, which forms an intrahelical hydrogen bond with the carbonyl group of V334. S338 is also engaged in an intersubunit VdW interaction with L347 in the IO model with a frequency of 0.7, as well as in the AO model, with a frequency of 0.6. As S338-L347 interaction is not present in the RC and AC models, these frequency differences suggest that this interaction is crucial for the K_V7.1 pore opening. In the previous chapter, we identified an intersubunit interaction between S338 and L262, present only in the AO state.

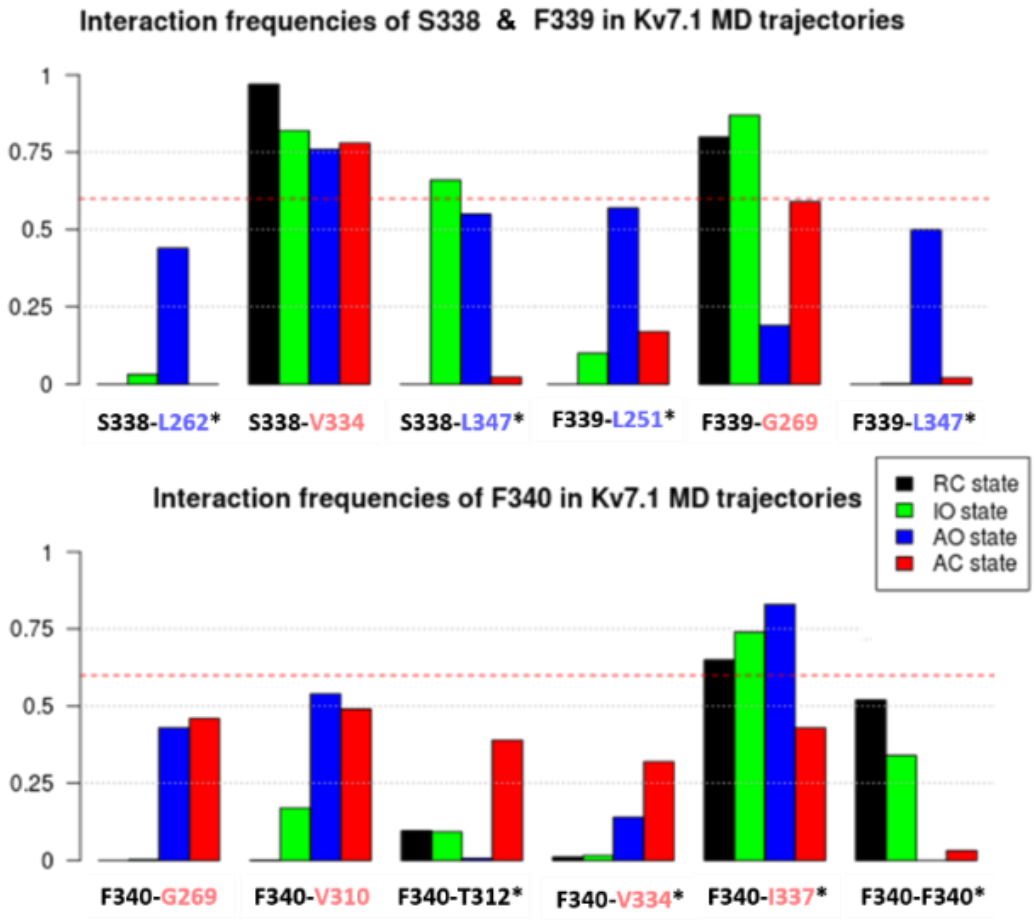

Figure III.2.3.4: Interactions of SFF residues in K_V7.1 models.
The barplots display the frequencies of the interactions involving S338, F339 and F340 side chains throughout the MD trajectories of K_V7.1 RC (black), IO (green), AO (blue) and AC (red) models. The residue pairs marked with an asterisk are intersubunit interactions. The frequency threshold of 0.6 is marked by a red dashed line. Among the residue pairs, those colored in pink and blue are PD middle and PD bottom pocket residues, respectively.

F339 is engaged in an intrasubunit interaction with the S5 residue G269 in the RC and IO models, with similar frequencies. In the AO models, F339 is oriented towards the S4-S5L residue L251 and the S6 residue L347 from an adjacent subunit, as its frequencies are 0.6 and 0.5, respectively. The F340 aromatic ring is engaged in an intersubunit interaction with adjacent F340 sidechains to form π-stacking interactions, with a frequency of 0.5 in the RC model. This frequency drops to 0.3 in the IO model, indicating that these interactions are impaired, and in the AO state, these interactions are absent. Moreover, F340 interacts with S6 residue I337 in all but the AC K_V7.1 model, which suggests that this interaction is crucial to stabilize the open state of K_V7.1 when the VSD is in its activated state. In the AO model, F340 interacts with G269 and V310 from the P-helix with a frequency of 0.4 and 0.6, respectively.

Interestingly, in the IK_S models, the interactions of SFF residues appear to be affected by the presence of KCNE1 (Figure III.2.3.5).

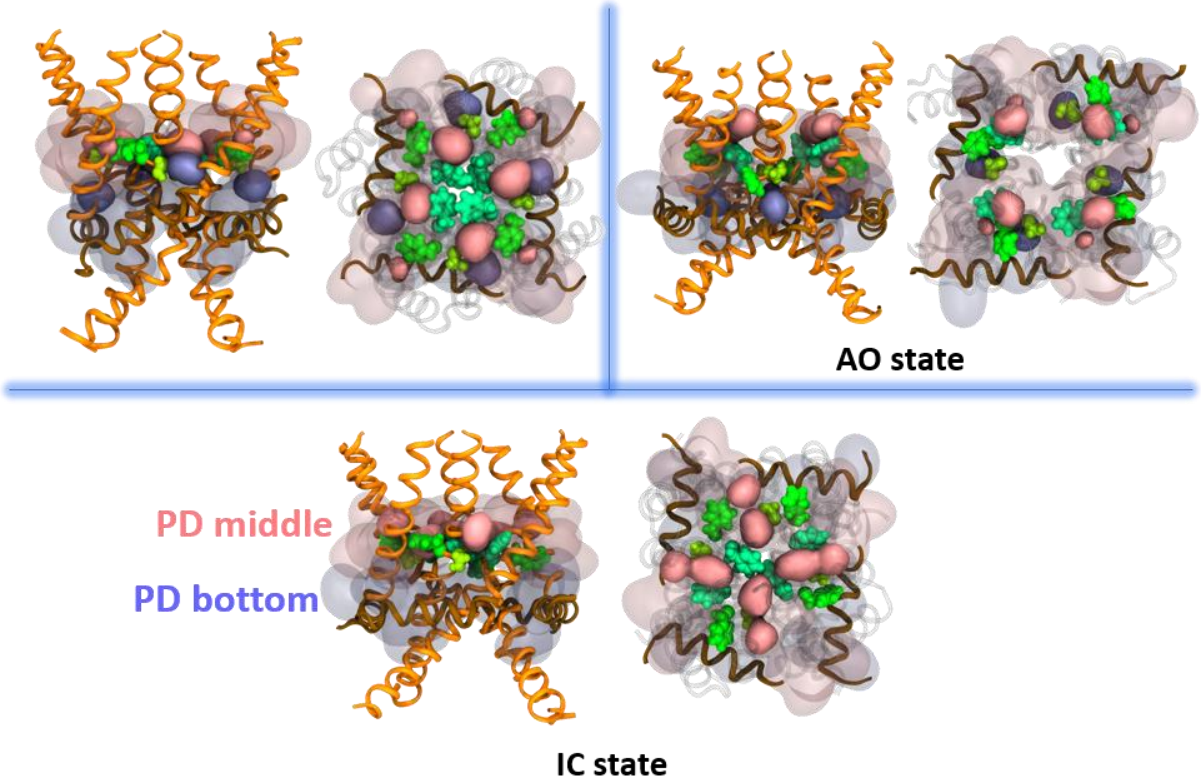

Figure III.2.3.5: State-dependent conformations of F340 residues in IK_S models.
Each panel displays a side view (left) and an extracellular view (right) of IKS pore domain segments in a cartoon representation on RC, IC and AO models. The color code we used to depict S4-S5 linker, S5 and S6 segments, S338, F339 and F340, S4-S5 bottom and S5 middle pockets is similar as in Figure III.2.3.2. Among PD middle and PD bottom residues, those which interact with SFF residues are depicted in solid colors.

As a consequence, S338 is engaged in an intersubunit interaction with S5 residue L262 in the RC model (and not in the AO model as seen in K_V7.1), while the S338-V334 interaction loses its state-independence, as these two residues only interact in the IC state (Figure III.2.3.6, upper left panel). In the AO model, S338 sidechains are engaged in a hydrogen bond with water molecules (data not shown), which may explain how its hydrogen bond with V334 is impaired. Furthermore, S338 interacts with L347 only in the AO model, which constitutes an additional proof that this interaction is crucial for the K_V7.1 VSD-PD coupling and/or for the stabilization of the K_V7.1 open state, as this interaction is also present in the K_V7.1 IO and AO models. F339 binds G269 in the RC model with a frequency of 0.7 but contrary to K_V7.1 IO model, this value is decreased to 0.4 in the IC model (Figure III.2.3.6, upper right panel). This frequency change suggests a loss of F339-G269 interaction during the VSD transition from the resting to the intermediate state. In AO model, F339 barely interacts with both L251 and L347, with frequencies of 0.3 and 0.4, respectively.

However, KCNE1 does not prevent F340 sidechains from interacting with each other in the RC model (Figure III.2.3.6, lower panel). The interactions between F340 sidechains are less frequent in the RC (0.3) and the IC (0.2) models of IK_S than in the K_V7.1 RC and IO models, respectively, which means that the "inside" conformation of F340 might be less important to maintain the pore closed in presence of KCNE1, as the loss of coupling induced by the ancillary subunit already prevents pore opening to occur. Nevertheless, KCNE1 does not prevent F340 sidechains from interacting with both G269 and V310 in the AO state. Interestingly, the interaction between F340 and I337 loses its state-independent aspect in the presence of KCNE1. Indeed, F340 interact mostly with I337 in the RC and IC models, with frequencies of 0.6 and 0.9, respectively. In the AO model, the frequency of this interaction drops to 0.2, indicating an absence of interaction.

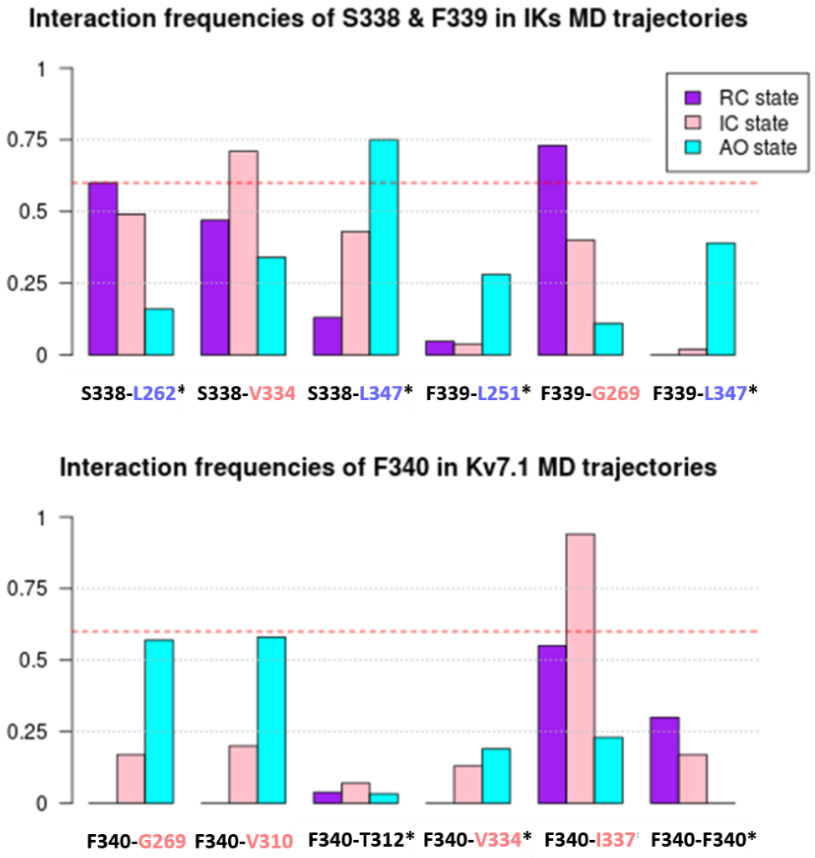

Figure III.2.3.6: Interactions of SFF residues in IK_S models.
The barplots display the frequencies of the interactions involving S338, F339 and F340 side chains throughout the MD trajectories of IK_S RC (purple), IC (pink) and AO (cyan) models. The residue pairs marked with an asterisk are intersubunit interactions. The frequency threshold of 0.6 is marked by a red dashed line. Among the residue pairs, those colored in pink and blue are PD middle and PD bottom pocket residues, respectively.

These results suggest that these interactions might be less important for the stabilization of the open state of $K_V7.1$ in the presence of KCNE1, since the open state of $K_V7.1$ pore is stabilized by the protein-protein interaction between the $K_V7.1$ PD middle pocket residue L266 and the KCNE1 TMD residue F57 (see Chapter III.2.2) and between F270 from PD middle pocket and F54 from KCNE1, with a frequency of 0.7. The changes we observed in the interactions of SFF residues in the IK_S models with respect to those of $K_V7.1$ alone might be due to some changes in the shape of the PD middle pocket (Figure III.2.3.7).

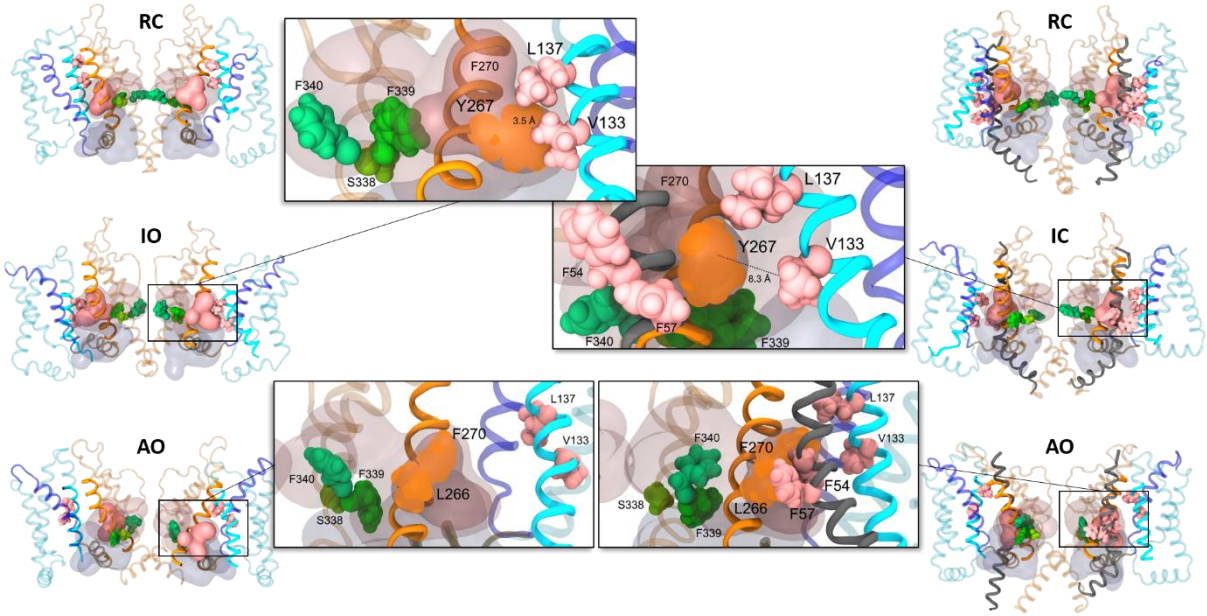

Figure III.2.3.8: Interactions of PD middle pocket residues in $K_V7.1$ and IK_S models.
The picture shows a cartoon representation of Kv7.1 (left) and IKS (right) models in a lateral view. It includes the VSD (cyan), S4 (blue), S4-S5linker (brown) PD segments (orange) and KCNE1 (gray). Two subunits are shown for clarity. The transmembrane segments that carry residues involved in the interactions of interest are depicted in solid colors. For intermediate (upper panels) and activated state models (lower panels), two enhanced views of the framed areas are shown in the center, in which PD middle pocket residues involved in interactions are shown in orange spheres, while residues engaged in interactions with PD middle residues are shown in pink spheres.

Indeed, in $K_V7.1$, L266 is engaged in a state-independent intersubunit VdW interaction with S6 residue V334 in both the absence and the presence of KCNE1 (Figure III.2.3.8). Similarly, I268 has already been shown to interact with L251 in all $K_V7.1$ and IK_S models except the RC ones through functional and computational studies [323] (see Chapter III.2.1-2). The last two residues of the PD middle pocket, Y267 and F270, are both aromatic and interact with S1 residues V133 and L137 in the $K_V7.1$ IO model, with frequencies of 0.9 and 0.6, respectively. However, the frequencies of Y267-V133 and F270-L137 interactions drop to 0.2 and 0.4, respectively in IK_S IC model, suggesting that these interactions are impaired in the presence of KCNE1.

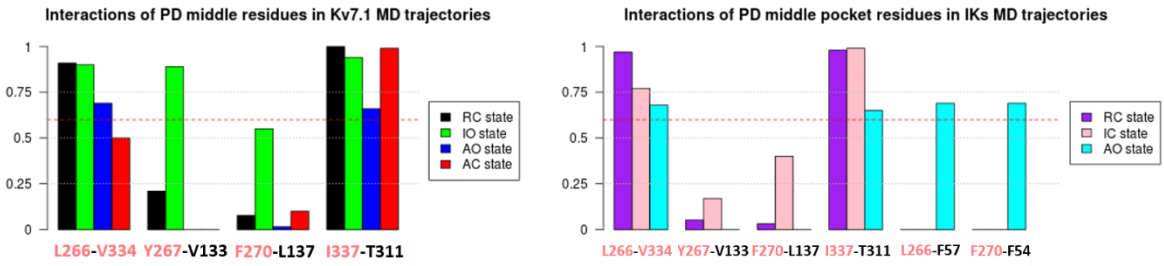

Figure III.2.3.7: Intersubunit interactions involving PD middle pocket residues.
The picture reports the barplots of the frequencies of the intersubunit interactions of PD middle pocket residues throughout the MD trajectories of $K_V7.1$ (left panel) and IK_S models (right panel). The frequency threshold of 0.6 is marked by a red dashed line.

Altogether, these interactions suggest that the PD middle pocket is moving away from the pore axis towards S1 during K_V7.1 RC-IO transition, dragging F339 in its motion as F339-G269 interaction is still present in K_V7.1 IO model. The VdW interaction between Y267 and V133, which is strictly specific of K_V7.1 IO model, may induce a specific orientation of PD segments with respect to the adjacent S4-S5L (Figure III.2.3.8) which might stabilize the interface between the linker and PD segments, which characterizes VSD-PD coupling in both IO and AO states. This might explain how pore opening occurs without any conformational change of F340 in K_V7.1 IO state. These results also support the idea that K_V7.1 pore opening, like K_V7.1 VSD-PD coupling, is mediated by different mechanisms in IO and AO states [173, 323]. In IK_S IC model, Y267-V133, F339-G269 and F270-L137 interactions are barely present. This suggests that KCNE1 might prevent PD middle pocket from moving away from the pore center. However, the impairment of F339-G269 interaction does not imply an interaction of F339 with any PD bottom pocket residue, therefore it cannot elicit a conformational change of F340 sidechains, as two of them remain engaged in a π-stacking interaction.

Meanwhile, in all but the AC K_V7.1 models, F340 are bound to I337 through an intersubunit VdW interaction, whereas in the IK_S models, this interaction is maintained only in the IC state. Moreover, I337 itself binds the P-helix residue T311 in a state independent fashion in both K_V7.1 and IK_S models. Noteworthy, residues T311, I337 and F340 were previously shown to be crucial for ion conduction by experimental [336] and modeling [337] investigations. Hence, our findings are supporting the importance of these residues in the pore opening mechanism of K_V7.1. The conformations adopted by SFF residues in our models suggest that the outside conformation is favored in the models in which the VSD and the PD are coupled (K_V7.1 IO, AO models and IK_S AO model), while the inside conformation is favored in the models in which VSD-PD coupling is lost (K_V7.1 RC, AC models and IK_S RC, IC models).

Our collaborators from WUSL obtained functional results that corroborate these MD findings. When mutated into Alanine, G269 I337 and F340 yield inactivated channels. This indicates that those mutant channels activate, open, and then close immediately, contrary to the wild-type $K_V7.1$ channel that remains open for a significant period of time, without inactivating in the presence of KCNE1. This particular gating behavior observed on these mutants might be explained by the fact that these mutations might destabilize the open conformation of the pore.

Taken together, the results obtained from both MD simulations and VCF studies of $K_V7.1$ channel can be interpreted as follows: considering the effects on Glycine on the flexibility of transmembrane helices [338, 339], one can predict that G269A might form a state-independent interaction with F339 from the RC state to AO state. This interaction might prevent F339 from leaving its anchor in S5 pocket to let F340 sidechains reach the pocket in the AO state. In addition, the I337A mutant might induce an impairment of its interactions with both T311 and F340. As a consequence, the conformational change of F340 from their inside conformation towards their outside conformation might be disturbed in the AO state. Given the size of Alanine compared to Phenylalanine, F340A mutant might impair its interactions with both G269 and V310 in the AO state. As a consequence, the outside conformation of F340 side chains may be destabilized, which can explain the inactivation phenotype observed for this mutant.

The conformational analysis of SFF motif in the previous section shed light on the differences of F340 conformations in the IK_S IC model with respect to those observed throughout the MD trajectory of the $K_V7.1$ IO model. The outside conformation of F340 appears to be more favored in absence of KCNE1 than in its presence, where the inside conformation is favored.

Interestingly, the pore radii profiles of the $K_V7.1$ and IK_S models also indicate that the average pore radii values at the level of the PAG motif, which is suspected to form the hinge region of the tetrameric structure of the $K_V7.1$ subunits, is also state-dependent and sensitive to the presence of KCNE1. Indeed, throughout the MD trajectories of the RC models, the average pore radii of the PAG motif is maximized at 3 Å for $K_V7.1$, against 2 Å for IK_S. This difference is also observed in the intermediate state models, in which the average pore radii of the PAG motif increases up to 3 Å in the direction of the cytoplasm for $K_V7.1$, whereas for IK_S the pore radii decrease down to 2 Å in the same direction. In the activated state models, the tendency is reversed, as the average pore radii of the PAG motif increases up to 4 Å for both $K_V7.1$ and IK_S. However, the height of the PAG motif backbone along the normal axis to the membrane is larger for $K_V7.1$ than for IK_S. This suggests that the hinge region is shorter in the presence of KCNE1, which might induce a larger tilt angle between S6 helices and the pore axis, and therefore, a larger conduction pathway. The pore size differences of the PAG motif, along with the functional results obtained for the mutations of its these three residues, which link them to the electromechanical coupling of $K_V7.1$ subunits, may probably participate in the VSD-PD coupling modulation by KCNE1. These interactions suggest that the S5 pocket is moving away from the pore axis towards S1 during $K_V7.1$ RC-IO transition, dragging F339 in its motion as F339-G269 interaction is still present in $K_V7.1$ IO model. The VdW interaction between Y267 and V133, which is strictly specific of the $K_V7.1$ IO model, may induce a specific orientation of PD segments with respect to the adjacent S4-S5L (Figure III.2.3.7, upper right panel) which might stabilize the interface between the linker and PD segments that characterizes the VSD-PD coupling in both the IO and AO states. This might explain how pore opening occurs in $K_V7.1$ IO state, especially since Y267-V133 and F270-L137 interactions are absent and barely present in the IK_S IC model, with frequencies of 0.0 and 0.4, respectively. These results also support the idea that the $K_V7.1$ pore opening, like the $K_V7.1$ VSD-PD coupling, is mediated by different mechanisms in the IO and AO states [173, 323].

Chapter III.2.4. The protein-lipid interactions that mediate the pore opening mechanism

Our previous MD study [249] of the $K_V7.1$ channel in the open and closed states, allowed to localize the PIP_2 binding site near the $K_V7.1$ subunit, and also to characterize the key elements of the $K_V7.1$ modulation by PIP_2 via two components of the VSD-PD coupling: the protein-protein component and the protein-lipid component. The protein-protein component of this mechanism was mostly characterized by electrostatic interactions between residues from S4-$S5_{LINKER}$ and residues from S6, while the protein-lipid component was characterized by state-dependent interactions between PIP_2 and the $K_V7.1$ subunits. The lipid was shown to participate in the VSD/PD coupling of $K_V7.1$ through state-independent interactions, preventing repulsive forces between basic residues from S2-$S3_{LOOP}$ and S4 in resting state, and between basic residues from S2-$S3_{LOOP}$ and S6 in open states [246, 248–250]. Moreover, the results of the MD analysis reported in Chapter III.2.2 highlighted the crucial role played by PIP_2 in the VSD-PD coupling mechanism through its state independent interaction with S4-$S5_L$. This interaction suggests that PIP_2 might be acting as an anchor for S4-$S5_L$ movements during this mechanism.

Moreover, the dependence of this lipid for $K_V7.1$ subunit function was also proved to increase in presence of KCNE1 due to the additional positive charges in carries its C_{TER} domain [162]. Our investigations indicate that the IK_S channel may carry an additional PIP_2 binding site with respect to the $K_V7.1$ subunits.

In our IK_S models, considering a second PIP_2 binding site per subunit was absolutely required in order to obtain a better agreement with experimental results. This work shows that in contrast to the case of $K_V7.1$, in IK_S, PIP_2 lipids engage in state-independent interactions with the $K_V7.1$ subunits: PIP_2 intra, which is required in both the $K_V7.1$ and IK_S models, predominantly binds the lower VSD basic residues, while PIP_2 inter, presumably most required in IK_S channels, binds the basic residues from S6 and KCNE1.

PIP_2 inter is located between the C_{TER} regions of both KCNE1 helix and S6 segment and characterized by several basic residues that might repel each other and prevent S6 residues to reach PIP_2 in the inner membrane surface in AO state, as observed in IK_S AO model of $4PIP_2$ system, (without PIP_2 inter). In the IK_S models of $8PIP_2$ systems, PIP_2 intra remain bound to the S6 residues K362 and R366 in a state independent manner, as well as the KCNE1 residues R67 K69 and K70 in a state dependent manner.

The molecular determinants of this second PIP_2 binding site we identified in our IK_S models are supported by previous functional studies [162] which shed light on several residues of KCNE1 subunit that act as molecular determinants of KCNE1-PIP_2 interaction in IK_S channels, including those we found here. In this study, the authors have shown that KCNE1 increases PIP_2 sensitivity 100-fold over channels formed by the pore-forming $K_V7.1$ α-subunits alone. They identified four residues (R67, K69, K70, and H73) in proximal C-terminus of KCNE1 as key determinants of PIP_2 sensitivity. Mutations of these key residues in KCNE1 (R67C, R67H, K70M, and K70N) are associated with long QT syndrome [340, 136, 320], as they reduce both IK_S currents and PIP_2 sensitivity. Application of exogenous PIP_2 to these mutants restores wild-type channel activity. Our results are also in agreement with an integrative study including both experimental and computational approaches [250], which aimed at identifying $K_V7.1$ interactions with PIP_2 in IK_S complex. Without considering the presence of KCNE1 basic residues, they obtained results that highlight the existence of two PIP_2 binding sites for this complex, one for VSD residues and a second one for PD residues.

Altogether, our IK_S models suggest that KCNE1 subunits are involved in a set of interactions with both PIP_2 and the pore domain. These interactions might modify the pore size in the IK_S models compared to the models of $K_V7.1$ channel alone. Noteworthy, KCNE1 residues bind both PIP_2 inter and PIP_2 intra in the RC and IC states, which may induce a tighter packing of the PD segments. Indeed, these KCNE1-PIP_2 interactions form a circle of electrostatic interactions around the cytoplasmic region of S6.

This circle may act as a tourniquet (Figure III.2.4.1), inducing a shrinkage of the conduction pathway, leading to the lower pore radii values we obtained for IK_S RC and IC models with respect to $K_V7.1$ RC and IO models, respectively (Figure III.1.3.4). In the AO models of IK_S, KCNE1 loses its interactions with PIP_2 intra and binds only PIP_2 inter. Through this interaction, one can predict that KCNE1 is pulling S6 helices towards the inner leaflet of the membrane, as PIP_2 inter remains bound to S6 basic residues.

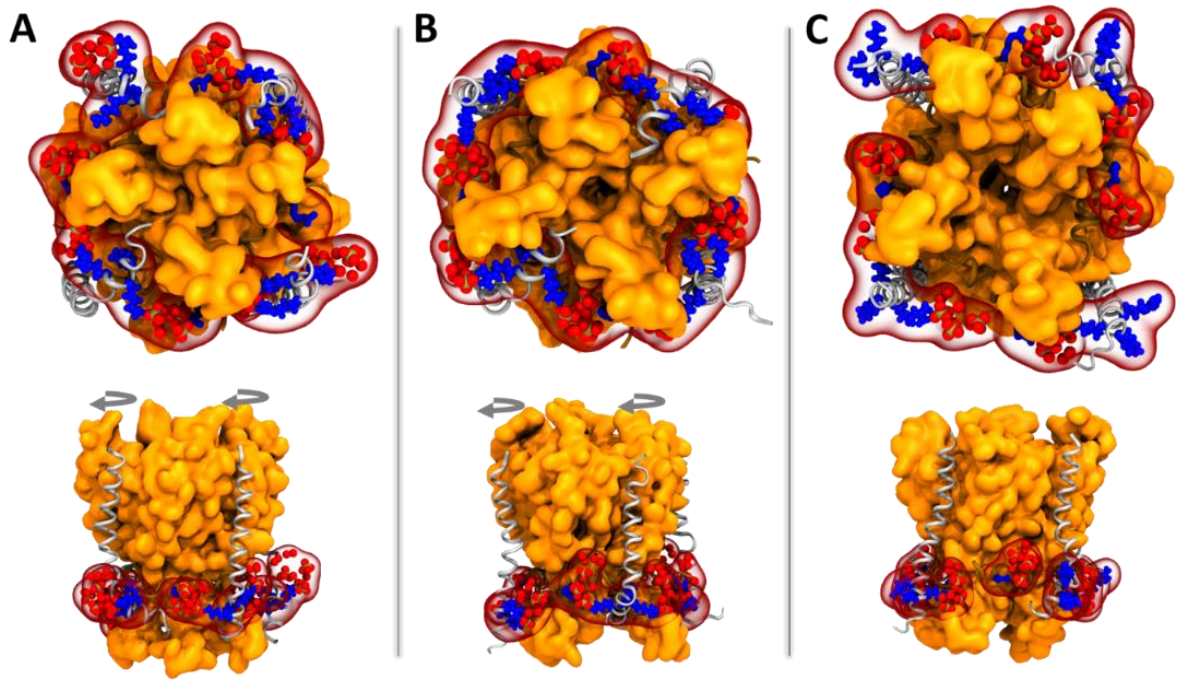

Figure III.2.4.1 Structural mapping of KCNE1 basic residues and PIP_2 lipids in the pore domain of IK_S models in 8PIP_2 systems.
Intracellular view (top panels) and side view (bottom panels) of $K_V7.1$ pore domain segments (in orange surface) along with S4-$S5_{LINKER}$ (in brown ribbons), KCNE1 subunits (in gray ribbons) and PIP_2 phosphate groups (in red spheres) in **A.** RC model, **B.** IO model and **C.** AO model. KCNE1 basic residues R67, K69 and K70 are shown in blue spheres. S4-$S5_{LINKER}$ residue R249 that interact with PIP_2 intra in a state independent fashion is shown in blue sticks. The successive rotational movements of KCNE1 subunits predicted to occur during RC-IC and IC-AO transitions are shown in gray circled arrows.

The results obtained by Li et al [162] revealed a vital role of PIP_2 for KCNE1 modulation of IK_S channels that may represent a common mechanism of auxiliary subunit modulation of many ion channels. The present investigation confirms that these residues are involved in specific interactions with PIP_2, by providing the key molecular elements that govern such a role.

Furthermore, the family of β-subunits contains several members (KCNE1-5) that have been reported to modulate the activity of a variety of channel α-subunits in ion channel complexes [196]. Many of these channel α-subunits or complexes are also modulated by PIP_2. The KCNE1 basic residues listed above as essential for the modulation of the IK_S PIP_2 sensitivity are highly conserved across all members of the KCNE family of peptides (Figure III.2.4.2), suggesting that modulation of PIP_2 sensitivity may be a common mechanism of current modulation by the KCNE β-subunits.

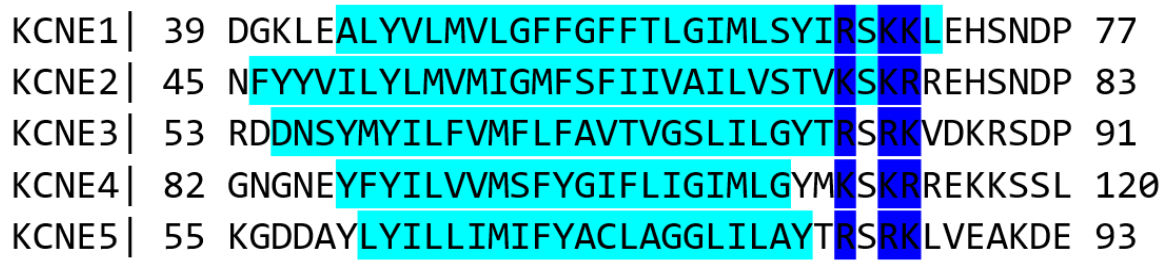

Figure III.2.4.2: Conserved basic residues in the of KCNE ancillary subunits.
The picture shows a sequence alignment of the transmembrane domains (TMD) of KCNE subunits, highlighted in cyan. The conserved basic residues, located at the end of the TMD, near their C_{TERM} domains, are highlighted in blue.

Chapter IV. General discussion

L'analyse complète des trajectoires DM des conformères du canal $K_V7.1$, à travers l'investigation des interactions protéine-protéine and protéine-lipide permettant de déterminer celles qui stabilisent chaque état du canal, ont généré une grande quantité de résultats à confronter aux données expérimentales. Plus précisément, nos analyses ont permis de prédire les aspects moléculaires clés des mécanismes d'activation du VSD, du couplage électromécanique VSD-PD, ainsi que celui du mécanisme d'ouverture du pore, et ce en l'absence et en la présence de KCNE1. Afin d'incorporer nos observations à la connaissance que nous avons déjà au sujet de la fonction des canaux K_V, et du canal $K_V7.1$ en particulier, il nous fallait confronter nos prédictions à la littérature actuelle, de manière à voir si ces dernières nécessitaient d'établir un nouveau modèle cinétique pour décrire la fonction de $K_V7.1$, ou alors si nos prédictions s'inscrivaient plutôt dans modèle cinétique préexistant. Curieusement, les nombreuses études effectuées en ce sens indiquent que le mécanisme d'action du canal $K_V7.1$ semblait enclin à suivre un modèle d'activation allostérique. Dans la première partie de ce chapitre, nous avons montré comment nos prédictions s'inscrivaient aisément au sein d'un modèle d'activation enzymatique de type allostérique développé il y a plus de cinq décennies (**Chapter IV.1**). Ensuite, nous avons expliqué comment PIP_2 (Chapter IV.1.1) et KCNE1 (Chapter IV.1.2) prenaient part à ce mécanisme allostérique, pour enfin terminer notre discussion avec une prédiction du mécanisme global du canal $K_V7.1$ incluant l'activation du VSD, le couplage électromécanique VSD-PD, ainsi que le mécanisme d'ouverture du pore (Chapter IV.1.3). Dans la seconde partie de chapitre, nous avons évoqué les nombreuses perspectives qu'offrent ce projet et l'ensemble de ses résultats (**Chapter IV.2**). Dans un premier temps, nous avons montré en quoi nos modèles sont d'un intérêt majeur pour l'amorce d'études de recherche thérapeutique computationnelle (Chapter IV.2.1), pour ensuite présenter le travail à venir qui pourrait assurément être effectué à partir de nos modèles du canal $K_V7.1$ afin d'élargir la vision que l'on sa de sa fonction, à l'aide de méthodes computationnelles inusités au cours de ce projet, et que nous avons brièvement présenté (Chapter IV.2.2).

En particulier, nous avons présenté les résultats préliminaires d'amarrage moléculaire de deux ligands connus pour être spécifiques aux canaux K_V, ainsi que le développement de leurs paramètres pour le champ de forces CHARMM (Chapter IV.2.1). Enfin, nous avons évoqué l'intérêt majeur de l'étude de la modulation du canal $K_V7.1$ par la sous-unité auxiliaire KCNE2, qui semble jouer un rôle dans le développement du diabète de type 2 (Chapter IV.2.2).

The extensive analysis of the $K_V7.1$ models MD trajectories via the investigation of protein-protein and protein-lipid interactions to determine those which stabilize each state of the channel, yielded to a tremendous number of results that have been confronted against experimental data. Specifically, our analyses allowed to predict the key molecular aspects of the VSD activation, the VSD-PD coupling, and the PD opening mechanisms of the $K_V7.1$ channel, in presence and absence of KCNE1. To incorporate our findings into the knowledge we already possess about the function of K_V channels, and the $K_V7.1$ channel in particular, we needed to confront our results with respect to the current literature in order to see whether our findings required an entire new kinetic model to describe $K_V7.1$ function or fell within a preexisting kinetic model. Interestingly, the numerous studies conducted in order to establish a kinetic model of the function of the $K_V7.1$ channel indicated that the $K_V7.1$ channel was more likely to follow an allosteric model of activation. In the first part of this chapter, we addressed how our findings are easily falling within a specific allosteric model which was developed five decades ago (**Chapter IV.1**). Then, we also explained how PIP_2 (Chapter IV.1.1) and KCNE1 (Chapter IV.1.2) take action in this allosteric mechanism, to finally end the discussion with a prediction of the overall mechanism of the $K_V7.1$ channel, which includes the VSD activation, the electromechanical VSD-PD coupling, and the PD opening mechanisms (Chapter IV.1.3). In the second part of this chapter, we addressed the numerous perspectives that this project and its results offer (**Chapter IV.2**). First, we presented how our models can constitute a major interest in the development of computational drug design studies (Chapter IV.2.1), and then we presented the ongoing work that could possibly be done with our $K_V7.1$ models, in order to gain a further insight into its function, with the help of additional computational techniques that we briefly presented (Chapter IV.2.2). Specifically, we presented the primary results we obtained from molecular docking calculations of KV7.1 conformers by two K_V7 specific ligands, and the CHARMM parameterization of these ligands (Chapter IV.2.1). Finally, we also showed a new modulation mechanism of the $K_V7.1$ subunits by the KCNE2 ancillary subunit that might constitute a major interest to be investigated, given its role in the development of the type 2 diabetes (Chapter IV.2.2).

Chapter IV.1. Predicting the overall $K_V7.1$ function

Several gating models have been proposed to schematize the main function of various voltage-gated ion channels [341], including Ca^{2+}-dependent K^+ channels [342, 343], $K_V1.2$ channel [344, 345], and $K_V7.1$ channel in particular [152, 156, 245, 257]. Considering the numerous experimental results which provided hints on the structure and the function of both $K_V7.1$ channel and the IK_S complex, the clearest approach to describe and understand the function of $K_V7.1$ channel was to consider the protein as an allosteric one. Indeed, its structure satisfies all the criteria of the structure-cooperativity relationship defined by Monod, Wyman and Changeux [346], as $K_V7.1$ tetramer possess a pair number of identical subunits with a four-fold rotational symmetry axis.

When the concept of allostery is applied to voltage-gated ion channels, pore opening/closing transition is considered as the main function of the allosteric protein [347]. In addition, the VSD activation and deactivation occur when S4 moves along the electric field created by membrane depolarization and hyperpolarization, respectively. Accordingly, the VSD of $K_V7.1$ channel can adopt three distinct conformations that induce PD opening/closing which itself directly depends on the VSD-PD coupling. This mechanism, considered here as an allosteric one according to the Monod-Wyman-Changeux (MWC) criteria, takes place at the interface between S4-S5L and the cytoplasmic part of S6. As such, this state-dependent S4-S5L/S6 interface is considered here as an allosteric site. In a protein which satisfies the MWC kinetic model, its function is defined by conformational changes that involve concerted motions at the level of this allosteric sites.

To that extent, several studies were conducted in order to determine if the mechanism of VSD activation was concerted or sequential in the four monomers. In the absence and the presence of KCNE1, several functional studies have demonstrated that the VSD motions of $K_V7.1$ subunits were sequential [152, 348, 349], while another one suggested that in presence of KCNE1, the VSD activates in two steps, the first one through sequential movements, the second one through a concerted movement [153, 185].

By performing VCF measurements on K_V7.1 channel mutants which prevent the VSD of each monomer from reaching the resting state (R228Q) and the activated state (R243Q), a VCF study [152] demonstrated two main modifications. The voltage-dependence of their both fluorescence and conductance signals were shifted to hyperpolarized and depolarized voltages, respectively, in relation with those recorded for WT K_V7.1 channel. By combining the resting and activated mutants with two subunits of each in one K_V7.1 tetramer, the fluorescence signals remained unchanged with respect to the four monomer mutants, but the G/V curves were shifted back to those of WT K_V7.1 channel, suggesting that VSD activation are not concerted, but VSD-PD coupling and PD opening might be probably concerted, which somehow supports the MWC model. A recent similar study performed VCF measurements on a K_V7.1 tetramer in which two subunits out of four contained the E160R mutation, known to prevent VSD activation, in the presence of KCNE1 [349]. While no fluorescence signals were recorded for these mutated VSD, as expected, the voltage-dependence of the VCF signals of the WT remaining VSD were shifted to more depolarized voltages in comparison with those of WT K_V7.1+KCNE1 construct. However, the voltage-dependence of channel conductance remained unchanged, suggesting that two activated VSD are enough for PD opening in presence of KCNE1 as well.

A second study reported the results of site-directed mutagenesis [348], in which they built concatenated K_V7.1 tetrameric mutants that prevent the VSD from reaching the resting state (R231W) and the activated state (R243W), respectively, as well as a third constitutively open (L253K) K_V7.1 channel mutant, all in an increasing number of subunits, ranging from one to four. They performed patch-clamp recording of these mutants in both the absence and the presence of KCNE1, in both whole-cell and inside-out configurations in mammalian cells, and the resulting G/V curves turned out to be quite interesting.

Indeed, in the absence of KCNE1, the minimal conductance of R231W and L353K mutants was gradually increasing, respectively, with the number of mutated subunits. In addition, the voltage-dependence of gating was gradually hyperpolarized as the number of mutated subunits increased up to 3 subunits, as the results obtained for the channels with four mutated subunits were similar to those of three mutated ones. These results agree with the previous study [152] that suggested that $K_V7.1$ PD opening can occur when at least two VSD are activated in absence of KCNE1. However, the results obtained for R243W are not following the same trend. Even though the maximal conductance was slightly increasing with the number of mutated subunits, no shift in voltage-dependence nor changes in minimal conductance were observed. In the presence of KCNE1, the effects of R231W mutants were slightly less pronounced, while those obtained for L353K were not observed [348].

This indicate that the ancillary subunit, by inhibiting VSD-PD coupling in both the resting and intermediate states of $K_V7.1$ subunits [161], might somehow bypass the gain-of-function effects of R231W and L353K, confirming that an activated VSD induces pore opening, while an open pore induces VSD activation. However, the results obtained for R243W mutant are showing that the voltage-dependence is gradually shifted to more depolarized voltages as the number of mutated subunits increases, which confirms that R243W mutant destabilizes VSD-PD coupling of IK_S AO state, in agreement with previous functional studies [161]. These results are not in agreement with the other studies that suggested that the presence of KCNE1 was somehow requiring the activation of all the VSDs prior to pore opening [153, 184, 350].

According to the MWC kinetic model, the allosteric relationships of a voltage-gated ion channel requires that allosteric transitions from closed state to open state alter the energetics of VSD activation, and vice-versa. Considering the results presented in the previous paragraph, despite the sequential motion of the VSD, these results cannot rule out the possibility of cooperative VSD-PD coupling and/or pore opening/closing mechanism. As a consequence, we still can hypothesize that both mechanisms are concerted, in which PD opening is assimilated as an allosteric transition induced by the structural change of the VSD-PD coupling interface.

The simplicity of the MWC model also allows to facilitate the description of the modulatory effects of allosteric effectors such as the PIP_2 lipid, KCNE1 ancillary subunits and more recently, Calmodulin [351, 352] on the gating properties of $K_V7.1$. To that extent, our collaborators have demonstrated that the VSD-PD coupling of the $K_V7.1$ channel depends on PIP_2, which acts as a cofactor in the VSD-PD coupling mechanism of $K_V7.1$ channel, by inducing pore opening when the VSD is activated, while inducing VSD activation when the pore is open [248]. In addition, our simulations revealed that the VSD-PD coupling mechanism induces a modification of PIP_2 binding site of $K_V7.1$ which shifts along the inner membrane surface between S4 residues in resting state and S6 residues in AO states, through S2-$S3_{LOOP}$ in both states [353]. Altogether, these results suggest that PIP_2 might act as an allosteric activator of the $K_V7.1$ tetramer, as it induces a catalytic effect (by promoting VSD-PD coupling mechanism) on $K_V7.1$ activity. Hence, if we assume $K_V7.1$ channel as an allosteric protein, the transmembrane potential would be its substrate, while PIP_2 would act as its cofactor, and KCNE1 would act as an allosteric inhibitor of $K_V7.1$, considering its right-shifting effect on the voltage-dependence of $K_V7.1$ VSD-PD coupling, as well as and its slowing effect of $K_V7.1$ activation/deactivation kinetics. Therefore, we started from the gating model we previously determined for $K_V7.1$ channel [156] to hypothesize that PIP_2 will induce $K_V7.1$ pore closure when the VSD reaches its resting state, and pore opening when the VSD reaches both intermediate and activated states (Figure IV.1, A). In presence of KCNE1, we hypothesize that the β-subunit and PIP_2 are both inducing pore closure when the VSD reaches resting and intermediate state, while inducing and enhancing pore opening only when the VSD reaches its activated state (Figure IV.1, B).

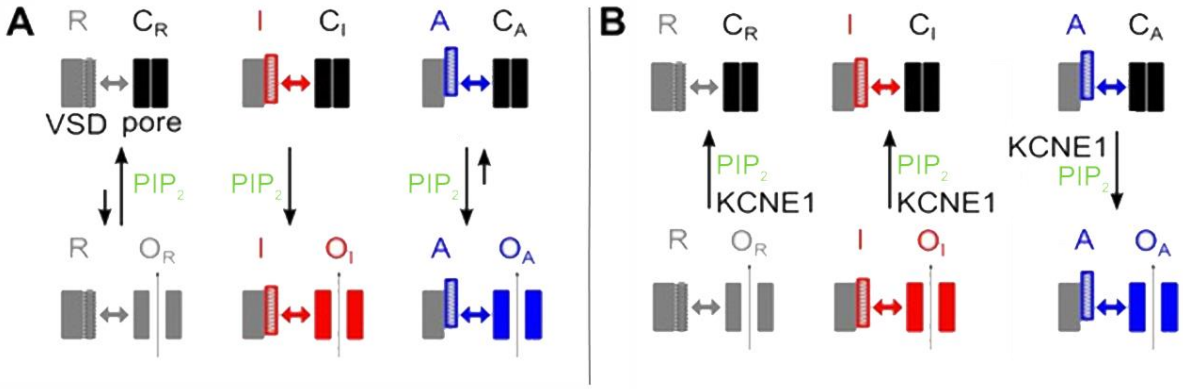

Figure IV.1.1: Schematic kinetic gating models of $K_V7.1$ channel and IK_S complex.
The pictures are showing the influence of $K_V7.1$ effectors (KCNE1, PIP_2) on the open (O)/closed(C) state equilibrium in each state (resting (R), intermediate (I), activated (A)) of the VSD, **A.** in the absence and **B.** in the presence of KCNE1. In both panels, the longest arrows are showing the direction of the equilibrium shift between open and closed conformation. The effectors that favor equilibrium shifts are indicated beside the arrows.

Indeed, KCNE1 modifies the affinity between the $K_V7.1$ channel and its cofactor PIP_2, as the dependence of PIP_2 for $K_V7.1$ subunit function was proved to be increased in presence of KCNE1 due to its additional positive charges in its C_{TER} domain [162]. In the frame of this functional study, Li et al. calculated the Hill coefficient [346] of the channel in order to assess the cooperativity associated with $K_V7.1$-PIP_2 binding upon membrane depolarization. In the absence of KCNE1, the Hill coefficient n_H was equal to 1.0, which indicates an absence of cooperativity for this protein-lipid interaction. However, in presence of KCNE1, the Hill coefficient n_H turned out to be increased up to 2.0, indicating a significant cooperativity for the protein-lipid interaction. This coefficient indicates that the presence of KCNE1 increases the cooperativity between $K_V7.1$ subunits and PIP_2, while confirming the inhibitory effect of KCNE1 on the VSD-PD coupling of $K_V7.1$ intermediate state [156, 161].

Overall, the allosteric transition mechanism of the $K_V7.1$ channel can be described as follows: the transmembrane potential changes account as the catalysts of voltage-gated ion channels, on which the motion of S4 gating charges (the substrates) depends. This VSD motion will induce a conformational change in both the active site (E1-S4 gating charge) and the allosteric site (VSD-PD coupling interface), leading to PD opening (Figure I.4.2.7). Interestingly, the mechanisms of VSD activation and VSD-PD coupling/PD opening of $K_V7.1$ channel appear to be well described by two distinct models. The functional studies which aimed as describing the allosteric gating of $K_V7.1$ channel showed that the motion of the VSD would rather be described by the Koshland-Némethy-Filmer (KNF) kinetic model [354] in which the conformational change of each subunit induces a small change in the whole protein conformation, leading to a complete transition of the oligomer once all the subunits conformation have changed. Nevertheless, these functional studies could not invalidate the idea that the motions of VSD-PD coupling/PD opening can be easily described by the MWC model.

In the first part of this chapter, we have thoroughly described the specific role played by $K_V7.1$ α-subunits, KCNE1 β-subunits, and PIP_2 lipids in the frame of a functional mechanism that satisfies the MWC model criteria. In the second part of this chapter, we have presented the numerous possible applications for our atomistic models, whose robustness have been proven by our results, including those validated by additional experimental studies.

The combination of the results we obtained confirmed our hypotheses, as the function of $K_V7.1$ channel, as well as its modulation by KCNE1 and PIP_2 hint to an allosteric mechanism. Considering the tetrameric structure of $K_V7.1$, its activation mechanism can be easily presented using the terms employed in the Monod-Wyman-Changeux kinetic model applied for allosteric enzymes. Despite the fact that the channel is not an enzyme *per se*, one can assume that PIP_2, due to its crucial role in the channel's function, can be considered as *both* its co-factor and allosteric activator, while KCNE1, due to its modulatory effects, can be considered as *both* its co-factor and allosteric inhibitor.

Chapter IV.1.1. VSD activation: PIP_2 as a $K_V7.1$ allosteric activator

Based on experiments and molecular modeling investigations of various K_V channels, there is a general consensus that S4 undergoes a clockwise rotation and a significant translation toward the extracellular surface of the membrane during their VSD activation [167]. The upward translation ensures interactions between S4 basic residues and negative residues from S2 as well as the sequential transition of S4 basic residues through the so-called charge transfer center. The analyses we conducted in order to validate our models of $K_V7.1$ channel against experimental data allowed for the identification of the molecular aspects of the state-dependent salt-bridges that stabilize two S4 gating charges in two negatively charged binding sites, located in S2 and S3 (see Chapter III.1.1). Our previous and present MD simulations suggest that PIP_2 intra may also constitute a (third) binding site for the S4 gating charges. Indeed, the lipid was found to form salt-bridges with R237 (R4) and R243 (R6) in RC and intermediate models of $K_V7.1$, and not in the AO model, in both the absence and the presence of KCNE1 (Figure IV.1.1.1). Furthermore, the neutralizing R243H [355, 356] and R243P [357] mutations are both associated with LQT syndrome, which indicate that its interaction with PIP_2 is crucial for the IK_S channel function, supporting the idea that PIP_2 might act as an additional binding site for the S4c gating charges R237 and R243 involved in VSD-PD coupling through its motion along the inner membrane.

In addition, R243 binds the charge transfer center when the VSD is activated, which also indicates that a mutation of the latter into Histidine might weaken its interaction with the CTC, and therefore the VSD conformation that allows to maintain the activated state, as well as the diffusion of the IK_S current during membrane repolarization. These state-dependent interactions between PIP_2 and the VSD agree with the previous studies conducted by our collaborators which suggested that PIP_2 favors pore opening of $K_V7.1$ when its VSD is in the activated state [248].

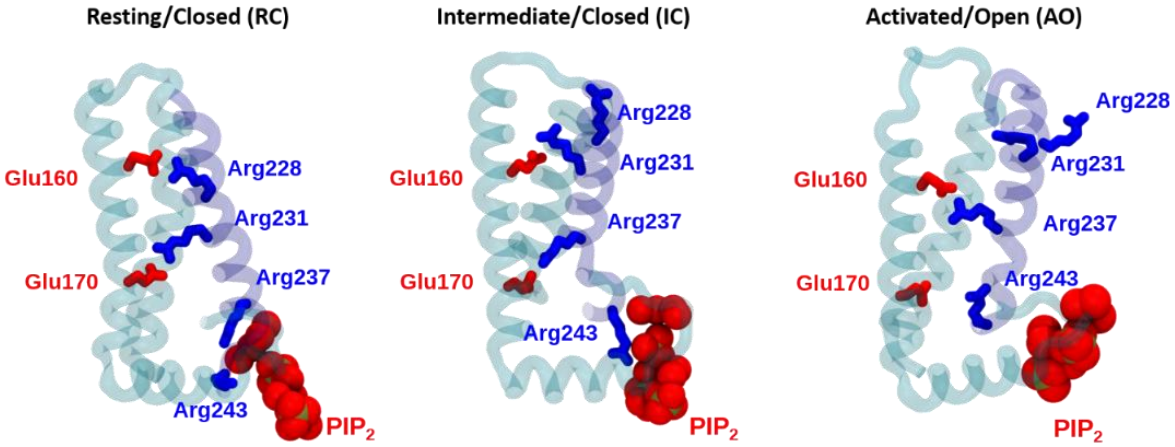

Figure IV.1.1.1: State-dependent interactions between S4 and PIP_2 in IK_S models.
This picture shows a cartoon representation of the $K_V7.1$ VSD segments in IK_S RC (left), IC (middle) and AO (right) models. S3 segment is hidden for clarity. S4 segment is depicted in transparent blue, while the rest of the VSD is depicted in transparent cyan. PIP_2 phosphate groups are represented in spheres, while S4 gating charges are shown in blue sticks. Their binding sites are shown in red sticks.

Interestingly, an integrative study was conducted on the recent structures of the $K_V7.1$ channel, resolved through CryoEM along with calmodulin (CaM) [79]. By combining functional studies and machine learning methods of molecular dynamics data [351], the authors suggest that both PIP_2 and CaM are able to interact with $K_V7.1$ in the PIP_2 intra binding site (located in S2-S3 loop), but not in the same state. MD simulations and DMC analyses both highlighted the H-bond interaction between CaM residue Y100 and residue S182 in IO state, while the depolarizing effects of R181H mutant on $K_V7.1$ activation was interpreted as a specific AO state binding between R181 and PIP_2. Despite the fact that these reported results describe the impact of CaM interactions in the gating mechanism of the $K_V7.1$ channel, the PIP_2 binding site we identified on the $K_V7.1$ models [249] and the IK_S ones (Chapter III.1.2) cannot be ruled out, as the S2-S3 loop residues that interact with PIP_2 in a state-independent fashion in our models have not been shown to interact with CaM in this recent study.

Chapter IV.1.2. VSD-PD coupling: KCNE1 as a $K_V7.1$ effector

In the frame of the allosteric properties of the IK_S complex, the state-dependent VSD-PD coupling interfaces we identified for the $K_V7.1$ IO state and both the $K_V7.1$ and IK_S AO states are indeed inducing a sort of catalytic effect on the channel which is characterized by the opening of the pore to conduct potassium ions. KCNE1 acts as an antagonist in both resting and intermediate states of $K_V7.1$, inhibiting the VSD-PD coupling mechanism by disrupting its key state-dependent and state-independent interactions (Chapter III.2.2). In the activated state, KCNE1 acts as an agonist of the coupling due to a conformational change which allows the ancillary subunit to engage into protein-protein interactions which may probably stabilize the open conformation of the pore, as well as the activated conformation of the VSD. This might explain how the IK_S current is sustained for such a larger duration than the current generated by $K_V7.1$ subunits in absence of KCNE1.

The set of exquisite results we collected from MD simulations of our models of $K_V7.1$ channel in absence and presence of KCNE1 allowed us to propose a description of two simple movements which explain its VSD-PD coupling mechanism. This mechanism is characterized by a motion of the PD cluster (W248 R249 L250 L251 V254 V255 F256 H258 and R259 from S4-$S5_{LINKER}$, residues E261 L262 from S5 and residues I346 L347 and V355 from S6) which translates upwards from the bottom of an adjacent S6, while rotating towards the bottom of S4 of its own subunit (Figure III.2.1.13-14). Indeed, in $K_V7.1$, the PD cluster residues are spread in two opposite areas with specified missions. The outer pore surface contains the hydrophobic residues W248 and L251 which are engaged in state-dependent interactions, depicting an upward movement of S4-$S5_{LINKER}$ along its adjoining PD segments to reach the bottom of S4 and S2-$S3_{LOOP}$ through R249-PIP_2 interaction in the AO model. This motion has been shown to be triggered by the VSD activation, defined by an upward motion of S4 along the electric field induced by membrane depolarization in excitable cells. The inner pore surface contains S4-$S5_{LINKER}$ residues engaged in state-independent VdW interactions with both S5 and S6 residues from the same subunit, which suggests a pulling of S6 segments from the pore axis toward the inner membrane surface upon S4 and S4-$S5_{LINKER}$ movements during VSD activation.

The specificity in our IK_S models in relation with the various IK_S models reported so far [154, 250–252, 337, 358] resides in the fact that the presence of PIP_2 intra is acting as a hook to ensure the leverage effect of $S4\text{-}S5_{LINKER}$ on S6 cytoplasmic region. Indeed, R249 from $S4\text{-}S5_{LINKER}$ is interacting with PIP_2 intra in all models, while PIP_2 intra itself progressively anchors $S2\text{-}S3_{LOOP}$ during S4 activation, while maintaining the $S4\text{-}S5_{LINKER}$ close to the inner membrane surface (Chapter III.2.4). Interestingly, the absence of PIP_2 in the $KCNQ1_{EM}$ structure results in a $S4\text{-}S5_{LINKER}$ located far from the $S2\text{-}S3_{LOOP}$ and rather bound to the S6 cytoplasmic region, leading to the three major constriction zones which close its conduction pathway.

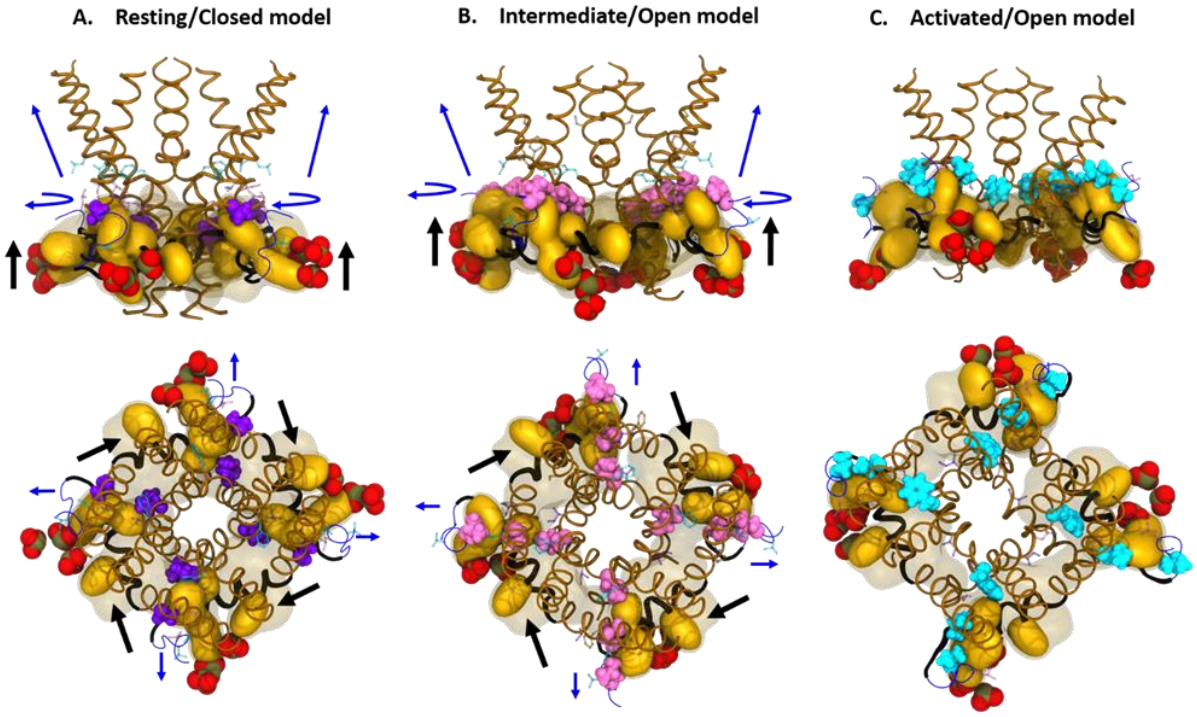

Figure IV.1.2.1: Prediction of $K_V7.1$ VSD-PD coupling mechanism which mediates RC→IO and IO→AO transitions of PD cluster in absence of KCNE1.
Side view (top) and extracellular view (bottom) of $K_V7.1$ transmembrane segments (in ribbons) involved in VSD-PD coupling mechanism, such as S4 (blue), $S4\text{-}S5_{LINKER}$ (black), and PD segments (brown). PD cluster residues are represented in transparent yellow surface, while PD cluster hook residues W248 R249 and L251 are represented in solid yellow surface. Residues that interact with PD cluster are represented in spheres, while those which do not are represented in transparent sticks. These residues are colored in purple in **A.** RC model, in pink in **B.** IO model and in cyan in **C.** AO model. PIP_2 phosphate groups are represented in red spheres. Translational motions $S4\text{-}S5_{LINKER}$ (black arrows), are triggered by those of S4 (blue arrows) during VSD activation.

Specifically, the MD analyses conducted on our IK_S models has shown that the presence of KCNE1 modifies the mechanism of $K_V7.1$ channel in such a way to split the movements of PD cluster hook residues into two distinct transitions. The upward translation of the PD cluster, driven by L251, occurs during the IK_S RC-IC transition, while the anticlockwise rotation of the PD cluster, driven by W248, occurs during the IK_S IC-AO transition.

At the end of the RC-IC transition, the IK_S channel is more likely to be closed, as the VSD-PD coupling mechanism is not completed in presence of KCNE1. Indeed, the protein-lipid component of this mechanism constitutes a tourniquet for S6 helices, preventing them from reaching the inner membrane surface, and leading to the interaction between the PD cluster and S4 as seen in both $K_V7.1$ IO and AO models. Besides, the presence of KCNE1 involves the participation of a third hook residue, F256. Located on the outer surface of the PD cluster, it directly interacts with KCNE1 in the IK_S IC model, which may hinder the progression of $S4\text{-}S5_{LINKER}$ along the membrane inner surface when the VSD adopts its intermediate conformation. As a consequence, the conduction pathway of the IK_S IC state is more likely to be closed, as found in its pore radii calculations.

During the IC-AO transition, KCNE1 loses its interaction with PIP_2 intra, which is allowed to anchor the PD cluster to the bottom of S4 segment and $S2\text{-}S3_{LOOP}$ in the AO state, while shifting the S6 cytoplasmic region away from the pore axis to open the pore, as the protein-lipid tourniquet around S6 helices (Figure III.2.4.1) has been dismantled (Figure IV.1.2.2, C). Through an additional H-bond interaction between Y46 and S6 residue S330 in the extracellular side of the lipid bilayer (Figure IV.1.2.2, C, cyan sticks) KCNE1 may enhance the ionic current of $K_V7.1$ subunits. As a matter of fact, this interaction may possibly explain the experimental results obtained for the IK_S channel mutant Y46A [195], whose current amplitude is lower than the wild-type IK_S channel current. These results have provided a molecular scale comprehension of the numerous experimental studies which unraveled the key aspects of VSD-PD coupling and the way KCNE1 can possibly modulate this mechanism.

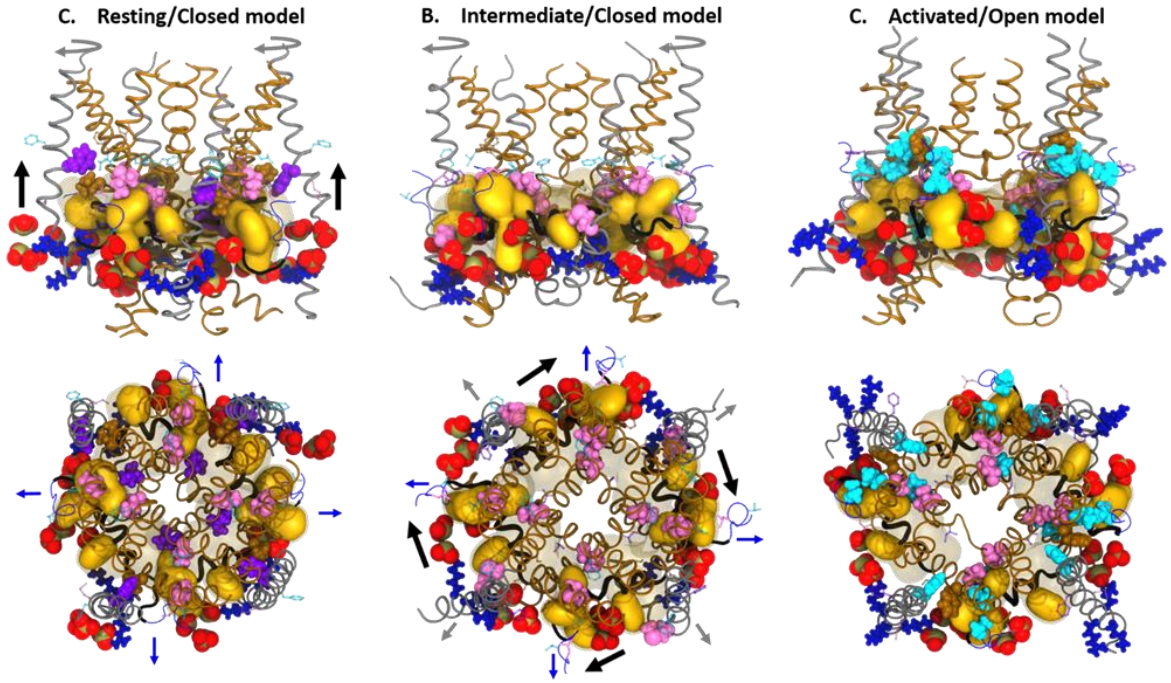

Figure IV.1.2.2: Prediction of K_V7.1 coupling mechanism which mediates RC→IC and IC→AO transitions of PD cluster in presence of KCNE1.
Side view (top) and extracellular view (bottom) of IK_S transmembrane segments (in ribbons) involved in VSD-PD coupling mechanism, such as S4 (blue), S4-$S5_{LINKER}$ (black), PD segments (brown) and KCNE1 (gray). PD cluster residues are represented in transparent yellow surface, while PD cluster hook residues W248 R249 and L251 are represented in solid yellow surface. Residues that interact with PD cluster are represented in spheres, while those which do not are represented in transparent sticks. These residues are colored in purple in **A.** RC model, in pink in **B.** IO model and in cyan in **C.** AO model. KCNE1 basic residues and PIP_2 phosphate groups are depicted in blue and red spheres, respectively. Translational motions of S4, S4-$S5_{LINKER}$ and KCNE1 are represented by blue, black, and grey arrows, respectively.

Overall, we have shown that protein-protein and protein-lipid components of K_V7.1 VSD-PD coupling mechanism are mediated by a cluster of 12 residues which are mostly hydrophobic and involved in state-dependent intersubunit VdW interactions between S4-$S5_{LINKER}$ and both S5 and S6 segments, as well as state-independent intrasubunit VdW interactions between hydrophobic residues from S4-$S5_{LINKER}$ and S6. This coupling mechanism we unveiled is similar to the mechanical lever model, in which S4 upward movement drags a S4-$S5_{LINKER}$ stuck to S6 cytoplasmic region, leading to pore opening of homologous K_V1 channels [247], as well as the reported integrative study conducted on homologous Shaker channel [359]. The large number of VdW interactions we have determined for the PD cluster residues testify for their importance in the coupling mechanism. Indeed, among the 12 PD cluster residues, 10 are associated with LQTS when deleted or mutated into residues whose sidechains are of either different size or chemical property (Tab IV.1.2.1).

For aliphatic residues, these pieces of information provide additional evidences of the importance of VdW interactions in conformational changes undergone by IK_S ion channels during membrane depolarization.

K_V7.1 residue	**Segment**	**LQTS mutation(s) [reference]**
W248	S4-S5$_{LINKER}$	W248R [360]
L250		L250H [361] L250P [136]
L251		L251P [362]
V254		V254M [127, 363, 364] V254L [365]
V255		Deletion V254-V255-F256 [365]
F256		
H258		H258R, H258N [365]
R259		R259H [357] R259L [364] R259C [366–368]
E261	S5	E261K [363] E261Q, E261D [136]
L262		L262V [365]

Tab IV.1.2.1: PD cluster residues associated with LQTS mutations.

Interestingly, our MD simulations of the AO state models of IK_S ($4PIP_2$ and $8PIP_2$) revealed an additional binding site for S4 gating charges which appears to be elicited by the presence of KCNE1 (Figure IV.1.2.3). Indeed, in IK_S models, R228 binds the residue D286 from the S5-P loop of an adjacent subunit (Figure IV.1.2.3, A-B, left panels). This binding site, which is absent in K_V7.1 AO and AC models (Figure IV.1.2.3, A-B, right panels), has also been reported in the K_V1.2 channel [369], in which the homologous residues R294 and D352 (Figure IV.1.2.3, C) are engaged in a H-bond interaction. Noteworthy, the second PIP_2 binding site induced by KCNE1, revealed by functional studies [162] along with the concerted action of both KCNE1 and PIP_2 inter to seal the conduction pathway in RC and IC states, and to enlarge the latter in AO state (Chapter III.2.4) revealed by our MD analyses, indicate that KCNE1 may have a positive heterotropic effect on the association between K_V7.1 and PIP_2.

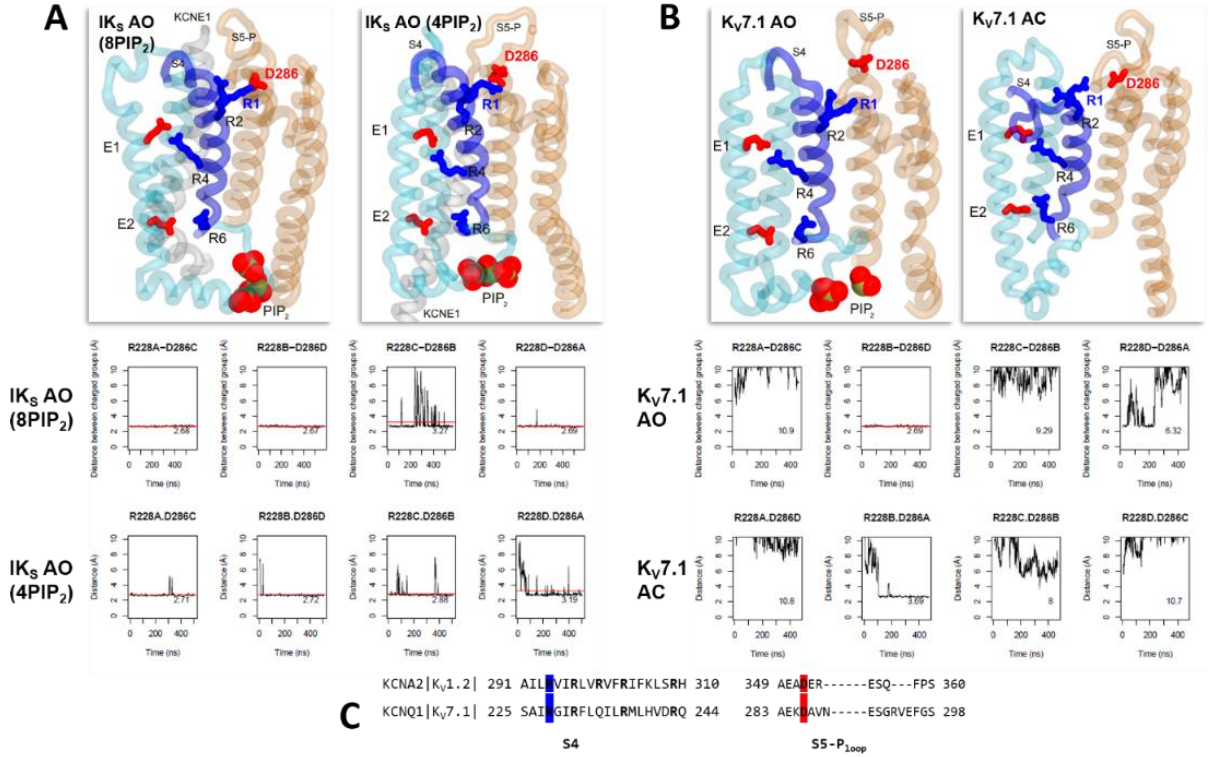

Figure IV.1.2.3: A S5 binding site for the first S4 gating charge in IKS models.
A-B.The upper panels display a transparent colored cartoon representation of the VSD (cyan) and the PD (orange) of two adjacent subunits, along with S4 (blue), its gating charges R1 (R228), R2 (R231) R4 (R237) and R6 (R243), depicted in blue sticks, as well as their countercharges E1 (E160), E2 (170) and D286, depicted in red sticks, and PIP_2, whose phosphate groups are depicted in red spheres. S3 segment has been hidden for clarity in **A.** IK_S models, in which KCNE1 segments are colored in gray; and **B.** $K_V7.1$ models. The lower panels shows the time evolution of the distance between R228 and D286 in each subunit (A,B,C,D) of $K_V7.1$ tetramer. A red line is present in the residue pairs whose average distance is below the distance cut-off of 3.5Å, suggesting a electrostatic ineraction. **C.** Sequence alignment of S4 and S5-P loop of $K_V1.2$ and $K_V7.1$. The residues of interest, R228 and D286 in $K_V7.1$, are highlighted in blue and red, respectively.

Thanks to the predictions we made for this mechanism, and their functional validation, we managed to predict, at a molecular level, a possible way in which KCNE1 subunit can inhibit this electromechanical coupling mechanism in both the RC and the IC states of $K_V7.1$ on one hand, while enhancing this same mechanism in the AO state of $K_V7.1$. The split of S4-$S5_{LINKER}$ motion during the VSD-PD coupling, and the effects of this split on the pore opening mechanisms of $K_V7.1$ subunits in presence of KCNE1 is also supported by the results obtained from a second structure-based model of the modulation of $K_V7.1$ activation by KCNE1 [358]. Indeed, our MD trajectories allowed for the prediction of two possible pore opening mechanisms, each specific for the IO and the AO states of $K_V7.1$, respectively. In the next section, we will describe in detail how KCNE1 subunits are, in addition to the electromechanical VSD-PD coupling mechanism, inhibiting the IO state pore opening mechanism, while enhancing the AO state specific pore opening mechanism.

Chapter IV.1.3. K_V7.1 pore opening mechanism is triggered by a wheelwork of conformational changes related to both VSD activation and VSD-PD coupling mechanisms

In this present work, we showed that the K_V7.1 pore gating mechanism is mediated by the state-dependent interactions of the SFF motif with residues from both the PD middle and PD bottom pocket (also named PD cluster). The MD trajectories suggest that these hydrophobic pockets act as double adhesive tape band, by communicating with the SFF residues on one hand, and with the S4 residues I235 and L236 on the other hand, in a state-dependent fashion (Figure IV.1.3.1). These S4 residues were reported to affect K_V7.1 VSD-PD coupling in absence [370] and presence [161] of KCNE1. In addition, the mutation I235N is associated with LQTS [309]. Through their state dependent VdW interactions with S1, S3 and with both PD pockets, these residues may possibly stabilize the position of S4 segment within the lipid bilayer. Yet the position of PD middle pocket residues, along with their interactions with SFF residues, turn out to depend themselves on the state-dependent position of S4 segment. This conformational interdependence between VSD residues and PD residues strongly support the idea of K_V7.1 function being mediated by an allosteric mechanism.

Indeed, the MD trajectories obtained for K_V7.1 models revealed that in the RC state, I235 interact with both S1 and PD middle pocket residue L271, while L236 is bound to the PD middle residues I268 and L271. These interactions might lock the S5 helix in an orientation which favors F339 anchoring into the PD middle pocket, and thereby the "inside" conformation of F340 sidechains. During the transition to the IO state, S4 moves upwards and rotates clockwise. Hence, in the IO state, I235 loses its interaction with S1 while remaining bound to the PD middle pocket through its interaction with L271, while L236 reaches S3 residue I201. This translational and rotational motions of S4 triggers S4-S5L motion and therefore the PD bottom pocket, yielding to an interaction between L239 and W248. In addition, S5 pocket residues Y267 and F270 are both binding the middle of S1 segment, while G269 remains bound to F339 during RC-IO transition. Thus, the PD middle pocket appears to pull F339 away from the pore axis, which leads to the widening of the conduction pathway in K_V7.1 IO model.

During the transition to the AO state, the state-dependent interactions of these three residues suggest that S4 undergoes a second upward translation, as I235 reaches S5 residue F279, while L236 has gone upwards along S3 to bind V205. The IO-AO transition of K_V7.1 has also been shown to be characterized by a counterclockwise rotation of S4-$S5_L$ that has been shown to be necessary for its electro-mechanical coupling mechanism (Chapter III.2.2). This rotation might trigger a counterclockwise rotation of PD middle pocket. Given the state-independent intersubunit interactions between L266 and V334 and between T311 and I337 (see Chapter III.2.3), the rotation of PD middle pocket must induce a counterclockwise rotation of S6 at the level of the SFF motif. As a consequence, residues S338 and F339 bind the PD bottom pocket, while F340 sidechains move towards PD middle pocket, which triggers its "outside" conformation (and therefore the widening of the pore). Interestingly, a similar rotational movement of S6 has already been reported as eliciting pore gating in a homologous K_V channel [371].

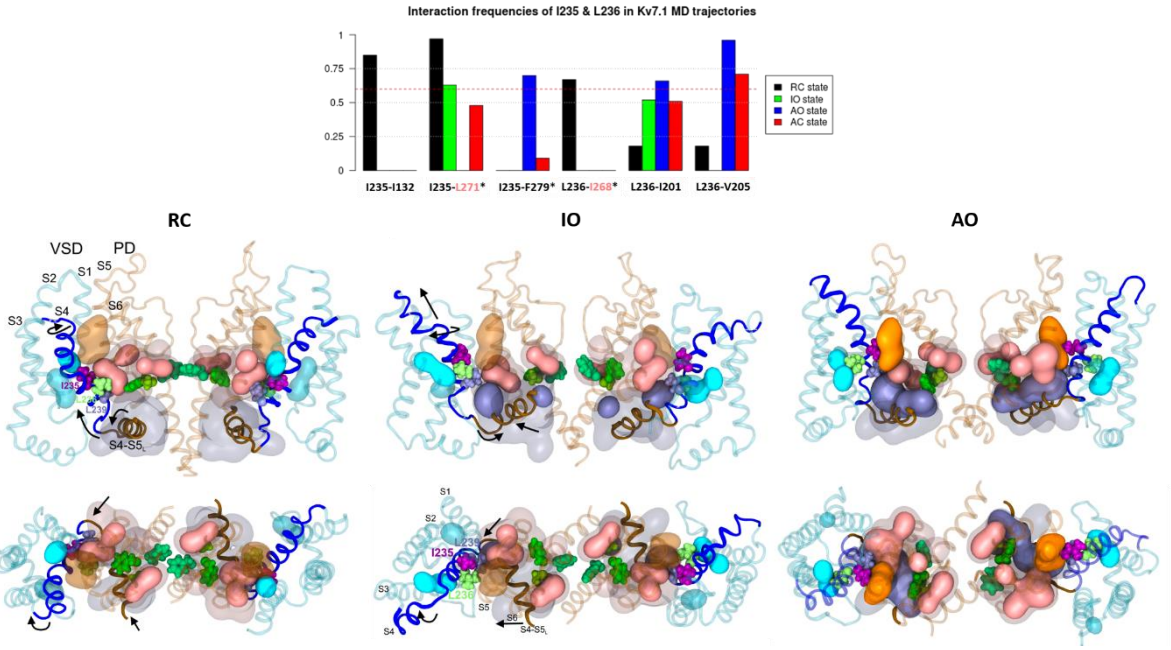

Figure IV.1.3.1: The motion of S4 aliphatic residues in K_V7.1 models.
The upper panel shows the state-dependent interactions in which S4 residues I235 and L236 are engaged in the RC (black) IO (green) AO (blue) and AC (red) states, respectively. The residue pairs marked by an asterisk are inter-subunit interactions. The residues colored in pink are PD middle pocket residues. The lower panel shows cartoon representations of two K_V7.1 VSD (cyan), S4 (blue) and S4-$S5_{LINKER}$ (brown) along with their respective adjacent PD (orange) in a side view (upper row) and a top view (lower row). SFF residues S338, F339 and F340 are represented in lime, bottle green and blue green shperes, respectively. PD middle pocket and PD cluster are shown in transparent pink and light blue, respectively. S4 residues I235, L236 and L239 are shown in purple, light green and light blue spheres, respectively. Their VSD and PD counterparts are shown in solid color surfaces, while the residues with which there are no interaction are shown in transparent ones. The movements of both S4 and S4-$S5_{LINKER}$ are shown in black arrows.

The analysis of the MD trajectories of the IK_S models suggest a slightly different mechanism, as the interactions of I235 and L236 in $K_V7.1$ and IK_S models are similar only in the RC states. In the IC state, the interactions we identified in the $K_V7.1$ IO model are modified (Figure IV.1.3.2). Indeed, I235 is not bound to the PD middle pocket, and L236 and L239 are not bound to I201 and PD bottom pocket, respectively. These interactions suggest that during the transition from the RC to the IC state, S4 moves upwards across the bilayer plan, without undergoing any rotational motion. This rotation is triggering an upward movement of $S4\text{-}S5_L$ which has been reported to be crucial for the electromechanical coupling of $K_V7.1$ channel alone [174, 176] is blocked by the presence of KCNE1, which itself rotates clockwise and repels S3 from S4 hydrophobic residues, as its TMD residue I61 forms a VdW interaction with $S2\text{-}S3_{LOOP}$ residue F193, which turns out to elicit a mild form of LQTS when mutated into a Leucine [372]. As a consequence, L236 cannot reach S3, nor does it leave space for PD middle residue Y267 to bind V133 from S1. In addition, the PD middle residue F270 interacts with L137 with a slightly lower frequency in comparison to the $K_V7.1$ IO model. These modifications impair the anchoring of F339 sidechains into the PD middle pocket. Furthermore, residue S338 is not interacting with PD bottom pocket as in $K_V7.1$ IO model. As a consequence, F340 sidechains remain close to each other despite significantly interacting with each other through π-stacking interactions. Hence, the conduction pathway does not widen in IK_S IC model as in $K_V7.1$ IO model.

During the IK_S IC-AO transition, the interactions of S4 hydrophobic residues suggest that S4 finally undergoes its clockwise rotation using $S2\text{-}S3_{LOOP}$ as a pivot center. Indeed, in the AO state I235 and L236 are bound to F279 and V205, respectively, as in $K_V7.1$ AO model. This interaction stabilizes the F340 “outside” conformation, as well as the S4 translation that has triggered the PD cluster residues in proximity with both S338 and F339 sidechains. This S4 rotation induces a counterclockwise rotation of the S5 pocket towards the F340 side chains. Besides, the S5 pocket residues L266 and F270 are both bound to F57 and F54, respectively from KCNE1 which also has undergone a second clockwise rotation, as its interaction with the $S2\text{-}S3_{LOOP}$ is absent in the AO state.

As a consequence, the S5 pocket is pulled away from the pore axis, as seen in the K_V7.1 IO model, while rotating anticlockwise along with S6 through the state-independent interaction between L266 and V334. This S6 rotation orients the sidechains of both S338 and F339 towards the PD cluster residues, and those of F340 towards the S5 pocket, inducing its "outside" conformation. Interestingly, the pore opening mechanisms predicted for both the K_V7.1 RC-IO and IO-AO transitions appear to occur simultaneously in the IK_S IC-AO transition. Indeed, the conformational change of the F340 sidechains and the translational movement of the S5 pocket, along the bilayer plan and away from the pore axis, were both predicted to occur during this transition.

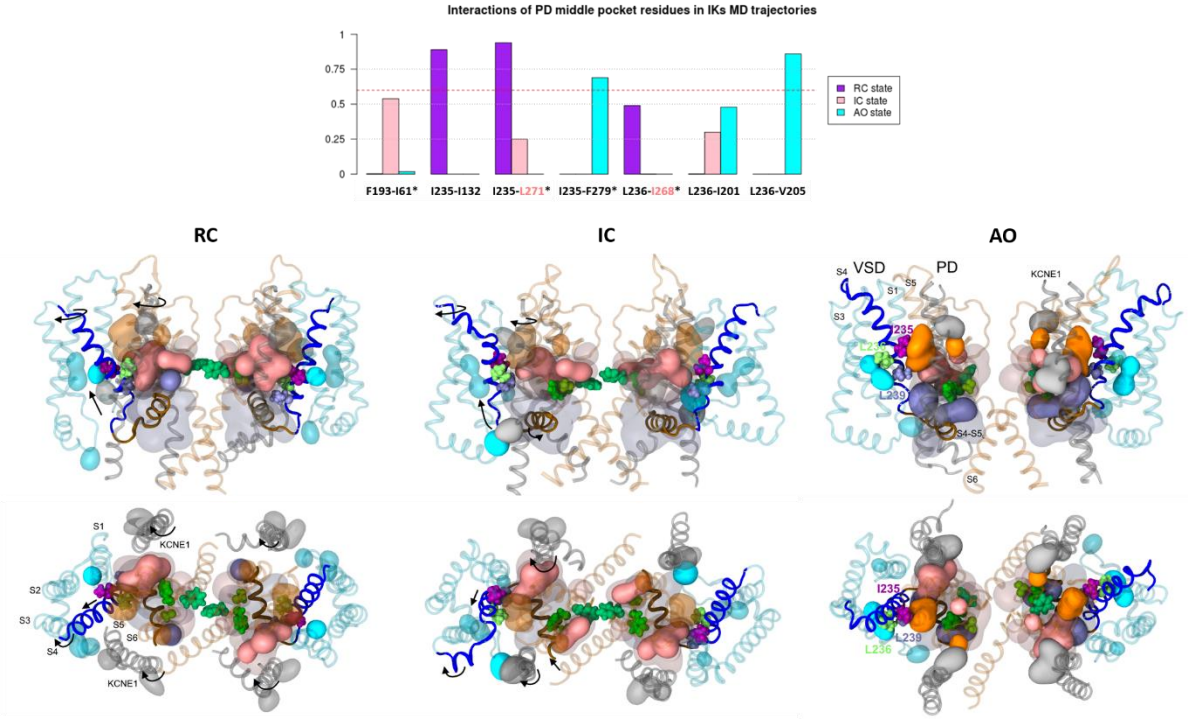

Figure IV.1.3.2: The motion of S4 aliphatic residues in IK_S models.
The upper panel shows the state-dependent interactions in which S4 residues I235 and L236 are engaged in the RC (purple) IC (pink) and AO (cyan) states, respectively. The residue pairs marked by an asterisk are inter-subunit interactions. The residues colored in pink are PD middle pocket residues. The lower panel shows cartoon representations of two K_V7.1 VSD (cyan), S4 (blue) and S4-$S5_{LINKER}$ (brown) along with their respective adjacent PD (orange) and KCNE1 (gray) in a side view (upper row) and a top view (lower row). SFF residues S338, F339 and F340 are represented in lime, bottle green and blue green shperes, respectively. PD middle pocket and PD cluster are shown in transparent pink and light blue, respectively. S4 residues I235, L236 and L239 are shown in purple, light green and light blue spheres, respectively. Their VSD, PD and KCNE1 counterparts are shown in solid color surfaces, while the residues with which there are no interaction are shown in transparent ones. The movements of S4, S4-$S5_{LINKER}$ and KCNE1 are shown in black arrows.

Noteworthy, the mechanism we presented here involves additional residues which have been associated with LQTS mutations (Tab IV.1.3.1), adding weight to their putative importance in the function of IK_S channel complex.

K_V7.1 residue	**Segment**	**LQTS mutation(s) [reference]**
V133	S1	V133I [365]
F193	S2-S3$_{LOOP}$	F193L[372]
I204	S3	I204M [373] I204F [365]
V205		V205M
L266	S5	L266P [134]
G269	S5	G269S [150, 364, 374] G269D [363, 364]
V310	P helix	V310I [134]
T311	Selectivity filter	T311I [355]

Tab IV.1.3.1: LQTS related residues involved in KV7.1 function according to MD simulations.

Our present work allowed us to predict possible transition mechanisms from the RC to the AO state for both K_V7.1 and the IK_S channels. Our investigations suggest a pore opening mechanism that involves a system composed of S1, S2-S3$_{LOOP}$, S5 and S6 transmembrane helices which rotate while binding each other as a wheelwork. In each VSD state, F339 and F340 interactions are more stable in absence of KCNE1. Indeed, the KCNE1's TMD residues interact with both the PD cluster residues we identified in a previous study (see Chapter III.2.2) and the PD middle pocket residues identified in this study. These interactions may add a supplementary energetic cost for the SFF residues to undergo a conformational change during the transition between the RC and IC states of IK_S complex. The conformational transition from the IK_S IC to AO state also requires higher-energy interactions in comparison with the K_V7.1 IO-AO transition. The relative positions of most of the residues are in agreement with functional results of alanine-scanning, [333] tryptophan-scanning [161] and the double mutant cycle analyses [323] which bring substantial support to our models.

Chapter IV.2. Perspectives: Atomistic scale investigation of the effects of other K_V7.1 effectors

Summing up our work presented in the present manuscript, we have built models of K_V7.1 channel in the absence and the presence of KCNE1 β-subunits and PIP_2 lipids whose features are in good agreement with experimental data. The trajectories that have been generated by MD simulations of these models shed light on the participation of both PIP_2 and the KCNE1 subunits in the K_V7.1 channel function in cardiomyocytes, in which K_V7.1 and KCNE1 subunits are responsible for the IK_S current. The extensive analyses of these MD trajectories led us to extract a set of 12 residues which play a central role in both K_V7.1 VSD-PD coupling and PD opening mechanism. It also led us to determine the way in which PIP_2 lipids work in concert with the KCNE1 subunits to modulate the conformation of the conduction pathway of K_V7.1. Altogether, these innovative results make our 3D models reliable and robust enough to be used for more advanced computational studies of the function of both K_V7.1 and IK_S, as their features allow for the explanation of the macroscopic ionic currents measured on K_V7.1 channel *in vitro* in presence or absence of KCNE1 and/or PIP_2 lipids [255].

The extended dataset of conformations generated by the MD simulations of our models of K_V7.1 can be used to perform further investigations of the mechanistic aspects we predicted. For instance, free-energy calculations would allow for the determination of the energetic aspects of the transitions between the stable states of K_V7.1 subunits, in absence and presence of KCNE1. Such calculations have already been conducted on the homologous K_V1.2 channel [375], and the obtained results are shown to provide crucial information in the comprehension of its VSD activation. In addition, brownian dynamics simulations can also be performed on these models in order to estimate *in silico* the state-specific conductances of K_V7.1 channel [376, 377]. The results obtained would provide additional weight to the robustness and the reliability of our models in the prediction of the molecular determinants of K_V7.1 channel function. Recent advances in MD simulations, conveyed by the hydrogen mass repartitioning method [378], allow to perform the aforementioned simulations with a higher speed without requiring additional computer resources.

Considering the ubiquitous expression of $K_V7.1$ channel [199], the models we designed in the frame of this present work have a significant amount of scientific applications. Indeed, $K_V7.1$ channel is widely expressed in various other tissues and is therefore a therapeutic target for numerous pathologies. First, our models can provide useful hints for the study of $K_V7.1$ function in other tissues of the human organism, such as the pancreatic β-cells where the channel appear to play a significant role.

In addition, the mechanistic aspects we determined can be used to study the interactions of $K_V7.1$ channel [217] and IK_S complex [207, 379] with other KCNE ancillary subunits, as they were reported to modulate their function. In the case of IK_S complex modulation, the investigation can be facilitated since new CryoEM structures of $K_V7.1$ subunits were resolved along with both PIP_2 and KCNE3 ancillary subunits [79]. Our mechanistic results can as well be used to unravel the function of related K_V channels, as the key residues we identified and validated through functional studies turned out to be evolutionarily related with most domain-swapped K_V channels [323] through statistical coupling analysis [380].

Chapter IV.2.1. Molecular modeling of IK_S channel along with small compound ligands

Considering the importance of the role played by the IK_S current in cardiac repolarization reserve, and its influence on the cardiac AP duration (QT interval) and the robustness of our built $K_V7.1$ molecular models make them suitable to be used as targets for structure-based drug design. Indeed, the plethora of interesting results we obtained from the simulation of our models provided crucial hints on the molecular mechanisms that underlie $K_V7.1$ function on one hand, and those that underlie $K_V7.1$ modulation by KCNE1 on the other hand, leading to the diffusion of IK_S current.

To date, several compounds were reported to be able to bind the $K_V7.1$ channel, including class I antiarrhythmic agents that act as non-specific channel blockers such as quinidine [381] and class III antiarrhythmic agents that also act as beta-blockers such as amiodarone [382] and its analog dronedarone [383]. Altogether, these three compounds [384] constitute the main anti-arrhythmic drugs for which approval for human use had been granted.

Finally, the IK_S channel complex started to be specifically targeted for antiarrhythmic treatment twenty years ago, leading to the development of KCNQ channel blockers such as chromanol 293B [385, 386], its analog HMR 1556 [384, 387], the benzodiazepines L7 [336] and L-768,673 [388] and the neural KCNQ blocker linopirdine, which was basically developed for the treatment of Alzheimer disease [389]. The linopirdine analog XE991 turned out to be potent against $K_V7.1$ [390] and its activity on voltage-gated ion channels has been largely studied until nowadays [156, 391]. As the IK_S channel was identified as the main target for the treatment of inherited LQT syndromes, two IK_S channel activators were developed. The first one, R-L3 [392] was shown to be active on five LQT related mutants of IK_S complex [393]. The second one, ML277 was recently developed from High Throughput Screening (HTS) assays of the Molecular Libraries Small Molecule Repository (MLSMR), which contains 350 000 compounds that were identified as novel modulators of drug target [394]. The screening was followed by the optimization of the lead compound, to finally obtain ML277 [395], which turned out to be potent only in absence of KCNE1 [333].

Interestingly, several integrative studies, which included electrophysiology experiments and site-directed mutagenesis, reported the sensitivity of K_V7.1 channel to polyunsaturated fatty acids (PUFA). A first study reported the sensitivity of K_V7.1 tetramer to docosahexaenoic acid (DHA) in the absence of KCNE1, but not in its presence. Indeed, the pKa of DHA is equal to 7.8 in presence of K_V7.1 alone but increases up to pKa=8.7 in presence of IK_S channel. This pKa difference shows that KCNE1 elicits a local pH decrease in the extracellular side of the lipid bilayer which itself favors protonation of this fatty acid at physiological pH=7.4 [396]. Its analogue, N-arachidonoyl taurine (N-AT), due to its lower pKa, turned out to be potent not only on the K_V7.1 tetramer in both the absence and presence of KCNE1, but also on several LQTS related mutants, which strongly advocate for a possible therapeutic effect of this fatty acid for the treatment of LQTS. Nevertheless, the authors stated that these effects have to be observed on mammalian cells, and also *in vivo* to get a confirmation of the aforementioned results [397]. Later, the authors reported additional results that allowed for a better understanding of the mechanistic aspects of the PUFA effects [398, 399]. Indeed, both DHA and N-AT are inducing a left-shift in voltage-dependence of conductance, as well as an increase in current amplitude.

The local pH change induced by KCNE1 in the presence of DHA was shown to be due to the displacement of the acidic residues that are located on the S5-P loop of K_V7.1 (E284, D286, E290, E295, D301) from the conduction pathway towards the binding site of DHA, located near S4 gating charge R228 [398]. The recent electrophysiology results suggest that N-AT interacts with both R228 from S4 and K326 from S6, stabilizing the activated state of the VSD, and the open state of the PD, respectively [399]. However, the authors were not able to determine whether these interactions were the result of one PUFA molecule with both binding sites, or two PUFA molecules, each binding the VSD and the PD. To that extent, our models can be of great use to address this question. Indeed, it is largely possible to create MD systems in which our K_V7.1 and IK_S models can be placed in the presence of any PUFA, as their FF parameters are largely developed within CHARMM36 FF [400].

Furthermore, the possibility to use IK_S channels for drug safety tests [251] along with IK_R ones has also been discussed. Indeed, studies reported the blockade IK_S channels as one of the side-effects of antifungal drugs such as isavuconazole [401] or clotrimazole [402], and more recently, the tricyclic antidepressant amitriptyline [403]. As a consequence, the IK_S channel complex was suspected to constitute a cardiovascular liability [404] for drug development. As such, it would be safer to submit new drug compounds to drug safety tests against IK_S channels in addition to the those that are already performed against IK_R ones, as strongly recommended by the international council of technical requirements for registration of pharmaceuticals for human use (ICH) [405]. To that extent, computational drug safety tools were developed in order to predict the cardiotoxicity of potential drug compounds by performing multi-scale simulations on human body models that include binding affinity assays on $K_V11.1$ (hERG) channel only [406], or on both IK_S and IK_R channels [407] to minimize the number of false positive and false negative results that are usually obtained when binding affinity assays are performed on hERG channels alone [408].

As the IK_S channel has also been identified as a target of drug-induced LQT [409], drug binding assays can also be performed in silico, between our IK_S models and the drugs that were suspected to be arrhythmogenic. One of the most blatant example is the famous, yet controverted, hydroxychloroquine. This drug, which is a by-product of quinine besides quinidine, has been widely used for many decades as an antimalarial drug, and then as an anti-inflammatory drug. Recently, the hydroxychloroquine has been basically considered for the treatment of the coronavirus disease 2019 (Covid-19), the current pandemic caused by the severe acute respiratory syndrome coronavirus 2 (SARS-CoV-2) prior to be removed from the market in several countries due to its supposed cardiotoxicity [410], revealed by several cases of arrhythmogenic episodes on patients that have been treated with hydroxychloroquine to treat Covid-19 and a case of hydroxychloroquine overdose [411], in addition to its known QT prolongation effect [412], and a case of heart failure following long-term treatment [413]. The suspicion of the cardiotoxicity effects of the hydroxychloroquine was probably amplified by previous studies conducted on its related compound chloroquine, which reported chloroquine-induced hypokalemia [414] and hERG channel blockade [415].

Based on these observations, and the fact that drug-induced cardiac arrhythmias are too often assumed to be due to hERG channel blockade, it can be interesting to investigate *in silico* the possible interactions between the hydroxychloroquine and IK_S channel, whose current was shown to be way less important than IK_R one for repolarization in human cardiomyocytes [416, 417], and therefore neglected as a potential target for arrhythmogenic drugs [408].

The molecular determinants of the $K_V7.1$ modulation (**Chapter III.2**), as well as the binding sites of the ligands that were previously identified for $K_V7.1$ channels can be used as onset strategies for the elaboration and the optimization of drug candidates for therapeutic research targeting $K_V7.1$ channel. Indeed, computational methods have already been used for the identification of the putative binding sites of several known $K_V7.1$ inhibitors. Molecular docking calculations were performed for several compounds, including the inhibitors quinidine [381] L7 [336] and amitriptyline [403] as well as activators R-L3 [393] and ML277 [227], all against homology models of $K_V7.1$ channel. As seen on hERG channels [418], MD simulations can also be conducted on the molecular structures obtained from molecular docking calculations of ML277 against IK_S models [227]. As the functional studies conducted by our collaborators showed that XE991 [156] and ML277 [333] present state-dependent affinities against $K_V7.1$, as well as KCNE1 dependent affinities, we harnessed molecular docking technique in order to predict their respective binding sites on the $K_V7.1$ AO state model for ML277 and on both the $K_V7.1$ IO state and the IK_S AO state models for XE991, without considering any confirmation bias from our part due to our obtained results.

The molecular docking technique aims at evaluating the complementarity between a protein and a ligand *in silico*, both in steric and energetic points of view. To achieve this goal, we used a well-known open source docking program called Autodock [419]. As for most molecular docking programs, Autodock performs its calculations by combining a docking search algorithm with a scoring function. With the use of Genetic docking search algorithm, followed by the calculation of a binding free-energy associated with the formation of the resulting complex, we performed bling docking in order to let the algorithm find a suitable binding site for the ligand.

Several docking search algorithms are available in AutoDock, yet we chose the Lamarckian Genetic Algorithm-Local Search (GA-LS) [420], namely a combination of the Genetic and the Local Search algorithm, which allows to perform the most thorough docking search. Indeed, the genetic algorithm consists in the generation of two random "genotypes", each defined by a set of four state variables (translation, rotation, orientation, conformation) which act as genes. At each step of the algorithm, two new genotypes are created from a random crossover of the genes of the previous ones. Then, both genotypes are translated into a pair of ligand coordinates, for which an energy minimization is performed by the Local Search algorithm in relation with the protein structure. For each phenotype, the energy score ΔG of interaction with the protein is calculated [421]. Among the pair of new genotypes, the one that yielded to the best energy score "survives", which means that it is selected to make other crossovers in order to create more genotypes, while the other genotypes "dies", which means that is simply discarded.

This binding free energy score ΔG is a sum of two pairwise intramolecular energy differences $(V_{bound}^{L-L} - V_{unbound}^{L-L})$ and $(V_{bound}^{P-P} - V_{unbound}^{P-P})$ between the bound and the unbound conformations of the ligand L and the protein P, respectively, along with a pairwise intermolecular energy difference $V_{bound}^{P-L} - V_{unbound}^{P-L}$ between the bound and unbound states of the protein-ligand complex and an entropy term ΔS_{conf} associated with the energy cost needed for the transition from the unbound conformation of the protein and the ligand, towards the bound conformation of the ligand and the protein, which is expressed as follows:

$$\Delta G = (V_{bound}^{L-L} - V_{unbound}^{L-L}) + (V_{bound}^{P-P} - V_{unbound}^{P-P}) + \left(V_{bound}^{P-L} - V_{unbound}^{P-L} + \Delta S_{conf}\right)$$

where the V energy terms are calculated with the help of a semi-empirical force-field expressed as:

$$V = W_{vdw} \sum_{i,j} \left(\frac{A_{ij}}{r_{ij}^{12}} - \frac{B_{ij}}{r_{ij}^{6}}\right) + W_{hbond} \sum_{i,j} E(\theta) \left(\frac{C_{ij}}{r_{ij}^{12}} - \frac{D_{ij}}{r_{ij}^{10}}\right) + W_{elec} \sum_{i,j} \frac{q_i q_j}{e(r_{ij}) r_{ij}}$$
$$+ W_{sol} \sum_{ij} (S_i V_i + S_j V_j) e^{(-r_{ij}^2/2\sigma^2)}$$

Where the first term is a typical 6/12 potential for dispersion/repulsion interactions. The parameters A and B are based on the AMBER force field. Noteworthy, these parameters can be edited. The second term is a directional h-bond term based on a 10/12 potential. The parameters C and D are assigned to give a maximal well depth of 5 kcal/mol at 1.9 Å for hydrogen bonds with nitrogen and oxygen and a well depth of 1 kcal/mol at 2.5 Å for hydrogen bonds with sulfur. The function $E(\theta)$ provides directionality based on the angle θ from an ideal h-bonding geometry. The third term is a screened Coulomb potential for electrostatic interactions.

The last term stands for the desolvation potential, which is the energy associated to the solvent molecules that need to be scattered in order to bind the ligand to the protein. This term is based on the volumes V_i and V_j of the atoms that surround the atoms i and j, respectively. These volumes are weighted by a solvation parameter S, and an exponential term with a distance weighting factor σ= 3.5 Å. The weighting constants W have been optimized to calibrate the empirical free energy based on a set of experimentally determined binding constants. Thus, the scoring function of Autodock generates a set of protein-ligand complexes, each with a predicted binding free energy, expressed in kcal/mol.

In order to perform fast and efficient docking calculations, the three first terms of the energy V (the non-bonded terms) are grid-based. The rapid energy evaluation is achieved by calculating atomic affinity potentials for each atom type in the ligand molecule, using the AutoGrid procedure, implemented in AutoDock. To do this, the protein is embedded in a three-dimensional grid. As we wanted to perform blind docking calculations, our original goal was to embed the entire protein structure. However, as we wanted our docking search as precise as possible, we also set a grid spacing distance of 0.375 Å, which is small enough to be the half of a simple carbon-carbon bond.

Thus, the resulting grid was not fully embedding our models, yet we decided to center the grid box on the selectivity filter (Figure IV.2.1.1). Within the grid, a probe atom is placed at each grid point, and the energy of interaction of this single atom with the protein is assigned to the grid point. The affinity grids, as well as the grids of electrostatic and desolvation potentials generated by AutoGrid are calculated for each type of atom in the ligand, typically carbon, oxygen, nitrogen, and hydrogen. Then, during the calculation using the AutoDock procedure, the energetics of a particular ligand configuration is evaluated using the values from the grids.

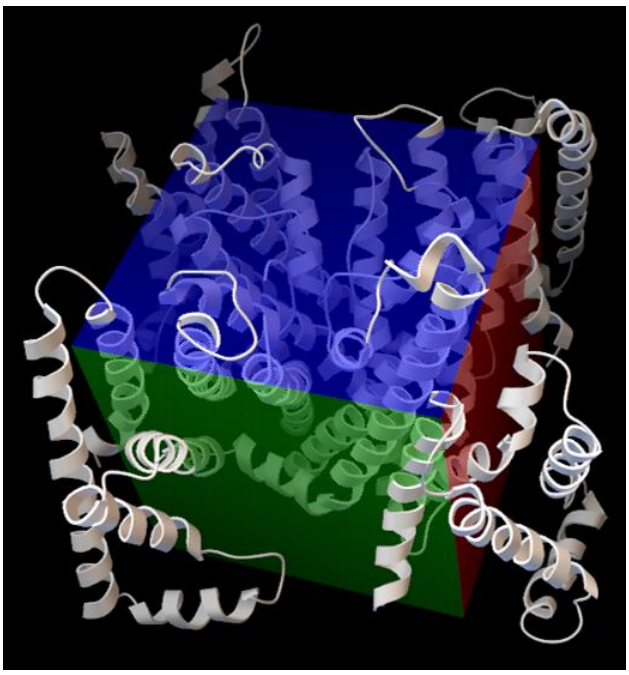

Figure IV.2.1.1: K_V7.1 IO model embedded in AutoDock grid box size.
The picture shows the cartoon representation of K_V7.1 IO model into the maximum box size available on AutoDock for our chosen grid spacing. The green, red and blue faces of the cubic box stand for the x, y and Z axes, respectively.

Here we present the docking results obtained for XE991 on the last frame of the MD trajectories of the K_V7.1 IO model and the IK_S AO model, as well as those obtained for ML277 on the last frame of the MD trajectory of the K_V7.1 AO model. For each model, we show the best ranked channel-ligand complexes according to the binding energy score implemented in AutoDock, which usually corresponds to the most stable protein-ligand complex. As K_V7.1 channel has never been resolved in the presence of any ligand (beside PIP_2), the obtained binding-energy scores and the accuracy of the docking score are not worth to be discussed. Instead, our observations will be focused on the residues that are in direct contact with each ligand, in each complex.

In K_V7.1 IO model (Figure IV.2.1.2), the best ranked docking complex with XE991 scored at -8.20 kcal/mol. The ligand is located between PD segments S5 and S6, surrounding the PD middle pocket and SFF residues. XE991 appears to be involved in π-stacking interactions with S6 residues F332, F335 and F339, and to bind I268 and V310 through VdW interactions. These contact residues are quite interesting to be found thanks to blind docking, as it strengthens the idea that SFF residues, as well as I268 and V310, are important for pore opening mechanism. It also suggest hints for the mechanism of K_V7.1 IO state inhibition by XE991, whose docking pose might favor the anchoring of F339 side chain within the PD middle pocket, and therefore preventing the VSD-PD coupling in the AO state of K_V7.1 subunits.

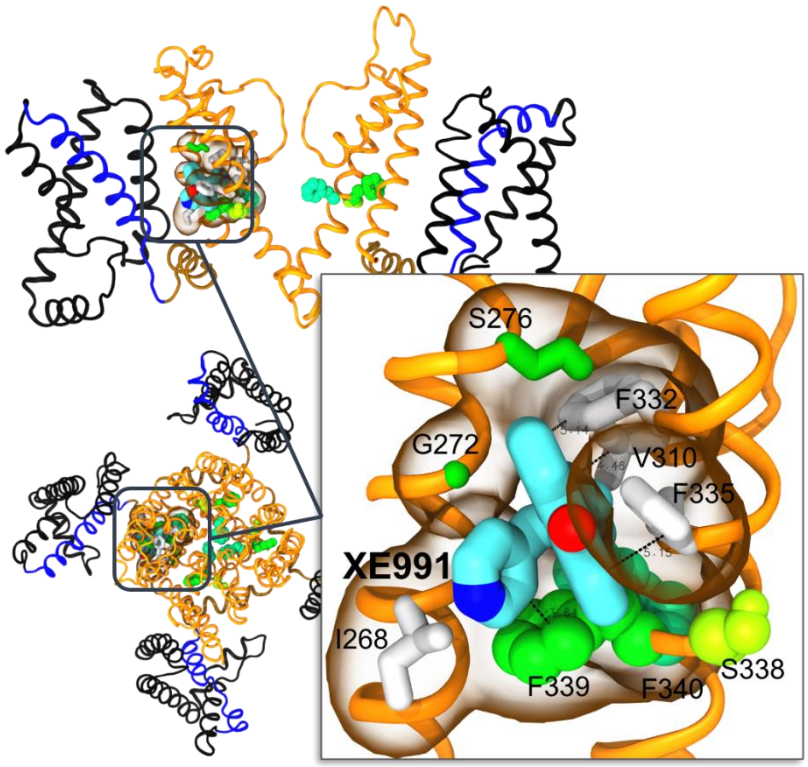

Figure IV.2.1.2: Primary result of XE991 Molecular Docking on K_V7.1 IO model.
The picture shows a cartoon representation of K_V7.1 IO model in side view (upper panel) and top view (lower panel). The segments S1-S3, S4, S4-$S5_{LINKER}$, and S5-S6 are colored in black, blue, brown and orange, respectively. The lower right panel is an enlarged view of the framed areas that show the docking pose of XE991 (in cyan sticks), as well as its closest channel residues in a radius of 4 Å. SFF residues S338, F339 and F340 are depicted in lime, bottle green and blue green spheres. The other residues are colored as per their chemical properties: the aliphatic residues are colored in white, while the polar residues are colored in green.

In IK_S AO model (Figure IV.2.1.3), the best ranked docking complex scored at -9.10 kcal/mol. Interestingly, the binding site is completely different to the one observed in the $K_V7.1$ IO model. Indeed, XE991 is located in the inner leaflet of the lipid bilayer, between S2-S3loop, PD cluster outer surface and KCNE1. While remaining farther from SFF residues, XE991 binds their AO state specific binding partners V255 and L262 from S4-$S5_{LINKER}$, residue I61 form KCNE1 through VdW interactions, as well as aromatic residues F256 from S4-$S5_{LINKER}$ and F57 form KCNE1 through π-stacking interactions.

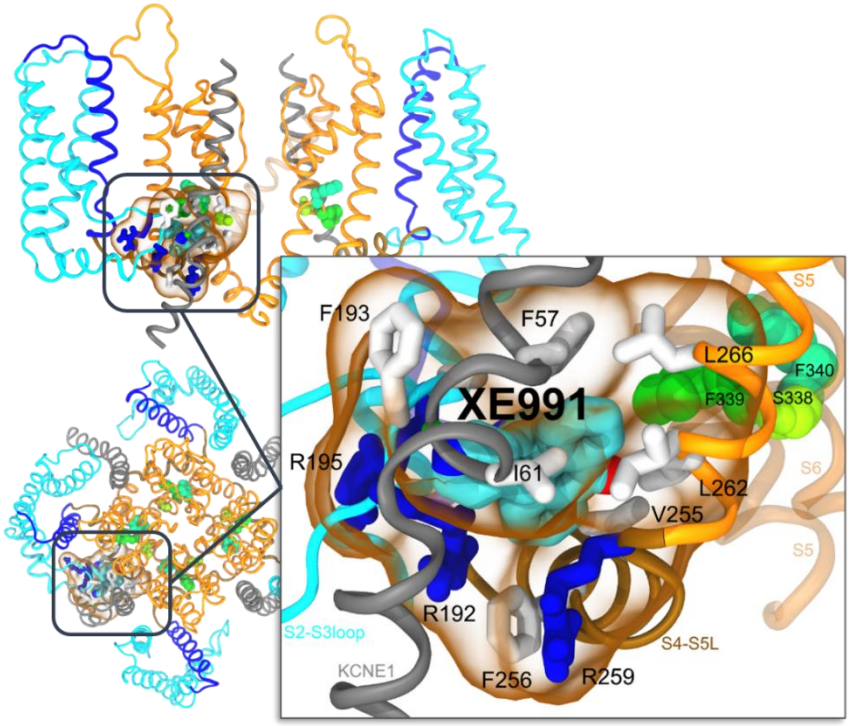

Figure IV.2.1.3: Primary result of XE991 Molecular Docking on IK_S AO model.
The picture shows a cartoon representation of IK_S AO model in side view (upper panel) and top view (lower panel). The segments S1-S3, S4, S4-$S5_{LINKER}$, S5-S6 and KCNE1 are colored in cyan, blue, brown, orange, and gray, respectively. The lower right panel is an enlarged view of the framed areas that show the docking pose of XE991 (in cyan sticks), as well as its closest channel residues in a radius of 4 Å. SFF residues S338, F339 and F340 are depicted in lime, bottle green and blue green spheres. The other residues are colored as per their chemical properties: the aliphatic residues are colored in white, while the basic residues are colored in blue.

In addition, the close proximity between the aromatic rings of XE991 and the one of F193 from S2-$S3_{loop}$, suggest that pi stacking interactions might be formed between XE991 and this residue, in addition to its putative VdW interactions. Furthermore, the proximity of XE991 and basic residues R192, R195 and R259 suggest possible cation-π stacking interactions.

By forming bridges between KCNE1 and both S2-S3$_{LOOP}$ and S4-S5$_{LINKER}$, the presence of XE991 might either induce the formation of IK_S IC state specific interactions such as F256-M62 and F193-I61, or at the very least might mimic those interactions, that we suspected to be the molecular determinants of K_V7.1 VSD-PD coupling inhibition (Chapter III.2.2) and PD opening inhibition (Chapter IV.1.3) by KCNE1. Altogether, these K_V7.1/XE991 docking complexes suggest that XE991 blocks K_V7.1 current by preventing the rotation of SFF residue F339, which appeared to induce the F340 conformational change, necessary for PD opening mechanism. However, XE991 might undertake a different inhibition mechanism in presence of KCNE1, which consists in assisting the latter to inhibit K_V7.1 VSD-PD coupling mechanism.

For the blind docking calculations of ML277 on the K_V7.1 AO model (Figure IV.2.1.4), the best ranked docking complex scored at -9.77 kcal/mol. Among the eleven closest residues of ML277, four of them (V255, F335, S338, F339) have already been identified as stabilizing the AO state in IK_S channel using VCF experiments on IK_S complex mutants (Chapter III.2.1). These residues, along with S5 residues L262, L266, G269 and S6 residues V334 and F340 were also identified as involved in the predicted VSD activation mechanism that we have drawn from our MD trajectories (Chapter IV.1.3). ML277 might constitute a bridge between S4-S5$_{LINKER}$ and the middle of S6 from an adjacent subunit which may strengthen the AO state coupling interface by leaving space for C_{TERM} region of S6 segments to spread away from the pore axis to elicit pore opening. Besides, its pi-stacking interaction with F340 might stabilize the “outside” conformation of F340 side chains, which may constitute a lead to explain how the ionic current of K_V7.1 is enhanced in presence of ML277. This primary result agrees with the docking results previously obtained for ML227 molecular docking on K_V7.1 3D models [227, 323].

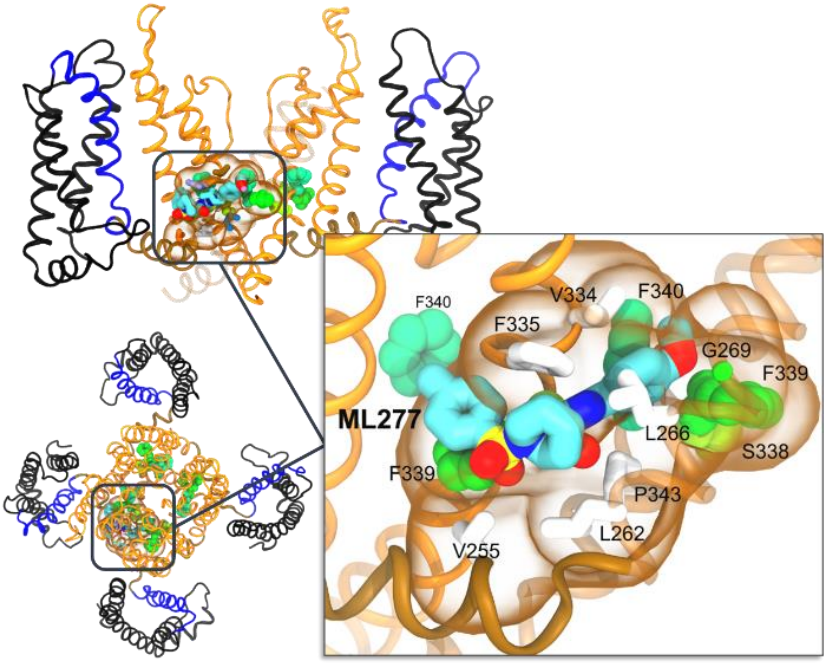

Figure IV.2.1.4: Primary result of ML277 Molecular Docking on K_V7.1 AO model.
The picture shows a cartoon representation of K_V7.1 AO model in side view (upper panel) and top view (lower panel). The segments S1-S3, S4, S4-$S5_{LINKER}$, and S5-S6 are colored in black, blue, brown and orange, respectively. The lower right panel is an enlarged view of the framed areas that show the docking pose of ML277 (in cyan sticks), as well as its closest channel residues in a radius of 4 Å. SFF residues S338, F339 and F340 are depicted in lime, bottle green and blue green spheres. The other residues are colored as per their chemical properties: the aliphatic residues are colored in white, while the polar residues are colored in green.

As the K_V7.1 channel has recently been resolved by CryoEM in the presence its known co-factor PIP_2 (PDB entry: 6V01) [79], it could be interesting to perform re-docking calculations of the lipid against the CryoEM structure, in order to constitute an element of comparison for the binding-energy scores obtained from the forthcoming docking calculations of our models. To increase the coherence of our docking complexes with respect to our MD simulation results, the A, B parameters used in the L-J term of AutoDock scoring function, based on the AMBER force field can be replaced by the CHARMM force field parameters. Ultimately, the goal of molecular docking calculations is to obtain energetically stable docking complexes to study their stability within a lipid membrane. To do that, we consider embedding the obtained complexes into a POPC lipid bilayer prior to perform MD simulations. This task, which can be done using CHARMM-GUI, is quite straightforward. However, the generation of CHARMM force field parameters for both ML277 and XE991 constitute the most challenging task. MD simulations of ion channel-ligand complexes using CHARMM force field require an accurate set of force field parameters for the ligands.

To address this task, we used the CHARMM General Force Field (CGenFF) [422] was first developed to simulate ”drug-like” molecules in the biological environment represented by the set of CHARMM biomolecular force fields. In order to facilitate the parameterization process, CGenFF developers built a program which provide a guess of atom types, as well as parameters for bonds, angles, and dihedral angles, for a given drug-like molecule [423, 424]. Partial charges are also guessed. Each guess is assigned by a penalty score to help the user in the parameterization process: Penalties between 0 and 10 are fair; penalties between 10 and 50 require validation; and penalties above 50 require optimization. For ML277, some atoms present high charge penalties (superior to 50) and/or are involved in guessed parameters with high penalties (Figure IV.2.1.5).

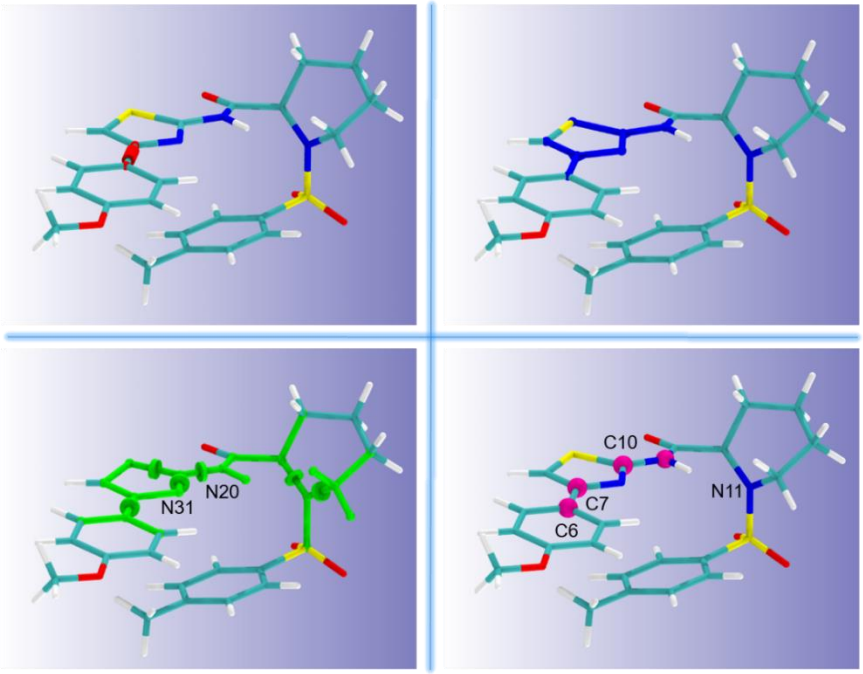

Figure IV.2.1.5: Mapping of CHARMM force field parameters to optimize for ML277.
The picture shows sticks representation of ML277 in which carbon, oxygen, sulfur, nitrogen and hydrogen are colored in cyan, red, yellow, blue and white, respectively. The labeled atoms are the ones that require new atom types. The fragments of the ligand that require parameter optimization are shown as follows: the bond (upper left) is depicted as a red cynlinder. The angles (upper right) are shown in cornered sticks in the upper right panel. The torsion angles (lower left) are shown in green disks, and the charges (lower right) are depicted in pink spheres.

In order to avoid overwriting of existing parameters, the best option is to set new atom types for these atoms, in order to obtain a whole new set of missing parameters to optimize. One has to make sure that new atom types are not already existing in CGenFF and must have a maximum of 7 characters. For ML277, six atoms had their guessed atom type modified prior to be optimized. (Tab IV.2.1.1).

ML277 : atom name	Penalty value/param	Guessed atom type	New atom type
C6	179.601/charge	CG2R61	CG2R61A
C7	182.441/charge	CG2R51	CG2R51A
C10	89.730/charge	CG2R53	CG2R53A
N11	91.663/charge	NG2S1	NG2S1A
N20	150.5/dihedral	NG301	NG301A
N31	201/dihedral	NG2R50	NG2R50A

Tab IV.2.1.1: New atom types assigned for ML277 in CHARMM FF parametrization.

For XE991 (Figure IV.2.1.6), no high penalties were found on partial charges or parameters guessed by CGenFF program. Therefore, only partial charges and parameters with a penalty value between 10 and 50 will only be validated.

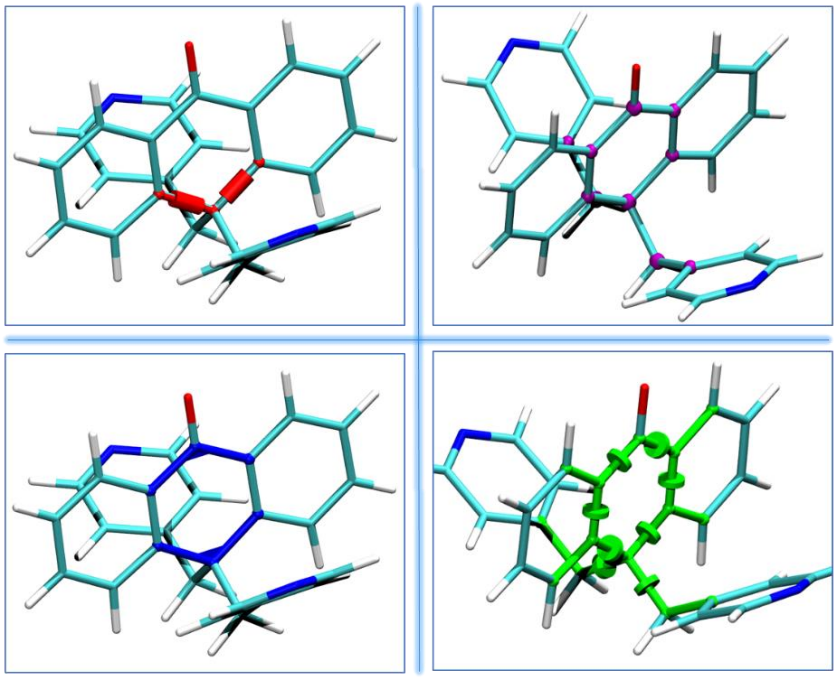

Figure IV.2.1.6: Mapping of CHARMM force field parameters to optimize for XE991.
The picture shows sticks representation of XE991 in which carbon, oxygen, sulfur, nitrogen and hydrogen are colored in cyan, red, yellow, blue and white, respectively. The labeled atoms are the ones that require new atom types. The fragments of the ligand that require parameter validation are shown as follows: the bonds (upper left) are depicted as red cynlinders. The angles (lower left) are shown in blue cornered sticks in the upper right panel. The torsion angles (lower right) are shown in green disks, and the charges (upper right) are depicted in pink spheres.

Noteworthy, this toolkit does not allow for the parametrization of the Van Der Waals (VdW) and Lennard-Jones (LJ) non bonded parameters. Instead, those are assigned by analogy with CGenFF VdW parameters. For both ligands, some atoms present high charge penalties (superior to 50) and/or are involved in guessed parameters with high penalties. In order to avoid overwriting of existing parameters, the best option is to set new atom types for these atoms, in order to obtain a whole new set of missing parameters to optimize. One has to make sure that new atom types are not already existing in CGenFF and must have a maximum of 7 characters.

The validation of the guessed parameters, which was performed with the help of FFToolkit (FFTK) [425] require QM calculations with Gaussian program [426], and fitting of MM objective functions. In that particular case, strong constraints can be applied to optimize the fitting of MM functions with respect to QM data. The optimization is required if the validation is not successful, because it means that CGenFF parameters cannot be transferred to the new molecule. This process requires to set new atom types, and new associated parameters drawn from the fitting of MM objective functions on QM data. This procedure will prevent overwriting of existing parameters, and therefore ensure the transferability of CGenFF. Following the protocol of FFTK, we managed to parameterize most bonded terms of XE991 and ML277. However, additional QM calculations remain to be performed for both ligands in order to establish the energetic profiles of some of their dihedrals. These QM calculations consist in performing dihedral scans which themselves consist in calculating the Hessian matrix associated which each dihedral angle value necessary for the energetic profile of one dihedral angle, which is quite time-consuming. These matrices will then be used to determine the force field parameters of the dihedrals. Once this step is completed, the validation of the new sets of parameters will be possible.

Chapter IV.2.2. Molecular modeling approaches to study the effects of K_V7.1 endogenous ligands

Given the robustness of our 3D models of the K_V7.1 channel, it is quite tempting to try to predict the macroscopic properties of our 3D structure, such as the state-dependent single-channel conductance or ionic current. Currently, the computational cost required for an all-atom simulation of the ion permeation process in an ion channel is way too expensive. Indeed, the timescale of this biological event is quite long, as the translocation of one potassium ion across a channel takes approximatively 1 µs [427]. However, by studying the behavior of ions across the conduction pathway of an ion channel while treating the ion solvent, the channel protein and the membrane as implicit, the trajectory of ions in aqueous solution across the pore of an ion channel structure can be simulated over experimentally relevant timescales by brownian dynamics (BD) simulations. With this method, the time-dependent position of an ion i along the pore axis is usually defined by a Langevin equation [428, 429]:

$$m_i \frac{d^2 r_i}{dt^2} = -\gamma_i \frac{dr_i}{dt} + f_i(t) + F_i$$

where m_i, r_i, γ_i are the mass, the position, and the friction coefficient of the ion i in the BD system, respectively. The forces $f_i(t)$ and F_i are the stochastic force elicited by the random collisions with water molecules, and the total systematic force acting on the ion i, respectively. As statistical thermodynamics are useful to describe macroscopic events from microscopic systems, a statistical thermodynamics study, focused on ion conduction through ion channels, reported that the Langevin equation is correct in equilibrium conditions [430]. However, as K_V7.1 channel is a voltage-gated ion channel, the simulation has to be conducted in non-equilibrium conditions (by applying a transmembrane potential). the ions are following a Grand Canonical ensemble, in which the number of ions and both the energy and the pressure of the system are allowed to fluctuate, while the chemical potential, the volume and the temperature are kept constant.

Starting from this premise, the authors developed later an algorithm called Grand Canonical Brownian Dynamics [429]. In the frame of this algorithm, the non-equilibrium conditions applied on the BD system imply that the movement of ions are overdamped, so their acceleration $\frac{d^2 r_i}{dt^2} = 0$. Thus, the aforementioned Langevin equation can be expressed as a first order equation:

$$\frac{dr_i}{dt} = \frac{D_i}{k_B T} \langle F_i \rangle + \zeta_i(t)$$

Where $D_i = \frac{k_B T}{\gamma_i}$ is the diffusion constant of the ion i, and $\zeta_i(t)$ is a random Gaussian noise acting on the ion i whose variance is defined by $\langle \zeta_i(t) \cdot \zeta_i(0) \rangle = 6 D_i \delta t$ where δt is the simulation time-step. Here the stochastic systematic force $\langle F_i \rangle$ is expressed as a mean force, defined as:

$$\langle F_i \rangle = -\nabla_i W(r_1, r_2, \dots, r_N)$$

where $W(r_1, r_2, \dots, r_N)$ is the potential of mean force (PMF) for each ion i of the BD system. Usually assimilated as a free energy, it represents, in a system of two ions, the work necessary to bring them from an infinite distance towards a distance r. In the frame of BD simulations of ion channel conduction, the PMF is actually expressed as a sum of potentials, including terms for the electrostatic potential of the implicit water, the protein, and the other ions, along with a transmembrane potential term, expressed as a Poisson-Boltzmann equation [429], or in some cases, based on the Nernst-Planck Theory [431–433].

Despite the complexity of the GCMC algorithm, it has not been used to study the ion permeation dynamics of any K_V channel. Indeed, several free-energy calculations studies conducted on voltage-gated K^+ channels such as the K^+ channel of Streptomyces Lividans (KcsA) [434, 435] and $K_V1.2$ [302, 435] reported the importance of the residues that face the pore surface in the energy associated with ion translocation. In the case of $K_V7.1$ channel, our results are also highlighting the importance of conserved S6 residues in the pore opening mechanism, therefore it would have been interesting to investigate the possible effects of their interactions with the solvent on the BD trajectory of K+ ions in the conduction pathway of the $K_V7.1$ channel.

To that extent, a very promising improved GCBD algorithm called BROMOCEA code was recently reported [377]. Indeed, this code features a PMF that includes CHARMM FF terms, allowing for the description of explicit channel atoms in the BD system (such as the PD or the selectivity filter ones). Despite the fact that the authors mentioned that the BROMOCEA code requires additional improvements, it remains interesting to conduct BD simulations on $K_V7.1$ models in order to predict their respective conductance. Ultimately, one could be able to reproduce all these computational methods on IK_S channel mutants in order to predict and to appreciate the effects of KCNE1 on the ionic conductance of $K_V7.1$ tetramer. Noteworthy, computational electrophysiology can also be performed with the help of other methods, such as free-energy calculations [436], or machine learning methods [251]. Free-energy calculations of both $K_V7.1$ and IK_S models can also be conducted in order to study the energetic aspects of the VSD-PD coupling mechanism. By using the molecular determinants identified in this study and validated by functional studies as collective variables, the free-energy profiles of $K_V7.1$ channel, and then IK_S complex can be calculated with well-temper meta-dynamics, for a better appreciation of KCNE1 modulation, as it has been previously done to study the VSD activation process of the homologous $K_V1.2$ channel [375, 437].

We obtained 500 ns MD simulations, which is far from the time-range of biological events in which the $K_V7.1$ channel is involved, which is in the millisecond time range. In order to extend our MD trajectories, additional MD runs of our models can be performed in order to reach the microsecond scale of simulation. To achieve that goal, the new accelerated MD method, can be used [378]. Called hydrogen mass repartitioning, it consists in increasing the mass of hydrogen atoms of the system, while slightly decreasing the mass of the atom that bears the hydrogens. This method allows to run MD simulations with a time step of 4 fs instead of the 2 fs that are commonly used in current MD simulations. As the authors of the HMR study provided input files that allow for the conversion of old NAMD input files (with a 2 fs time step), it became possible to perform microsecond scale MD simulations of our $K_V7.1$ models.

To unravel the allosteric aspects of the VSD-PD coupling and the pore opening mechanisms, one can harness machine learning methods to analyze the obtained MD trajectories. According to a previous ML methods benchmark [438], the most accurate method for ion channel MD trajectories is the non-linear neural networks. However, considering the results we obtained from knowledge based MD trajectory analysis, the best way to accurately predict the molecular determinants of $K_V7.1$ channel function while reducing the bias as best as possible is to merge neural networks with knowledge-based MD analysis. As such, the knowledge-based neural networks appears to be the most efficient ML method [439] to be developed for this topic, as it can merge the advantages of knowledge based learning that we used in this present work with the powerful ML methods that have already allowed for the characterization of the allosteric aspects of KCNQ1 channel pore opening mechanism in its cytoplasmic regions [352, 440].

Finally, several studies reported the identification of KCNQ1 gene as a predisposition gene of the appearance of Type 2 diabetes (T2D) [441–443]. T2D is currently a widespread disease whose prevalence is increasing in both western and emerging countries due to globalization [281, 444]. Interestingly, several single nucleotide polymorphisms (SNP) of KCNQ1 have been linked to T2D [445]. Indeed, these T2D-related SNPs of KCNQ1 usually elicit overexpression of KCNQ1 gene in β-pancreatic cells [446], in which KCNQ1 is usually co-expressed with KCNE2 as suggested by the authors of this recent in vitro studies of knockout KCNE2 mice [447]. This overexpression of KCNQ1, increases the K^+ current repolarization current in β-cells, which shortens their action potential that is necessary for insulin exocytosis. An additional study reported cases of hyperinsulinemia in LQT1 patients [448], which suggests that KCNQ1 loss-of-function induces an increase in insulin secretion, confirming that the overexpression of KCNQ1 does inhibit insulin secretion. Moreover, a recent clinical study of the effects of the anti-diabetic compound repaglinide on a cohort of patients carrying KCNQ1 SNP reported the potential role played by KCNQ1 channel on the insulino-resistance, notably by modifying insulin signaling [449]. Therefore, $K_V7.1$ channel might constitute a therapeutic target for type 2 diabetes as it participates in the action potential which occur in pancreatic β-cells to elicit the exocytosis of the insulin hormone.

Given this beam of results, the computational study of the K_V7.1-KCNE2 channel complex might be of great interest. As we did for K_V7.1-KCNE1 complex modeling, we can used our K_V7.1 models to build constructs of K_V7.1-KCNE2 model, since a 3D structure of the ancillary subunit has been obtained by NMR (PDB entry: 2M0Q). Plus, as it has been shown that KCNE2 reduces the current amplitude of K_V7.1 channel, we can harness molecular dynamics and computational electrophysiology Ultimately, the investigation dynamics of the T2D-related mutants and the determination of their effects on insulin secretion would may allow for the prediction of the molecular determinants of insulin-resistance, and/or providing hints for therapeutic research for the treatment of diabetes.

References

1. Singer SJ (2004) Some Early History of Membrane Molecular Biology. Annu Rev Physiol 66:1–27 . https://doi.org/10.1146/annurev.physiol.66.032902.131835

2. Stansfeld PJ, Goose JE, Caffrey M, Carpenter EP, Parker JL, Newstead S, Sansom MSP (2015) MemProtMD: Automated Insertion of Membrane Protein Structures into Explicit Lipid Membranes. Structure 23:1350–1361 . https://doi.org/10.1016/j.str.2015.05.006

3. Piccolino M (1997) Luigi Galvani and animal electricity: two centuries after the foundation of electrophysiology. Trends Neurosci 20:443–448 . https://doi.org/10.1016/S0166-2236(97)01101-6

4. Piccolino M (2000) The bicentennial of the Voltaic battery (1800-2000): The artificial electric organ. Trends Neurosci 23:147–151 . https://doi.org/10.1016/S0166-2236(99)01544-1

5. Maex R (2017) On the Nernst–Planck equation. J Integr Neurosci 16:73–91 . https://doi.org/10.3233/JIN-170008

6. Seyfarth E-A (2006) Julius Bernstein (1839–1917): pioneer neurobiologist and biophysicist. Biol Cybern 94:2–8 . https://doi.org/10.1007/s00422-005-0031-y

7. Gorter E, Grendel F (1925) ON BIMOLECULAR LAYERS OF LIPOIDS ON THE CHROMOCYTES OF THE BLOOD. J Exp Med 41:439–443 . https://doi.org/10.1084/jem.41.4.439

8. Roberts GG (1990) Langmuir-Blodgett Films. Springer US, Boston, MA

9. Danielli JF, Davson H (1935) A contribution to the theory of permeability of thin films. J Cell Comp Physiol 5:495–508 . https://doi.org/10.1002/jcp.1030050409

10. Robertson JD (1959) The ultrastructure of cell membranes and their derivatives. Biochem Soc Symp 16:3–43

11. Robertson JL (2018) The lipid bilayer membrane and its protein constituents. J Gen Physiol 150:1472–1483 . https://doi.org/10.1085/jgp.201812153

12. Stefani E, Toro L, Perozo E, Bezanilla F (1994) Gating of Shaker K+ channels: I. Ionic and gating currents. Biophys J 66:996–1010 . https://doi.org/10.1016/S0006-3495(94)80881-1

13. Bezanilla F (2005) Voltage-gated ion channels. IEEE Trans Nanobioscience 4:34–48 . https://doi.org/10.1109/TNB.2004.842463

14. Detta N, Frisso G, Limongelli G, Marzullo M, Calabrò R, Salvatore F (2014) Genetic analysis in a family affected by sick sinus syndrome may reduce the sudden death risk in a young aspiring competitive athlete. Int J Cardiol 170:e63–e65 . https://doi.org/10.1016/j.ijcard.2013.11.013

15. Hodgkin AL, Huxley AF (1952) A quantitative description of membrane current and its application to conduction and excitation in nerve. J Physiol 117:500–544 . https://doi.org/10.1113/jphysiol.1952.sp004764

16. Singer SJ, Nicolson GL (1972) The Fluid Mosaic Model of the Structure of Cell Membranes. Science (80-) 175:720–731 . https://doi.org/10.1126/science.175.4023.720

17. Bar RS, Deamer DW, Cornwell DG (1966) Surface Area of Human Erythrocyte Lipids: Reinvestigation of Experiments on Plasma Membrane. Science (80-) 153:1010–1012 . https://doi.org/10.1126/science.153.3739.1010

18. Parsegian A (1969) Energy of an ion crossing a low dielectric membrane: solutions to four relevant electrostatic problems. Nature 221:844–846

19. Nicolson GL (2014) The Fluid - Mosaic Model of Membrane Structure: Still relevant to understanding the structure, function and dynamics of biological membranes after more than 40 years. Biochim Biophys Acta - Biomembr 1838:1451–1466 . https://doi.org/10.1016/j.bbamem.2013.10.019

20. Neher E, Sakmann B (1976) Single-channel currents recorded from membrane of denervated frog muscle fibres. Nature 260:799–802 . https://doi.org/10.1038/260799a0

21. Narahashi T, Moore JW, Scott WR (1964) Tetrodotoxin Blockage of Sodium Conductance Increase in Lobster Giant Axons. J Gen Physiol 47:965–974 . https://doi.org/10.1085/jgp.47.5.965

22. Catterall WA (1980) Pharmacologic properties of voltage-sensitive sodium channels in chick muscle fibers developing in vitro. Dev Biol 78:222–230 . https://doi.org/10.1016/0012-1606(80)90331-0

23. Hille B (1978) Ionic channels in excitable membranes. Current problems and biophysical approaches. Biophys J 22:283–294 . https://doi.org/10.1016/S0006-3495(78)85489-7

24. Noda M, Shimizu S, Tanabe T, Takai T, Kayano T, Ikeda T, Takahashi H, Nakayama H, Kanaoka Y, Minamino N, Kangawa K, Matsuo H, Raftery MA, Hirose T, Inayama S, Hayashida H, Miyata T, Numa S (1984) Primary structure of Electrophorus electricus sodium channel deduced from cDNA sequence. Nature 312:121–127 . https://doi.org/10.1038/312121a0

25. Tempel BL, Papazian DM, Schwarz TL, Jan YN, Jan LY (1987) Sequence of a probable potassium channel component encoded at Shaker locus of Drosophila. Science 237:770–775 . https://doi.org/10.1126/science.2441471

26. Yu FH, Catterall WA (2004) The VGL-chanome: a protein superfamily specialized for electrical signaling and ionic homeostasis. Sci STKE 2004:re15–re15 . https://doi.org/10.1126/stke.2532004re15

27. Kaupp UB, Niidome T, Tanabe T, Terada S, Bönigk W, Stühmer W, Cook NJ, Kangawa K, Matsuo H, Hirose T, Miyata T, Numa S (1989) Primary structure and functional expression from complementary DNA of the rod photoreceptor cyclic GMP-gated channel. Nature 342:762–766 . https://doi.org/10.1038/342762a0

28. Zagotta WN, Siegelbaum SA (1996) Structure and function of cyclic nucleotide-gated channels. Annu Rev Neurosci 19:235–263 . https://doi.org/10.1146/annurev.ne.19.030196.001315

29. Xia XM, Fakler B, Rivard A, Wayman G, Johnson-Pais T, Keen JE, Ishii T, Hirschberg B, Bond CT, Lutsenko S, Maylie J, Adelman JP (1998) Mechanism of calcium gating in small-conductance calcium-activated potassium channels. Nature 395:503–507 . https://doi.org/10.1038/26758

30. Zagotta WN, Olivier NB, Black KD, Young EC, Olson R, Gouaux E (2003) Structural basis for modulation and agonist specificity of HCN pacemaker channels. Nature 425:200–205 . https://doi.org/10.1038/nature01922

31. Caterina MJ, Julius D (2001) The vanilloid receptor: a molecular gateway to the pain pathway. Annu Rev Neurosci 24:487–517 . https://doi.org/10.1146/annurev.neuro.24.1.487

32. Jaye DA, Xiao Y-F, Sigg DC (2010) Basic Cardiac Electrophysiology: Excitable Membranes. In: Sigg DC, Iaizzo PA, Xiao Y-F, He B (eds) Cardiac Electrophysiology Methods and Models. Springer US, Boston, MA, MA, pp 41–51

33. Aggarwal SK, MacKinnon R (1996) Contribution of the S4 segment to gating charge in the Shaker K+ channel. Neuron 16:1169–1177 . https://doi.org/10.1016/S0896-6273(00)80143-9

34. Seoh S-AA, Sigg D, Papazian DM, Bezanilla F (1996) Voltage-sensing residues in the S2 and S4 segments of the Shaker K+ channel. Neuron 16:1159–1167 . https://doi.org/10.1016/S0896-6273(00)80142-7

35. Zheng J, Zagotta WN (2003) Patch-Clamp Fluorometry Recording of Conformational Rearrangements of Ion Channels. Sci Signal 2003:pl7–pl7 . https://doi.org/10.1126/stke.2003.176.pl7

36. Cowgill J, Chanda B (2019) The contribution of voltage clamp fluorometry to the understanding of channel and transporter mechanisms. J Gen Physiol 151:1163–1172 . https://doi.org/10.1085/jgp.201912372

37. Armstrong CM, Bezanilla F (1973) Currents related to movement of the gating particles of the sodium channels. Nature 242:459–461 . https://doi.org/10.1038/242459a0

38. Perozo E, MacKinnon R, Bezanilla F, Stefani E (1993) Gating currents from a nonconducting mutant reveal open-closed conformations in Shaker K+ channels. Neuron 11:353–358 . https://doi.org/10.1016/0896-6273(93)90190-3

39. Bezanilla F, Perozo E, Stefani E (1994) Gating of Shaker K+ channels: II. The components of gating currents and a model of channel activation. Biophys J 66:1011–1021 . https://doi.org/10.1016/S0006-3495(94)80882-3

40. Bezanilla F (2000) The voltage sensor in voltage-dependent ion channels. Physiol Rev 80:555–592 . https://doi.org/10.1152/physrev.2000.80.2.555

41. Dascal N (1987) The use of xenopus oocytes for the study of ion channel. Crit Rev Biochem 22:317–387 . https://doi.org/10.3109/10409238709086960

42. Boyle MB, Kaczmarek LK (1991) Electrophysiological Expression of Ion Channels in Xenopus Oocytes. In: Clare JJ, Trezise DJ (eds) Methods in Neurosciences. Wiley-VCH Verlag GmbH & Co. KGaA, Weinheim, FRG, pp 157–173

43. Puthenveetil R, Vinogradova O (2019) Solution NMR: A powerful tool for structural and functional studies of membrane proteins in reconstituted environments. J Biol Chem 294:15914–15931 . https://doi.org/10.1074/jbc.REV119.009178

44. Henderson R, Unwin PNT (1975) Three-dimensional model of purple membrane obtained by electron microscopy. Nature 257:28–32 . https://doi.org/10.1038/257028a0

45. De Rosier DJ, Klug A (1968) Reconstruction of three dimensional structures from electron micrographs. Nature 217:130–134 . https://doi.org/10.1038/217130a0

46. Taylor KA, Glaeser RM (1974) Electron Diffraction of Frozen, Hydrated Protein Crystals. Science (80-) 186:1036–1037 . https://doi.org/10.1126/science.186.4168.1036

47. Knapek E, Dubochet J (1980) Beam damage to organic material is considerably reduced in cryo-electron microscopy. J Mol Biol 141:147–161 . https://doi.org/10.1016/0022-2836(80)90382-4

48. Dubochet J, Knapek E (2018) Ups and downs in early electron cryo-microscopy. PLoS Biol 16: . https://doi.org/10.1371/journal.pbio.2005550

49. Adrian M, Dubochet J, Lepault J, McDowall AW (1984) Cryo-electron microscopy of viruses. Nature 308:32–36 . https://doi.org/10.1038/308032a0

50. Henderson R, Baldwin JM, Ceska TA, Zemlin F, Beckmann E, Downing KH (1990) Model for the structure of bacteriorhodopsin based on high-resolution electron cryo-microscopy. J Mol Biol 213:899–929 . https://doi.org/10.1016/S0022-2836(05)80271-2

51. Auer M (2000) Three-dimensional electron cryo-microscopy as a powerful structural tool in molecular medicine. J Mol Med 78:191–202 . https://doi.org/10.1007/s001090000101

52. Liu X, Wang H-WW (2011) Single particle electron microscopy reconstruction of the exosome complex using the random conical tilt method. J Vis Exp. https://doi.org/10.3791/2574

53. Frank J, Penczek P, Grassucci R, Srivastava S (1991) Three-dimensional reconstruction of the 70S Escherichia coli ribosome in ice: the distribution of ribosomal RNA. J Cell Biol 115:597–605 . https://doi.org/10.1083/jcb.115.3.597

54. Frank J, Zhu J, Penczek P, Li Y, Srivastava S, Verschoor A, Radermacher M, Grassucci R, Lata RK, Agrawal RK (1995) A model of protein synthesis based on cryo-electron microscopy of the E. coli ribosome. Nature 376:441–444 . https://doi.org/10.1038/376441a0

55. Taylor KA, Glaeser RM (2008) Retrospective on the early development of cryoelectron microscopy of macromolecules and a prospective on opportunities for the future. J Struct Biol 163:214–223 . https://doi.org/10.1016/j.jsb.2008.06.004

56. Faruqi AR, Henderson R (2007) Electronic detectors for electron microscopy. Curr Opin Struct Biol 17:549–555 . https://doi.org/10.1016/j.sbi.2007.08.014

57. Miyazawa A, Fujiyoshi Y, Unwin N (2003) Structure and gating mechanism of the acetylcholine receptor pore. Nature 423:949–955 . https://doi.org/10.1038/nature01748

58. Gonen T, Cheng Y, Sliz P, Hiroaki Y, Fujiyoshi Y, Harrison SC, Walz T (2005) Lipid–protein interactions in double-layered two-dimensional AQP0 crystals. Nature 438:633–638 . https://doi.org/10.1038/nature04321

59. Kühlbrandt W, Kuhlbrandt W (2014) The Resolution Revolution. Science (80-) 343:1443–1444 . https://doi.org/10.1126/science.1251652

60. Brown A, Amunts A, Bai X-C, Sugimoto Y, Edwards PC, Murshudov G, Scheres SHW, Ramakrishnan V (2014) Structure of the large ribosomal subunit from human mitochondria. Science 346:718–722 . https://doi.org/10.1126/science.1258026

61. Liao M, Cao E, Julius D, Cheng Y (2013) Structure of the TRPV1 ion channel determined by electron cryo-microscopy. Nature 504:107–112 . https://doi.org/10.1038/nature12822

62. Autzen HE, Julius D, Cheng Y (2019) Membrane mimetic systems in {CryoEM}: keeping membrane proteins in their native environment. Curr Opin Struct Biol 58:259–268 . https://doi.org/10.1016/j.sbi.2019.05.022

63. Doyle DA, Morais Cabral J, Pfuetzner RA, Kuo A, Gulbis JM, Cohen SL, Chait BT, MacKinnon R (1998) The structure of the potassium channel: molecular basis of K+ conduction and selectivity. Science 280:69–77

64. Jiang Y, Lee A, Chen J, Ruta V, Cadene M, Chait BT, MacKinnon R (2003) X-ray structure of a voltage-dependent K+ channel. Nature 423:33–41 . https://doi.org/10.1038/nature01580

65. Hendrickson WA (2016) Atomic-level analysis of membrane-protein structure. Nat Struct Mol Biol 23:464–467 . https://doi.org/10.1038/nsmb.3215

66. Ishchenko A, Abola EE, Cherezov V (2017) Crystallization of Membrane Proteins: An Overview. In: Methods in Molecular Biology (Clifton, N.J.). pp 117–141

67. Long SB, Campbell EB, MacKinnon R (2005) Crystal Structure of a Mammalian Voltage-Dependent Shaker Family K+ Channel. Science (80-) 309:897–903 . https://doi.org/10.1126/science.1116269

68. Fernandez-Leiro R, Scheres SHW (2016) Unravelling biological macromolecules with cryo-electron microscopy. Nature 537:339–346 . https://doi.org/10.1038/nature19948

69. Park E, Campbell EB, MacKinnon R (2017) Structure of a CLC chloride ion channel by cryo-electron microscopy. Nature 541:500–505 . https://doi.org/10.1038/nature20812

70. Park E, MacKinnon R (2018) Structure of the CLC-1 chloride channel from Homo sapiens. Elife 7: . https://doi.org/10.7554/eLife.36629

71. Hite RK, Yuan P, Li Z, Hsuing Y, Walz T, MacKinnon R (2015) Cryo-electron microscopy structure of the Slo2.2 Na+-activated K+ channel. Nature 527:198–203 . https://doi.org/10.1038/nature14958

72. Lee KPK, Chen J, MacKinnon R (2017) Molecular structure of human katp in complex with ATP and ADP. Elife 6: . https://doi.org/10.7554/eLife.32481

73. Tao X, Hite RK, MacKinnon R (2017) Cryo-EM structure of the open high-conductance Ca2+-activated K+ channel. Nature 541:46–51 . https://doi.org/10.1038/nature20608

74. Lee C-HH, MacKinnon R (2018) Activation mechanism of a human SK-calmodulin channel complex elucidated by cryo-EM structures. Science (80-) 360:508–513 . https://doi.org/10.1126/science.aas9466

75. Lee C-H, MacKinnon R (2017) Structures of the Human HCN1 Hyperpolarization-Activated Channel. Cell 168:111-120.e11 . https://doi.org/10.1016/j.cell.2016.12.023

76. Whicher JR, MacKinnon R (2016) Structure of the voltage-gated K+ channel Eag1 reveals an alternative voltage sensing mechanism. Science (80-) 353:664–669 . https://doi.org/10.1126/science.aaf8070

77. Wang W, MacKinnon R (2017) Cryo-EM Structure of the Open Human Ether-à-go-go -Related K + Channel hERG. Cell 169:422-430.e10 . https://doi.org/10.1016/j.cell.2017.03.048

78. Sun J, MacKinnon R (2017) Cryo-EM Structure of a KCNQ1/CaM Complex Reveals Insights into Congenital Long QT Syndrome. Cell 169:1042–1050 . https://doi.org/10.1016/j.cell.2017.05.019

79. Sun J, MacKinnon R (2020) Structural Basis of Human KCNQ1 Modulation and Gating. Cell 180:340-347.e9 . https://doi.org/10.1016/j.cell.2019.12.003

80. Loussouarn G, Park K-HH, Bellocq C, Baro I, Charpentier F, Escande D, Baró I, Charpentier F, Escande D (2003) Phosphatidylinositol-4, 5-bisphosphate, PIP2, controls KCNQ1/KCNE1 voltage-gated potassium channels: A functional homology between voltage-gated and inward rectifier K+ channels. EMBO J 22:5412–5421 . https://doi.org/10.1093/emboj/cdg526

81. Kim J-B (2014) Channelopathies. Korean J Pediatr 57:1–18 . https://doi.org/10.3345/kjp.2014.57.1.1

82. Durell SR, Hao Y, Guy HR (1998) Structural Models of the Transmembrane Region of Voltage-Gated and Other K+Channels in Open, Closed, and Inactivated Conformations. J Struct Biol 121:263–284 . https://doi.org/10.1006/jsbi.1998.3962

83. Hille B, Ovchinnikov YA (1981) Ion Channels of Excitable Membranes. In: Science and Scientists. Springer Netherlands, Dordrecht, pp 235–241

84. Kennedy A, Finlay DD, Guldenring D, Bond R, Moran K, McLaughlin J (2016) The Cardiac Conduction System: Generation and Conduction of the Cardiac Impulse. Crit Care Nurs Clin North Am 28:269–279 . https://doi.org/10.1016/j.cnc.2016.04.001

85. DiFrancesco D (1993) PACEMAKER MECHANISMS IN CARDIAC TISSUE. Annu Rev Physiol 55:455–472 . https://doi.org/10.1146/annurev.ph.55.030193.002323

86. Anderson RH, Yanni J, Boyett MR, Chandler NJ, Dobrzynski H (2009) The anatomy of the cardiac conduction system. Clin Anat 22:99–113 . https://doi.org/10.1002/ca.20700

87. King JH, Huang CL-H, Fraser JA (2013) Determinants of myocardial conduction velocity: implications for arrhythmogenesis. Front Physiol 4: . https://doi.org/10.3389/fphys.2013.00154

88. Franke WW, Borrmann CM, Grund C, Pieperhoff S (2006) The area composita of adhering junctions connecting heart muscle cells of vertebrates. I. Molecular definition in intercalated disks of cardiomyocytes by immunoelectron microscopy of desmosomal proteins. Eur J Cell Biol 85:69–82 . https://doi.org/10.1016/j.ejcb.2005.11.003

89. Larsson HP (2010) How is the heart rate regulated in the sinoatrial node? Another piece to the puzzle. J Gen Physiol 136:237–241 . https://doi.org/10.1085/jgp.201010506

90. Gaborit N, Le Bouter S, Szuts V, Varro A, Escande D, Nattel S, Demolombe S (2007) Regional and tissue specific transcript signatures of ion channel genes in the non-diseased human heart. J Physiol 582:675–693 . https://doi.org/10.1113/jphysiol.2006.126714

91. Chen L, Sampson KJ, Kass RS (2016) Cardiac Delayed Rectifier Potassium Channels in Health and Disease. Card Electrophysiol Clin 8:307–322 . https://doi.org/10.1016/j.ccep.2016.01.004

92. DiFrancesco D (2010) The role of the funny current in pacemaker activity. Circ Res 106:434–446 . https://doi.org/10.1161/CIRCRESAHA.109.208041

93. Ludwig A, Zong X, Jeglitsch M, Hofmann F, Biel M (1998) A family of hyperpolarization-activated mammalian cation channels. Nature 393:587–591 . https://doi.org/10.1038/31255

94. Baruscotti M, Bucchi A, DiFrancesco D (2005) Physiology and pharmacology of the cardiac pacemaker ("funny") current. Pharmacol Ther 107:59–79 . https://doi.org/10.1016/j.pharmthera.2005.01.005

95. Mesirca P, Torrente AG, Mangoni ME (2014) T-type channels in the sino-atrial and atrioventricular pacemaker mechanism. Pflugers Arch Eur J Physiol 466:791–799 . https://doi.org/10.1007/s00424-014-1482-6

96. Seifert R, Scholten A, Gauss R, Mincheva A, Lichter P, Kaupp UB (1999) Molecular characterization of a slowly gating human hyperpolarization-activated channel predominantly expressed in thalamus, heart, and testis. Proc Natl Acad Sci 96:9391–9396 . https://doi.org/10.1073/pnas.96.16.9391

97. Ludwig A, Zong X, Stieber J, Hullin R, Hofmann F, Biel M (1999) Two pacemaker channels from human heart with profoundly different activation kinetics. EMBO J 18:2323–2329 . https://doi.org/10.1093/emboj/18.9.2323

98. Tseng G-NN (2001) IKr: The hERG channel. J Mol Cell Cardiol 33:835–849 . https://doi.org/10.1006/jmcc.2000.1317

99. Sanguinetti MC, Sachse FB (2018) Structural Determinants and Biophysical Properties of hERG1 Channel Gating. In: Cardiac Electrophysiology: From Cell to Bedside: Seventh Edition. pp 113–121

100. Grant AO (2009) Cardiac Ion Channels. Circ Arrhythmia Electrophysiol 2:185–194 . https://doi.org/10.1161/CIRCEP.108.789081

101. Rohr S (2004) Role of gap junctions in the propagation of the cardiac action potential. Cardiovasc Res 62:309–322 . https://doi.org/10.1016/j.cardiores.2003.11.035

102. Shy D, Gillet L, Abriel H (2013) Cardiac sodium channel NaV1.5 distribution in myocytes via interacting proteins: the multiple pool model. Biochim Biophys Acta 1833:886–894 . https://doi.org/10.1016/j.bbamcr.2012.10.026

103. Niwa N, Nerbonne JM (2010) Molecular determinants of cardiac transient outward potassium current (I(to)) expression and regulation. J Mol Cell Cardiol 48:12–25 . https://doi.org/10.1016/j.yjmcc.2009.07.013

104. Catterall WA, Perez-Reyes E, Snutch TP, Striessnig J (2005) International Union of Pharmacology. XLVIII. Nomenclature and Structure-Function Relationships of Voltage-Gated Calcium Channels. Pharmacol Rev 57:411–425 . https://doi.org/10.1124/pr.57.4.5

105. Feng J, Wible B, Li G-RR, Wang Z, Nattel S (1997) Antisense Oligodeoxynucleotides Directed Against Kv1.5 mRNA Specifically Inhibit Ultrarapid Delayed Rectifier K + Current in Cultured Adult Human Atrial Myocytes. Circ Res 80:572–579 . https://doi.org/10.1161/01.RES.80.4.572

106. Sun XH, Protasi F, Takahashi M, Takeshima H, Ferguson DG, Franzini-Armstrong C (1995) Molecular architecture of membranes involved in excitation-contraction coupling of cardiac muscle. J Cell Biol 129:659–671 . https://doi.org/10.1083/jcb.129.3.659

107. Gong D, Chi X, Wei J, Zhou G, Huang G, Zhang L, Wang R, Lei J, Chen SRW, Yan N (2019) Modulation of cardiac ryanodine receptor 2 by calmodulin. Nature 572:347–351 . https://doi.org/10.1038/s41586-019-1377-y

108. Zhang L, Kelley J, Schmeisser G, Kobayashi YM, Jones LR (1997) Complex Formation between Junctin, Triadin, Calsequestrin, and the Ryanodine Receptor. J Biol Chem 272:23389–23397 . https://doi.org/10.1074/jbc.272.37.23389

109. Sigalas C, Bent S, Kitmitto A, O'Neill S, Sitsapesan R (2009) Ca(2+)-calmodulin can activate and inactivate cardiac ryanodine receptors. Br J Pharmacol 156:794–806 . https://doi.org/10.1111/j.1476-5381.2008.00092.x

110. Sipido KR, Callewaert G, Carmeliet E (1995) Inhibition and Rapid Recovery of Ca 2+ Current During Ca 2+ Release From Sarcoplasmic Reticulum in Guinea Pig Ventricular Myocytes. Circ Res 76:102–109 . https://doi.org/10.1161/01.RES.76.1.102

111. Bers DM (2002) Cardiac excitation–contraction coupling. Nature 415:198–205 . https://doi.org/10.1038/415198a

112. Eisner DA, Caldwell JL, Kistamás K, Trafford AW (2017) Calcium and Excitation-Contraction Coupling in the Heart. Circ Res 121:181–195 . https://doi.org/10.1161/CIRCRESAHA.117.310230

113. Fujioka Y, Komeda M, Matsuoka S (2000) Stoichiometry of Na+-Ca2+ exchange in inside-out patches excised from guinea-pig ventricular myocytes. J Physiol 523:339–351 . https://doi.org/10.1111/j.1469-7793.2000.t01-2-00339.x

114. Takano M, Noma A (1993) The ATP-sensitive K+ channel. Prog Neurobiol 41:21–30 . https://doi.org/10.1016/0301-0082(93)90039-U

115. Marx SO, Kurokawa J, Reiken S, Motoike H, D'Armiento J, Marks AR, Kass RS (2002) Requirement of a macromolecular signaling complex for β adrenergic receptor modulation of the KCNQ1-KCNE1 potassium channel. Science (80-) 295:496–499 . https://doi.org/10.1126/science.1066843

116. O-Uchi J, Rice JJ, Ruwald MH, Parks XX, Ronzier E, Moss AJ, Zareba W, Lopes CM (2015) Impaired IKs channel activation by Ca2+-dependent PKC shows correlation with emotion/arousal-triggered events in LQT1. J Mol Cell Cardiol 79:203–211 . https://doi.org/10.1016/j.yjmcc.2014.11.020

117. Nerbonne JM, Kass RS (2005) Molecular physiology of cardiac repolarization. Physiol Rev 85:1205–1253 . https://doi.org/10.1152/physrev.00002.2005

118. Tristani-Firouzi M, Sanguinetti MC (1998) Voltage-dependent inactivation of the human K + channel KvLQT1 is eliminated by association with minimal K + channel (minK) subunits. J Physiol 510:37–45 . https://doi.org/10.1111/j.1469-7793.1998.037bz.x

119. Barhanin J, Lesage F, Guillemare E, Fink M, Lazdunski M, Romey G (1996) KvLQT1 and IsK (minK) proteins associate to form the IKS cardiac potassium current. Nature 384:78–80 . https://doi.org/10.1038/384078a0

120. Sanguinetti MC, Jurkiewicz NK (1990) Two components of cardiac delayed rectifier K+ current: Differential sensitivity to block by class III antiarrhythmic agents. J Gen Physiol 96:195–215 . https://doi.org/10.1085/jgp.96.1.195

121. Noble D, Tsien RW (1969) Reconstruction of the repolarization process in cardiac Purkinje fibres based on voltage clamp measurements of membrane current. J Physiol 200:233–254 . https://doi.org/10.1113/jphysiol.1969.sp008690

122. Noble D, Tsien RW (1969) Outward membrane currents activated in the plateau range of potentials in cardiac Purkinje fibres. J Physiol 200:205–231 . https://doi.org/10.1113/jphysiol.1969.sp008689

123. Keating M, Dunn C, Atkinson D, Timothy K, Vincent GM, Leppert M (1991) Consistent linkage of the long-QT syndrome to the Harvey ras-1 locus on chromosome 11. Am J Hum Genet 49:1335–1339

124. WARD OC (1964) A NEW FAMILIAL CARDIAC SYNDROME IN CHILDREN. J Ir Med Assoc 54:103–106

125. Romano C (1965) CONGENITAL CARDIAC ARRHYTHMIA. Lancet (London, England) 1:658–659 . https://doi.org/10.1016/S0140-6736(65)91761-7

126. Michael Vincent G, Abildskov JA, Burgess MJ (1974) Q-T interval syndromes. Prog Cardiovasc Dis 16:523–530 . https://doi.org/10.1016/0033-0620(74)90016-4

127. Wang Q, Curran ME, Splawski I, Burn TC, Millholland JM, VanRaay TJ, Shen J, Timothy KW, Vincent GM, de Jager T, Schwartz PJ, Toubin JA, Moss AJ, Atkinson DL, Landes GM, Connors TD, Keating MT, Towbin JA, Moss AJ, Atkinson DL, Landes GM, Connors TD, Keating MT, Toubin JA, Moss AJ, Atkinson DL, Landes GM, Connors TD, Keating MT (1996) Positional cloning of a novel potassium channel gene: KVLQT1 mutations cause cardiac arrhythmias. Nat Genet 12:17–23 . https://doi.org/10.1038/ng0196-17

128. Sanguinetti MC, Curran ME, Zou A, Shen J, Specter PS, Atkinson DL, Keating MT (1996) Coassembly of KVLQT1 and minK (IsK) proteins to form cardiac IKS potassium channel. Nature 384:80–83 . https://doi.org/10.1038/384080a0

129. Chevillard C, Attali B, Lesage F, Fontes M, Barhanin J, Lazdunski M, Mattei MG (1993) Localization of a potassium channel gene (kcne1) to 21q22.1-q22.2 by in situ hybridization and somatic cell hybridization. Genomics 15:243–245 . https://doi.org/10.1006/geno.1993.1051

130. Malo MS, Srivastava K, Ingram VM (1995) Gene assignment by polymerase chain reaction: localization of the human potassium channel Isκ gene to the Down's syndrome region of chromosome 21q22.1-q22.2. Gene 159:273–275 . https://doi.org/10.1016/0378-1119(95)00102-C

131. Murai T, Kakizuka A, Takumi T, Ohkubo H, Nakanishi S (1989) Molecular cloning and sequence analysis of human genomic DNA encoding A novel membrane protein which exhibits a slowly activating potassium channel activity. Biochem Biophys Res Commun 161:176–181 . https://doi.org/10.1016/0006-291X(89)91577-5

132. Caro M, Conde D, Pérez-Riera AR, de Almeida AP, Baranchuk A (2015) The electrocardiogram in Down syndrome. Cardiol Young 25:8–14 . https://doi.org/10.1017/S1047951114000420

133. Lai L-P, Deng C-L, Moss AJ, Kass RS, Liang C (1994) Polymorphism of the gene encoding a human minimal potassium ion channel (minK). Gene 151:339–340 . https://doi.org/10.1016/0378-1119(94)90685-8

134. Splawski I, Shen J, Timothy KW, Lehmann MH, Priori S, Robinson JL, Moss AJ, Schwartz PJ, Towbin JA, Vincent GM, Keating MT (2000) Spectrum of mutations in long-QT syndrome genes. KVLQT1, HERG, SCN5A, KCNE1, and KCNE2. Circulation 102:1178–1185 . https://doi.org/10.1161/01.CIR.102.10.1178

135. Napolitano C, Priori SG, Schwartz PJ, Bloise R, Ronchetti E, Nastoli J, Bottelli G, Cerrone M, Leonardi S (2005) Genetic testing in the long QT syndrome: Development and validation of an efficient approach to genotyping in clinical practice. J Am Med Assoc 294:2975–2980 . https://doi.org/10.1001/jama.294.23.2975

136. Kapplinger JD, Tester DJ, Salisbury BA, Carr JL, Harris-Kerr C, Pollevick GD, Wilde AAM, Ackerman MJ (2009) Spectrum and prevalence of mutations from the first 2,500 consecutive unrelated patients referred for the FAMILION® long QT syndrome genetic test. Hear Rhythm 6:1297–1303 . https://doi.org/10.1016/j.hrthm.2009.05.021

137. Medeiros-Domingo A, Iturralde-Torres P, Ackerman MJ (2007) Clinical and Genetic Characteristics of Long QT Syndrome. Rev Española Cardiol (English Ed 60:739–752 . https://doi.org/10.1016/S1885-5857(08)60010-9

138. Jervell A, Lange-Nielsen F (1957) Congenital deaf-mutism, functional heart disease with prolongation of the Q-T interval, and sudden death. Am Heart J 54:59–68 . https://doi.org/10.1016/0002-8703(57)90079-0

139. Neyroud N, Tesson F, Denjoy I, Leibovici M, Donger C, Barhanin J, Fauré S, Gary F, Coumel P, Petit C, Schwartz K, Guicheney P (1997) A novel mutation in the potassium channel gene KVLQT1 causes the Jervell and Lange-Nielsen cardioauditory syndrome. Nat Genet 15:186–189 . https://doi.org/10.1038/ng0297-186

140. Schulze-Bahr E, Haverkamp W, Wedekind H, Rubie C, Hördt M, Borggrefe M, Assmann G, Breithardt G, Funke H (1997) Autosomal recessive long-QT syndrome (Jervell Lange-Nielsen syndrome) is genetically heterogeneous. Hum Genet 100:573–576 . https://doi.org/10.1007/s004390050554

141. Bianchi L, Priori SG, Napolitano C, Surewicz KA, Dennis AT, Memmi M, Schwartz PJ, Brown AM (2000) Mechanisms of I(Ks) suppression in LQT1 mutants. Am J Physiol - Hear Circ Physiol 279:H3003--H3011 . https://doi.org/10.1152/ajpheart.2000.279.6.h3003

142. Splawski I, Tristani-Firouzi M, Lehmann MH, Sanguinetti MC, Keating MT (1997) Mutations in the hminK gene cause long QT syndrome and suppress I(Ks) function. Nat Genet 17:338–340 . https://doi.org/10.1038/ng1197-338

143. Nicolas M-T, Demêmes D, Martin A, Kupershmidt S, Barhanin J (2001) KCNQ1/KCNE1 potassium channels in mammalian vestibular dark cells. Hear Res 153:132–145 . https://doi.org/10.1016/S0378-5955(00)00268-9

144. Zaklyazminskaya E V., Abriel H (2012) Prevalence of Significant Genetic Variants in Congenital Long QT Syndrome is Largely Underestimated. Front Pharmacol 3: . https://doi.org/10.3389/fphar.2012.00072

145. Nicolas CS, Park KH, El Harchi A, Camonis J, Kass RS, Escande D, Mérot J, Loussouarn G, Le Bouffant F, Baró I (2008) IKs response to protein kinase A-dependent KCNQ1 phosphorylation requires direct interaction with microtubules. Cardiovasc Res 79:427–435 . https://doi.org/10.1093/cvr/cvn085

146. Thompson E, Eldstrom J, Westhoff M, McAfee D, Fedida D (2018) The IKs Channel Response to cAMP Is Modulated by the KCNE1:KCNQ1 Stoichiometry. Biophys J 115:1731–1740 . https://doi.org/10.1016/j.bpj.2018.09.018

147. Shugg T, Johnson DE, Shao M, Lai X, Witzmann F, Cummins TR, Rubart-Von-der Lohe M, Hudmon A, Overholser BR (2018) Calcium/calmodulin-dependent protein kinase II regulation of I Ks during sustained β-adrenergic receptor stimulation. Hear Rhythm 15:895–904 . https://doi.org/10.1016/j.hrthm.2018.01.024

148. Hong K, Piper DR, Diaz-Valdecantos A, Brugada J, Oliva A, Burashnikov E, Santos-de-Soto J, Grueso-Montero J, Diaz-Enfante E, Brugada P, Sachse F, Sanguinetti MC, Brugada R (2005) De novo KCNQ1 mutation responsible for atrial fibrillation and short QT syndrome in utero. Cardiovasc Res 68:433–440 . https://doi.org/10.1016/j.cardiores.2005.06.023

149. Bellocq C, Van Ginneken ACG, Bezzina CR, Alders M, Escande D, Mannens MMAM, Baró I, Wilde AAM (2004) Mutation in the KCNQ1 gene leading to the short QT-interval syndrome. Circulation 109:2394–2397 . https://doi.org/10.1161/01.CIR.0000130409.72142.FE

150. Chen Y-H, Xu S-J, Bendahhou S, Wang X-L, Wang Y, Xu W-Y, Jin H-W, Sun H, Su X-Y, Zhuang Q-N, Yang Y-Q, Li Y-B, Liu Y, Xu H-J, Li X-F, Ma N, Mou C-P, Chen Z, Barhanin J, Huang W (2003) KCNQ1 Gain-of-Function Mutation in Familial Atrial Fibrillation. Science (80-) 299:251–254 . https://doi.org/10.1126/science.1077771

151. Lundby A, Ravn LS, Svendsen JH, Olesen S-P, Schmitt N (2007) KCNQ1 mutation Q147R is associated with atrial fibrillation and prolonged QT interval. Hear Rhythm 4:1532–1541 . https://doi.org/10.1016/j.hrthm.2007.07.022

152. Osteen JD, Barro-Soria R, Robey S, Sampson KJ, Kass RS, Larsson HP (2012) Allosteric gating mechanism underlies the flexible gating of KCNQ1 potassium channels. Proc Natl Acad Sci 109:7103–7108

153. Barro-Soria R, Rebolledo S, Liin SI, Perez ME, Sampson KJ, Kass RS, Larsson HP (2014) KCNE1 divides the voltage sensor movement in KCNQ1/KCNE1 channels into two steps. Nat Commun 5: . https://doi.org/10.1038/ncomms4750

154. Kang C, Tian C, Sönnichsen FD, Smith JA, Meiler J, George AL, Vanoye CG, Kim HJ, Sanders CR (2008) Structure of KCNE1 and Implications for How It Modulates the KCNQ1 Potassium Channel † ‡. Biochemistry 47:7999–8006 . https://doi.org/10.1021/bi800875q

155. Xu Y, Wang Y, Meng X-YY, Zhang M, Jiang M, Cui M, Tseng G-NN (2013) Building KCNQ1/KCNE1 Channel Models and Probing their Interactions by Molecular-Dynamics Simulations. Biophys J 105:2461–2473 . https://doi.org/10.1016/j.bpj.2013.09.058

156. Zaydman MA, Kasimova MA, McFarland K, Beller Z, Hou P, Kinser HE, Liang H, Zhang G, Shi J, Tarek M, others (2014) Domain–domain interactions determine the gating, permeation, pharmacology, and subunit modulation of the IKs ion channel. Elife 3:e03606 . https://doi.org/10.7554/eLife.03606

157. Park K-H, Piron J, Dahimene S, Mérot J, Baró I, Escande D, Loussouarn G (2005) Impaired KCNQ1–KCNE1 and Phosphatidylinositol-4,5-Bisphosphate Interaction Underlies the Long QT Syndrome. Circ Res 96:730–739 . https://doi.org/10.1161/01.RES.0000161451.04649.a8

158. Seebohm G, Strutz-Seebohm N, Ureche ON, Henrion U, Baltaev R, MacK AF, Korniychuk G, Steinke K, Tapken D, Pfeufer A, Kääb S, Bucci C, Attali B, Merot J, Tavare JM, Hoppe UC, Sanguinetti MC, Lang F, Kääb S, Bucci C, Attali B, Merot J, Tavare JM, Hoppe UC, Sanguinetti MC, Lang F (2008) Long QT syndrome-associated mutations in KCNQ1 and KCNE1 subunits disrupt normal endosomal recycling of IKs channels. Circ Res 103:1451–1457 . https://doi.org/10.1161/CIRCRESAHA.108.177360

159. Hoosien M, Ellen Ahearn M, Myerburg RJ, Pham T V, Miller TE, Smets MJ, Baumbach-Reardon L, Young M-L, Farooq A, Bishopric NH (2013) Dysfunctional potassium channel subunit interaction as a novel mechanism of long QT syndrome. Hear Rhythm 10:728–737 . https://doi.org/10.1016/j.hrthm.2012.12.033

160. Moreno C, Oliveras A, Bartolucci C, Muñoz C, de la Cruz A, Peraza DA, Gimeno JR, Martín-Martínez M, Severi S, Felipe A, Lambiase PD, Gonzalez T, Valenzuela C (2017) D242N, a KV7.1 LQTS mutation uncovers a key residue for IKs voltage dependence. J Mol Cell Cardiol 110:61–69 . https://doi.org/10.1016/j.yjmcc.2017.07.009

161. Wu D, Pan H, Delaloye K, Cui J (2010) KCNE1 Remodels the Voltage Sensor of Kv7.1 to Modulate Channel Function. Biophys J 99:3599–3608 . https://doi.org/10.1016/j.bpj.2010.10.018

162. Li Y, Zaydman MA, Wu D, Shi J, Guan M, Virgin-Downey B, Cui J (2011) KCNE1 enhances phosphatidylinositol 4,5-bisphosphate (PIP2) sensitivity of IKs to modulate channel activity. Proc Natl Acad Sci U S A 108:9095–9100 . https://doi.org/10.1073/pnas.1100872108

163. Wiener R, Haitin Y, Shamgar L, Fernández-Alonso MC, Martos A, Chomsky-Hecht O, Rivas G, Attali B, Hirsch JA (2008) The KCNQ1 (Kv7.1) COOH terminus, a multitiered scaffold for subunit assembly and protein interaction. J Biol Chem 283:5815–5830 . https://doi.org/10.1074/jbc.M707541200

164. Ghosh S, Nunziato DA, Pitt GS (2006) KCNQ1 Assembly and Function Is Blocked by Long-QT Syndrome Mutations That Disrupt Interaction With Calmodulin. Circ Res 98:1048–1054 . https://doi.org/10.1161/01.RES.0000218863.44140.f2

165. Shamgar L, Ma L, Schmitt N, Haitin Y, Peretz A, Wiener R, Hirsch J, Pongs O, Attali B (2006) Calmodulin Is Essential for Cardiac I KS Channel Gating and Assembly. Circ Res 98:1055–1063 . https://doi.org/10.1161/01.RES.0000218979.40770.69

166. Freites JA, Tobias DJ (2015) Voltage Sensing in Membranes: From Macroscopic Currents to Molecular Motions. J Membr Biol 248:419–430 . https://doi.org/10.1007/s00232-015-9805-x

167. Cui J (2016) Voltage-Dependent Gating: Novel Insights from KCNQ1 Channels. Biophys J 110:14–25 . https://doi.org/10.1016/j.bpj.2015.11.023

168. Wu D, Delaloye K, Zaydman MA, Nekouzadeh A, Rudy Y, Cui J (2010) State-dependent electrostatic interactions of S4 arginines with E1 in S2 during Kv7.1 activation. J Gen Physiol 135:595–606 . https://doi.org/10.1085/jgp.201010408

169. Tao X, Lee A, Limapichat W, Dougherty DA, MacKinnon R (2010) A gating charge transfer center in voltage sensors. Science (80-) 328:67–73 . https://doi.org/10.1126/science.1185954

170. Lin MA, Hsieh J-Y, Mock AF, Papazian DM (2011) R1 in the Shaker S4 occupies the gating charge transfer center in the resting state. J Gen Physiol 138:155–163 . https://doi.org/10.1085/jgp.201110642

171. Lacroix JJ, Bezanilla F (2011) Control of a final gating charge transition by a hydrophobic residue in the S2 segment of a K+ channel voltage sensor. Proc Natl Acad Sci U S A 108:6444–6449 . https://doi.org/10.1073/pnas.1103397108

172. Roux B (2006) Dissecting the Coupling between the Voltage Sensor and Pore Domains. Neuron 52:568–569 . https://doi.org/10.1016/j.neuron.2006.11.002

173. Hou P, Eldstrom J, Shi J, Zhong L, McFarland K, Gao Y, Fedida D, Cui J (2017) Inactivation of KCNQ1 potassium channels reveals dynamic coupling between voltage sensing and pore opening. Nat Commun 8: . https://doi.org/10.1038/s41467-017-01911-8

174. Choveau FS, Rodriguez N, Ali FA, Labro AJ, Rose T, Dahimène S, Boudin H, Le Hénaff C, Escande D, Snyders DJ, Charpentier F, Mérot J, Baró I, Loussouarn G (2011) KCNQ1 Channels Voltage Dependence through a Voltage-dependent Binding of the S4-S5 Linker to the Pore-Domain. J Biol Chem 286:707–716 . https://doi.org/10.1074/jbc.M110.146324

175. Choveau FS, Bierbower SM, Shapiro MS (2012) Pore Helix-S6 Interactions Are Critical in Governing Current Amplitudes of KCNQ3 K+ Channels. Biophys J 102:2499–2509 . https://doi.org/10.1016/j.bpj.2012.04.019

176. Labro AJ, Boulet IR, Choveau FS, Mayeur E, Bruyns T, Loussouarn G, Raes AL, Snyders DJ (2011) The S4-S5 linker of KCNQ1 channels forms a structural scaffold with the S6 segment controlling gate closure. J Biol Chem 286:717–725 . https://doi.org/10.1074/jbc.M110.146977

177. Yellen G (1998) The moving parts of voltage-gated ion channels. Q Rev Biophys 31:239–295 . https://doi.org/10.1017/s0033583598003448

178. Labro AJ, Raes AL, Bellens I, Ottschytsch N, Snyders DJ (2003) Gating of Shaker-type Channels Requires the Flexibility of S6 Caused by Prolines. J Biol Chem 278:50724–50731 . https://doi.org/10.1074/jbc.M306097200

179. Seebohm G, Westenskow P, Lang F, Sanguinetti MC (2005) Mutation of colocalized residues of the pore helix and transmembrane segments S5 and S6 disrupt deactivation and modify inactivation of KCNQ1 K + channels. J Physiol 563:359–368 . https://doi.org/10.1113/jphysiol.2004.080887

180. Seebohm G, Strutz-Seebohm N, Ureche ON, Baltaev R, Lampert A, Kornichuk G, Kamiya K, Wuttke T V., Lerche H, Sanguinetti MC, Lang F (2006) Differential Roles of S6 Domain Hinges in the Gating of KCNQ Potassium Channels. Biophys J 90:2235–2244 . https://doi.org/10.1529/biophysj.105.067165

181. Panaghie G, Purtell K, Tai K-K, Abbott GW (2008) Voltage-Dependent C-Type Inactivation in a Constitutively Open K+ Channel. Biophys J 95:2759–2778 . https://doi.org/10.1529/biophysj.108.133678

182. Boulet IR, Labro AJ, Raes AL, Snyders DJ (2007) Role of the S6 C-terminus in KCNQ1 channel gating. J Physiol 585:325–337 . https://doi.org/10.1113/jphysiol.2007.145813

183. Osteen JD, Sampson KJ, Kass RS (2010) The cardiac IKs channel, complex indeed. Proc Natl Acad Sci U S A 107:18751–18752 . https://doi.org/10.1073/pnas.1014150107

184. Nakajo K, Kubo Y (2015) KCNQ1 channel modulation by KCNE proteins via the voltage-sensing domain: KCNQ1 channel modulation by KCNE. J Physiol 593:2617–2625 . https://doi.org/10.1113/jphysiol.2014.287672

185. Nakajo K (2019) Gating modulation of the KCNQ1 channel by KCNE proteins studied by voltage-clamp fluorometry. Biophys Physicobiology 16:121–126 . https://doi.org/10.2142/biophysico.16.0_121

186. Nakajo K, Kubo Y (2007) KCNE1 and KCNE3 stabilize and/or slow voltage sensing S4 segment of KCNQ1 channel. J Gen Physiol 130:269–281 . https://doi.org/10.1085/jgp.200709805

187. Pusch M, Magrassi R, Wollnik B, Conti F (1998) Activation and Inactivation of Homomeric KvLQT1 Potassium Channels. Biophys J 75:785–792 . https://doi.org/10.1016/S0006-3495(98)77568-X

188. Sun X, Zaydman MA, Cui J (2012) Regulation of Voltage-Activated K+ Channel Gating by Transmembrane β Subunits. Front Pharmacol 3: . https://doi.org/10.3389/fphar.2012.00063

189. Tian C, Vanoye CG, Kang C, Welch RC, Kim HJ, George AL, Sanders CR, Hak JK, George AL, Sanders CR, Kim HJ, George, AL, Sanders CR (2007) Preparation, Functional Characterization, and NMR Studies of Human KCNE1, a Voltage-Gated Potassium Channel Accessory Subunit Associated with Deafness and Long QT Syndrome † , ‡. Biochemistry 46:11459–11472 . https://doi.org/10.1021/bi700705j

190. Tapper AR, George AL (2001) Location and Orientation of minK within the IKs Potassium Channel Complex. J Biol Chem 276:38249–38254 . https://doi.org/10.1074/jbc.M103956200

191. Xu X, Jiang M, Hsu K-L, Zhang M, Tseng G-N (2008) KCNQ1 and KCNE1 in the IKs Channel Complex Make State-dependent Contacts in their Extracellular Domains. J Gen Physiol 131:589–603 . https://doi.org/10.1085/jgp.200809976

192. Chung DY, Chan PJ, Bankston JR, Yang L, Liu G, Marx SO, Karlin A, Kass RS (2009) Location of KCNE1 relative to KCNQ1 in the IKS potassium channel by disulfide cross-linking of substituted cysteines. Proc Natl Acad Sci 106:743–748 . https://doi.org/10.1073/pnas.0811897106

193. Lvov A, Gage SD, Berrios VMVM, Kobertz WR (2010) Identification of a protein–protein interaction between KCNE1 and the activation gate machinery of KCNQ1. J Gen Physiol 135:607–618 . https://doi.org/10.1085/jgp.200910386

194. Wang YH, Jiang M, Xu XL, Hsu K-LL, Zhang M, Tseng G-NN (2011) Gating-Related Molecular Motions in the Extracellular Domain of the IKs Channel: Implications for IKs Channelopathy. J Membr Biol 239:137–156 . https://doi.org/10.1007/s00232-010-9333-7

195. Gofman Y, Shats S, Attali B, Haliloglu T, Ben-Tal N (2012) How Does KCNE1 Regulate the Kv7.1 Potassium Channel? Model-Structure, Mutations, and Dynamics of the Kv7.1-KCNE1 Complex. Structure 20:1343–1352 . https://doi.org/10.1016/j.str.2012.05.016

196. McCrossan ZA, Abbott GW (2004) The MinK-related peptides. Neuropharmacology 47:787–821 . https://doi.org/10.1016/j.neuropharm.2004.06.018

197. Yang W-P, Levesque PC, Little WA, Conder ML, Shalaby FY, Blanar MA (1997) KvLQT1, a voltage-gated potassium channel responsible for human cardiac arrhythmias. Proc Natl Acad Sci 94:4017–4021 . https://doi.org/10.1073/pnas.94.8.4017

198. Wrobel E, Tapken D, Seebohm G (2012) The KCNE Tango – How KCNE1 Interacts with Kv7.1. Front Pharmacol 3 AUG: . https://doi.org/10.3389/fphar.2012.00142

199. Jespersen T, Grunnet M, Olesen S-PP (2005) The KCNQ1 potassium channel: From gene to physiological function. Physiology 20:408–416 . https://doi.org/10.1152/physiol.00031.2005

200. Chouabe C, Neyroud N, Guicheney P, Lazdunski M, Romey G, Barhanin J (1997) Properties of KvLQT1 K+ channel mutations in Romano-Ward and Jervell and Lange-Nielsen inherited cardiac arrhythmias. EMBO J 16:5472–5479 . https://doi.org/10.1093/emboj/16.17.5472

201. Chen H, Kim LA, Rajan S, Xu S, Goldstein SAN (2003) Charybdotoxin Binding in the IKs Pore Demonstrates Two MinK Subunits in Each Channel Complex. Neuron 40:15–23 . https://doi.org/10.1016/S0896-6273(03)00570-1

202. Vallon V, Grahammer F, Volkl H, Sandu CD, Richter K, Rexhepaj R, Gerlach U, Rong Q, Pfeifer K, Lang F (2005) KCNQ1-dependent transport in renal and gastrointestinal epithelia. Proc Natl Acad Sci 102:17864–17869 . https://doi.org/10.1073/pnas.0505860102

203. Vallon V, Grahammer F, Richter K, Bleich M, Lang F, Barhanin J, Völkl H, Warth R (2001) Role of KCNE1-dependent K+ fluxes in mouse proximal tubule. J Am Soc Nephrol 12:2003–2011

204. Schroeder BC, Waldegger S, Fehr S, Bleich M, Warth R, Greger R, Jentsch TJ (2000) A constitutively open potassium channel formed by KCNQ1 and KCNE3. Nature 403:196–199 . https://doi.org/10.1038/35003200

205. Tinel N (2000) KCNE2 confers background current characteristics to the cardiac KCNQ1 potassium channel. EMBO J 19:6326–6330 . https://doi.org/10.1093/emboj/19.23.6326

206. Wu D-MM, Jiang M, Zhang M, Liu X-SS, Korolkova Y V., Tseng G-NN (2006) KCNE2 is colocalized with KCNQ1 and KCNE1 in cardiac myocytes and may function as a negative modulator of IKs current amplitude in the heart. Hear Rhythm 3:1469–1480 . https://doi.org/10.1016/j.hrthm.2006.08.019

207. Toyoda F, Ueyama H, Ding W-GG, Matsuura H (2006) Modulation of functional properties of KCNQ1 channel by association of KCNE1 and KCNE2. Biochem Biophys Res Commun 344:814–820 . https://doi.org/10.1016/j.bbrc.2006.03.213

208. Jiang M, Xu X, Wang Y, Toyoda F, Liu X-SS, Zhang M, Robinson RB, Tseng G-NN (2009) Dynamic partnership between KCNQ1 and KCNE1 and influence on cardiac IKs current amplitude by KCNE2. J Biol Chem 284:16452–16462 . https://doi.org/10.1074/jbc.M808262200

209. Yang Y, Xia M, Jin Q, Bendahhou S, Shi J, Chen YY, Liang B, Lin J, Liu Y, Liu B, Zhou Q, Zhang D, Wang R, Ma N, Su X, Niu K, Pei Y, Xu W, Chen Z, Wan H, Cui J, Barhanin J, Chen YY (2004) Identification of a KCNE2 gain-of-function mutation in patients with familial atrial fibrillation. Am J Hum Genet 75:899–905 . https://doi.org/10.1086/425342

210. Roepke TK, King EC, Reyna-Neyra A, Paroder M, Purtell K, Koba W, Fine E, Lerner DJ, Carrasco N, Abbott GW (2009) KCNE2 deletion uncovers its crucial role in thyroid hormone biosynthesis. Nat Med 15:1186–1194 . https://doi.org/10.1038/nm.2029

211. Grahammer F, Wittekindt OH, Nitschke R, Herling AW, Lang HJ, Bleich M, Schmitt–Gräff A, Barhanin J, Warth R (2001) The cardiac K+ channel KCNQ1 is essential for gastric acid secretion. Gastroenterology 120:1363–1371 . https://doi.org/10.1053/gast.2001.24053

212. Roepke TK, Anantharam A, Kirchhoff P, Busque SM, Young JB, Geibel JP, Lerner DJ, Abbott GW (2006) The KCNE2 potassium channel ancillary subunit is essential for gastric acid secretion. J Biol Chem 281:23740–23747 . https://doi.org/10.1074/jbc.M604155200

213. Grahammer F, Warth R, Barhanin J, Bleich M, Hug MJ (2001) The Small Conductance K + Channel, KCNQ1. J Biol Chem 276:42268–42275 . https://doi.org/10.1074/jbc.M105014200

214. Abbott GW (2016) KCNE1 and KCNE3: The yin and yang of voltage-gated K+ channel regulation. Gene 576:1–13 . https://doi.org/10.1016/j.gene.2015.09.059

215. Panaghie G, Tai K-K, Abbott GW (2006) Interaction of KCNE subunits with the KCNQ1 K + channel pore. J Physiol 570:455–467 . https://doi.org/10.1113/jphysiol.2005.100644

216. Melman YF, Domènech A, De la Luna S, McDonald T V., Luna S de la, McDonald T V., De la Luna S, McDonald T V. (2001) Structural Determinants of KvLQT1 Control by the KCNE Family of Proteins. J Biol Chem 276:6439–6444 . https://doi.org/10.1074/jbc.M010713200

217. Bendahhou S, Marionneau C, Haurogne K, Larroque M-M, Derand R, Szuts V, Escande D, Demolombe S, Barhanin J (2005) In vitro molecular interactions and distribution of KCNE family with KCNQ1 in the human heart. Cardiovasc Res 67:529–538 . https://doi.org/10.1016/j.cardiores.2005.02.014

218. Lundquist AL, Manderfield LJ, Vanoye CG, Rogers CS, Donahue BS, Chang PA, Drinkwater DC, Murray KT, George AL (2005) Expression of multiple KCNE genes in human heart may enable variable modulation of IKs. J Mol Cell Cardiol 38:277–287 . https://doi.org/10.1016/j.yjmcc.2004.11.012

219. Grunnet M, Olesen S-P, Klaerke DA, Jespersen T (2005) hKCNE4 inhibits the hKCNQ1 potassium current without affecting the activation kinetics. Biochem Biophys Res Commun 328:1146–1153 . https://doi.org/10.1016/j.bbrc.2005.01.071

220. Grunnet M, Jespersen T, Rasmussen HB, Ljungstrøm T, Jorgensen NK, Olesen SP, Klaerke DA (2002) KCNE4 is an inhibitory subunit to the KCNQ1 channel. J Physiol 542:119–130 . https://doi.org/10.1113/jphysiol.2002.017301

221. Angelo K, Jespersen T, Grunnet M, Nielsen MS, Klaerke DA, Olesen SP (2002) KCNE5 induces time- and voltage-dependent modulation of the KCNQ1 current. Biophys J 83:1997–2006 . https://doi.org/10.1016/S0006-3495(02)73961-1

222. McDonald T V., Yu Z, Ming Z, Palma E, Meyers MB, Wang KW, Goldstein SAN, Fishman GI (1997) A mink-HERG complex regulates the cardiac potassium current/(Kr). Nature 388:289–292 . https://doi.org/10.1038/40882

223. Deschênes I, Tomaselli GF (2002) Modulation of Kv4.3 current by accessory subunits. FEBS Lett 528:183–188 . https://doi.org/10.1016/S0014-5793(02)03296-9

224. Cui J, Kagan A, Qin D, Mathew J, Melman YF, McDonald T V. (2001) Analysis of the Cyclic Nucleotide Binding Domain of the HERG Potassium Channel and Interactions with KCNE2. J Biol Chem 276:17244–17251 . https://doi.org/10.1074/jbc.M010904200

225. Abbott GW, Sesti F, Splawski I, Buck ME, Lehmann MH, Timothy KW, Keating MT, Goldstein SAN (1999) MiRP1 Forms I Kr Potassium Channels with HERG and Is Associated with Cardiac Arrhythmia. Cell 97:175–187 . https://doi.org/10.1016/S0092-8674(00)80728-X

226. Zhang M, Jiang M, Tseng GN (2001) MinK-related peptide 1 associates with Kv4.2 and modulates its gating function: Potential role as β subunit of cardiac transient outward channel? Circ Res 88:1012–1019 . https://doi.org/10.1161/hh1001.090839

227. Xu Y, Wang Y, Zhang M, Jiang M, Rosenhouse-Dantsker A, Wassenaar T, Tseng G-N (2015) Probing Binding Sites and Mechanisms of Action of an I Ks Activator by Computations and Experiments. Biophys J 108:62–75 . https://doi.org/10.1016/j.bpj.2014.10.059

228. Yu H, Wu J, Potapova I, Wymore RT, Holmes B, Zuckerman J, Pan Z, Wang H, Shi W, Robinson RB, El-Maghrabi MR, Benjamin W, Dixon J, McKinnon D, Cohen IS, Wymore R (2001) MinK-Related Peptide 1. Circ Res 88: . https://doi.org/10.1161/hh1201.093511

229. Decher N, Bundis F, Vajna R, Steinmeyer K (2003) KCNE2 modulates current amplitudes and activation kinetics of HCN4: Influence of KCNE family members on HCN4 currents. Pflugers Arch Eur J Physiol 446:633–640 . https://doi.org/10.1007/s00424-003-1127-7

230. Suh BC, Hille B (2005) Regulation of ion channels by phosphatidylinositol 4,5-bisphosphate. Curr Opin Neurobiol 15:370–378 . https://doi.org/10.1016/j.conb.2005.05.005

231. Hilgemann DW, Feng S, Nasuhoglu C (2001) The Complex and Intriguing Lives of PIP2 with Ion Channels and Transporters. Sci STKE signal Transduct Knowl Environ 2001:re19–re19 . https://doi.org/10.1126/stke.2001.111.re19

232. Suh B-C, Hille B (2008) PIP 2 Is a Necessary Cofactor for Ion Channel Function: How and Why? Annu Rev Biophys 37:175–195 . https://doi.org/10.1146/annurev.biophys.37.032807.125859

233. Woodcock EA, Kistler PM, Ju YK (2009) Phosphoinositide signalling and cardiac arrhythmias. Cardiovasc. Res. 82:286–295

234. Pian P, Bucchi A, Robinson RB, Siegelbaum SA (2006) Regulation of gating and rundown of HCN hyperpolarization-activated channels by exogenous and endogenous PIP2. J Gen Physiol 128:593–604 . https://doi.org/10.1085/jgp.200609648

235. Bian J, Cui J, McDonald T V. (2001) HERG K+ channel activity is regulated by changes in phosphatidyl inositol 4,5-bisphosphate. Circ Res 89:1168–1176 . https://doi.org/10.1161/hh2401.101375

236. Hilgemann D 'W. W, Ball R (1996) Regulation of Cardiac Na+,Ca2+ Exchange and. Science (80-) 273:20–23 . https://doi.org/10.1126/science.273.5277.956

237. Zhang H, He C, Yan X, Mirshahi T, Logothetis DE (1999) Activation of inwardly rectifying K+ channels by distinct Ptdlns(4,5)P2 interactions. Nat Cell Biol 1:183–188 . https://doi.org/10.1038/11103

238. Shyng SL, Cukras CA, Harwood J, Nichols CG (2000) Structural determinants of PIP2 regulation of inward rectifier K(ATP) channels. J Gen Physiol 116:599–607 . https://doi.org/10.1085/jgp.116.5.599

239. Lopes CMB, Zhang H, Rohacs T, Jin T, Yang J, Logothetis DE (2002) Alterations in Conserved Kir Channel-PIP2 Interactions Underlie Channelopathies. Neuron 34:933–944 . https://doi.org/10.1016/S0896-6273(02)00725-0

240. Loussouarn G, Charpentier F, Escande D Phosphatidylinositol-4,5-bisphosphate, PIP2, controls KCNQ1/KCNE1 voltage-gated potassium channels: a functional homology between voltage-gated and inward rectifier K+ channels. 10

241. Zhang H, Craciun LC, Mirshahi T, Rohács T, Lopes CMB, Jin T, Logothetis DE (2003) PIP2 Activates KCNQ Channels, and Its Hydrolysis Underlies Receptor-Mediated Inhibition of M Currents. Neuron 37:963–975 . https://doi.org/10.1016/S0896-6273(03)00125-9

242. Li Y, Gamper N, Hilgemann DW, Shapiro MS (2005) Regulation of Kv7 (KCNQ) K+ Channel Open Probability by Phosphatidylinositol 4,5-Bisphosphate. J Neurosci 25:9825–9835 . https://doi.org/10.1523/JNEUROSCI.2597-05.2005

243. Murata Y, Iwasaki H, Sasaki M, Inaba K, Okamura Y (2005) Phosphoinositide phosphatase activity coupled to an intrinsic voltage sensor. Nature 435:1239–1243 . https://doi.org/10.1038/nature03650

244. Murata Y, Okamura Y (2007) Depolarization activates the phosphoinositide phosphatase Ci-VSP, as detected in Xenopus oocytes coexpressing sensors of PIP2. J Physiol 583:875–889 . https://doi.org/10.1113/jphysiol.2007.134775

245. Zaydman MA, Cui J (2014) PIP2 regulation of KCNQ channels: biophysical and molecular mechanisms for lipid modulation of voltage-dependent gating. Front Physiol 5:195 . https://doi.org/10.3389/fphys.2014.00195

246. Thomas AM, Harmer SC, Khambra T, Tinker A (2011) Characterization of a Binding Site for Anionic Phospholipids on KCNQ1. J Biol Chem 286:2088–2100 . https://doi.org/10.1074/jbc.M110.153551

247. Choveau FS, Abderemane-Ali F, Coyan FC, Es-Salah-Lamoureux Z, Baró I, Loussouarn G (2012) Opposite Effects of the S4–S5 Linker and PIP2 on Voltage-Gated Channel Function: KCNQ1/KCNE1 and Other Channels. Front Pharmacol 3: . https://doi.org/10.3389/fphar.2012.00125

248. Zaydman MA, Silva JR, Delaloye K, Li Y, Liang H, Larsson HP, Shi J, Cui J (2013) Kv7.1 ion channels require a lipid to couple voltage sensing to pore opening. Proc Natl Acad Sci 110:13180–13185 . https://doi.org/10.1073/pnas.1305167110

249. Kasimova MA, Zaydman MA, Cui J, Tarek M (2015) PIP2-dependent coupling is prominent in Kv7.1 due to weakened interactions between S4-S5 and S6. Sci Rep 5:7474 . https://doi.org/10.1038/srep07474

250. Eckey K, Wrobel E, Strutz-Seebohm N, Pott L, Schmitt N, Seebohm G (2014) Novel Kv7.1-Phosphatidylinositol 4,5-Bisphosphate Interaction Sites Uncovered by Charge Neutralization Scanning. J Biol Chem 289:22749–22758 . https://doi.org/10.1074/jbc.M114.589796

251. Ramasubramanian S, Rudy Y (2018) The Structural Basis of IKs Ion-Channel Activation: Mechanistic Insights from Molecular Simulations. Biophys J 114:2584–2594 . https://doi.org/10.1016/j.bpj.2018.04.023

252. Jalily Hasani H, Ahmed M, Barakat K (2017) A comprehensive structural model for the human KCNQ1/KCNE1 ion channel. J Mol Graph Model 78:26–47 . https://doi.org/10.1016/j.jmgm.2017.09.019

253. Nakajo K, Ulbrich MH, Kubo Y, Isacoff EY (2010) Stoichiometry of the KCNQ1 - KCNE1 ion channel complex. Proc Natl Acad Sci U S A 107:18862–18867 . https://doi.org/10.1073/pnas.1010354107

254. Murray CI, Westhoff M, Eldstrom J, Thompson E, Emes R, Fedida D (2016) Unnatural amino acid photo-crosslinking of the IKs channel complex demonstrates a KCNE1:KCNQ1 stoichiometry of up to 4:4. Elife 5: . https://doi.org/10.7554/eLife.11815

255. Wang Y, Eldstrom J, Fedida D (2020) Gating and Regulation of KCNQ1 and KCNQ1 + KCNE1 Channel Complexes. Front Physiol 11:504 . https://doi.org/10.3389/fphys.2020.00504

256. Morin TJ, Kobertz WR (2008) Counting membrane-embedded KCNE-subunits in functioning K+ channel complexes. Proc Natl Acad Sci 105:1478–1482 . https://doi.org/10.1073/pnas.0710366105

257. Ma L-JJ, Ohmert I, Vardanyan V (2011) Allosteric Features of KCNQ1 Gating Revealed by Alanine Scanning Mutagenesis. Biophys J 100:885–894 . https://doi.org/10.1016/j.bpj.2010.12.3726

258. Smith JA, Vanoye CG, George AL, Meiler J, Sanders CR (2007) Structural Models for the KCNQ1 Voltage-Gated Potassium Channel †. Biochemistry 46:14141–14152 . https://doi.org/10.1021/bi701597s

259. Pons J-L, Labesse G (2009) @TOME-2: a new pipeline for comparative modeling of protein-ligand complexes. Nucleic Acids Res 37:W485–W491 . https://doi.org/10.1093/nar/gkp368

260. Biasini M, Bienert S, Waterhouse A, Arnold K, Studer G, Schmidt T, Kiefer F, Cassarino TG, Bertoni M, Bordoli L, Schwede T (2014) SWISS-MODEL: modelling protein tertiary and quaternary structure using evolutionary information. Nucleic Acids Res 42:W252--W258 . https://doi.org/10.1093/nar/gku340

261. Yu J, Picord G, Tuffery P, Guerois R (2015) HHalign-Kbest: exploring sub-optimal alignments for remote homology comparative modeling: Fig. 1. Bioinformatics btv441 . https://doi.org/10.1093/bioinformatics/btv441

262. Arthur H, Cameron M, Joubert E, Witthuhn RC (2011) Gapped BLAST and PSI-BLAST: a new generation of protein database search programs. World J Microbiol Biotechnol 27:3389–3402 . https://doi.org/10.1016/0956-7135(96)00004-7

263. Chen X, Wang Q, Ni F, Ma J (2010) Structure of the full-length Shaker potassium channel Kv1.2 by normal-mode-based X-ray crystallographic refinement. Proc Natl Acad Sci U S A 107:11352–11357 . https://doi.org/10.1073/pnas.1000142107

264. Delemotte L, Tarek M, Klein ML, Amaral C, Treptow W (2011) Intermediate states of the Kv1.2 voltage sensor from atomistic molecular dynamics simulations. Proc Natl Acad Sci 108:6109–6114 . https://doi.org/10.1073/pnas.1102724108

265. Larkin MAA, Blackshields G, Brown NPP, Chenna R, Mcgettigan PAA, McWilliam H, Valentin F, Wallace IMM, Wilm A, Lopez R, Thompson JDD, Gibson TJJ, Higgins DGG (2007) Clustal W and Clustal X version 2.0. Bioinformatics 23:2947–2948 . https://doi.org/10.1093/bioinformatics/btm404

266. Webb B, Sali A (2016) Comparative Protein Structure Modeling Using MODELLER. Curr Protoc Bioinforma 54:5.6.1-5.6.37 . https://doi.org/10.1002/cpbi.3

267. Peng D, Kim J-HH, Kroncke BM, Law CL, Xia Y, Droege KD, Van Horn WD, Vanoye CG, Sanders CR (2014) Purification and Structural Study of the Voltage-Sensor Domain of the Human KCNQ1 Potassium Ion Channel. Biochemistry 53:2032–2042 . https://doi.org/10.1021/bi500102w

268. Shen M, Sali A (2006) Statistical potential for assessment and prediction of protein structures. Protein Sci 15:2507–2524 . https://doi.org/10.1110/ps.062416606

269. Laskowski RA, MacArthur MW, Moss DS, Thornton JM (1993) PROCHECK: a program to check the stereochemical quality of protein structures. J Appl Crystallogr 26:283–291 . https://doi.org/10.1107/S0021889892009944

270. Allen M. P, Tildesley D. J (1987) Computer simulation of liquids. Clarendon Press ; Oxford University Press, Oxford [England] : New York

271. Leach AR (2001) Molecular modelling: principles and applications, 2nd ed. Prentice Hall, Harlow, England ; New York

272. Frenkel D, Smit B (2002) Understanding molecular simulation: from algorithms to applications, 2nd ed. Academic Press, San Diego

273. Schuler LD, Daura X, van Gunsteren WF (2001) An improved GROMOS96 force field for aliphatic hydrocarbons in the condensed phase. J Comput Chem 22:1205–1218 . https://doi.org/10.1002/jcc.1078

274. MacKerell AD, Bashford D, Bellott M, Dunbrack RL, Evanseck JD, Field MJ, Fischer S, Gao J, Guo H, Ha S, Joseph-McCarthy D, Kuchnir L, Kuczera K, Lau FTKK, Mattos C, Michnick S, Ngo T, Nguyen DT, Prodhom B, Reiher WE, Roux B, Schlenkrich M, Smith JC, Stote R, Straub J, Watanabe M, Wiórkiewicz-Kuczera J, Yin D, Karplus M (1998) All-Atom Empirical Potential for Molecular Modeling and Dynamics Studies of Proteins †. J Phys Chem B 102:3586–3616 . https://doi.org/10.1021/jp973084f

275. Ponder JW, Case DA (2003) Force fields for protein simulations. Adv Protein Chem 66:27–85

276. Jorgensen WL, Maxwell DS, Tirado-Rives J (1996) Development and Testing of the OPLS All-Atom Force Field on Conformational Energetics and Properties of Organic Liquids. J Am Chem Soc 118:11225–11236 . https://doi.org/10.1021/ja9621760

277. Verlet L (1967) Computer "experiments" on classical fluids. I. Thermodynamical properties of Lennard-Jones molecules. Phys Rev 159:98–103 . https://doi.org/10.1103/PhysRev.159.98

278. Darden T, York D, Pedersen L (1993) Particle mesh Ewald: An N·log(N) method for Ewald sums in large systems. J Chem Phys 98:10089–10092 . https://doi.org/10.1063/1.464397

279. Jo S, Kim T, Iyer VG, Im W (2008) CHARMM-GUI: A web-based graphical user interface for CHARMM. J Comput Chem 29:1859–1865 . https://doi.org/10.1002/jcc.20945

280. Wu EL, Cheng X, Jo S, Rui H, Song KC, Dávila-Contreras EM, Qi Y, Lee J, Monje-Galvan V, Venable RM, Klauda JB, Im W (2014) CHARMM-GUI Membrane Builder toward realistic biological membrane simulations. J Comput Chem 35:1997–2004 . https://doi.org/10.1002/jcc.23702

281. Shaw DE, Dror RO, Salmon JK, Grossman JP, Mackenzie KM, Bank JA, Young C, Deneroff MM, Batson B, Bowers KJ, Chow E, Eastwood MP, Ierardi DJ, Klepeis JL, Kuskin JS, Larson RH, Lindorff-Larsen K, Maragakis P, Moraes MA, Piana S, Shan Y, Towles B (2009) Millisecond-scale molecular dynamics simulations on Anton. In: Proceedings of the {Conference} on {High} {Performance} {Computing} {Networking}, {Storage} and {Analysis}. ACM, New York, NY, USA, NY, USA, p 11

282. Martyna GJ, Klein ML, Tuckerman M (1992) Nosé–Hoover chains: The canonical ensemble via continuous dynamics. J Chem Phys 97:2635–2643 . https://doi.org/10.1063/1.463940

283. Pastor RW, Brooks BR, Szabo A (1988) An analysis of the accuracy of langevin and molecular dynamics algorithms. Mol Phys 65:1409–1419 . https://doi.org/10.1080/00268978800101881

284. Feller SE, Zhang Y, Pastor RW, Brooks BR (1995) Constant pressure molecular dynamics simulation: The Langevin piston method. J Chem Phys 103:4613–4621 . https://doi.org/10.1063/1.470648

285. Berendsen HJC, Postma JPM, Van Gunsteren WF, Dinola A, Haak JR (1984) Molecular dynamics with coupling to an external bath. J Chem Phys 81:3684–3690 . https://doi.org/10.1063/1.448118

286. Brooks BR, Brooks CL, Mackerell AD, Nilsson L, Petrella RJ, Roux B, Won Y, Archontis G, Bartels C, Boresch S, Caflisch A, Caves L, Cui Q, Dinner AR, Feig M, Fischer S, Gao J, Hodoscek M, Im W, Kuczera K, Lazaridis T, Ma J, Ovchinnikov V, Paci E, Pastor RW, Post CB, Pu JZ, Schaefer M, Tidor B, Venable RM, Woodcock HL, Wu X, Yang W, York DM, Karplus M (2009) CHARMM: The biomolecular simulation program. J Comput Chem 30:1545–1614 . https://doi.org/10.1002/jcc.21287

287. Case DA, Cheatham TE, Darden T, Gohlke H, Luo R, Merz KM, Onufriev A, Simmerling C, Wang B, Woods RJ (2005) The Amber biomolecular simulation programs. J Comput Chem 26:1668–1688 . https://doi.org/10.1002/jcc.20290

288. Van Der Spoel D, Lindahl E, Hess B, Groenhof G, Mark AE, Berendsen HJCC (2005) GROMACS: Fast, flexible, and free. J Comput Chem 26:1701–1718 . https://doi.org/10.1002/jcc.20291

289. Phillips JC, Braun R, Wang W, Gumbart J, Tajkhorshid E, Villa E, Chipot C, Skeel RD, Kalé L, Schulten K (2005) Scalable molecular dynamics with NAMD. J Comput Chem 26:1781–1802 . https://doi.org/10.1002/jcc.20289

290. Bowers KJ, Chow E, Xu H, Dror RO, Eastwood MP, Gregersen BA, Klepeis JL, Kolossvary I, Moraes MA, Sacerdoti FD, others (2006) Scalable algorithms for molecular dynamics simulations on commodity clusters. In: Proceedings of the 2006 ACM/EEE conference on Supercomputing. ACM, p 84

291. Klauda JB, Venable RM, Freites JA, O'Connor JW, Tobias DJ, Mondragon-Ramirez C, Vorobyov I, MacKerell AD, Pastor RW (2010) Update of the CHARMM All-Atom Additive Force Field for Lipids: Validation on Six Lipid Types. J Phys Chem B 114:7830–7843 . https://doi.org/10.1021/jp101759q

292. Lupyan D, Mezei M, Logothetis DE, Osman R (2010) A molecular dynamics investigation of lipid bilayer perturbation by PIP2. Biophys J 98:240–247 . https://doi.org/10.1016/j.bpj.2009.09.063

293. Buck M, Bouguet-Bonnet S, Pastor RW, MacKerell AD (2006) Importance of the CMAP correction to the CHARMM22 protein force field: Dynamics of hen lysozyme. Biophys J 90:L36–L38 . https://doi.org/10.1529/biophysj.105.078154

294. Ryckaert JP, Ciccotti G, Berendsen HJC (1977) Numerical integration of the cartesian equations of motion of a system with constraints: molecular dynamics of n-alkanes. J Comput Phys 23:327–341 . https://doi.org/10.1016/0021-9991(77)90098-5

295. Careaga CL, Falke JJ (1992) Structure and dynamics of Escherichia coli chemosensory receptors. Engineered sulfhydryl studies. Biophys J 62:209–219 . https://doi.org/10.1016/S0006-3495(92)81806-4

296. Kumar S, Nussinov R (2002) Relationship between ion pair geometries and electrostatic strengths in proteins. Biophys J 83:1595–1612

297. McLaughlin S, Wang J, Gambhir A, Murray D (2002) PIP 2 and Proteins: Interactions, Organization, and Information Flow. Annu Rev Biophys Biomol Struct 31:151–175 . https://doi.org/10.1146/annurev.biophys.31.082901.134259

298. Humphrey W, Dalke A, Schulten K (1996) VMD: Visual molecular dynamics. J Mol Graph 14:33–38 . https://doi.org/10.1016/0263-7855(96)00018-5

299. Heiner Schwarte, Guido Masarotto, Seth Falcon, Douglas Bates, John Chambers, Peter Dalgaard, Robert Gentleman, Kurt Hornik, Ross Ihaka, Tomas Kalibera, Michael Lawrence, Friedrich Leisch, Uwe Ligges, Thomas Lumley, Martin Maechler, Martin Morgan, Duncan Murdoch, Paul Murrell, Martyn Plummer, Brian Ripley, Deepayan Sarkar, Duncan Temple Lang, Luke Tierney, Simon Urbanek, Schwarte H, Masarotto G, Falcon S (2017) R: A language and environment for statistical computing. R Foundation for Statistical Computing, Vienna, Austria

300. Beckstein O, Tai K, Sansom MSP (2004) Not ions alone: Barriers to ion permeation in nanopores and channels. J Am Chem Soc 126:14694–14695 . https://doi.org/10.1021/ja045271e

301. Peter C, Hummer G (2005) Ion Transport through Membrane-Spanning Nanopores Studied by Molecular Dynamics Simulations and Continuum Electrostatics Calculations. Biophys J 89:2222–2234 . https://doi.org/10.1529/biophysj.105.065946

302. Treptow W, Tarek M (2006) Molecular restraints in the permeation pathway of ion channels. Biophys J 91:L26--28 . https://doi.org/10.1529/biophysj.106.087437

303. Smart OS, Neduvelil JG, Wang X, Wallace BA, Sansom MSP (1996) HOLE: A program for the analysis of the pore dimensions of ion channel structural models. J Mol Graph 14:354–360 . https://doi.org/10.1016/S0263-7855(97)00009-X

304. Page RC, Li C, Hu J, Gao FP, Cross TA (2007) Lipid bilayers: an essential environment for the understanding of membrane proteins. Magn Reson Chem 45:S2--S11 . https://doi.org/10.1002/mrc.2077

305. Langosch D, Arkin IT (2009) Interaction and conformational dynamics of membrane-spanning protein helices. Protein Sci 18:1343–1358 . https://doi.org/10.1002/pro.154

306. Senes A, Ubarretxena-Belandia I, Engelman DM (2001) The C --H***O hydrogen bond: A determinant of stability and specificity in transmembrane helix interactions. Proc Natl Acad Sci 98:9056–9061 . https://doi.org/10.1073/pnas.161280798

307. Johnson RM, Hecht K, Deber CM (2007) Aromatic and cation-pi interactions enhance helix-helix association in a membrane environment. Biochemistry 46:9208–9214 . https://doi.org/10.1021/bi7008773

308. Valley CC, Cembran A, Perlmutter JD, Lewis AK, Labello NP, Gao J, Sachs JN (2012) The Methionine-aromatic Motif Plays a Unique Role in Stabilizing Protein Structure. J Biol Chem 287:34979–34991 . https://doi.org/10.1074/jbc.M112.374504

309. Bartos DC, Giudicessi JR, Tester DJ, Ackerman MJ, Ohno S, Horie M, Gollob MH, Burgess DE, Delisle BP (2014) A KCNQ1 mutation contributes to the concealed type 1 long QT phenotype by limiting the Kv7.1 channel conformational changes associated with protein kinase A phosphorylation. Hear Rhythm 11:459–468 . https://doi.org/10.1016/j.hrthm.2013.11.021

310. Gómez-Tamayo JC, Cordomí A, Olivella M, Mayol E, Fourmy D, Pardo L (2016) Analysis of the interactions of sulfur-containing amino acids in membrane proteins. Protein Sci 25:1517–1524 . https://doi.org/10.1002/pro.2955

311. McGaughey GB, Gagné M, Rappé AK (1998) π-Stacking interactions. Alive and well in proteins. J Biol Chem 273:15458–15463 . https://doi.org/10.1074/jbc.273.25.15458

312. Dalke A, Schulten K (1997) Using Tcl for molecular visualization and analysis. In: Pacific Symposium on Biocomputing. Pacific Symposium on Biocomputing. pp 85–96

313. Durell SR, Guy HR (1992) Atomic scale structure and functional models of voltage-gated potassium channels. Biophys J 62:238–250

314. Catterall WA (1986) Voltage-dependent gating of sodium channels: correlating structure and function. Trends Neurosci 9:7–10 . https://doi.org/10.1016/0166-2236(86)90004-4

315. Nakajo K, Kubo Y (2014) Steric hindrance between S4 and S5 of the KCNQ1/KCNE1 channel hampers pore opening. Nat Commun 5: . https://doi.org/10.1038/ncomms5100

316. Xu S-Z, Sukumar P, Zeng F, Li J, Jairaman A, English A, Naylor J, Ciurtin C, Majeed Y, Milligan CJ, Bahnasi YM, Al-Shawaf E, Porter KE, Jiang L-H, Emery P, Sivaprasadarao A, Beech DJ (2008) TRPC channel activation by extracellular thioredoxin. Nature 451:69–72 . https://doi.org/10.1038/nature06414

317. Chan PJ, Osteen JD, Xiong D, Bohnen MS, Doshi D, Sampson KJ, Marx SO, Karlin A, Kass RS (2012) Characterization of KCNQ1 atrial fibrillation mutations reveals distinct dependence on KCNE1. J Gen Physiol 139:135–144 . https://doi.org/10.1085/jgp.201110672

318. Díaz-Franulic I, Sepúlveda R V., Navarro-Quezada N, González-Nilo F, Naranjo D (2015) Pore dimensions and the role of occupancy in unitary conductance of Shaker K channels. J Gen Physiol 146:133–146 . https://doi.org/10.1085/jgp.201411353

319. Taylor KC, Kang PW, Hou P, Yang N-D Du, Kuenze G, Smith JA, Shi J, Huang H, White KM, Peng D, George AL, Meiler J, McFeeters RL, Cui J, Sanders CR (2020) Structure and physiological function of the human KCNQ1 channel voltage sensor intermediate state. Elife 9:1–31 . https://doi.org/10.7554/eLife.53901

320. Hedley PL, Jørgensen P, Schlamowitz S, Wangari R, Moolman-Smook J, Brink PA, Kanters JK, Corfield VA, Christiansen M (2009) The genetic basis of long QT and short QT syndromes: A mutation update. Hum Mutat 30:1486–1511 . https://doi.org/10.1002/humu.21106

321. Huang H, Kuenze G, Smith JA, Taylor KC, Duran AM, Hadziselimovic A, Meiler J, Vanoye CG, George AL, Sanders CR (2018) Mechanisms of KCNQ1 channel dysfunction in long QT syndrome involving voltage sensor domain mutations. Sci Adv 4:13 . https://doi.org/10.1126/sciadv.aar2631

322. Vanoye CG, Desai RR, Fabre KL, Gallagher SL, Potet F, DeKeyser J-MM, Macaya D, Meiler J, Sanders CR, George AL (2018) High-Throughput Functional Evaluation of KCNQ1 Decrypts Variants of Unknown Significance. Circ Genomic Precis Med 11:e002345 . https://doi.org/10.1161/CIRCGEN.118.002345

323. Hou P, Kang PW, Kongmeneck AD, Yang N-D, Liu Y, Shi J, Xu X, White KM, Zaydman MA, Kasimova MA, Seebohm G, Zhong L, Zou X, Tarek M, Cui J (2020) Two-stage electro–mechanical coupling of a KV channel in voltage-dependent activation. Nat Commun 11:676 . https://doi.org/10.1038/s41467-020-14406-w

324. Crotti L, Spazzolini C, Schwartz PJ, Shimizu W, Denjoy I, Schulze-Bahr E, Zaklyazminskaya E V, Swan H, Ackerman MJ, Moss AJ, Wilde AAM, Horie M, Brink PA, Insolia R, De Ferrari GM, Crimi G (2007) The common long-QT syndrome mutation KCNQ1/A341V causes unusually severe clinical manifestations in patients with different ethnic backgrounds: toward a mutation-specific risk stratification. Circulation 116:2366–2375 . https://doi.org/10.1161/CIRCULATIONAHA.107.726950

325. Liin SI, Barro-Soria R, Larsson HP (2015) The KCNQ1 channel – remarkable flexibility in gating allows for functional versatility. J Physiol 593:2605–2615 . https://doi.org/10.1113/jphysiol.2014.287607

326. WILSON AJ, QUINN K V., Graves FM, Bitner-Glindzicz M, Tinker A, BITNERGLINDZICZ M, Tinker A (2005) Abnormal KCNQ1 trafficking influences disease pathogenesis in hereditary long QT syndromes (LQT1). Cardiovasc Res 67:476–486 . https://doi.org/10.1016/j.cardiores.2005.04.036

327. Chen J, Mitcheson JS, Tristani-Firouzi M, Lin M, Sanguinetti MC (2001) The S4-S5 linker couples voltage sensing and activation of pacemaker channels. Proc Natl Acad Sci U S A 98:11277–11282 . https://doi.org/10.1073/pnas.201250598

328. Long SB, Campbell EB, MacKinnon R (2005) Voltage sensor of Kv1.2: Structural basis of electromechanical coupling. Science (80-) 309:903–908 . https://doi.org/10.1126/science.1116270

329. Yu H, Lin Z, Mattmann ME, Zou B, Terrenoire C, Zhang H, Wu M, McManus OB, Kass RS, Lindsley CW, Hopkins CR, Li M (2013) Dynamic subunit stoichiometry confers a progressive continuum of pharmacological sensitivity by KCNQ potassium channels. Proc Natl Acad Sci 110:8732–8737 . https://doi.org/10.1073/pnas.1300684110

330. Liu W, Yang J, Hu D, Kang C, Li C, Zhang S, Li P, Chen Z, Qin X, Ying K, Li Y, Li Y, Li Z, Cheng X, Li L, Qi Y, Chen S, Wang Q (2002) KCNQ1 and KCNH2 mutations associated with long QT syndrome in a Chinese population. Hum Mutat 20:475–476 . https://doi.org/10.1002/humu.9085

331. Horovitz A (1996) Double-mutant cycles: A powerful tool for analyzing protein structure and function. Fold Des 1:121–126 . https://doi.org/10.1016/S1359-0278(96)00056-9

332. Schreiber G, Fersht AR (1995) Energetics of protein-protein interactions: Analysis ofthe Barnase-Barstar interface by single mutations and double mutant cycles. J Mol Biol 248:478–486 . https://doi.org/10.1016/S0022-2836(95)80064-6

333. Hou P, Shi J, White KM, Gao Y, Cui J (2019) ML277 specifically enhances the fully activated open state of KCNQ1 by modulating VSD-pore coupling. Elife 8:e48576 . https://doi.org/10.7554/eLife.48576

334. Liao S-M, Du Q-S, Meng J-Z, Pang Z-W, Huang R-B (2013) The multiple roles of histidine in protein interactions. Chem Cent J 7:44 . https://doi.org/10.1186/1752-153X-7-44

335. Melman YF, Um SY, Krumerman A, Kagan A, McDonald T V. (2004) KCNE1 binds to the KCNQ1 pore to regulate potassium channel activity. Neuron 42:927–937 . https://doi.org/10.1016/j.neuron.2004.06.001

336. Seebohm G, Chen J, Strutz N, Culberson C, Lerche C, Sanguinetti MC (2003) Molecular Determinants of KCNQ1 Channel Block by a Benzodiazepine. Mol Pharmacol 64:70–77 . https://doi.org/10.1124/mol.64.1.70

337. Jalily Hasani H, Ganesan A, Ahmed M, Barakat KH (2018) Effects of protein-protein interactions and ligand binding on the ion permeation in KCNQ1 potassium channel. PLoS One 13:e0191905 . https://doi.org/10.1371/journal.pone.0191905

338. Jacob J, Duclohier H, Cafiso DS (1999) The Role of Proline and Glycine in Determining the Backbone Flexibility of a Channel-Forming Peptide. Biophys J 76:1367–1376 . https://doi.org/10.1016/S0006-3495(99)77298-X

339. Högel P, Götz A, Kuhne F, Ebert M, Stelzer W, Rand KD, Scharnagl C, Langosch D (2018) Glycine Perturbs Local and Global Conformational Flexibility of a Transmembrane Helix. Biochemistry 57:1326–1337 . https://doi.org/10.1021/acs.biochem.7b01197

340. Lai L-P, Su Y-N, Chiang F-T, Juang J-M, Liu Y-B, Ho Y-L, Chen W-J, Yeh S-J, Wang C-C, Ko Y-L, Wu T-J, Ueng K-C, Lei M-H, Tsao H-M, Chen S-A, Lin T-K, Wu M-H, Lo H-M, Huang SKS, Lin J-L (2005) Denaturing high-performance liquid chromatography screening of the long QT syndrome-related cardiac sodium and potassium channel genes and identification of novel mutations and single nucleotide polymorphisms. J Hum Genet 50:490–496 . https://doi.org/10.1007/s10038-005-0283-3

341. Chowdhury S, Chanda B (2012) Thermodynamics of electromechanical coupling in voltage-gated ion channels. J Gen Physiol 140:613–623 . https://doi.org/10.1085/jgp.201210840

342. Horrigan FT, Aldrich RW (1999) Allosteric voltage gating of potassium channels II: mSlo channel gating charge movement in the absence of Ca2+. J Gen Physiol 114:305–336 . https://doi.org/10.1085/jgp.114.2.305

343. Cox DH, Cui J, Aldrich RW (1997) Allosteric gating of a large conductance Ca-activated K+ channel. J Gen Physiol 110:257–281 . https://doi.org/10.1085/jgp.110.3.257

344. Zagotta WN, Hoshl T, Dittman J, Aldrich RW (1994) Shaker potassium channel gating II: Transitions in the activation pathway. J Gen Physiol 103:279–319 . https://doi.org/10.1085/jgp.103.2.279

345. Mannuzzu LM, Isacoff EY (2000) Independence and cooperativity in rearrangements of a potassium channel voltage sensor revealed by single subunit fluorescence. J Gen Physiol 115:257–268 . https://doi.org/10.1085/jgp.115.3.257

346. Monod J, Wyman J, Changeux J-PP (1965) On the nature of allosteric transitions: A plausible model. J Mol Biol 12:88–118 . https://doi.org/10.1016/S0022-2836(65)80285-6

347. Changeux J-P (2012) Allostery and the Monod-Wyman-Changeux Model After 50 Years. Annu Rev Biophys 41:103–133 . https://doi.org/10.1146/annurev-biophys-050511-102222

348. Meisel E, Dvir M, Haitin Y, Giladi M, Peretz A, Attali B (2012) KCNQ1 channels do not undergo concerted but sequential gating transitions in both the absence and the presence of KCNE1 protein. J Biol Chem 287:34212–34224 . https://doi.org/10.1074/jbc.M112.364901

349. Westhoff M, Eldstrom J, Murray CI, Thompson E, Fedida D (2019) IKs ion-channel pore conductance can result from individual voltage sensor movements. Proc Natl Acad Sci U S A 116:7879–7888 . https://doi.org/10.1073/pnas.1811623116

350. Osteen JD, Gonzalez C, Sampson KJ, Iyer V, Rebolledo S, Larsson HP, Kass RS (2010) KCNE1 alters the voltage sensor movements necessary to open the KCNQ1 channel gate. Proc Natl Acad Sci U S A 107:22710–22715 . https://doi.org/10.1073/pnas.1016300108

351. Kang PW, Westerlund AM, Shi J, White KM, Dou AK, Cui AH, Silva JR, Delemotte L, Cui J (2020) Calmodulin acts as a state-dependent switch to control a cardiac potassium channel opening. bioRxiv 2020.07.04.187161 . https://doi.org/10.1101/2020.07.04.187161

352. Westerlund AM, Fleetwood O, Perez-conesa S, Delemotte L (2020) Network analysis reveals how lipids and other cofactors influence membrane protein allostery. bioRxiv 1–19 . https://doi.org/10.1101/2020.07.06.187484

353. Kasimova MA, Tarek M, Shaytan AK, Shaitan K V, Delemotte L (2014) Voltage-gated ion channel modulation by lipids: insights from molecular dynamics simulations. Biochim Biophys Acta 1838:1322–1331 . https://doi.org/10.1016/j.bbamem.2014.01.024

354. Koshland DE, Némethy G, Filmer D (1966) Comparison of Experimental Binding Data and Theoretical Models in Proteins Containing Subunits *. Biochemistry 5:365–385 . https://doi.org/10.1021/bi00865a047

355. Saarinen K, Swan H, Kainulainen K, Toivonen L, Viitasalo M, Kontula K (1998) Molecular genetics of the long QT syndrome: Two novel mutations of the KVLQT1 gene and phenotypic expression of the mutant gene in a large kindred. Hum Mutat 11:158–165 . https://doi.org/10.1002/(SICI)1098-1004(1998)11:2<158::AID-HUMU9>3.0.CO;2-F

356. Mohammad-Panah R, Demolombe S, Neyroud N, Guicheney P, Kyndt F, Van Den Hoff M, Barö I, Escande D (1999) Mutations in a dominant-negative isoform correlate with phenotype in inherited cardiac arrhythmias. Am J Hum Genet 64:1015–1023 . https://doi.org/10.1086/302346

357. Millat G, Chevalier P, Restier-Miron L, Da Costa A, Bouvagnet P, Kugener B, Fayol L, Gonzàlez Armengod C, Oddou B, Chanavat V, Froidefond E, Perraudin R, Rousson R, Rodriguez-Lafrasse C (2006) Spectrum of pathogenic mutations and associated polymorphisms in a cohort of 44 unrelated patients with long QT syndrome. Clin Genet 70:214–227 . https://doi.org/10.1111/j.1399-0004.2006.00671.x

358. Xu J, Rudy Y (2018) Effects of β-subunit on gating of a potassium ion channel: Molecular simulations of cardiac IKs activation. J Mol Cell Cardiol 124:35–44 . https://doi.org/10.1016/j.yjmcc.2018.10.003

359. Fernández-Mariño AI, Harpole TJ, Oelstrom K, Delemotte L, Chanda B (2018) Gating interaction maps reveal a noncanonical electromechanical coupling mode in the Shaker K+ channel. Nat Struct Mol Biol 25:320–326 . https://doi.org/10.1038/s41594-018-0047-3

360. Franqueza L, Lin M, Splawski I, Keating MT, Sanguinetti MC (1999) Long QT Syndrome-associated Mutations in the S4-S5 Linker of KvLQT1 Potassium Channels Modify Gating and Interaction with minK Subunits. J Biol Chem 274:21063–21070 . https://doi.org/10.1074/jbc.274.30.21063

361. Itoh T, Tanaka T, Nagai R, Kikuchi K, Ogawa S, Okada S, Yamagata S, Yano K, Yazaki Y, Nakamura Y (1998) Genomic organization and mutational analysis of KVLQT1, a gene responsible for familial long QT syndrome. Hum Genet 103:290–294 . https://doi.org/10.1007/s004390050819

362. Deschênes D, Acharfi S, Pouliot V, Hegele R, Krahn A, Daleau P, Chahine M (2003) Biophysical characteristics of a new mutation on the KCNQ1 potassium channel (L251P) causing long QT syndrome. Can J Physiol Pharmacol 81:129–134 . https://doi.org/10.1139/y02-162

363. Donger C, Denjoy I, Berthet M, Neyroud N, Cruaud C, Bennaceur M, Chivoret G, Schwartz K, Coumel P, Guicheney P (1997) KVLQT1 C-terminal missense mutation causes a forme fruste long-QT syndrome. Circulation 96:2778–2781 . https://doi.org/10.1161/01.CIR.96.9.2778

364. Choi G, Kopplin LJ, Tester DJ, Will ML, Haglund CM, Ackerman MJ (2004) Spectrum and frequency of cardiac channel defects in swimming-triggered arrhythmia syndromes. Circulation 110:2119–2124 . https://doi.org/10.1161/01.CIR.0000144471.98080.CA

365. Tester DJ, Will ML, Haglund CM, Ackerman MJ (2005) Compendium of cardiac channel mutations in 541 consecutive unrelated patients referred for long QT syndrome genetic testing. Hear Rhythm 2:507–517 . https://doi.org/10.1016/j.hrthm.2005.01.020

366. Kubota T, Shimizu W, Kamakura S, Horie M (2000) Hypokalemia-induced long QT syndrome with an underlying novel missense mutation in S4-S5 linker of KCNQ1. J Cardiovasc Electrophysiol 11:1048–1054 . https://doi.org/10.1111/j.1540-8167.2000.tb00178.x

367. Jongbloed R, Marcelis C, Velter C, Doevendans P, Geraedts J, Smeets H (2002) DHPLC analysis of potassium ion channel genes in congenital long QT syndrome. Hum Mutat 20:382–391 . https://doi.org/10.1002/humu.10131

368. Van Langen IM, Birnie E, Alders M, Jongbloed RJ, Le Marec H, Wilde AAM (2003) The use of genotype-phenotype correlations in mutation analysis for the long QT syndrome [1]. J. Med. Genet. 40:141–145

369. Lewis A, Jogini V, Blachowicz L, Lainé M, Roux B (2008) Atomic Constraints between the Voltage Sensor and the Pore Domain in a Voltage-gated K+ Channel of Known Structure. J Gen Physiol 131:549–561 . https://doi.org/10.1085/jgp.200809962

370. Shamgar L, Haitin Y, Yisharel I, Malka E, Schottelndreier H, Peretz A, Paas Y, Attali B (2008) KCNE1 Constrains the Voltage Sensor of Kv7.1 K+ Channels. PLoS One 3:e1943 . https://doi.org/10.1371/journal.pone.0001943

371. Perozo E, Cortes DM, Cuello LG (1999) Structural rearrangements underlying K+-channel activation gating. Science (80-) 285:73–78 . https://doi.org/10.1126/science.285.5424.73

372. YAMAGUCHI M, SHIMIZU M, INO H, TERAI H, HAYASHI K, MABUCHI H, HOSHI N, HIGASHIDA H (2003) Clinical and electrophysiological characterization of a novel mutation (F193L) in the KCNQ1 gene associated with long QT syndrome. Clin Sci 104:6 . https://doi.org/10.1042/CS20020152

373. Napolitano C, Priori SG, Schwartz PJ, Bloise R, Ronchetti E, Nastoli J, Bottelli G, Cerrone M, Leonardi S (2005) Genetic Testing in the Long QT Syndrome. J Am Med Assoc 294:2975 . https://doi.org/10.1001/jama.294.23.2975

374. Ackerman MJ, Tester DJ, Porter CBJ, Edwards WD (1999) Molecular diagnosis of the inherited long-QT syndrome in a woman who died after near-drowning. N Engl J Med 341:1121–1125 . https://doi.org/10.1056/NEJM199910073411504

375. Delemotte L, Kasimova MA, Klein ML, Tarek M, Carnevale V (2015) Free-energy landscape of ion-channel voltage-sensor–domain activation. Proc Natl Acad Sci 112:124–129 . https://doi.org/10.1073/pnas.1416959112

376. Sigg D, Bezanilla F, Stefani E (2003) Fast gating in the Shaker K+ channel and the energy landscape of activation. Proc Natl Acad Sci 100:7611–7615 . https://doi.org/10.1073/pnas.1332409100

377. Solano CJF, Pothula KR, Prajapati JD, De Biase PM, Noskov SY, Kleinekathöfer U (2016) BROMOCEA Code: An Improved Grand Canonical Monte Carlo/Brownian Dynamics Algorithm Including Explicit Atoms. J Chem Theory Comput 12:2401–2417 . https://doi.org/10.1021/acs.jctc.5b01196

378. Balusek C, Hwang H, Lau CH, Lundquist K, Hazel A, Pavlova A, Lynch DL, Reggio PH, Wang Y, Gumbart JC (2019) Accelerating Membrane Simulations with Hydrogen Mass Repartitioning. J Chem Theory Comput 15:4673–4686 . https://doi.org/10.1021/acs.jctc.9b00160

379. Manderfield LJ, George AL (2008) KCNE4 can co-associate with the IKs (KCNQ1-KCNE1) channel complex. FEBS J 275:1336–1349 . https://doi.org/10.1111/j.1742-4658.2008.06294.x

380. Rivoire O, Reynolds KA, Ranganathan R (2016) Evolution-Based Functional Decomposition of Proteins. PLoS Comput Biol 12:1004817 . https://doi.org/10.1371/journal.pcbi.1004817

381. Yang T, Smith JA, Leake BF, Sanders CR, Meiler J, Roden DM (2013) An Allosteric Mechanism for Drug Block of the Human Cardiac Potassium Channel KCNQ1. Mol Pharmacol 83:481–489 . https://doi.org/10.1124/mol.112.081513

382. Kodama I, Kamiya K, Toyama J (1997) Cellular electropharmacology of amiodarone. Oxford Academic

383. Heijman J, Heusch G, Dobrev D (2013) Pleiotropic effects of antiarrhythmic agents: Dronedarone in the treatment of atrial fibrillation. Clin. Med. Insights Cardiol. 7:127–140

384. Gogelein H, Bruggemann A, Gerlach U, Brendel J, Busch AE (2000) Inhibition of I(Ks) channels by HMR 1556. Naunyn Schmiedebergs Arch Pharmacol 362:480–488 . https://doi.org/10.1007/s002100000284

385. Bosch RF, Gaspo R, Busch AE, Lang HJ, Li GR, Nattel S (1998) Effects of the chromanol 293B, a selective blocker of the slow, component of the delayed rectifier K+ current, on repolarization in human and guinea pig ventricular myocytes. Cardiovasc Res 38:441–450 . https://doi.org/10.1016/S0008-6363(98)00021-2

386. Lerche C, Bruhova I, Lerche H, Steinmeyer K, Wei AD, Strutz-Seebohm N, Lang F, Busch AE, Zhorov BS, Seebohm G (2007) Chromanol 293B Binding in KCNQ1 (Kv7.1) Channels Involves Electrostatic Interactions with a Potassium Ion in the Selectivity Filter. Mol Pharmacol 71:1503–1511 . https://doi.org/10.1124/mol.106.031682

387. Gallacher DJ, Van de Water A, van der Linde H, Hermans AN, Lu HR, Towart R, Volders PGA (2007) In vivo mechanisms precipitating torsades de pointes in a canine model of drug-induced long-QT1 syndrome. Cardiovasc Res 76:247–256 . https://doi.org/10.1016/j.cardiores.2007.06.019

388. Butcher JW, Liverton NJ, Claremon DA, Freidinger RM, Jurkiewicz NK, Lynch JJ, Salata JJ, Wang J, Dieckhaus CM, Slaughter DE, Vyas K (2003) Novel 5-cyclopropyl-1,4-benzodiazepin-2-ones as potent and selective IKs-blocking class III antiarrhythmic agents. Bioorganic Med Chem Lett 13:1165–1168 . https://doi.org/10.1016/S0960-894X(03)00049-0

389. Fontana DJ, Inouye GT, Johnson RM, Fontana DJ, Inouye GT, Linopirdine RMJ (1994) Linopirdine (DuP 996) Improves Performance in Several Tests of Learning and Memory by Modulation of Cholinergic Neurotransmission

390. Wang H-S, Brown BS, McKinnon D, Cohen IS (2000) Molecular Basis for Differential Sensitivity of KCNQ and IKs Channels to the Cognitive Enhancer XE991. Mol Pharmacol 57:1218–1223

391. Greene DL, Kang S, Hoshi N (2017) XE991 and linopirdine are state-dependent inhibitors for Kv7/KCNQ channels that favor activated single subunits. J Pharmacol Exp Ther 362:177–185 . https://doi.org/10.1124/jpet.117.241679

392. Salata JJ, Jurkiewicz NK, Wang J, Evans BE, Orme HT, Sanguinetti MC (1998) A novel benzodiazepine that activates cardiac slow delayed rectifier K+ currents. Mol Pharmacol 54:220–230 . https://doi.org/10.1124/mol.54.1.220

393. Seebohm G, Pusch M, Chen J, Sanguinetti MC (2003) Pharmacological Activation of Normal and Arrhythmia-Associated Mutant KCNQ1 Potassium Channels. Circ Res 93:941–947 . https://doi.org/10.1161/01.RES.0000102866.67863.2B

394. Leite TB, Gomes D, Miteva MA, Chomilier J, Villoutreix BO, Tuffery P (2007) Frog: a FRee Online druG 3D conformation generator. Nucleic Acids Res 35:W568–W572 . https://doi.org/10.1093/nar/gkm289

395. Mattmann ME, Yu H, Lin Z, Xu K, Huang X, Long S, Wu M, McManus OB, Engers DW, Le UM, Li M, Lindsley CW, Hopkins CR (2012) Identification of (R)-N-(4-(4-methoxyphenyl)thiazol-2-yl)-1-tosylpiperidine-2-carboxamide, ML277, as a novel, potent and selective Kv7.1 (KCNQ1) potassium channel activator. Bioorg Med Chem Lett 22:5936–5941 . https://doi.org/10.1016/j.bmcl.2012.07.060

396. Liin SI, Ejneby MS, Barro-Soria R, Skarsfeldt MA, Larsson JE, Härlin FS, Parkkari T, Bentzen BH, Schmitt N, Larsson HP, Elinder F (2015) Polyunsaturated fatty acid analogs act antiarrhythmically on the cardiac IKs channel. Proc Natl Acad Sci U S A 112:5714–5719 . https://doi.org/10.1073/pnas.1503488112

397. Liin SI, Larsson JE, Barro-Soria R, Bentzen BH, Peter Larson H (2016) Fatty acid analogue N-arachidonoyl taurine restores function of IKs channels with diverse long QT mutations. Elife 5:1–19 . https://doi.org/10.7554/eLife.20272

398. Larsson JE, Larsson HP, Liin SI (2018) KCNE1 tunes the sensitivity of K v 7.1 to polyunsaturated fatty acids by moving turret residues close to the binding site. Elife 7: . https://doi.org/10.7554/eLife.37257

399. Liin SI, Yazdi S, Ramentol R, Barro-Soria R, Larsson HP (2018) Mechanisms Underlying the Dual Effect of Polyunsaturated Fatty Acid Analogs on Kv7.1. Cell Rep 24:2908–2918 . https://doi.org/10.1016/j.celrep.2018.08.031

400. Klauda JB, Monje V, Kim T, Im W (2012) Improving the CHARMM force field for polyunsaturated fatty acid chains. J Phys Chem B 116:9424–9431 . https://doi.org/10.1021/jp304056p

401. Keirns J, Desai A, Kowalski D, Lademacher C, Mujais S, Parker B, Schneidkraut MJ, Townsend R, Wojtkowski T, Yamazaki T, Yen M, Kowey PR (2017) QT Interval Shortening With Isavuconazole: In Vitro and In Vivo Effects on Cardiac Repolarization. Clin Pharmacol Ther 101:782–790 . https://doi.org/10.1002/cpt.620

402. Tian M, Dong MQ, Chiu SW, Lau CP, Li GR (2006) Effects of the antifungal antibiotic clotrimazole on human cardiac repolarization potassium currents. Br J Pharmacol 147:289–297 . https://doi.org/10.1038/sj.bjp.0706590

403. Villatoro-Gómez K, Pacheco-Rojas DO, Moreno-Galindo EG, Navarro-Polanco RA, Tristani-Firouzi M, Gazgalis D, Cui M, Sánchez-Chapula JA, Ferrer T (2018) Molecular determinants of Kv7.1/KCNE1 channel inhibition by amitriptyline. Biochem Pharmacol 152:264–271 . https://doi.org/10.1016/j.bcp.2018.03.016

404. Banyasz T, Koncz R, Fulop L, Szentandrassy N, Magyar J, Nanasi P (2005) Profile of IKs During the Action Potential Questions the Therapeutic Value of IKs Blockade. Curr Med Chem 11:45–60 . https://doi.org/10.2174/0929867043456304

405. (2008) International Conference on Harmonisation of Technical Requirements for Registration of Pharmaceuticals for Human Use (ICH)

406. Zemzemi N, Bernabeu MO, Saiz J, Cooper J, Pathmanathan P, Mirams GR, Pitt-Francis J, Rodriguez B (2013) Computational assessment of drug-induced effects on the electrocardiogram: From ion channel to body surface potentials. Br J Pharmacol 168:718–733 . https://doi.org/10.1111/j.1476-5381.2012.02200.x

407. Obiol-Pardo C, Gomis-Tena J, Sanz F, Saiz J, Pastor M (2011) A multiscale simulation system for the prediction of drug-induced cardiotoxicity. J Chem Inf Model 51:483–492 . https://doi.org/10.1021/ci100423z

408. Towart R, Linders JTM, Hermans AN, Rohrbacher J, van der Linde HJ, Ercken M, Cik M, Roevens P, Teisman A, Gallacher DJ (2009) Blockade of the IKs potassium channel: An overlooked cardiovascular liability in drug safety screening? J Pharmacol Toxicol Methods 60:1–10 . https://doi.org/10.1016/j.vascn.2009.04.197

409. Roden DM (2016) Predicting drug-induced QT prolongation and torsades de pointes. J Physiol 594:2459–2468 . https://doi.org/10.1113/JP270526

410. Jankelson L, Karam G, Becker ML, Chinitz LA, Tsai M-CC (2020) QT prolongation, torsades de pointes, and sudden death with short courses of chloroquine or hydroxychloroquine as used in COVID-19: A systematic review. Hear Rhythm 17:1472–1479 . https://doi.org/10.1016/j.hrthm.2020.05.008

411. de Olano J, Howland MA, Su MK, Hoffman RS, Biary R (2019) Toxicokinetics of hydroxychloroquine following a massive overdose. Am J Emerg Med 37:2264.e5-2264.e8 . https://doi.org/10.1016/j.ajem.2019.158387

412. Hooks M, Bart B, Vardeny O, Westanmo A, Adabag S (2020) Effects of hydroxychloroquine treatment on QT interval. Hear Rhythm 6–11 . https://doi.org/10.1016/j.hrthm.2020.06.029

413. Joyce E, Fabre A, Mahon N (2013) Hydroxychloroquine cardiotoxicity presenting as a rapidly evolving biventricular cardiomyopathy: Key diagnostic features and literature review. Eur Hear J Acute Cardiovasc Care 2:77–83 . https://doi.org/10.1177/2048872612471215

414. Clemessy JL, Borron SW, Baud FJ, Favier C, Hantson PE, Vicaut E (1995) Hypokalaemia related to acute chloroquine ingestion. Lancet 346:877–880 . https://doi.org/10.1016/S0140-6736(95)92711-5

415. Traebert M, Dumotier B, Meister L, Hoffmann P, Dominguez-Estevez M, Suter W (2004) Inhibition of hERG K+ currents by antimalarial drugs in stably transfected HEK293 cells. Eur J Pharmacol 484:41–48 . https://doi.org/10.1016/j.ejphar.2003.11.003

416. Beuckelmann DJ, Näbauer M, Erdmann E (1993) Alterations of K+ currents in isolated human ventricular myocytes from patients with terminal heart failure. Circ Res 73:379–385 . https://doi.org/10.1161/01.RES.73.2.379

417. Virág L, Iost N, Opincariu M, Szolnoky J, Szécsi J, Bogáts G, Szenohradszky P, Varró A, Papp JG (2001) The slow component of the delayed rectifier potassium current in undiseased human ventricular myocytes. Cardiovasc Res 49:790–797 . https://doi.org/10.1016/S0008-6363(00)00306-0

418. Anwar-Mohamed A, Barakat KH, Bhat R, Noskov SY, Tyrrell DL, Tuszynski JA, Houghton M (2014) A human ether-á-go-go-related (hERG) ion channel atomistic model generated by long supercomputer molecular dynamics simulations and its use in predicting drug cardiotoxicity. Toxicol Lett 230:382–392 . https://doi.org/10.1016/j.toxlet.2014.08.007

419. Morris GM, Goodsell DS, Halliday RS, Huey R, Hart WE, Belew RK, Olson AJ, Lindstrom W, Sanner MF, Belew RK, Goodsell DS, Olson AJ, Halliday RS, Huey R, Hart WE, Belew RK, Olson AJ (2009) AutoDock4 and AutoDockTools4: Automated docking with selective receptor flexibility. J Comput Chem 30:2785–2791 . https://doi.org/10.1002/jcc.21256

420. Morris GM, Goodsell DS, Halliday RS, Huey R, Hart WE, Belew RK, Olson AJ (1998) Automated docking using a Lamarckian genetic algorithm and an empirical binding free energy function. J Comput Chem 19:1639–1662 . https://doi.org/10.1002/(SICI)1096-987X(19981115)19:14<1639::AID-JCC10>3.0.CO;2-B

421. Huey R, Morris GM, Olson AJ, Goodsell DS (2007) Software news and update a semiempirical free energy force field with charge-based desolvation. J Comput Chem 28:1145–1152 . https://doi.org/10.1002/jcc.20634

422. Vanommeslaeghe K, Hatcher E, Acharya C, Kundu S, Zhong S, Shim J, Darian E, Guvench O, Lopes P, Vorobyov I, Mackerell AD (2009) CHARMM general force field: A force field for drug-like molecules compatible with the CHARMM all-atom additive biological force fields. J Comput Chem NA-NA . https://doi.org/10.1002/jcc.21367

423. Vanommeslaeghe K, MacKerell AD (2012) Automation of the CHARMM General Force Field (CGenFF) I: bond perception and atom typing. J Chem Inf Model 52:3144–3154 . https://doi.org/10.1021/ci300363c

424. Vanommeslaeghe K, Raman EP, MacKerell AD, Raman EP, MacKerell AD (2012) Automation of the {CHARMM} {General} {Force} {Field} ({CGenFF}) {II}: {Assignment} of {Bonded} {Parameters} and {Partial} {Atomic} {Charges}. J Chem Inf Model 52:3155–3168 . https://doi.org/10.1021/ci3003649

425. Mayne CG, Saam J, Schulten K, Tajkhorshid E, Gumbart JC (2013) Rapid parameterization of small molecules using the force field toolkit. J Comput Chem 34:2757–2770 . https://doi.org/10.1002/jcc.23422

426. M. J. Frisch, G. W. Trucks, H. B. Schlegel, G. E. Scuseria, M. A. Robb, J. R. Cheeseman, G. Scalmani, V. Barone, G. A. Petersson, H. Nakatsuji, X. Li, M. Caricato, A. Marenich, J. Bloino, B. G. Janesko, R. Gomperts, B. Mennucci, H. P. Hratchian, J. V. Ort DJF (2016) Gaussian 09

427. Hille B (1992) Ionic channels of excitable membranes, Second edi. Sinauer Associates, Sunderland Mass.

428. Chung S-H, Allen TW, Hoyles M, Kuyucak S (1999) Permeation of Ions Across the Potassium Channel: Brownian Dynamics Studies. Biophys J 77:2517–2533 . https://doi.org/10.1016/S0006-3495(99)77087-6

429. Im W, Seefeld S, Roux B (2000) A grand canonical Monte Carlo-Brownian Dynamics algorithm for simulating ion channels. Biophys J 79:788–801 . https://doi.org/10.1016/S0006-3495(00)76336-3

430. Roux B (1999) Statistical mechanical equilibrium theory of selective ion channels. Biophys J 77:139–153 . https://doi.org/10.1016/S0006-3495(99)76878-5

431. Im W, Roux B (2002) Ion Permeation and Selectivity of OmpF Porin: A Theoretical Study Based on Molecular Dynamics, Brownian Dynamics, and Continuum Electrodiffusion Theory. J Mol Biol 322:851–869 . https://doi.org/10.1016/S0022-2836(02)00778-7

432. Song C, Corry B (2011) Testing the Applicability of Nernst-Planck Theory in Ion Channels: Comparisons with Brownian Dynamics Simulations. PLoS One 6:e21204 . https://doi.org/10.1371/journal.pone.0021204

433. Kutzner C, Grubmüller H, de Groot BL, Zachariae U (2011) Computational Electrophysiology: The Molecular Dynamics of Ion Channel Permeation and Selectivity in Atomistic Detail. Biophys J 101:809–817 . https://doi.org/10.1016/j.bpj.2011.06.010

434. Berneche S, Roux B (2003) A microscopic view of ion conduction through the K+ channel. Proc Natl Acad Sci 100:8644–8648

435. Treptow W, Tarek M (2006) K+ Conduction in the Selectivity Filter of Potassium Channels Is Monitored by the Charge Distribution along Their Sequence. Biophys J 91:L81–L83 . https://doi.org/10.1529/biophysj.106.095992

436. Kutzner C, Köpfer DA, Machtens J-P, de Groot BL, Song C, Zachariae U (2016) Insights into the function of ion channels by computational electrophysiology simulations. Biochim Biophys Acta - Biomembr 1858:1741–1752 . https://doi.org/10.1016/j.bbamem.2016.02.006

437. Delemotte L, Kasimova M, Sigg D, Klein M, Carnevale V, Tarek M (2017) Exploring the Complex Dynamics of an Ion Channel Voltage Sensor Domain via Computation. bioRxiv 108217 . https://doi.org/10.1101/108217

438. Fleetwood O, Kasimova MA, Westerlund AM, Delemotte L (2020) Molecular Insights from Conformational Ensembles via Machine Learning. Biophys J 118:765–780 . https://doi.org/10.1016/j.bpj.2019.12.016

439. Towell GG, Shavlik JW (1994) Knowledge-based artificial neural networks

440. Verkhivker GM, Agajanian S, Hu G, Tao P (2020) Allosteric Regulation at the Crossroads of New Technologies: Multiscale Modeling, Networks, and Machine Learning. Front. Mol. Biosci. 7:136

441. Mussig K, Staiger H, Machicao F, Kirchhoff K, Guthoff M, Schafer SA, Kantartzis K, Silbernagel G, Stefan N, Holst JJ, Gallwitz B, Haring H-U, Fritsche A (2009) Association of Type 2 Diabetes Candidate Polymorphisms in KCNQ1 With Incretin and Insulin Secretion. Diabetes 58:1715–1720 . https://doi.org/10.2337/db08-1589

442. van Vliet-Ostaptchouk J V, van Haeften TW, Landman GWD, Reiling E, Kleefstra N, Bilo HJG, Klungel OH, de Boer A, van Diemen CC, Wijmenga C, Boezen HM, Dekker JM, van 't Riet E, Nijpels G, Welschen LMC, Zavrelova H, Bruin EJ, Elbers CC, Bauer F, Onland-Moret NC, van der Schouw YT, Grobbee DE, Spijkerman AMW, van der A DL, Simonis-Bik AM, Eekhoff EMW, Diamant M, Kramer MHH, Boomsma DI, de Geus EJ, Willemsen G, Slagboom PE, Hofker MH, 't Hart LM (2012) Common Variants in the Type 2 Diabetes KCNQ1 Gene Are Associated with Impairments in Insulin Secretion During Hyperglycaemic Glucose Clamp. PLoS One 7:e32148 . https://doi.org/10.1371/journal.pone.0032148

443. Adeyemo AA, Tekola-Ayele F, Doumatey AP, Bentley AR, Chen G, Huang H, Zhou J, Shriner D, Fasanmade O, Okafor G, Eghan BJ, Agyenim-Boateng K, Adeleye J, Balogun W, Elkahloun A, Chandrasekharappa S, Owusu S, Amoah A, Acheampong J, Johnson T, Oli J, Adebamowo C, Collins F, Dunston G, Rotimi CN (2015) Evaluation of Genome Wide Association Study Associated Type 2 Diabetes Susceptibility Loci in Sub Saharan Africans. Front Genet 6: . https://doi.org/10.3389/fgene.2015.00335

444. Chen L, Magliano DJ, Zimmet PZ (2012) The worldwide epidemiology of type 2 diabetes mellitus - Present and future perspectives. Nat Rev Endocrinol 8:228–236 . https://doi.org/10.1038/nrendo.2011.183

445. Unoki H, Takahashi A, Kawaguchi T, Hara K, Horikoshi M, Andersen G, Ng DPK, Holmkvist J, Borch-Johnsen K, Jørgensen T, Sandbæk A, Lauritzen T, Hansen T, Nurbaya S, Tsunoda T, Kubo M, Babazono T, Hirose H, Hayashi M, Iwamoto Y, Kashiwagi A, Kaku K, Kawamori R, Tai ES, Pedersen O, Kamatani N, Kadowaki T, Kikkawa R, Nakamura Y, Maeda S (2008) SNPs in KCNQ1 are associated with susceptibility to type 2 diabetes in East Asian and European populations. Nat Genet 40:1098–1102 . https://doi.org/10.1038/ng.208

446. Yamagata K, Senokuchi T, Lu M, Takemoto M, Fazlul Karim M, Go C, Sato Y, Hatta M, Yoshizawa T, Araki E, Miyazaki J, Song W-J (2011) Voltage-gated K+ channel KCNQ1 regulates insulin secretion in MIN6 β-cell line. Biochem Biophys Res Commun 407:620–625 . https://doi.org/10.1016/j.bbrc.2011.03.083

447. Min Lee S, Baik J, Nguyen D, Nguyen V, Liu S, Hu Z, Abbott GW (2017) Kcne2 deletion impairs insulin secretion and causes type 2 diabetes mellitus. FASEB J 31:2674–2685 . https://doi.org/10.1096/fj.201601347

448. Torekov SS, Iepsen E, Christiansen M, Linneberg A, Pedersen O, Holst JJ, Kanters JK, Hansen T (2014) KCNQ1 Long QT Syndrome Patients Have Hyperinsulinemia and Symptomatic Hypoglycemia. Diabetes 63:1315–1325 . https://doi.org/10.2337/db13-1454

449. Zhou X, Zhu J, Bao Z, Shang Z, Wang T, Song J, Sun J, Li W, Adelusi TI, Wang Y, Lv D, Lu Q, Yin X (2016) A variation in KCNQ1 gene is associated with repaglinide efficacy on insulin resistance in Chinese Type 2 Diabetes Mellitus Patients. Sci Rep 6:1–11 . https://doi.org/10.1038/srep37293

Résumé

Le canal $K_V7.1$ est une protéine transmembranaire diffusant des ions K^+ de manière sélective à travers la membrane plasmique lorsque cette dernière se dépolarise. Au sein du myocarde, $K_V7.1$ est co-exprimé avec la sous-unité auxiliaire KCNE1. Plusieurs expériences ont mis en évidence les effets de KCNE1 sur l'activité de $K_V7.1$, lui conférant des propriétés permettant au complexe $K_V7.1$-KCNE1 de générer le courant IK_S lors du potentiel d'action cardiaque. Les nombreuses mutations au niveau des séquences de $K_V7.1$ et KCNE1 associées à des arythmies cardiaques sévères font du canal $K_V7.1$ une cible thérapeutique majeure.

$K_V7.1$ est un tétramère dont chaque sous-unité α compte six hélices transmembranaires (S1 à S6). Les quatre premières hélices forment le domaine sensible au voltage (VSD), tandis que les deux dernières forment celui du pore (PD). Le mécanisme d'activation de $K_V7.1$ s'effectue par le biais d'une translation de l'hélice S4 vers le haut en deux étapes, stabilisant le VSD en trois états stables : repos, intermédiaire, et activé. Ces conformations sont capables d'ouvrir ou de fermer le pore via un processus appelé couplage. Ainsi, les états du canal $K_V7.1$ sont Repos/Fermé (RC), Intermédiaire/Ouvert (IO) et Activé/Ouvert. En présence de KCNE1, le couplage n'a pas lieu à l'état intermédiaire, donc les états du canal IK_S sont RC, Intermédiaire/Fermé (IC) et AO. En outre, le phospholipide PIP_2 (phosphatidylinositol-4,5-bisphosphate) joue un rôle crucial dans le couplage VSD-PD et l'ouverture du pore des canaux K_V7.

Malgré les informations apportées par les études fonctionnelles et structurales du canal $K_V7.1$, en absence et en présence de ses modulateurs KCNE1 et PIP_2, le mécanisme de son couplage à l'échelle atomistique reste à découvrir.

Nous avons abordé ce problème en exploitant des techniques computationnelles telles la dynamique moléculaire (DM). Etant donnée la complexité de la fonction de $K_V7.1$, cette étude avait deux objectifs, le premier étant d'identifier les interactions protéine-protéine stabilisant chacun de ses états, le deuxième étant de décrire les effets de ses modulateurs. Nous avons bâti des modèles par homologie de $K_V7.1$ dans ses trois états, en utilisant la structure cristallographique du canal homologue $K_V1.2$ comme patron. Nous avons effectué des simulations de DM de 500 ns pour chaque modèle, encastré dans une membrane virtuelle entourée de deux couches d'une solution de [KCl] à 150 mM, afin de reproduire une dynamique réaliste du canal dans nos systèmes, et ce en absence et en présence de KCNE1 et de PIP_2.

L'analyse des trajectoires DM obtenues visait à valider nos modèles par rapport aux données expérimentales. Par la suite, nous avons identifié les interactions « état-dépendantes » dans les modèles les plus robustes, permettant de prédire les changements de conformation inhérents à l'activation de $K_V7.1$. Nos modèles ont été validés par des études fonctionnelles menées par nos collaborateurs (Pr. Jianmin Cui) de l'université Washington de Saint-Louis, Etats-Unis. Cette étude intégrative a révélé un couplage inédit, conceptualisé par un modèle « main- et-coude » ayant lieu dans l'ensemble des familles de canaux K_V1 à K_V9.

L'hélice S6 de $K_V7.1$ présente un motif SFF (338-340) fortement conservé au sein des canaux de la famille K_V7. L'espace conformationnel des résidus SFF au sein des trajectoires DM de $K_V7.1$ et d'IK_S ont révélé l'existence d'une porte hydrophobe inédite, définie par des orientations « état-dépendantes » de F339 et F340, et validée par des études fonctionnelles.

Les analyses des trajectoires DM de IK_S indiquent qu'un garrot, formé par les interactions entre KCNE1 et PIP_2 autour de la région intracellulaire des hélices S6, induisent la fermeture du pore dans les états RC et IC. Enfin, la recherche des déterminants moléculaires de la modulation du couplage de $K_V7.1$ par KCNE1 indique que ce dernier perturbe le modèle « main-et-coude » conçu à la base pour le canal $K_V7.1$.

Mots clés :
Canaux ioniques voltage-dépendants, Activation des canaux ioniques, lipides PIP_2, Modélisation moléculaire, Dynamique moléculaire.

Abstract

$K_V7.1$ channel is a transmembrane protein that open to selectively diffuse K^+ ions across the plasma membrane upon membrane depolarization. In the myocardium tissue, $K_V7.1$ channel is co-expressed with the ancillary subunit KCNE1. Several experiments conducted on $K_V7.1$ along with KCNE1 revealed its effects on $K_V7.1$ function, which modify its properties allowing for $K_V7.1$-KCNE1 complex to generate the IK_S current during cardiac action potential. As numerous mutations of $K_V7.1$ and KCNE1 sequences are linked to severe cardiac arrhythmias, $K_V7.1$ channel constitutes a major therapeutic target.

Each α-subunit of $K_V7.1$ tetramer counts six transmembrane helices (S1 to S6), the first four ones forming the voltage-sensor domain (VSD), and the last two ones forming the pore domain (PD). This channel has a 2-step activation mechanism involving an upward translation of S4 across the membrane and stabilizing the VSD in three stable states: resting, intermediate and activated. These conformations can induce pore opening or closure by a process called VSD-PD coupling. Accordingly, the states for $K_V7.1$ channel are Resting/Closed (RC), Intermediate/Open (IO) and Activated/Open (AO). In the presence of KCNE1, the coupling is suppressed for the intermediate state, thus the states for IK_S channel are RC, Intermediate/Closed (IC) and AO. Furthermore, the phospholipid PIP_2 (phosphatidylinositol-4,5-bisphosphate) plays a crucial role in the VSD-PD coupling and pore opening of K_V7 channels.

Despite the information drawn from both functional and structural studies of $K_V7.1$ channel in absence and presence of its modulators KCNE1 and PIP_2, its VSD-PD coupling mechanism remains unclear at an atomistic level.

To address this issue, we harnessed computational techniques, including molecular dynamics (MD) simulations. Given the complexity of $K_V7.1$ function, the study had two main objectives. The first one was the identification of the protein-protein interactions which stabilize each $K_V7.1$ state model. The second one was the characterization of the modulation effects of PIP_2 and KCNE1 on $K_V7.1$ α-subunits. We built homology models of $K_V7.1$ in its three states, using the crystallographic structure of homologous $K_V1.2$ channel as a template. We conducted 500 ns MD simulations on each model embedded in a virtual membrane surrounded by two slabs of a 150 mM [KCl] solution to reproduce a realistic dynamics of the channel in our MD systems, in absence and presence of KCNE1 subunits and PIP_2 molecules. The analyses of MD trajectories aimed at validating the models with respect to experimental data. Then, we proceeded to identify the state-dependent interactions in the most robust models, allowing for the prediction of the conformational changes required for $K_V7.1$ activation.

Our Kv7.1 models were validated via functional studies conducted by our collaborators (Pr. Jianmin Cui) from Washington University of Saint-Louis in the USA. Altogether, the joint study revealed a novel VSD-PD coupling mechanism that we conceptualized by a "hand-and-elbow model" likely to occur in all domain swapped (K_V1- K_V7) channels.

The S6 helix of $K_V7.1$ has a motif SFF (338-340), highly conserved in K_V7 family. The conformational space of SFF residues in $K_V7.1$ and IK_S MD trajectories revealed the existence of an unidentified hydrophobic gate defined by state-dependent orientations of F339 and F340, which was also validated by functional studies.

The analyses of IK_S MD trajectories suggest that the interactions between KCNE1 and PIP_2 form a tourniquet around the cytoplasmic region of S6, leading to pore closure in both RC and IC models. Finally, the investigation of the molecular determinants of the modulation of $K_V7.1$ VSD-PD coupling mechanism by KCNE1 in our IK_S models suggests that KCNE1 disrupts the "hand-and-elbow model" of the VSD-PD coupling we previously designed for $K_V7.1$ channel.

Keywords:
Voltage-gated Ion channels, Ion channels activation, PIP_2 lipids, molecular modeling, molecular dynamics.